Measurement of time-dependent CP asymmetries in the decays $B \to D^*\pi$ using a partial reconstruction technique

A dissertation submitted to the

Doctorate of Research and Advanced Studies
of the University of Cincinnati,

in partial fulfillment of the
requirements for the degree of

DOCTORATE OF PHILOSOPHY (Ph.D.)

in the Department of Physics
of the College of Arts and Sciences

2007

by

Seema Bahinipati

M.S., Utkal University, 1999
M.S., University of Cincinnati, 2002

Committee chair: Dr. Kay Kinoshita

Abstract

Study of time dependence of $B^0 \to D^{*-}\pi^+$ decays leads to the measurement of CP violation and extraction of $\sin(2\phi_1 + \phi_3)$, where ϕ_1 and ϕ_3 are the angles of the Cabibbo-Kobayashi-Maskawa(CKM) unitarity triangle. We use a partially reconstructed $B \to D^*\pi$ event sample in the data sample that contains 387 million $B\overline{B}$ pairs that was collected near the $\Upsilon(4S)$ resonance, with the Belle detector at the KEKB asymmetric energy e^+e^- collider.

Acknowledgments

I would like to thank my advisor Dr. Kay Kinoshita for her help and guidance. I want to express my sincere thanks to all the professors in physics department both in Cincinnati and in Utkal University, India and all my teachers. I would like to express my special thanks to my professor, Dr. Puspa Khare for providing me the opportunity to come to University of Cincinnati for pursuing my doctorate degree.

I am also very thankful to all the referees of my dissertation committee, Dr. Brian Meadows, Dr. Rostislav Serota and Dr.Hans-Peter Wagner.

I want to thank all the Belle collaborators, especially my sub-group members, Dr. Kazuo Abe, Dr. Timothy Gershon, Dr. Frederic Ronga, Dr. Yoshihide Sakai, Dr. Pavel Krokovny, Dr. Karim Trablesi and Dr. Tapas Sarangi. I want to express my sincere gratitude to Dr. Karim Trablesi for his valuable help and guidance that has enriched my work immensely.

I want to thank the Belle secretaries Ritsuko Ota, Miyuki Hatogai, Atsuko Naka and Imai Chihiro and the User's Office and IPNS office staff members at KEK, Japan.

I would like to thank all my friends in Cincinnati, Japan and India for being there for me always. I feel blessed to have such good friends, who always believed in me and stood by me in hard times.

Last but not the least, I would like to thank everyone in our extended family for bestowing their good wishes on me. I want to also express my deepest gratitude to my roommate's parents for taking care of me as their own daughter when I was preparing for my defence. Finally, it would not have been possible for me to achieve this milestone in my career without the love and support of my parents, Mr. Prakash Chandra Bahinipati and Mrs. Pratima Manjari Devi and my brother, Vikas Bahinipati.

Contents

List of Figures

List of Tables

Chapter 1

Introduction

The only thing constant in life is change.
- by François de la Rochefoucauld

Our universe has a clear dominance of matter over anti-matter. According to the Big Bang theory, one prediction is that early universe had no matter, only energy. This energy produced matter and antimatter in equal proportion, as the universe expaned. However, the world around us is dominated by matter. The pursuit of the cause of the annihilation of antimatter in our universe after its creation is of great interest to the scientific community. CP violation, violation of the combined operation of C (charge-conjugation) that changes matter to anti-matter and vice-versa and P (parity) that reverses space-coordinates, is one of the three necessary conditions for dominance of matter over antimatter, as described by A. D.Sakharov [1].

In this chapter we describe charge conjugation, parity transformation, and CP transformations and focus on the formalism of CP violation in K-meson system and B-meson system. Then we concentrate on the description of CP violation in $B^0 \to D^*\pi$ decays and the mechanism to extract $\sin(2\phi_1 + \phi_3)$.

1.1 Fundamental constituents of matter

The study of the fundamental constituents of matter around us and the forces that allow them to interact is the core of particle physics. Until 1900's, atoms were believed to be the fundamental particles. Several experiments were done to confirm or refute this theory. It was then found that atoms are made up of a positively charged nucleus surrounded by a cloud of negative electrons. The nucleus is further made up of positive protons and neutral neutrons. Until 1950's, it was believed that electrons, protons and neutrons are the most fundamental particles. However, in

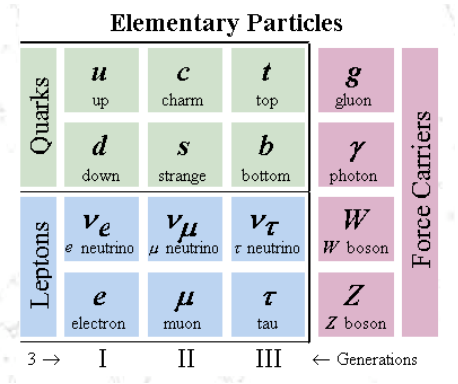

Figure 1.1: Quarks and leptons and their force carriers

1964, it was discovered that the protons and neutrons are made up of yet smaller particles, called with "quarks". Electrons are fundamental particles and they belong to a family of particles called "leptons". Thus, quarks and leptons are the fundamental constituents of mater and alongwith the four fundamental forces (Table 1.3) that allow them to interact make a theory called "Standard model". Fig. 1.1 shows the quarks and leptons and their force carriers. Tables 1.1 and 1.2 summarize the some of the intrinsic properties of quarks and leptons respectively.

The four fundamental forces in nature are gravity, electromagnetic, strong and weak force. The mediator of these forces are called intermediate bosons. Table 1.3 shows the range, strength and mediator particles for these forces. Gravity is mediated by gravitons, which are yet to be observed. Electromagnetic force is mediated by photons. Weak force appears mostly in nuclear decays and are mediated by intermediate vector bosons ($W^{\pm}$, Z^0). Strong force is mediated by gluons and it helps bind the quarks together.

Flavor	Mass (GeV/c^2) m	Electric charge (e) q	Isospin I	Spin-parity J^P
u	0.0015 - 0.003	$+2/3$	$+1/2$	$1/2^+$
d	0.003 - 0.007	$-1/3$	$+1/2$	$1/2^+$
c	1.25 ± 0.09	$+2/3$	0	$1/2^+$
s	0.095 ± 0.025	$-1/3$	0	$1/2^+$
t	174.2 ± 3.3	$+2/3$	0	$1/2^+$
b	4.2 ± 0.07	$-1/3$	0	$1/2^+$

Table 1.1: Quarks and their properties

Flavor	Mass (GeV/c^2) m	Electric charge (e) q	Spin J
e^-	0.0005	-1	+1/2
ν_{e^-}	$< 7 \times 10^{-9}$	0	
μ^-	0.106	-1	+1/2
ν_{μ^-}	< 0.0003	0	
τ^-	1.777	-1	+1/2
ν_{τ^-}	< 0.03	0	

Table 1.2: Leptons and their properties

Type	Strength	Range (m)	Particles
Strong	1	10^{-15}	8 gluons (g) (massless, spin 1)
Electro-magnetic	1/137	Infinite	photons (γ) (massless, spin 1)
Weak	10^{-6}	10^{-18}	intermediate vector bosons ($W^{\pm}$, Z^0) (heavy, spin 1)
Gravity	6×10^{-39}	Infinite	gravitons (massless, spin 2)

Table 1.3: Four fundamental forces

1.2 Symmetries and conservation laws

Symmetries in systems under an operation is a vital concept in physics. The conservation of symmetries, also called as invariance principle leads to the laws of conservation in nature. For instance, invariance of a system or a set of equations under translation or rotation operations in space lead to the conservation of linear and angular momentum respectively. The equations or the system is said to be symmetric or invariant under the operations.

These operations (or transformations) can be either continuous or discrete. Examples of continuous transformations are the translation or rotation operations in space, whereas that of discrete symmetry is spatial reflection through the origin of coordinates, called the parity operation. Another important feature of these opearations is that the conservations laws related to continuous symmetries are additive in nature, whereas those related to discrete symmetries are multiplicative. The next section describes three discrete transformations, parity (P), charge-conjugation (C) and time-reversal (T) in some detail.

1.3 Discrete transformations (parity (P), charge-conjugation (C) and time-reversal (T))

1.3.1 Parity

A parity transformation P reverses all space coordinates and particle momenta p of a state $\psi(x,t)$ while leaving their orbital angular momenta $r \times p$ unchanged.

$$P(\boldsymbol{x}) = -\boldsymbol{x} \tag{1.1}$$

$$P(\boldsymbol{p}) = -\boldsymbol{p} \tag{1.2}$$

$$P(\boldsymbol{l}) = \boldsymbol{l} \tag{1.3}$$

since $l = x \times p$ and parity transformation is multiplicative.

Table 1.4 summarizes the result of parity operation on few quantities in the classical mechanics sector.

Quantity	Initial	Under P transformation
Polar vector ($\boldsymbol{V}$)	$\boldsymbol{V}$	$-\boldsymbol{V}$
Axial vector ($\boldsymbol{A}$)	$\boldsymbol{A}$	$-\boldsymbol{A}$
Scalar (S)	S	S
Pseudoscalar (P)	P	$-P$

Table 1.4: P transformation

$$P\psi(x,t) = \xi_p \psi(-x,t). \tag{1.4}$$

Here, in Eqn 1.4 ξ_p is the eigenvalue of the P operator, where $\xi_p^2 = 1$.

1.3.2 Charge conjugation

A charge conjugation C changes a particle to its antiparticle, which has equal mass, momentum and spin as its associated particle, but opposite quantum numbers such as charge.

$$C(particle) = anti - particle \tag{1.5}$$

$$C\psi(x,t) = \xi_c \bar{\psi}(x,t). \tag{1.6}$$

where ξ_c are the eigenvalue of the C operator, which can be $+1$ or -1 $\xi_c^2 = 1$.

1.3.3 Time reversal

$$T(t) = -t \tag{1.7}$$

$$T(\boldsymbol{x}) = -\boldsymbol{x} \tag{1.8}$$

$$T(\boldsymbol{p}) = -\boldsymbol{p} \tag{1.9}$$

$$T(\boldsymbol{l}) = -\boldsymbol{l} \tag{1.10}$$

1.3.4 CP

Similarly operating CP will reverse the sign of the charge as well as the space coordinates,

$$CP\psi(x,t) = \xi_{CP}\bar{\psi}(-x,t) \tag{1.11}$$

where ξ_{CP} can be ± 1 and are the eigenvalues of the CP operator.

1.3.5 CPT

The time reversal and CP transformations are connected by the well-known CPT theorem, which states that all interactions are invariant under the combined operation of the three operations P, C and T in any order. The consequences of the CPT theorem such as equal mass and life-time, but opposite sign of magnetic moments of particles and their respective anti-particles have been experimetally verified. However, the CPT invariance has not been experimentally tested.

1.3.6 Conservation principles of P, C, T, CP and CPT transformations

Parity transformation is conserved in strong and electromagnetic interactions. In 1956, Lee and Yang proposed that parity transformation is violated in weak interactions [2]. This was demonstrated by C.Wu from a study of β-decay of ^{60}Co nuclei in 1957 [3].

The study of neutrinos and anti-neutrinos with respect to the helicity states [1] also explains the parity violation in weak interaction. Two kinds of neutrino, *left-handed neutrinos* (ν_L) which has negative helicity state and *right-handed anti-neutrinos*($\bar{\nu}_R$) having a positive helicity state are observed in nature. The neutrinos are completely

[1] direction of spin is quantized along the direction of momentum

polarized, and operating P or C transformation results a forbidden state. Therefore parity and charge-conjugation violations occur separately in β decays and other weak interactions. If CP transformation is applied to a *left-handed neutrino*, *right-handed anti-neutrino* is obtained, which is allowed in nature. This led to the belief that although parity and charge-conjugation are violated separately in weak interactions, their combined operation CP is conserved. However, this belief was proved to be wrong by the discovery of CP violation in K meson system in (described in the next section). Table 1.5 summarizes the conservation laws of the four fundamental forces under the discrete transformations of P, C, T, CP and CPT.

Fundamental force	P	C	T	CP	CPT
Strong	Yes	Yes		Yes	Yes
Electro-magnetic	Yes	Yes		Yes	Yes
Weak	No	No		No	Yes

Table 1.5: Fundamental forces and their conservation under P, C, T, CP and CPT transformations

1.4 The discovery of CP violation in the K meson

M. Gell-Mann and A. Pais predicted the mixing in neutral K mesons denoted as K^0 and $\bar{K}^0$ [4]. The Gell-Mann-Nishijima formula

$$\frac{Q}{e} = I_3 + \frac{B+S}{2}, \tag{1.12}$$

where I_3, B and S are z-component of isospin, baryon number and strangeness quantum number respectively. This indicates that in addition to the charged kaons $K^{\pm}$, of $S = \pm 1$, two neutral kaons, K^0 and $\bar{K}^0$ to complete $I = \frac{1}{2}$ doublets. Gell-Mann and Pais pointed out that K^0 with strangeness quantum number $+1$ can change into its antiparticle $\bar{K}^0$ with strangeness -1.

$$K^0 \Leftrightarrow \bar{K}^0. \tag{1.13}$$

The observed particles are a linear combination of K^0 and $\bar{K}^0$. The normalized eigenstates of CP are

$$|K_1\rangle = \frac{1}{\sqrt{2}}(\left|K^0\right\rangle + \left|\bar{K}^0\right\rangle), \quad |K_2\rangle = \frac{1}{\sqrt{2}}(\left|K^0\right\rangle - \left|\bar{K}^0\right\rangle). \tag{1.14}$$

Using $CP\,|K^0\rangle = \left|\bar{K^0}\right\rangle$,

$$CP\,|K_1\rangle = |K_1\rangle\,(CPeven), \quad CP\,|K_2\rangle = -\,|K_2\rangle\,(CPodd). \tag{1.15}$$

Since $CP\,|\pi\pi\rangle = +\,|\pi\pi\rangle$,
K_1 decays into two pions, but K_2 does not. K_2 decays into three pions. The phase space for K_2 decays into three pions is quite restricted. So, the CP odd state (K_2) has longer life-time than the CP even state (K_1). This long lived K_2 meson was discovered by Lederman and his collaborators in 1956 [5]. The two lifetimes are,

$$\tau_1 = 0.89 \times 10^{-10}\text{sec}, \quad \tau_2 = 5.2 \times 10^{-8}\text{sec}, \tag{1.16}$$

named as K_S and K_L mesons. The CP violation in the K meson sector can be proved if we observe a 2π decay for the long lived K_L mesons. Such an experiment was reported by Cronin and Fitch in 1964 [6] where they found that long-lived neutral kaon K_L contains an admixture of K_1 as:

$$|K_L\rangle = \frac{1}{\sqrt{1+|\epsilon|^2}}(|K_2\rangle + \epsilon\,|K_1\rangle) \tag{1.17}$$

with

$$\epsilon \approx 2.3 \times 10^{-3} \tag{1.18}$$

CP violation is also seen in the leptonic decay modes of K_L such as
$K_L \to \pi^- l^+ \nu_l$ and $K_L \to \pi^+ l^- \bar{\nu}_l$, where, l = e, μ.
The CP asymmetry observed in these decays is
$\Delta = \frac{\Gamma(K_L \to \pi^- l^+ \nu_l) - \Gamma(K_L \to \pi^+ l^- \bar{\nu}_l)}{\Gamma(K_L \to \pi^- l^+ \nu_l) + \Gamma(K_L \to \pi^+ l^- \bar{\nu}_l)}$, where Γ stands for decay rate. The value of Δ was experimentally observed to be $(0.330 \pm 0.012) \times 10^{-3}$. Thus, it was confirmed that CP violation exists in neutral K meson system.

1.5 Quark mixing in the Standard Model and KM Mechanism

In the Standard model, there are three generations of the fundamental particles, quarks and leptons. Weak interaction between them is mediated by heavy particles called intermediate vector bosons ($W^{\pm}$, Z^0). The CP violation in weak interaction occurs due to the ability of the $W^{\pm}$ bosons to mix different quark generations.

At first, it was known that weak interaction exists between the following pairs of (left-handed) fermion states and first generation of quarks:

$$\begin{pmatrix} \nu_e \\ e^-, \end{pmatrix} \begin{pmatrix} \nu_\mu \\ \mu^- \end{pmatrix}, and \begin{pmatrix} u \\ d \end{pmatrix} \tag{1.19}$$

through charged weak currents, that couple with a universal coupling constant G. Addition of the second generation of quarks

$$\begin{pmatrix} c \\ s \end{pmatrix} \tag{1.20}$$

seemed incorrect then due to the experimental evidence of $K^+ \to \mu^+\nu_\mu$ decays, as K^+ is made up of u and $\bar{s}$. This suggested that the weak current should include flavour-changing $u \leftrightarrow s$ transition.

This puzzle was solved in 1963 by N. Cabibbo. He formulated the notion of flavour-mixing in weak interaction using the three lightest quarks, u, d and s. According to his proposal, the d and s quark participating a weak interaction are not pure flavor eigenstates, but the mixture of them, i.e. the state of

$$|d'\rangle = \cos\theta_c\,|d\rangle + \sin\theta_c\,|s\rangle \tag{1.21}$$

where θ_c is called the *Cabibbo angle*. Thus, Cabibbo could explain the weak decay of strange particles. However, he could not explain flavour changing neutral current transition $s \to d$, such as $K^0\bar{K}^0$ mass difference. This problem was solved by Glashow, Iliopoulos, and Maiani (GIM).

Glashow, Iliopoulos, and Maiani proposed the existence of a fourth quark c before its discovery. In addition to the quark doublet

$$\begin{pmatrix} u \\ d' \end{pmatrix}, \tag{1.22}$$

, there exists a second quark doublet

$$\begin{pmatrix} c \\ s' \end{pmatrix}. \tag{1.23}$$

In nut-shell, we have the following relations:

$$\begin{pmatrix} d' \\ s' \end{pmatrix} = \begin{pmatrix} \cos\theta_c & \sin\theta_c \\ -\sin\theta_c & \cos\theta_c \end{pmatrix} \begin{pmatrix} d \\ s \end{pmatrix} \tag{1.24}$$

The unitary matrix

$$\begin{pmatrix} \cos\theta_c & \sin\theta_c \\ -\sin\theta_c & \cos\theta_c \end{pmatrix} \tag{1.25}$$

works as the quark mixing matrix.

The complete picture with all the three quark generations was illustrated in 1973 by M. Kobayashi, T.Maskawa [12]. They extended the framework of the quark mixing proposed by Cabibbo-GIM from 2-generations, u, d and c, s, to general N generations. The quark mixing matrix in Eqn. 1.25 is extended to $N \times N$ complex matrix, V_{ij}, which has $2N^2$ real parameters. The unitarity matrix requirement implies it to follow

$$\sum_i V_{ij} V_{jk}^* = \delta_{ik} \tag{1.26}$$

Thus, the number of free parameters of the matrix reduced to N^2. Since the relative phase of the quark fields can rotate arbitrarily, it implies that $2N-1$ relative phase can be removed from $\mathbf{V}$. Thus there are $(N-1)^2$ independent physical parameters remaining in $\mathbf{V}$. A $N \times N$ orthogonal matrix has $N(N-1)/2$ independent real parameters,

$$N_{\text{angles}} = \frac{N(N-1)}{2} \tag{1.27}$$

Thus the number of independent phases remain in $\mathbf{V}$ is given by,

$$N_{\text{phases}} = \frac{(N-1)(N-2)}{2} \tag{1.28}$$

According to the Cabibbo-GIM theory, in the two quark-generation model, the quark mixing matrix has one angle and no complex phase. If there are three quark-generations, then the quark-mixing matrix has three angles and one complex phase. Discovery of bottom(b) or beauty quark, and the top(t) quark made it possible for KM theory to be an essential part of the Standard Model. The 3×3 quark-mixing matrix in the Standard Model is now called the Cabibbo-Kobayashi-Maskawa (CKM) matrix, V_{CKM}:

$$V_{CKM} = \begin{pmatrix} V_{ud} & V_{us} & V_{ub} \\ V_{cd} & V_{cs} & V_{cb} \\ V_{td} & V_{ts} & V_{tb} \end{pmatrix} \tag{1.29}$$

$$\begin{pmatrix} d' \\ s' \\ b' \end{pmatrix} = V_{CKM} \begin{pmatrix} d \\ s \\ b \end{pmatrix} \tag{1.30}$$

The most useful representations for the CKM matrix is the Wolfenstein parametrization [13] which expresses the CKM matrix as an expansion in powers of $\lambda = \sin\theta_c$.

$$V_{CKM} \approx \begin{pmatrix} 1 - \frac{1}{2}\lambda^2 & \lambda & A\lambda^3(\rho - i\eta) \\ -\lambda & 1 - \frac{1}{2}\lambda^2 & A\lambda^2 \\ A\lambda^3(1 - \rho - i\eta) & -A\lambda^2 & 1 \end{pmatrix} + \mathcal{O}(\lambda^4) \tag{1.31}$$

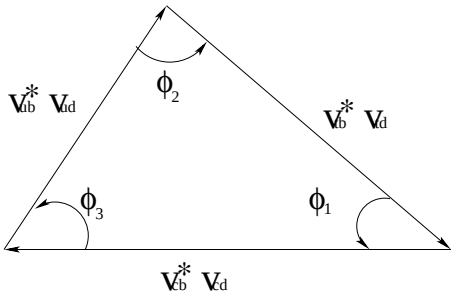

Figure 1.2: The unitarity triangle of the CKM matrix.

1.6 The unitarity triangle

The unitarity of the CKM matrix leads to the relation,

$$\sum_j V_{ij} V_{jk}^* = 0. \quad (i \neq k) \tag{1.32}$$

The unitarity of the CKM matrix implies the following six relations among its elements.

$$\underbrace{V_{ub}V_{us}^*}_{\lambda} + \underbrace{V_{cd}V_{cs}^*}_{\lambda} + \underbrace{V_{td}V_{ts}^*}_{\lambda^5} = 0, \tag{1.33}$$

$$\underbrace{V_{ud}V_{cd}^*}_{\lambda} + \underbrace{V_{us}V_{cs}^*}_{\lambda} + \underbrace{V_{ub}V_{cb}^*}_{\lambda^5} = 0, \tag{1.34}$$

$$\underbrace{V_{us}V_{ub}^*}_{\lambda^4} + \underbrace{V_{cs}V_{cb}^*}_{\lambda^2} + \underbrace{V_{ts}V_{tb}^*}_{\lambda^2} = 0, \tag{1.35}$$

$$\underbrace{V_{cd}V_{td}^*}_{\lambda^4} + \underbrace{V_{cs}V_{ts}^*}_{\lambda^2} + \underbrace{V_{cb}V_{tb}^*}_{\lambda^2} = 0, \tag{1.36}$$

$$\underbrace{V_{ud}V_{td}^*}_{\lambda^3} + \underbrace{V_{us}V_{ts}^*}_{\lambda^3} + \underbrace{V_{ub}V_{tb}^*}_{\lambda^3} = 0, \tag{1.37}$$

$$\underbrace{V_{ud}V_{ub}^*}_{\lambda^3} + \underbrace{V_{cd}V_{cb}^*}_{\lambda^3} + \underbrace{V_{td}V_{tb}^*}_{\lambda^3} = 0. \tag{1.38}$$

The CKM matrix elements are complex. Since each of the above six relations requires the sum of three complex quantities to be zero, they can be represented as six triangles in complex plane. These triangles are called the unitarity triangles.

The four unitarity triangles corresponding to Eqn. 1.33 to 1.36 are extremely squeezed in shape since the magnitudes of one of the sides of the triangle is much

shorter than the other two. On the contrary, all the sides in Eqn. 1.37 and 1.38 are of the same order ($\mathcal{O}(\lambda^3)$). Hence, the unitary triangles corresponding to these two relations are more open than the first four. Eqn. 1.33 and 1.34 are related to physics in K meson system. Eqn. 1.35 and 1.36 are related to physics in B_s meson system. Eqn. 1.37 and 1.38 are related to physics in B_d meson system. Since the unitary triangles corresponding to B_d meson system are more open than the other four, the amount of CP violation in B_d meson decay is expected to be larger than in K meson and B_s meson decays. This makes B meson decays the most promising sector to examine the Kobayashi-Maskawa mechanism. In the neutral B_d^0 system we use only Eqn. 1.38, since it involves mixing, $b \to c$ and $b \to u$ transitions while in Eqn. 1.37 it has transitions that includes K meson decays.

Fig. 1.2 corresponds to Eqn. 1.38. The unitarity triangle that corresponds to B decays has six parameters; three angles and three sides. The sides of the triangle can be obtained by measuring specific decay rates, and the angles can be derived from measurements of CP asymmetries. The angles $\phi_1(\beta)$, $\phi_2(\alpha)$, and $\phi_3(\gamma)$ are defined the following way

$$\begin{aligned}
\phi_1 &\equiv \arg\left(\frac{V_{cb}^* V_{cd}}{-V_{tb}^* V_{td}}\right), \\
\phi_2 &\equiv \arg\left(\frac{V_{tb}^* V_{td}}{-V_{ub}^* V_{ud}}\right), \\
\phi_3 &\equiv \arg\left(\frac{V_{ub}^* V_{ud}}{-V_{cb}^* V_{cd}}\right).
\end{aligned} \tag{1.39}$$

Intuitively, the amount of CP violation is directly proportional to the openness of the unitary triangle. This implies that the angles should take nonzero values and the sides should be comparable, if CP invariance is violated in B meson system. The measurement of the angles and sides of the unitary triangle is one of the prominent goals of the B factory.

1.7 B-mesons

B-mesons are bound states of a b quark/antiquark with a u quark/antiquark ($B^{\pm}$) or a d quark/antiquark ($B^0/\bar{B}^0$). The charged $B^{\pm}$ mesons are $\bar{b}u/b\bar{u}$ bound-states and the neutral $B^0/\bar{B}^0$ mesons are $\bar{b}d/b\bar{d}$ bound-states. Table 1.6 summarizes few basic characteristics of the B-mesons.

The difference between the masses and life-times of the neutral and charged B-mesons are given below:

Quantity	$B^{\pm}$	$B^0/\bar{B}^0$
J^P	0^-	0^-
Mass m (GeV/c^2)	5.2790 ± 0.0005	5.2794 ± 0.0005
Life-time τ (ps)	1.638 ± 0.011	1.530 ± 0.009
$c\tau(\mu m)$	491.1	457.8

Table 1.6: B mesons and their properties

$m_{B^+} - m_{\bar{B^0}} = 0.33 \pm 0.28$ MeV,
$\frac{\tau_{B^+}}{\tau_{B^0}} = 1.071 \pm 0.009$.

Since charge is a conserved quantity, no mixing occurs in the charged B mesons. However, mixing in the neutal b sector exists and was first observed in . B^0-$\bar{B}^0$ mixing happens due to the box-diagram, illustrated in Fig 1.3. The B^0-$\bar{B}^0$ mixing frequency is given as:
$\Delta m_{B^0} = (0.507 \pm 0.005) ps^{-1}$.

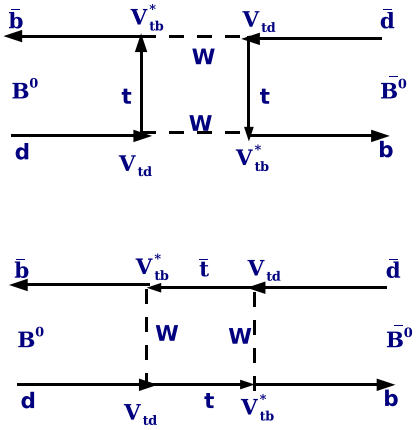

Figure 1.3: B^0-$\bar{B}^0$ mixing.

1.8 Phenomena of B^0-$\bar{B}^0$ mixing and CP violation in B decays

The time dependent wave function of a neutral B meson in the weak interaction eigenstate (or mass eigenstate) is written as a linear combination of the flavor eigen-

states $|B^0\rangle$ and $\left|\bar{B}^0\right\rangle$ as

$$|B(t)\rangle = \alpha(t)\left|\bar{B}^0\right\rangle + \beta(t)\left|B^0\right\rangle, \tag{1.40}$$

where we use $CP\,|B^0\rangle = -\left|\bar{B}^0\right\rangle$. By Schrödinger's time dependent wave function, the above equation can be expressed as

$$i\hbar\frac{d}{dt}\begin{pmatrix}\alpha(t)\\ \beta(t)\end{pmatrix} = \begin{pmatrix}H_{11} & H_{12}\\ H_{21} & H_{22}\end{pmatrix}\begin{pmatrix}\alpha(t)\\ \beta(t)\end{pmatrix}, \tag{1.41}$$

where assuming CPT invariance Hamiltonian H is given by

$$H_{11} = H_{22} = M - \frac{i}{2}\Gamma, \quad H_{12} = M_{12} - \frac{i}{2}\Gamma_{12}, \quad H_{21} = M_{12}^* - \frac{i}{2}\Gamma_{12}^*. \tag{1.42}$$

where M in the diagonal term is the mass of the flavor eigenstates of B^0 and $\bar{B}^0$, and Γ is their decay widths. Eqn 1.41 then becomes

$$i\hbar\frac{d}{dt}\begin{pmatrix}\alpha(t)\\ \beta(t)\end{pmatrix} = \begin{pmatrix}M - \frac{i}{2}\Gamma & M_{12} - \frac{i}{2}\Gamma_{12}\\ M_{12}^* - \frac{i}{2}\Gamma_{12}^* & M - \frac{i}{2}\Gamma\end{pmatrix}\begin{pmatrix}\alpha(t)\\ \beta(t)\end{pmatrix}, \tag{1.43}$$

The mass eigenstates and their eigenvalues are given as,

$$\left|B_\pm^0\right\rangle = p\left|B^0\right\rangle \pm q\left|\bar{B}^0\right\rangle, \tag{1.44}$$

$$\mu_\pm = M - \frac{i}{2}\Gamma \pm \sqrt{(M_{12} - \frac{i}{2}\Gamma_{12})(M_{12}^* - \frac{i}{2}\Gamma_{12}^*)}, \tag{1.45}$$

Assuming normalization, $|p|^2 + |q|^2 = 1$. p and q are expressed in terms of Hamiltonian components as

$$\frac{q}{p} = \sqrt{\frac{M_{12} - \frac{i}{2}\Gamma_{12}}{M_{12}^* - \frac{i}{2}\Gamma_{12}^*}}. \tag{1.46}$$

The time evolution of the mass eigenstates $|B_\pm\rangle$ can be expressed as

$$\left|B_\pm^0, t\right\rangle = e^{-i(m_\pm - i\Gamma_\pm/2)t}\left|B_\pm^0\right\rangle, \tag{1.47}$$

where,$m_\pm$ and $\Gamma_\pm$ are the masses and decay width of the mass eigenstates $|B_+\rangle$ and $|B_-\rangle$, and

$$\Delta m = m_- - m_+ = -2\Re[(M_{12} - \frac{i}{2}\Gamma_{12})(M_{12}^* - \frac{i}{2}\Gamma_{12}^*)]^{1/2} \tag{1.48}$$

$$\Delta\Gamma = \Gamma_+ - \Gamma_- = -4\Re(M_{12}\Gamma_{12})/\Delta m \tag{1.49}$$

The time evolution of the states $|B^0\rangle$ or $\left|\bar{B}^0\right\rangle$ at a later time t can be described as,

$$\left|B^0(t)\right\rangle = f_+(t)\left|B^0\right\rangle - \frac{q}{p}f_-(t)\left|\bar{B}^0\right\rangle \tag{1.50}$$

$$\left|\bar{B}^0(t)\right\rangle = f_+(t)\left|\bar{B}^0\right\rangle - \frac{q}{p} f_-(t)\left|B^0\right\rangle \tag{1.51}$$

where,

$$f_\pm(t) = \frac{1}{2}[e^{-i(m_+ - i\Gamma_+/2)t} \pm e^{-i(m_- - i\Gamma_-/2)t}]. \tag{1.52}$$

In the Standard Model, M_{12} is contributed by a higher order weak interaction diagram called "box diagram" as shown in Fig. 1.3, whereas Γ_{12} is contributed by the presence of physical states to which both B^0 and $\bar{B}^0$ can decay. It is roughly given as

$$\left|\frac{\Gamma_{12}}{M_{12}}\right| \simeq \frac{3\pi m_b^2}{2m_t^2} \sim \mathcal{O}(10^{-2}) \ll 1. \tag{1.53}$$

where m_b and m_t are the mass of the b and t quarks, respectively. Using Eqn. 1.53 and calculating the box diagram of B^0-$\bar{B}^0$ mixing , p/q becomes

$$\frac{p}{q} \simeq \sqrt{\frac{M_{12}^*}{M_{12}}} = \frac{-V_{tb}V_{td}^*}{V_{tb}^*V_{td}}. \tag{1.54}$$

Now, Eqn 1.50 and 1.51 can be written as,

$$\begin{aligned}
\left|B^0(t)\right\rangle &= e^{-\frac{\gamma}{2}t}\left(\cos\frac{\Delta mt}{2}\left|B^0\right\rangle - i\frac{q}{p}\sin\frac{\Delta mt}{2}\left|\bar{B}^0\right\rangle\right), \\
\left|\bar{B}^0(t)\right\rangle &= e^{-\frac{\gamma}{2}t}\left(\cos\frac{\Delta mt}{2}\left|\bar{B}^0\right\rangle - i\frac{p}{q}\sin\frac{\Delta mt}{2}\left|B^0\right\rangle\right)
\end{aligned} \tag{1.55}$$

We define $\gamma = \frac{\Gamma_+ + \Gamma_-}{2}$ as the average mass and decay width of the two eigenstates.

1.9 Types of CP violation (CPV) in B-mesons

The CP violating decays in the B-meson sector can be broadly categorized into the following 3 types:

- CPV in decay or direct CPV ($DCPV$)
  CPV in decay can occurr in both neutral and charged B decays. B^0-$\bar{B}^0$ mixing is not involved in this case. If A_f and $\bar{A}_{\bar{f}}$ are the amplitudes of $B \to f$ and $\bar{B} \to \bar{f}$ decays respectively, then the condition for CPV in decay is given by:
  $\frac{\bar{A}_{\bar{f}}}{A_f} \neq 1$. The amount of CP asymmetry is denoted as A_{CP} and defined as:

$$A_{CP} = \frac{1 - |\frac{\bar{A}_{\bar{f}}}{A_f}|^2}{1 + |\frac{\bar{A}_{\bar{f}}}{A_f}|^2} \neq 1 \tag{1.56}$$

Since this type of CPV occurs directly in the decay, its called direct CPV. A non-zero coefficient in front of the cosine mixing term is characteristic of this CPV. Decays of the type $B^0 \to K^+\pi^-$ exhibit direct CPV.

- CPV in mixing or indirect CPV ($ICPV$)

$$|\left\langle \bar{B}^0 \right| \left| B^0(t) \right\rangle|^2 = |\frac{p}{q}|^2 |f_(t)|^2 |\left\langle B^0 \right| \left| \bar{B}^0(t) \right\rangle|^2 = |\frac{p}{q}|^2 |f_(t)|^2 \tag{1.57}$$

$$|\left\langle \bar{B}^0 \right| \left| B^0(t) \right\rangle|^2 \neq |\left\langle B^0 \right| \left| \bar{B}^0(t) \right\rangle|^2 \tag{1.58}$$

, when $|\frac{q}{p}| \neq 1$. A non-zero coefficient in front of the cosine mixing term is characteristic of this CPV. $\bar{B^0} \to l^+\nu^- X$ decays exhibit indirect CPV $\approx O(10^{-2})$ (small).

- CPV in interference between mixing and decay
  A non-zero coefficient in front of the sine mixing term is characteristic of this CPV.

$$|\frac{q}{p}| \frac{1 - |\frac{\bar{A}_{\bar{f}}}{A_f}|^2}{1 + |\frac{\bar{A}_{\bar{f}}}{A_f}|^2} \neq 1 \tag{1.59}$$

CPV in charged B mesons is only of $DCPV$ type, whereas all three types of CPV are possible in neutral B mesons.

1.9.1 B meson decays to non-CP eigenstates

Let us now consider B^0 or $\bar{B}^0$ at time t=0 which decays to a final state f and its charge conjugate state $\bar{f}$ at time t.

From Eqn. 1.55

$$\begin{aligned}
A_{B^0\to f}(t) &= e^{-\frac{\gamma}{2}t} A(f) \left(\cos\frac{\Delta m t}{2} - i\lambda \sin\frac{\Delta m t}{2} \right) \\
A_{B^0\to \bar{f}}(t) &= e^{-\frac{\gamma}{2}t} \bar{A}(\bar{f}) \left(\bar{\lambda} \cos\frac{\Delta m t}{2} - i \sin\frac{\Delta m t}{2} \right) \\
A_{\bar{B}^0\to f}(t) &= e^{-\frac{\gamma}{2}t} A(f) \left(\lambda \cos\frac{\Delta m t}{2} - i \sin\frac{\Delta m t}{2} \right) \\
A_{\bar{B}^0\to \bar{f}}(t) &= e^{-\frac{\gamma}{2}t} \bar{A}(\bar{f}) \left(\cos\frac{\Delta m t}{2} - i\bar{\lambda} \sin\frac{\Delta m t}{2} \right),
\end{aligned} \tag{1.60}$$

$A(f)$ and its conjugate notations are for the decay amplitudes at time $t = 0$

$$\begin{aligned} A(f) &\equiv A(B^0 \to f) \\ A(\bar{f}) &\equiv A(B^0 \to \bar{f}) \\ \bar{A}(f) &\equiv A(\bar{B}^0 \to f) \\ \bar{A}(\bar{f}) &\equiv A(\bar{B}^0 \to \bar{f}) \end{aligned} \tag{1.61}$$

and we introduce parameters λ and $\bar{\lambda}$ as

$$\lambda \equiv \frac{q\bar{A}(f)}{pA(f)}, \quad \bar{\lambda} \equiv \frac{pA(\bar{f})}{q\bar{A}(\bar{f})}$$

. Thus the time dependent decay rates can be obtained by taking squared absolute values of Eqn 1.60,

$$\begin{aligned} \Gamma_{B^0 \to f}(t) &= |A(f)|^2 \frac{e^{-\gamma t}}{2}[(1 + |\lambda|^2) + (1 - |\lambda|^2)\cos\Delta m t + 2\Im\lambda \sin\Delta m t] \\ \Gamma_{B^0 \to \bar{f}}(t) &= |\bar{A}(\bar{f})|^2 \frac{e^{-\gamma t}}{2}[(1 + |\bar{\lambda}|^2) - (1 - |\bar{\lambda}|^2)\cos\Delta m t - 2\Im\bar{\lambda} \sin\Delta m t] \\ \Gamma_{\bar{B}^0 \to f}(t) &= |A(f)|^2 \frac{e^{-\gamma t}}{2}[(1 + |\lambda|^2) - (1 - |\lambda|^2)\cos\Delta m t - 2\Im\lambda \sin\Delta m t] \\ \Gamma_{\bar{B}^0 \to \bar{f}}(t) &= |\bar{A}(\bar{f})|^2 \frac{e^{-\gamma t}}{2}[(1 + |\bar{\lambda}|^2) + (1 - |\bar{\lambda}|^2)\cos\Delta m t + 2\Im\bar{\lambda} \sin\Delta m t] \end{aligned} \tag{1.62}$$

1.10 CP violation in $B \to D^*\pi$ decays

The neutral B-meson decay, $\bar{B}^0 \to D^{*+}\pi^-$ can be used to probe the amount of CP violation for $D^*\pi$ decays. This decay, along with B^0-$\bar{B}^0$ mixing can provide sensitivity to $\sin(2\phi_1 + \phi_3)$ measurement, where ϕ_1 and ϕ_3 are angles of the unitary triangle, also named β and γ respectively.

The final state $D^{*\pm}\pi^{\mp}$ in these decays are not CP eigenstates. However, CP violation in these decays occurr due to interference between B^0-$\bar{B}^0$ mixing and decay, it can be put in the third category of CP violation in B meson decays.

In the Standard model, the decays $B^0 \to D^{*-}\pi^+$ and $\bar{B}^0 \to D^{*+}\pi^-$ proceed through the Cabbibo-favoured (CFD) $\bar{b} \to \bar{c}u\bar{d}$ decay and doubly-Cabbibo-suppressed (DCSD) $b \to u\bar{c}d$ decays (Fig. 1.4). The relative weak phase between these amplitudes is referred to ϕ_3. The interplay of this weak phase with the $B\bar{B}$

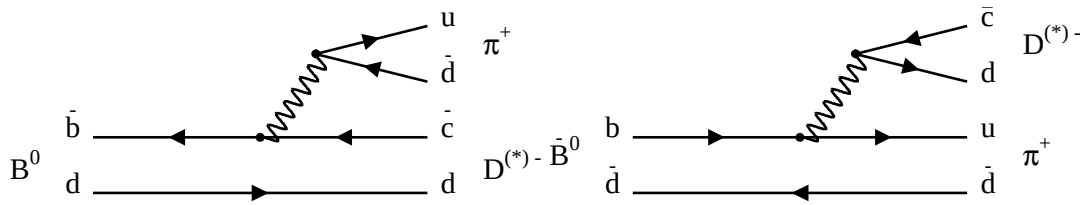

Figure 1.4: Diagrams for $B^0 \to D^{*-}\pi^+$ (left) and $\overline{B}^0 \to D^{*-}\pi^+$ (right). The Feynman diagrams for $\overline{B}^0 \to D^{*+}\pi^-$ and $B^0 \to D^{*+}\pi^-$ can be obtained by charge conjugation.

mixing yields the weak phase difference of $\sin(2\phi_1 + \phi_3)$ between them.

The probability $\Gamma(\Delta t)$ that a state produced at time 0 as a B^0 or $\bar{B}^0$ decays into the final state $D^{*\mp}\pi^{\pm}$ at a given time Δt is

$$\begin{aligned}
\Gamma(B^0 \to D^{*+}\pi^-) &= \alpha[1 - C\cos(\Delta m \Delta t) - S^+ \sin(\Delta m \Delta t)], \\
\Gamma(B^0 \to D^{*-}\pi^+) &= \alpha[1 + C\cos(\Delta m \Delta t) - S^- \sin(\Delta m \Delta t)], \\
\Gamma(\bar{B}^0 \to D^{*+}\pi^-) &= \alpha[1 + C\cos(\Delta m \Delta t) + S^+ \sin(\Delta m \Delta t)], \\
\Gamma(\bar{B}^0 \to D^{*-}\pi^+) &= \alpha[1 - C\cos(\Delta m \Delta t) + S^- \sin(\Delta m \Delta t)].
\end{aligned} \tag{1.63}$$

where $\alpha = (e^{-|\Delta t|/\tau_{B^0}})/8\tau_{B^0}$ with τ_{B^0} denoting the lifetime of the neutral B meson, Δm is the B^0-$\bar{B}^0$ mixing frequency, Δt is the difference between the time of the $B \to D^{*\mp}\pi^{\pm}(B_{CP})$ decay and the deacy of the other $B(B_{tag})$ in the event, $S^{\pm} = -(2R/1 + R^2)\sin(2\phi_1 + \phi_3 \pm \delta)$ and $C = (1 - R^2)/(1 + R^2)$. R and δ are the ratio of the magnitudes and the strong phase difference of the DCSD and CFD amplitudes, respectively. The values of R are expected to be ≈ 0.02 [17]. Assuming a perfect detector, Eq.1 can be visualized as shown in Fig. 1.5.

At the KEKB asymmetric-energy e^+e^- (3.5 GeV on 8 GeV) collider, operating at the $\Upsilon(4S)$ resonance ($\sqrt{s} = 10.58$ GeV), the $\Upsilon(4S)$ is produced with a Lorentz boost of $\beta\gamma = 0.425$, almost along the electron beamline (z) at KEKB. In the $\Upsilon(4S)$ rest frame, B^0 and $\bar{B}^0$ mesons are approximately at rest. So, Δt can be determined from the displacement in z between the CP-side and tag-side vertices:

$$\Delta t \approx (z_{CP} - z_{tag})/\beta\gamma c. \tag{1.64}$$

The CP-side (z_{CP}) and tag-side (z_{tag}) vertices are obtained from the hard pion from B (CP-side) and the tagging lepton or kaon respectively.The hard pion and lepton

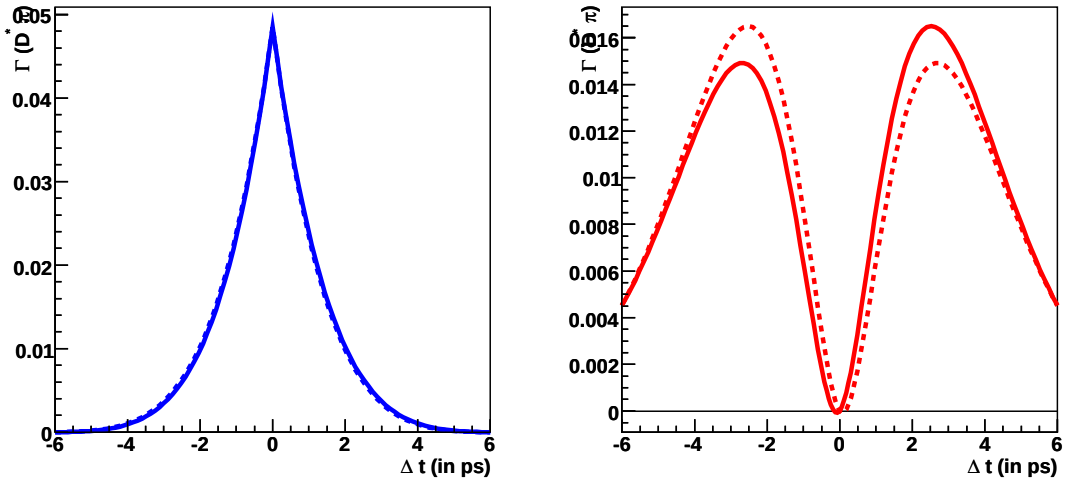

Figure 1.5: The CFD (blue) and DCSD (red) decay rates of B^0 (solid line) or $\bar{B}^0$ (dotted line) into the final state $D^{(*)\mp}\pi^{\pm}$ assuming a perfect detector, with $\phi_3 = 60.0°$, $\phi_1 = 21.7°$, $\delta = 0.0$ and $R = 0.02$.

tracks are consistent with having originated from the interaction profile (IP).

The $S^{\pm}$ and C parameters, used in Eq.1 are defined as: $S^{\pm} = -(2R/1 + R^2)\sin(2\phi_1 + \phi_3 \pm \delta)$ and $C = (1 - R^2)/(1 + R^2)$. Since the value of R is small (R^2 terms are suppressed), we can use the following approximations:

$$\begin{aligned} S^{\pm} &= -2R\sin(2\phi_1 + \phi_3 \pm \delta), \\ C &= 1. \end{aligned} \tag{1.65}$$

BaBar introduced the following notations:

$$\begin{aligned} a &= 2R\sin(2\phi_1 + \phi_3)\cos\delta, \\ b &= 2R^{'}\sin(2\phi_1 + \phi_3)\cos\delta^{'}, \\ c &= 2\cos(2\phi_1 + \phi_3)[R\sin\delta - R^{'}\sin\delta^{'}]. \end{aligned} \tag{1.66}$$

We can convert the BaBar convention to Belle in the following manner:

$$\begin{aligned} a &= -(S^{+} + S^{-})/2, \\ c &= -(S^{+} - S^{-})/2. \end{aligned} \tag{1.67}$$

where R' is the effective ratio between the magnitudes of the DCSD and CFD amplitudes and δ' is the effective strong phase difference between them in the tag-side B-decay. R' and δ' are included to account for the cases where the tag-side B undergoes a $b \to u\bar{c}d$ decay, and the kaon produced in the subsequent charm decay is used for tagging. R' is expected to be of the order of 0.02 [19]. However, in lepton-tagged events, $R' = 0$, since such events are free of tag-side CP violation. The reason of absence of tag-side CP violation in lepton tagging case is that most of the leptons come from semileptonic B decays, to which no suppressed amplitude with a different weak phase can contribute. For lepton tag reduce to:

$$\begin{aligned} a &= 2R\sin(2\beta+\gamma)\cos\delta, \\ b &= 0, \\ c &= 2R\cos(2\beta+\gamma)\sin\delta. \end{aligned} \tag{1.68}$$

The amount of CP violation in this decay depends on R, the ratio of the magnitudes of the DCSD and CFD amplitudes. Since the expected value of R is small ($\approx$ 0.02), the expected CP violation for $\bar{B}^0 \to D^{*+}\pi^-$ decay is small. Current Standard Model fits give $\sin(2\phi_1 + \phi_3) \approx 1$. So, we expect $|S^{\pm}| \sim 0.04$. The expected order of time-dependent CP asymmetry in this mode is as low as 2%. So, large statistic is required to observe it. Partial reconstruction technique provides a way to obtain very large signal sample, unlike full reconstruction technique. These techniques are described in the next sub-section.

Chapter 2

Experimental Apparatus

This analysis is done using 657 million $B\bar{B}$ pairs, collected with the Belle detector. B mesons are produced via $e^+e^- \to \Upsilon(4S) \to B\overline{B}$. The e^+ and e^- beams are produced at the KEKB asymmetric-energy e^+e^- (3.5 GeV on 8 GeV) collider, operating at the $\Upsilon(4S)$ resonance ($\sqrt{s}$ = 10.58 GeV). This chapter describes the KEKB accelerator which produces e^+ and e^- beams and the Belle detector.

The e^+ and e^- beams have finite crossing angle of $\pm 11 m$rad to avoid parasitic collision. The energies of the e^+ and e^- beams are 3.5 GeV and 8 GeV respectively. Since the lower-momentum beam particles would suffer more bending in the solenoid field if they were off-axis, the low energy beam line (e^+) is aligned with the axis of the solenoid magnetic field (z). Recently, crab-crossing has been implemented, wherein the beams have head-on collison. Further details are provided later in this section.

2.1 The KEKB Accelerator

KEKB [29] accelerator facility is an asymmetric-energy e^+e^- collider in Tsukuba, Japan. The beams are provided from a linear injection accelerator and collide at the Belle detector in Tsukuba experimental hall as shown in Fig. 2.1. To produce B mesons the center of mass system (c.m.s.) energy is set at 10.58 GeV which corresponds to the mass of $\Upsilon(4S)$ meson [1]. The mass of $\Upsilon(4S)$ particle is described in terms of beam energies as

$$m_{\Upsilon(4S)} = \sqrt{(E_{e^-} + E_{e^+})^2 - (\boldsymbol{p}_{e^-} + \boldsymbol{p}_{e^+})^2} \simeq \sqrt{4E_{e^-}E_{e^+}}. \tag{2.1}$$

Hence, to produce $\Upsilon(4S)$ meson with e^+e^- collider, any energies of beams can be used provided their product is 27.984 GeV^2.

[1] $\mathcal{B}(\Upsilon(4S) \to B\overline{B}) > 96\%$ [30]

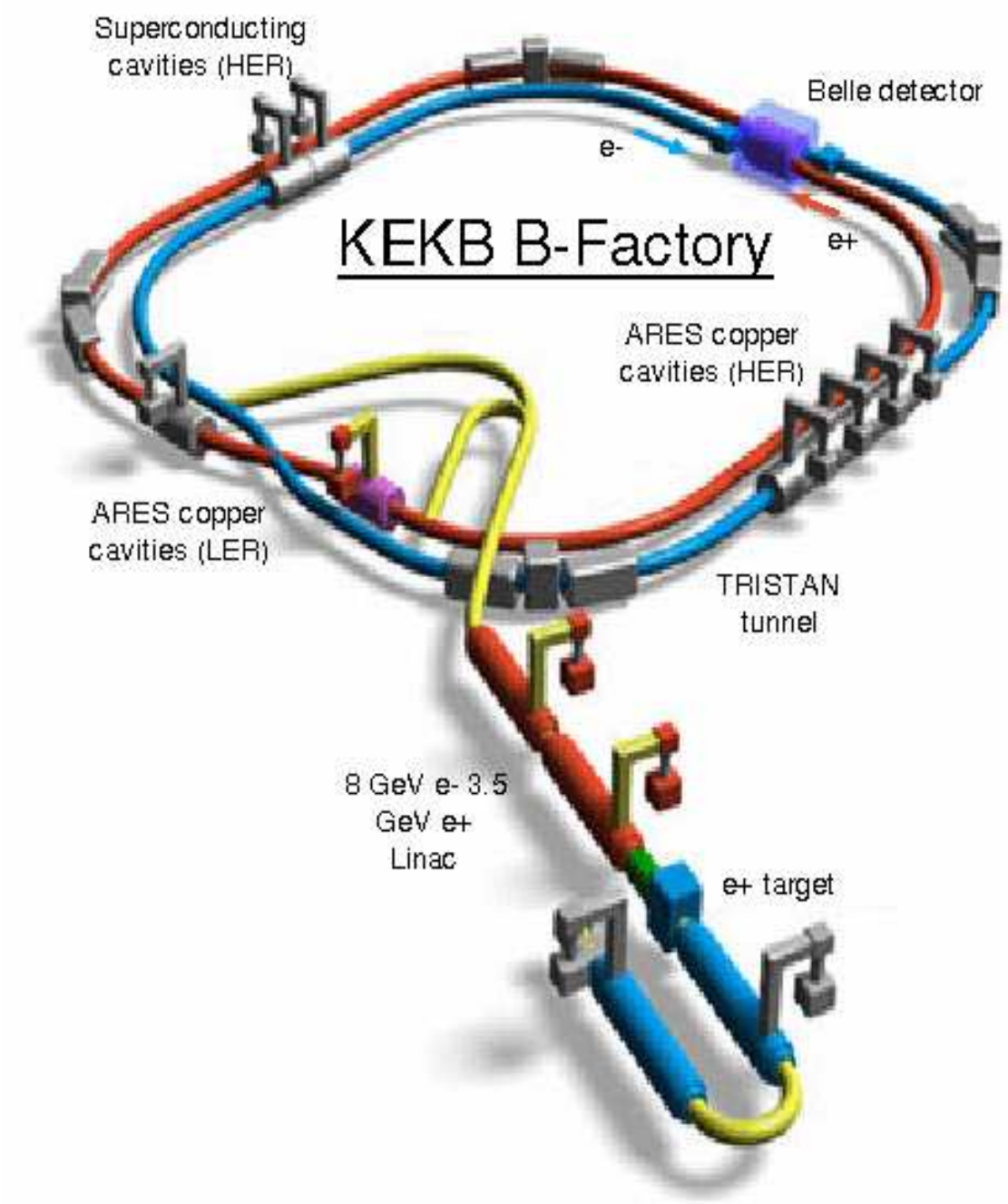

Figure 2.1: KEKB B-factory.

The measurement of amount of CP violation in the B-meson system is one of the primary research interests at the KEKB B factory. This requires measurement of the decay time distribution of the B-meson. However, since B mesons decay almost instantenously ($\sim 10^{-10}$ ps), its difficult to directly measure the decay time of B-meson. So, we Lorentz-boost the B mesons and measure their vertex points. For this purpose KEKB has an asymmetric energy of 8 GeV ($= E^-$) and 3.5 GeV ($= E^+$) for e^- and e^+, respectively, which provides the Lorentz boost factor of

$$\beta\gamma = \frac{p_{\Upsilon(4S)}}{m_{\Upsilon(4S)}} = \frac{E_{e^-} - E_{e^+}}{\sqrt{s}} = 0.425. \tag{2.2}$$

The average decay length of a B^0 meson is

$$l = c\beta\gamma\tau_B = 464\mu\text{m} \times 0.425 = 200\mu\text{m}, \tag{2.3}$$

with a B meson life time τ_B. This length is measurable with our vertex detector whose vertex resolution is $\sim$100 μm.

The convention used to define the coordinates in Belle and KEKB is

x	horizontal direction, outward to the KEKB ring.
y	vertical direction, upward.
z	opposite of the positron beam direction.
r	$\sqrt{x^2 + y^2}$.
θ	the polar angle with respect to z axis.
φ	the azimuthal angle around z axis.

In principle, the origin of x, y and z can be any point on normal beam orbit $\boldsymbol{r}_0$. However, for the Belle experiment it is fixed at the interaction point (IP), namely, $\boldsymbol{r}_0 =$ IP. We use an asterisk to signify parameters at IP in this section.

The main parameters of KEKB are listed in Table 2.1. The most important parameter that demonstrates ability of an accelerator is a luminosity $\mathcal{L}$ since it is directly related to the event rate $\dot{N}$ following the relation $\dot{N} = \sigma\mathcal{L}$, where σ is a cross section. The luminosity is expressed by

$$\mathcal{L} = \frac{N_+ N_- f}{4\pi\sigma_x^*\sigma_y^*} \tag{2.4}$$

$$\simeq \frac{1+r}{2er_e}\frac{\gamma_\pm\xi_y I_\pm}{\beta_y^*}, \tag{2.5}$$

$N_\pm$	number of particle $e^\pm$ per a bunch
f	collision frequency
$\sigma^*_{x,y}$	beam size at IP in x or y direction
r	aspect ratio of the beam at IP, σ^*_y/σ^*_x
e	elementary charge
$I_\pm$	current, $eN_\pm f$
$\gamma_\pm$	Lorentz factor
r_e	classical electron radius, $e^2/4\pi\epsilon_0$
$\xi_{x,y}$	beam-beam parameter in x or y direction
$\beta^*_{x,y}$	β function at IP in x or y direction,

under assumptions that beam particles have Gaussian distribution in x and y direction in a bunch, the beam sizes $\sigma^*_{x,y}$ and the functions $\beta^*_{x,y}$ are equal between two beams, beam shape at IP is flat ($\sigma^*_x >> \sigma^*_y$), and energy transparency condition, $N_+\gamma_+ = N_-\gamma_-$ is assumed.

The β function is defined in the betatron oscillation

$$\chi(s) = A\sqrt{\beta_\chi}\cos(\phi_\chi(s) - \theta), \tag{2.6}$$

where χ is x or y, s denotes the distance along with the beam orbit, and A and θ are integral constants. $\phi(s)$ is a phase advance, which satisfies $\phi'(s) = 1/\beta(s)$. The β function has periodicity $\beta(s + C) = \beta(s)$ with circumference C. Eqn. (2.6) is a general solution for the linearized equation of motion for a beam particle [31]

$$\frac{d^2\chi}{ds^2} + K_\chi(s)\chi = 0, \tag{2.7}$$

where $K_\chi(s)$ is a function determined by formation of magnets, hence $K_\chi(s) = K_\chi(s + C)$. The beam size is determined by the distribution amplitude of the betatron oscillation amplitude $\langle\sqrt{\epsilon_\chi\beta_y(s)}\,\rangle$ of particles in the beam, where ϵ_χ is the beam emittance. At KEKB, the small beam size at IP is realized by focusing the beam strongly with superconducting final focus quadruples which suppress the $\beta_y(s)$ at IP to $\beta^*_y = 5 - 6$ mm.

The beam-beam parameter ξ is given by the expression of

$$\xi^\pm_{x,y} = \frac{N^\mp r_e}{\gamma^\pm}\frac{\beta^*_{x,y}}{2\pi\sigma^*_{x,y}(\sigma^*_x + \sigma^*_y)}, \tag{2.8}$$

which is the betatron tune shift caused by the Coulomb force resulted from the opposite beam in beam-beam collision.

For precise measurement, a number of events are needed to reduce statistical uncertainty. Since the cross section σ is a physics parameter that cannot be changed artificially, we must increase the luminosity to obtain higher event rate. According to Eqn. (2.5), larger $I_\pm$ and ξ_y and smaller β^*_y are required for high luminosity.

KEKB has achieved its design luminosity of $1.6 \times 10^{34}\mathrm{cm}^{-2}s^{-1}$ in June 29, 2006.

Table 2.1: Main parameters of KEKB.

Ring		LER	HER	unit
Particle		e^+	e^-	
Energy	E	3.5	8.0	GeV
Boost factor	$\beta\gamma$	0.425		
Circumference	C	3016.26		m
Luminosity	$\mathcal{L}$	1.6×10^{34}		$\mathrm{cm}^{-2}\mathrm{s}^{-1}$
Crossing angle	θ_x	± 11		mrad
Beam-beam parameters	ξ_x/ξ_y	0.113/0.074	0.072/0.057	
Vertical beam size at IP	σ_y^*	2.1	2.1	μm
Beta function at IP	β_x^*/β_y^*	59/0.52	56/0.65	cm
Beam current	I	1580	1200	mA
Natural bunch length	σ_z	0.4		cm
Number of bunches		1289	1289	
Energy spread	σ_ε	7.1×10^{-4}	6.7×10^{-4}	
Bunch spacing	s_b	2.34		m
Particle/bunch	N	3.3×10^{10}	1.4×10^{10}	
Emittance	$\varepsilon_x/\varepsilon_y$	18	24	nm
Synchrotron tune	ν_s	-0.0249	-0.0216	
Betatron tune	ν_x/ν_y	45.505/43.535	44.513/41.582	
Momentum	α_p	$1 \times 10^{-4} \sim 2 \times 10^{-4}$		
RF voltage	V_c	8.0	14.0	MV
RF frequency	f_{RF}	508.887		MHz
Harmonic number	h	5120		
HOM power	P_{HOM}	0.57	0.15	MW
Bending radius	ρ	16.3	104.5	m
Length of bending	ℓ_B	0.915	5.86	m

2.2 Belle Event

In the e^+e^- collision at $\sqrt{s} = 10.58$ GeV, various physics modes listed in Table 2.2 can occur.

The Bhabha events are easily detected using the CDC and ECL and used to measure the integrated luminosity. The $e^+e^- \to \mu^+\mu^-$ events are suitable for detector calibration such as alignments because of the absence of the hadronic effects.

The Bhabha and $e^+e^- \to \gamma\gamma$ events are scaled down due to their necessity and the large cross section. The total trigger rate including detection inefficiency for the physics event is ~ 100 Hz at luminosity of $1.6 \times 10^{34}\mathrm{cm}^{-2}s^{-1}$.

Table 2.2: Physics modes in the Belle experiment.

Process	σ(nb)	Purpose
$B\overline{B}$	1.05	Physics Analysis
$q\overline{q}(udsc)$	3.39	Physics Analysis
$\tau^+\tau^-$	0.892	Physics Analysis
$\mu^+\mu^-$	1.16	Detector Calibration
Bhabha ($\theta > 17°$)	~ 40	Detector Calibration
$\gamma\gamma$ ($\theta > 17°$)	2.4	Detector Calibration
e^+e^-X ($\theta > 17°, p_t \geq 0.1\mathrm{GeV}/c$)	~ 15	Physics Analysis
total with scale down	$\sim$10	

2.3 The Belle Detector

The Belle detector was designed and constructed to carry out quantitative studies of B meson decays and in particular rare B decay modes with very small branching fractions using an asymmetric e^+e^- collider operating at the $\Upsilon(4S)$ resonance, the KEKB factory. B-mesons are very short-lived particles and decay almost instantenously into relatively long life time particles before they reach the innermost detector. The Belle detector detects these fairly stable particles, namely $e^\pm$, $\mu^\pm$, $\pi^\pm$, $K^\pm$, $p, \bar{p}$, γ, and K_L. The neutron and anti-neutron cannot be detected although they are also produced.

The Belle detector is configured around a 1.5 T superconducting solenoidal magnet and iron structure surronding the KEKB beams at the Tsukuba interaction region of accelerator as wide solid angle as possible. It (Fig. 2.2) is comprised of seven sub-detectors which can detect the decay products of B meson, i.e. it can measure their position, momentum and energy, identify particle species. The B mesons

Table 2.3: Sub-detectors which measure each particle property.

	Position	Momentum	Energy	Particle Identification
$e^-(e^+)$	SVD, CDC	CDC	ECL	ECL, ACC, TOF, CDC
$\mu^-(\mu^+)$	SVD, CDC	CDC	×	KLM, ACC, TOF, CDC
$\pi^+(\pi^-)$	SVD, CDC	CDC	×	ACC, TOF, CDC
$K^+(K^-)$	SVD, CDC	CDC	×	ACC, TOF, CDC
$p(\bar{p})$	SVD, CDC	CDC	×	ACC, TOF, CDC
γ	ECL	×	ECL	ECL, CDC
K_L	KLM	×	×	KLM

decay vertices are measured by a Silicon Vertex Detector (SVD) [32] situated just outside of the cylindrical beryllium beam pipe. Charged particle tracking is performed by a wire drift chamber known as Central Drift Chamber (CDC) [34]. Particle identification is provided by dE/dx measurements in CDC, Aerogel $\check{C}$erenkov Counter (ACC) [36] and Time-Of-Flight (TOF) [38] detector placed radially outside the CDC. Electromagnetic showers are detected in an array of CsI (Tl) crystals of Electromagnetic Calorimeter (ECL) located inside the solenoid coil. The Muons and K_L^0 mesons are identified by KLM detector which consists of arrays of resistive plate counters interspersed in the iron yoke. The detector covers the θ region extending from 17^o - 150^o. The part of the uncovered small angle region is instrumented with a pair of BGO crystal arrays (EFC) placed on the surfaces of the QCS cryostats in the forward and backward directions. The roles of sub-detectors in terms of the particle properties are listed in Table 2.3 and performance of sub-detectors are listed in Table 2.4.

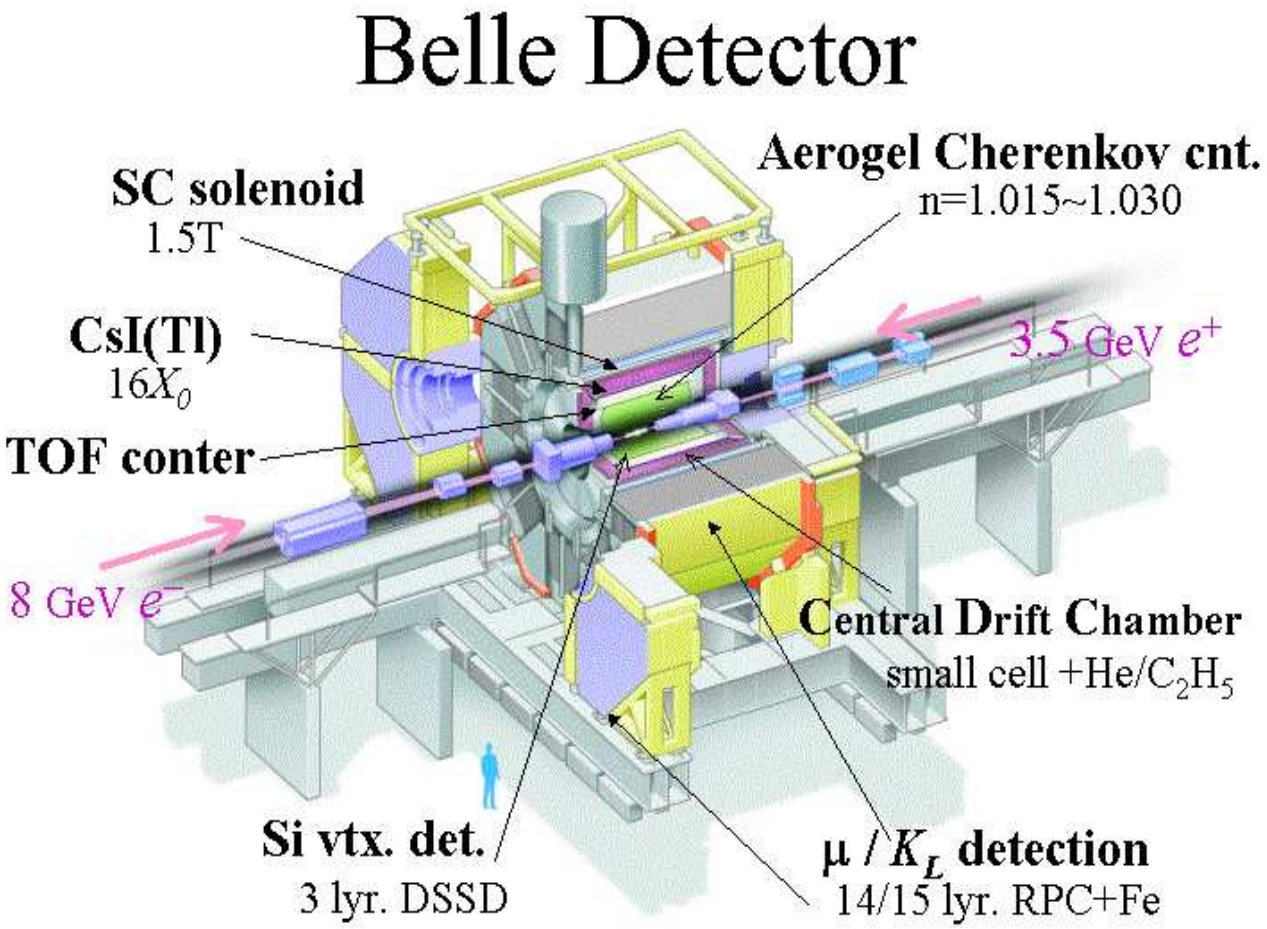

Figure 2.2: Belle Detector.

Table 2.4: Performance of detectors and subsystems. p and p_t in GeV/c, E in GeV.

Detector	Type	Configuration	Readout	Performance
Beam pipe(SVDI) SVDII	Beryllium double-wall	inner $r = 20$mm, 0.5(Be)/2.5(He)/0.5(Be)mm inner $r = 15$mm, 0.5(Be)/2.5(PF200)/0.5(Be)mm		
SVDI	Double sided Si-strip	300 μm thick 3-layers $r = 3.0 \sim 6.05$ cm	φ: 40.96 k θ: 40.96 k	$\sigma_\Delta z \sim 100\mu$m
SVDII	Double sided Si-strip	300 μm thick 4-layers $r = 2.0 \sim 8.8$ cm	φ: 55.296 k θ: 55.296 k	$\sigma_\Delta z \sim 100\mu$m
CDC	Small-cell drift chamber	Anode: 50 layer Cathode: 3 layers $r = 8.3$–86.3 cm	A: 8.4 k C: 1.8 k	$\sigma_{r\varphi} = 130\mu$m $\sigma_{p_t}/p_t = 0.3\%\sqrt{p_t^2+1}$ $\sigma_{dE/dx} = 6\%$
ACC	Threshold Čerenkov n =1.01–1.03 Silica aerogel	960 barrel 228 end-cap FM-PMT readout	1788	K/π separation: $1.2 < p < 3.5$ GeV/c
TOF/TSC	Plastic scintillator	φ segmentation: 128/64 $r = 120$ cm	128 × 2 / 64	$\sigma_t = 100$ ps K/π separation: $p < 1.2$ GeV/c
ECL	CsI(Tl) crystal	Barrel: $r = 125$–162 cm End-cap: z =-102/ +196 cm	B: 6624 FE: 1152 BE: 960	$\sigma_E/E = 0.066\%/E$ $\oplus 0.81\%/E^{1/4} \oplus 1.34\%$
KLM	Glass resistive plate counter	14 layers	φ: 16k θ: 16k	$\Delta\varphi = \Delta\theta = 30$ mrad for K_L 1% hadron fake rate for muon
EFC	BGO crystal 14 layers	Segmentation: 32 in φ, 5 in θ	160 × 2	$\sigma_E/E = (0.3-1)\%/\sqrt{E}$
Magnet	Superconducting	Inner radius 170 cm		B=1.5 T

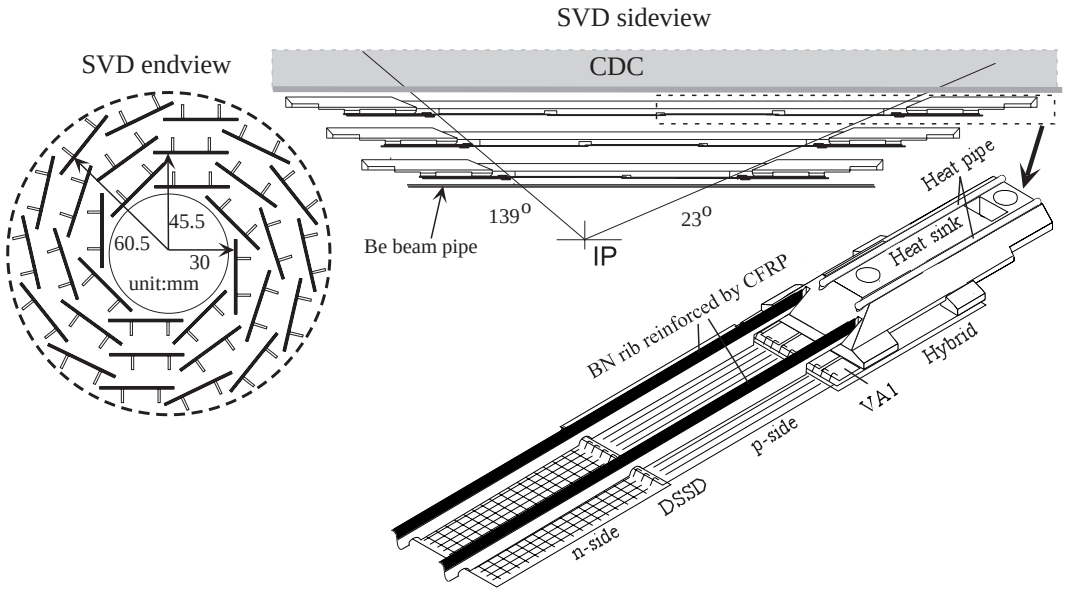

Figure 2.3: Configuration of SVD1.

2.3.1 Silicon Vertexing Detector (SVDI)

The main role of the Silicon Vertexing Detector (SVD) [32] is to provide precise measurement of the decay vertices of B mesons, which is essential to study a time-dependent CP asymmetry. The required Δz resolution is $\lesssim$ 200 μm since the averaged separation of two B meson vertices is $\sim 200\mu$m. The SVD is also useful for identifying and measuring the decay vertices of D and τ particles and it also contributes to the track reconstruction of charged particles and helps to improve the momentum resolution of the particle.

Since most particles of interest in Belle have momenta less than 1 GeV/c the vertex resolution is dominated by the multiple Coulomb scattering. This imposes strict constraints on the design of the detector. In particular, the innermost layer of the vertex detector must be placed as close to the interaction point as possible. Also, the support structure must be low in mass; and the readout electronics must be placed outside of the tracking volume.

Since the vertex resolution improves inversely with the distance to the first detection layer, the vertex detector has to be placed as close as possible to the interaction point and thus to the beam pipe wall. Another reason for placing the SVD around the beam pipe in order to withstand large beam backgrounds. However, with the high luminosity operation of KEKB, the radiation dose to the detector is measured to be 10 kRad/month. Radiation doses of this level both degrade the noise perfor-

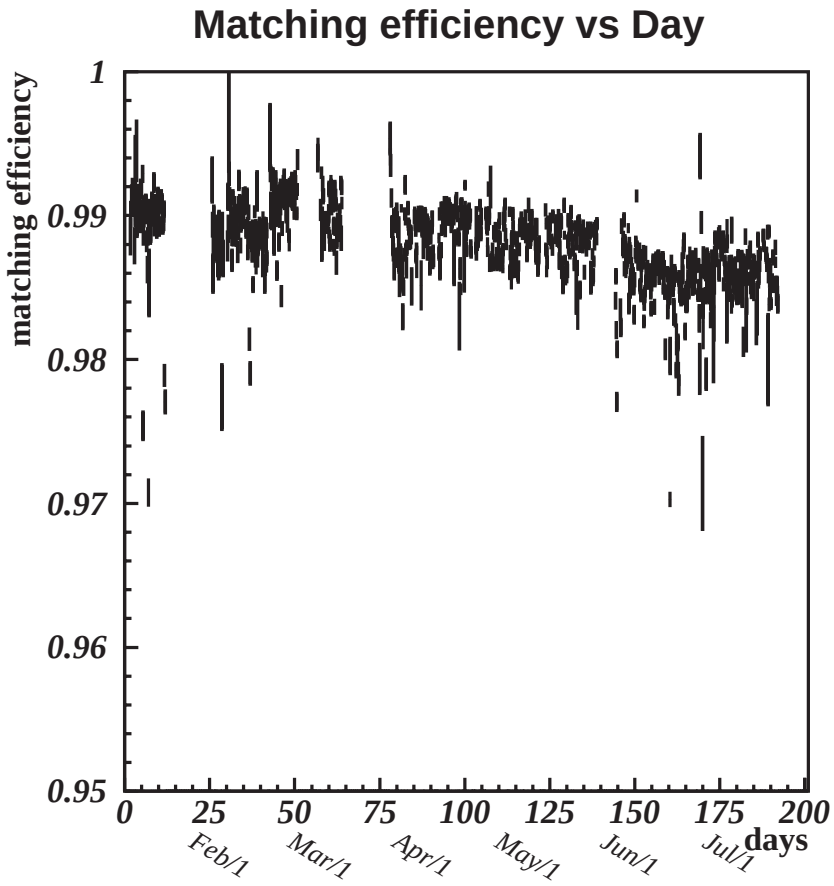

Figure 2.4: SVD-CDC track matching efficiency as a function of the date of data taking.

mance of the electronics and increase leakage currents in the silicon detector.

Fig. 2.3 shows the side and end views of the SVD. The SVD consists of three concentric cylindrical layers arranged in a barrel and covers a solid angle range $23^\circ < \theta < 139^\circ$, which corresponds to 86% of the full solid angle in the c.m.s. The three layers at radii of 30.0 mm, 45.5 mm, and 60.5 mm surround the beam pipe, a double-wall beryllium cylinder of 2.3 cm radius and 1 mm thickness. Three layers are constructed from eight, ten, and fourteen independent ladders from inner to outer, respectively. Each ladder consists of double-sided silicon strip detectors (DSSDs) reinforced by boron-nitride support ribs. In total, there are 32 ladders and 102 DSSDs. Each DSSD has 1280 sense strips and 640 readout pads on both side.

The S6936 DSSDs fabricated by Hamamatsu Photonics (HPK) are used for the SVD. Each DSSD size is $57.5 \times 33.5\text{mm}^2$ with 300 μm thickness. Signal from DSSDs

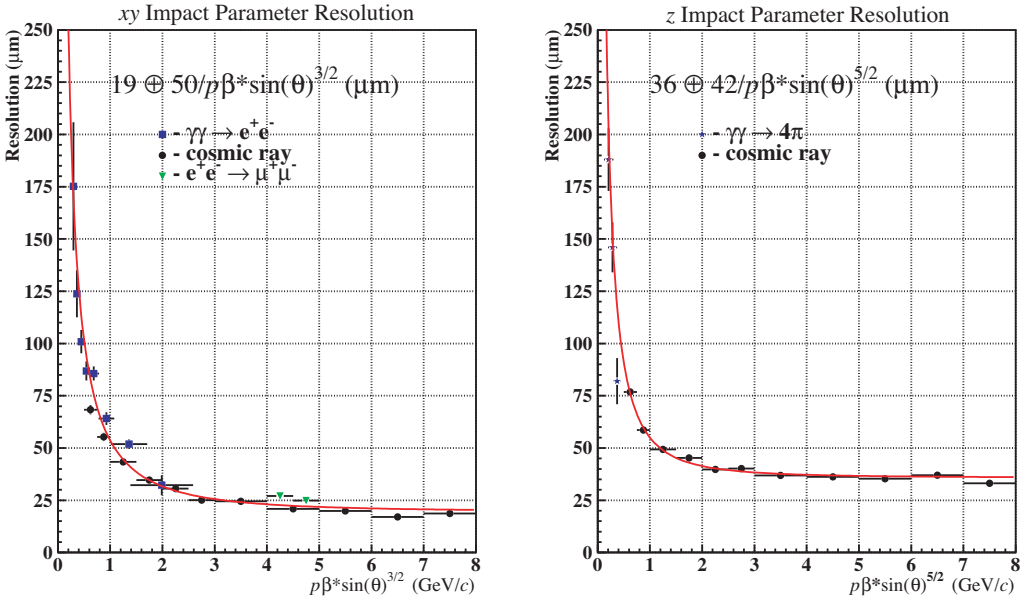

Figure 2.5: Impact parameter resolutions for the r-φ (left) and z direction (right).

are read out by 128 channel VA1 chips placed on both sides of the ladder. Inside the VA1 chip, signals are amplified and sent to shaping circuits, where the shaping time is adjusted to about 1 μs. Then, the outputs of the shaper are held when the VA1 chips recieve a Level-0 (L0) trigger signal provided by TOF. This analog information is passed to fast analog-to-digital converters (FADC) in the electronic hut if a Level-1 (L1) trigger occurs. The total number of readout channels are 81920.

The readout chain for DSSDs is based on the VA1 integrated circuit fabricated in the Austrian Micro Systems (AMS) 1.2-μm CMOS process. It was specially designed for the readout of silicon vertex detectors and other small-signal devices. VA1 has excellent noise performance and reasonably good radiation tolerance of 500 kRad.

For the z-coordinate measurement, the n-side strips are used and a double-metal structure running parallel to z is employed to route the signals from orthogonal z-sense strips to the ends of the detector. Adjacent strips are connected to a single readout trace on the second metal layer which gives an effective strip pitch of 84 μm. A p-stop structure is employed to isolate the z-sense strips. A relatively large thermal noise ($\sim 600e^-$) is observed due to the common-p-stop design. On the φ side only every other sense-strip is connected to a readout channel. Charged collected by the floating strips in between is read from adjacent strips by means of capacitive charge division.

The track-matching efficiency is defined as the probability that a CDC track

within the SVD acceptance associates SVD hits in at least two layers, and in at least one layer with both the r-φ and r-z information. Tracks from K^0_S decays are excluded since these tracks do not necessarily go through the SVD. Fig. 2.4 shows efficiency for hadronic events as a function of time. The averaged matching efficiency is better than 98.7%, although slight degradation is observed after one year operation as a result of the gain loss of VA1 from radiation damage [32].

The impact parameter resolution for reconstructed track is measured as a function of the track momentum p (measured in GeV/c) and the polar angle θ to be

$$\sigma_{r\varphi} = 19 \oplus \frac{50}{p\beta \sin^{3/2}\theta}\ \mu\mathrm{m}, \tag{2.9}$$

$$\sigma_z = 36 \oplus \frac{42}{p\beta \sin^{5/2}\theta}\ \mu\mathrm{m}, \tag{2.10}$$

as shown in Fig. 2.5.

2.3.2 Silicon Vertexing Detector (SVDII)

New SVD(SVDII) [33] has been installed in the summer of 2003. There are many improvement from SVDI. The geometrical configuration of SVDII is shown in Fig. 2.6 and 2.7. The SVDII consists of four cylindrical layers whose the radii are 20.0mm,

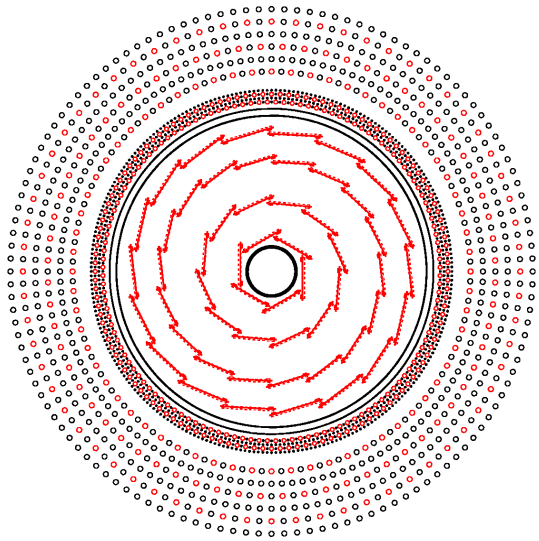

Figure 2.6: Configuration of SVDII.

43.5mm, 70.0mm and 88.0mm. The angular acceptance covers from 17° to 150°, which is same as CDC acceptance. The four layers have 6,12,18 and 18 ladders

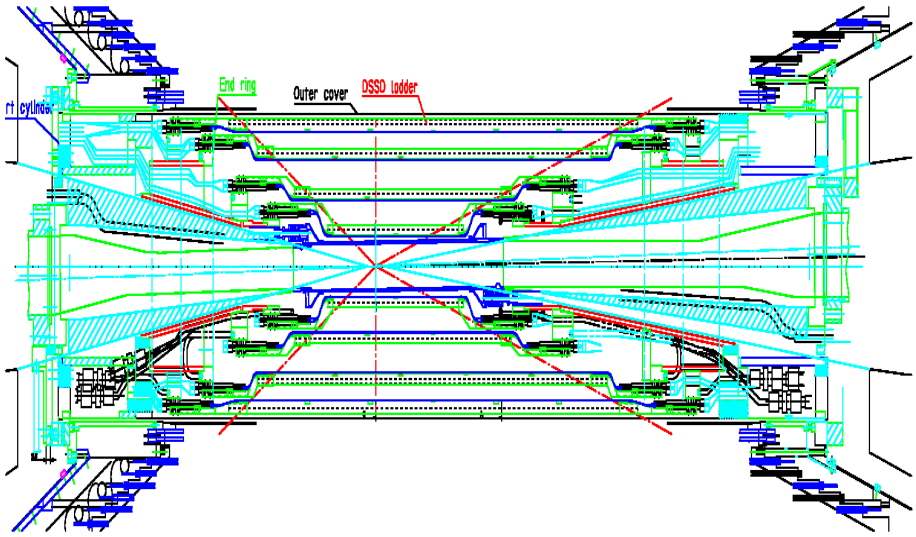

Figure 2.7: Side-view of SVDII.

to cover all the ϕ region and in each ladder are consisted with 2,3,5 and 6 DSSDs which are fabricated by Hamamatsu Photonics. There are two kinds of DSSDs. One is used in 1st, 2nd and 3rd layers, the size is $28.4 \times 79.6 \mathrm{m}m^2$, the strip pitch is 75μm on p-side and 50μm on n-side. The other one is used in 4th layer, the size is $34.9 \times 76.4 \mathrm{m}m^2$, the strip pitch is 73μm on p-side and 65μm on n-side. The n-side of DSSDs is used for measurement of the $r-\phi$ coordinate and the n-side is used for measurement of the z coordinate. The number of strip is 512 in the both n-side and p-side. The total number of DSSDs is 246. Therefore the total number of readout channel is $110592 (= 216 \times 512)$. As in SVDI each ladder is read out by four hybrids. Each hybrid employs four VA1TA (VA1 with trigger functions) chips, each VA1TA chips amplifies the signals from 128 strips, whose pulse heights are held and sent out serially. To minimize the readout deadtime the four chips on each hybrid are readin parallel. In contrast to SVDI where the chips were read sequentially. This represents a significant reduction in the overall deadtime of the Belle DAQ system The VAITA also incorporates a fast shaper and discriminator that provide digital signal use in the trigger. The signals are demultiplexed in the FADC boards housed in the electronics hut.

2.3.3 Central Drift Chamber (CDC)

The primary role of Central Drift Chamber (CDC) is the determination of three dimensional trajectories of charged particles and precise measurement of their momenta. The physics goals of the Belle experiment require a transverse momentum

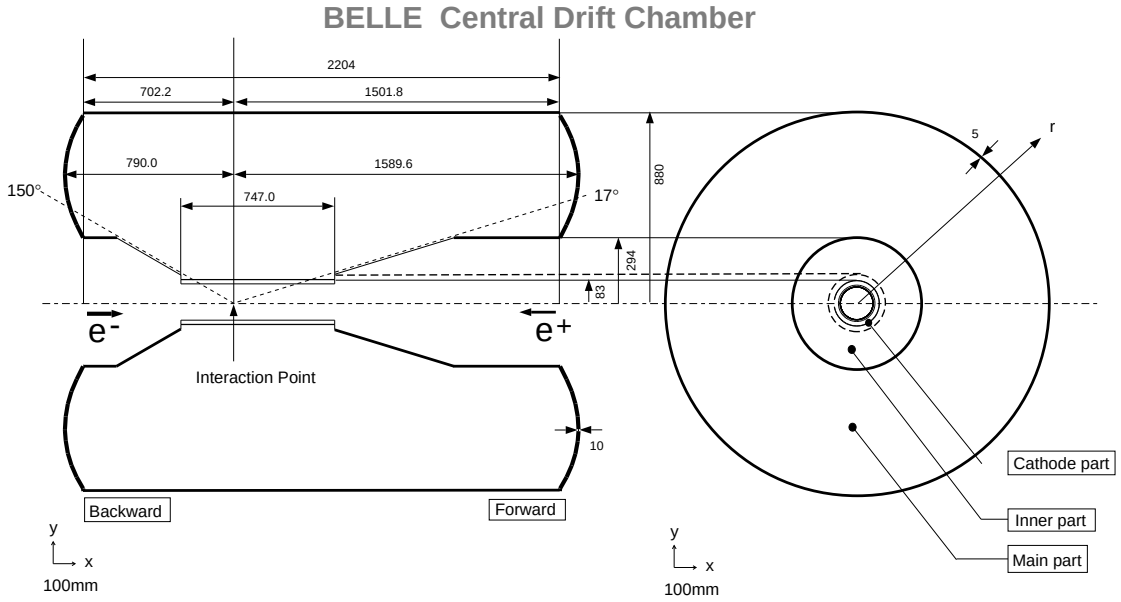

Figure 2.8: Schematic view of the CDC structure. The lengths in the figure are in units of mm.

resolution of

$$\frac{\sigma_{p_t}}{p_t} \sim \sigma_{MS} \oplus \sigma_r \sim 0.5 \oplus 0.5 p_t \ \% \tag{2.11}$$

for all charged particles with $p_t \geq 0.1$ GeV/c in the polar angle region $17° < \theta < 150°$. Here σ_{MS} denotes the error which comes from the multiple Coulomb scattering and shows constant contribution in above p_t region, and σ_r denotes the error proportional to p_t, which arises from the position measurement. One can calculate p_t from the radius of curvature r as

$$p_t = 0.3Br \tag{2.12}$$

where p_t is in units of GeV/c, B is the magnetic field in Tesla, and r is in meter.

The main purpose of the CDC [34] is to provide good momentum and position resolution for charged tracks. It is essential to reduce the amount of material in the tracking volume in order to obtain good momentum resolution since the effects of the multiple Coulomb scattering on the resolution are dominant for the charged particles below 1.0 GeV/c where our target events decay into. In addition, the CDC is used to measure the energy loss (dE/dx) of charged particles for their particle identification. The amount of dE/dx depends on $\beta = v/c$ of the charged particle (Bethe-Bloch formula). Another important role of the CDC is to provide an important information regarding trigger system in the r-ϕ and z dimensions.

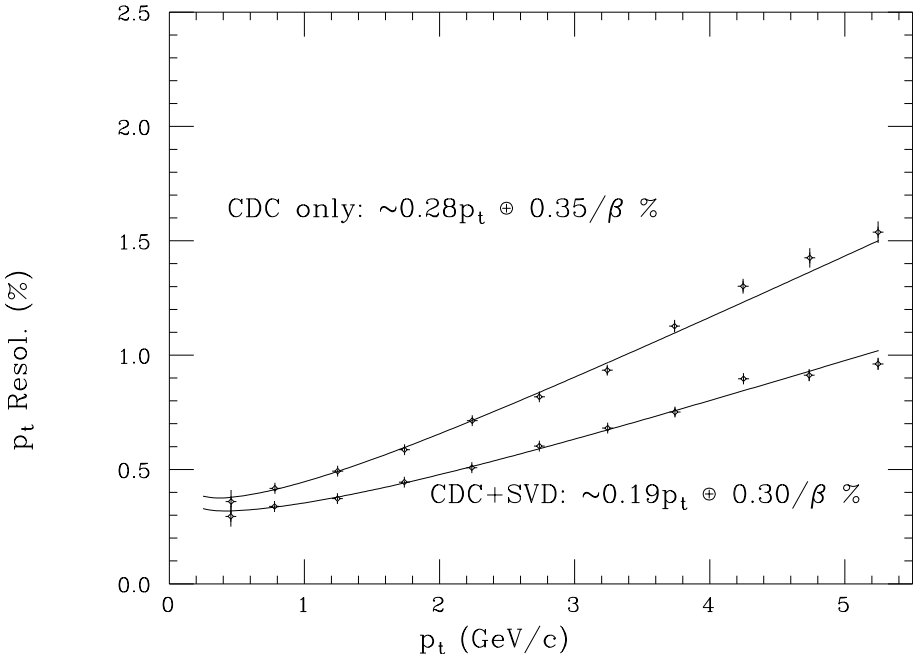

Figure 2.9: p_t dependence of p_t resolution for cosmic rays. The curves are the fit results for the cases with CDC and with CDC+SVD.

The structure of the CDC is shown in Fig. 2.8. It is a cylindrical chamber with inner radius 77 mm, outer radius 880 mm, and length 2400 mm and consists of 50 sense wire layers and three cathode strip layers. The sense wire layers are grouped into 11 super layers, where six of them are axial and five are small-angle stereo super layers. Each super-layer consists of between three and six radial layers, all with the same number of drift cells in azimuthal direction. The small-angle stereo layers are used in conjunction with the axial layers to provide z coordinate measurements. Stereo layers also provide a highly-efficient fast z-trigger combined with the cathode strips. We determined the stereo angles in each stereo super layer by maximizing the z-measurement capability while keeping the gain variations along the wire below 10%. Total number of sense wires is 8400, of which 5280 is axial and 3120 is stereo. The cathode strips are divided into eight segments in φ direction and 64 segments (8.2 mm pitch) in z to provide z-coordinate information used for the fast trigger.

Low-Z gas (50% helium, 50% ethane) is chosen in order to minimize multiple Coulomb scattering contribution to the momentum resolution. The average spatial resolution for whole drift space is measured to be approximately 130 μm in r-φ direction.

Charged particle tracking is done by Kalman filtering method [35], taking into account the effect of multiple Coulomb scattering, energy loss, and non-uniformity

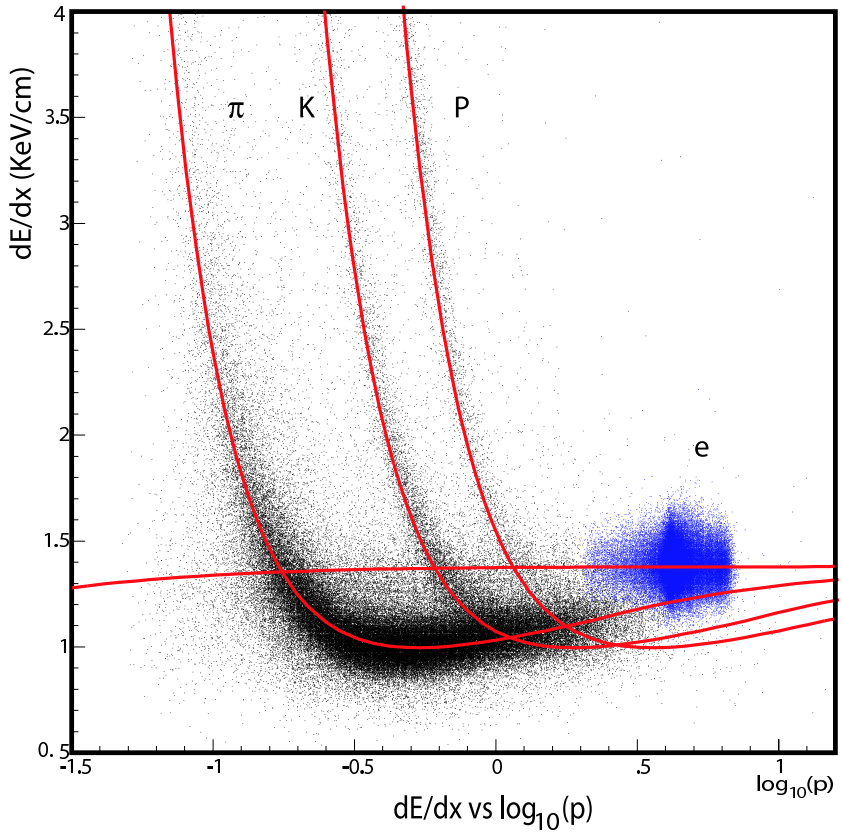

Figure 2.10: Measured dE/dx *vs.* momentum in collision data. The expected mean energy loss for different species are shown.

of the magnetic field. The transverse momentum resolution as a function of p_t measured using cosmic ray tracks during collision runs, is shown in Fig. 2.9. The upper result is for the case we use only CDC information. The lower is for the case we also use SVD hit information in the track parameter fit. The resolution is substantially improved by including SVD. The p_t resolution is measured to be

$$\frac{\sigma_{p_t}}{p_t} = (0.30 \oplus 0.19 p_t)\%. \tag{2.13}$$

The mean rate of energy loss (dE/dx) of a charged particle is given by the Bethe-Bloch equation,

$$-\frac{dE}{dx} = 4\pi N_A r_e^2 m_e c^2 \frac{Z}{A}\Big(\frac{z}{\beta}\Big)\Big[\ln\Big(\frac{2m_e c^2\beta^2\gamma^2}{I}\Big) - \beta^2 - \frac{\delta}{2}\Big] \tag{2.14}$$

where N_A is the Avogadro's number, r_e is the classical electron radius, m_e is the mass of electron. Z and A are the atomic number and mass number of the atoms of the

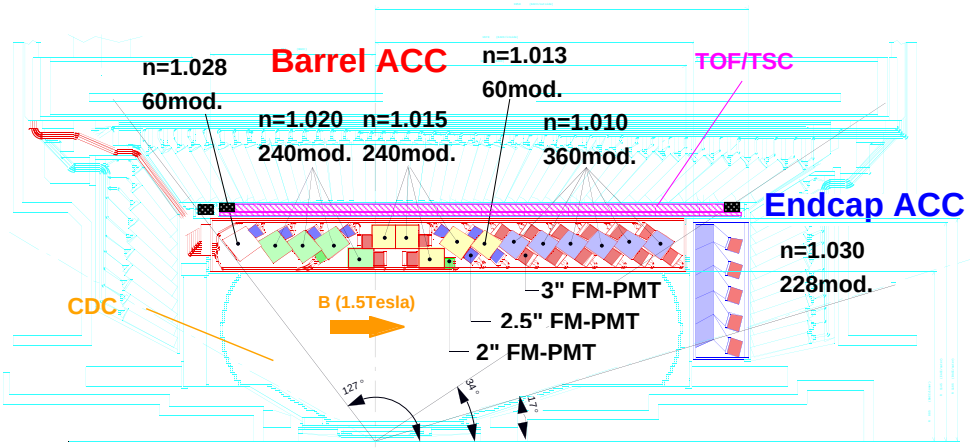

Figure 2.11: Configuration of ACC and TOF system

medium, z and v are the charge (in units of e) and velocity of the particle, $\beta = v/c$, $\gamma = 1/\sqrt{1-\beta^2}$, $I \simeq 16Z^{0.9}$ eV is the mean excitation energy of the medium, and x is the path length in the medium, measured in gcm^{-2}. Eqn. (2.14) shows that dE/dx is independent of the mass of the particle and depends on β. Therefore we can estimate β from a measurement of dE/dx. The measurement of β can provide a useful method for estimating the rest mass and thus differentiating particle species in conjunction with the momentum measurement.

Fig. 2.10 shows the measured dE/dx as a function of momentum, together with the expected mean values for different species. Populations of pions, kaons, protons and electrons are clearly seen. The dE/dx resolution is measured to be 7.8% for pions in the momentum range from 0.4 to 0.6 GeV/c, while the resolution for Bhabha and muon pair events is measured to be about 6%. The dE/dx information provides $\geq 3\sigma$ K/π separation up to 0.8 GeV/c. The dE/dx for kaons and pions have cross-over around 1 GeV/c, however they can provide some discrimination between kaons and pions above 2 GeV/c. It also provides more than 3 σ e/π separation for the momentum range from 0.3 GeV/c to 3 GeV/c.

2.3.4 Aerogel Čerenkov Counter System (ACC)

In the momentum region below 1 GeV/c, the K/π separations have been performed by dE/dx measurement from CDC and time of flight measurements. The Aerogel Čerenkov Counter System (ACC) [36] provides particle identification information (basically π/K separation) in the momentum range from 1.2 GeV/c to 3.5 GeV/c by detection of the *Č*erenkov light from particle penetrating through silica aerogel radiator, where the CDC and TOF are not available for the particle identification. The Belle ACC is threshold type Čerenkov detector, which identifies particle species according to whether Čerenkov light is emitted or not in the material. Čerenkov light is emitted if the velocity of the charged particle, β satisfies

$$\beta = \frac{p}{\sqrt{p^2 + m^2}} > 1/n, \tag{2.15}$$

where n is the refractive index of the matter, m and p are the mass and momentum of the charged particle, respectively. Therefore there is a momentum region where pions emit Čerenkov light while kaons do not, depending on the refractive index of the matter. For example, pions with momentum 2 GeV/c emit Čerenkov light in the matter if $n > 1.002$, while $n > 1.030$ is necessary for kaons with the same momentum.

The ACC consists of 960 counter modules segmented into 60 cells in the φ direction and 16 cells in z direction for the barrel part and 228 modules arranged in 5 concentric layers for the forward endcap part of the detector (Fig. 2.11). The possible momentum range of charged particles from B decays depends on the polar angle at Belle due to the asymmetric beam energy, that is, higher momentum particles could come into forward endcap part. In order to obtain good π/K separation for the momentum range from 1.2 GeV/c to 3.5 GeV/c, the refractive indices of aerogels in the barrel region are selected to be between 1.01 and 1.028, depending on their polar angle. For the endcap ACC where particles come into with relatively higher momentum due to asymmetric beam energy, because we failed to produce extremely low refractive index aerogel, those with the refractive index 1.03 are used to cover lower momentum region and to tag the B meson flavor, helping absence of the TOF system in the endcap. Aerogel tiles are stacked in 0.2 mm-thick aluminum boxes. Each aerogel radiator module is viewed by one fine-mesh photomultiplier (FMPMT) in the endcap and two FMPMT's in the barrel. The FMPMT can be operated in a magnetic field of 1.5T [37].

Fig. 2.12 shows the measured pulse height distributions for barrel ACC for $e^{\pm}$ tracks in Bhabha events and $K^{\pm}$ candidates in hadronic events, together with the expectations from Monte Carlo simulation. $K^{\pm}$ tracks are selected by TOF and dE/dx measurements. Clear separation can be seen from the distributions.

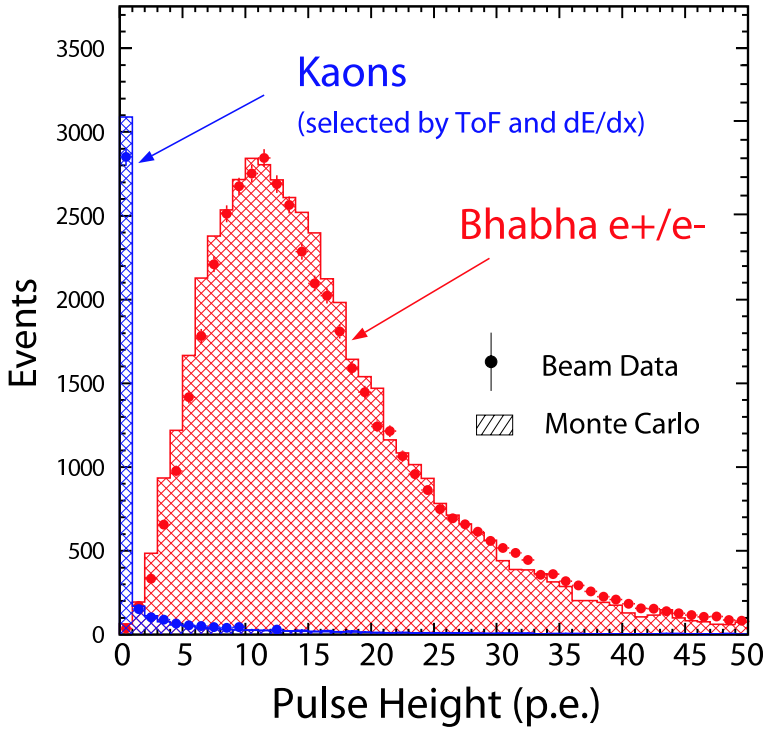

Figure 2.12: Pulse-height spectra in units of photoelectrons observed by ACC for electrons and kaons. The Monte Carlo expectations are superimposed.

2.3.5 Time-of-Flight Counters (TOF)

A time-of-flight (TOF) detector system [38] provides particle identification information for momentum below 1.2 GeV/c with time resolution 100 ps. It also provides fast timing signals for the trigger system.

The TOF system consists of 128 plastic scintillation counters and 64 thin Trigger Scintillation Counters (TSC). Two trapezoidal shaped TOF counters and one TSC counter form a module. Each TOF (TSC) counter is read out by two (one) fine-mesh photomultipliers. In total, 64 TOF/TSC modules located at a radius of 1.2 m from the interaction point cover a polar angle range from 33° to 121°. The configuration of the TOF is shown in Fig. 2.11.

The flight time T of particle in length L is expressed as

$$T = \frac{L}{c}\sqrt{1 + c^2(m/p)^2}. \tag{2.16}$$

Given the momentum from CDC, the time-of-flight can be used for the particle identification by calculating the mass of the particle. For the case of particles with

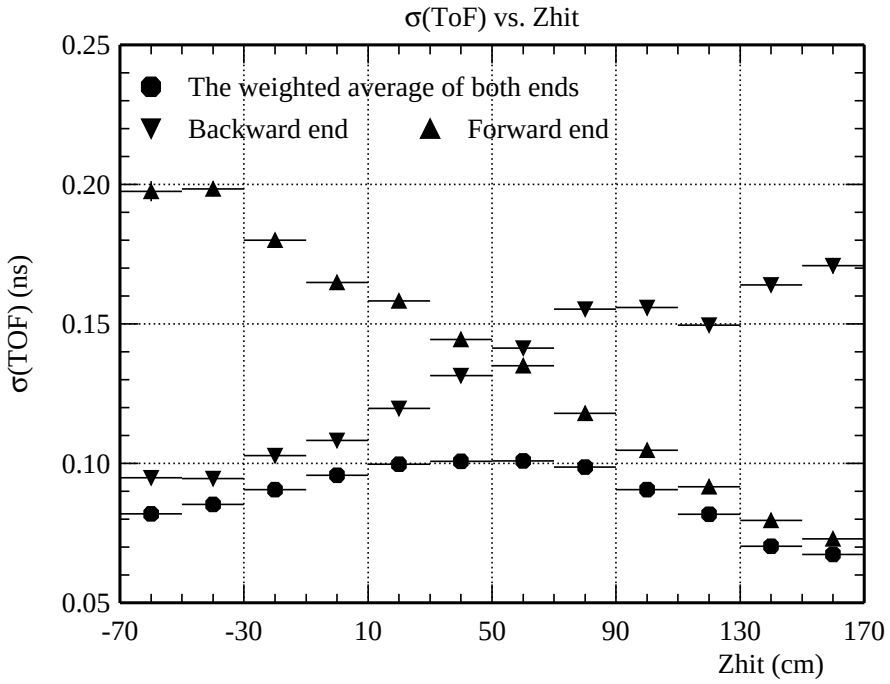

Figure 2.13: Measured time resolution of the TOF as a function of z hit position for μ pair events.

momentum of 1.2 GeV/c, $T = 4.0$ ns for pions and $T = 4.3$ ns for kaons with $L = 1.2$ m. Thus, time resolution of 100 ps would provide more than 3 standard deviation separation below 1.2 GeV/c.

The time resolution of Belle TOF system is measured to be about 100 ps with a small z hit position dependence as shown in Fig. 2.13. Fig. 2.14 shows the particle mass distribution calculated from measured time-of-flight for particles with momentum less than 1.25 GeV/c. Clear peaks corresponding to pions, kaons, and protons can be seen.

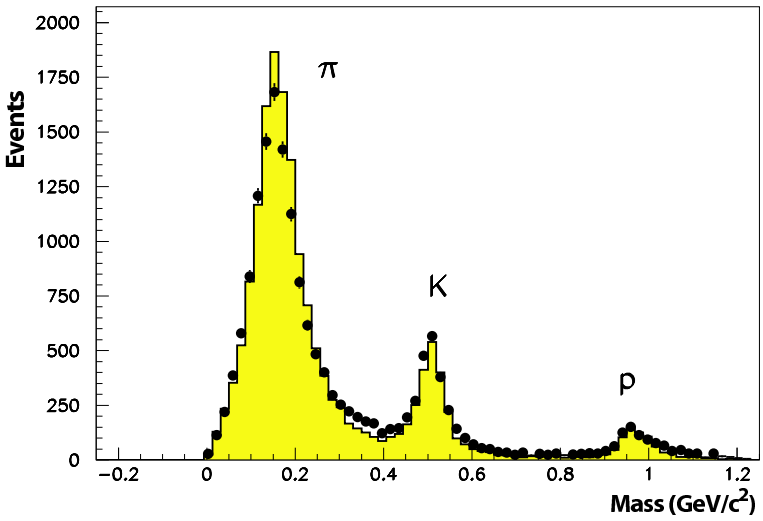

Figure 2.14: Distributions of hadron masses calculated from measured time-of-flight for particles with momenta less than 1.25 GeV/c. Histogram shows Monte Carlo prediction obtained by assuming $\sigma_{\rm TOF} = 100$ ps.

Hadron Identification

π/K separation is very important for the measurement of $\gamma\gamma \to \pi^+\pi^-$ and $\gamma\gamma \to K^+K^-$ processes as well as the study of B meson decays, and is designed to cover the momentum range up to 3.5 GeV/c with more than three standard deviation, which is the kinematic upper limit of particle momenta from B decays in the Belle experiment. Momentum coverage of each detector for K/π separation is shown in Fig. 2.15. We combine information from three independent measurements: energy loss (dE/dx) measurement in the CDC, time-of-flight measurement by the TOF, and the number of photoelectrons (N_{pe}) in the ACC.

For each charged track, we calculate three likelihood functions using subdetector information with kaon and pion hypothesis, $\mathcal{L}_h^{\rm ACC}$, $\mathcal{L}_h^{\rm TOF}$ and $\mathcal{L}_h^{\rm CDC}$, where h denotes assumed particle species. Then, a combined likelihood is calculated by a product of these likelihood functions for a specific hadron species,

$$\mathcal{L}_h = \mathcal{L}_h^{\rm ACC} \times \mathcal{L}_h^{\rm TOF} \times \mathcal{L}_h^{\rm CDC}. \tag{2.17}$$

By combining them, a normalized likelihood function is calculated in such way that kaon-like particle gives about one and pion-like particle gives value close to zero,

$$\mathcal{R}(K|\pi) = \frac{\mathcal{L}_K}{\mathcal{L}_K + \mathcal{L}_\pi}\,. \tag{2.18}$$

We use this ratio to discriminate kaons from pions. The efficiency is measured to be about 85% with charged pion fake rate below 10% for all momenta up to 3.5 GeV/c

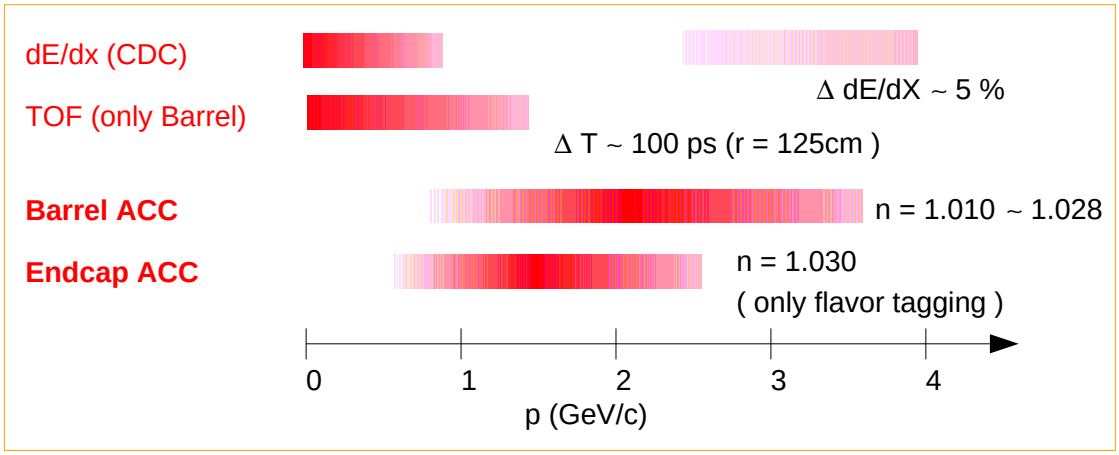

Figure 2.15: Momentum coverage of each detector used for K/π separation.

with nominal likelihood requirement. Fig. 2.16 shows the kaon identification efficiency and fake rate as a function of momentum, measured using $D^{*+} \to D^0(K\pi)\pi^+$ decays.

The $\mathcal{R}(p|K)$ is defined in similar manner as $\mathcal{R}(\pi|K)$.

2.3.6 Electromagnetic Calorimeter (ECL)

When a high-energy electron or photon is incident on a thick absorber, it initiates an electromagnetic cascade as pair production and bremsstrahlung which generate more electrons and photons with lower energy. The longitudinal development of the electromagnetic shower scales with the radiation length X_0 of the matter, which is defined as the mean distance over which a high-energy electron loses all but $1/e$ of its energy by bremsstrahlung.

The main purpose of Electromagnetic Calorimeter (ECL) [39] is the detection of photons with high efficiency and good resolutions in energy and position. It also plays a primary role in the electron identification in Belle.

The ECL consists of 8736 CsI(Tl) crystals covering the polar angle region of $17° < \theta < 150°$. CsI(Tl) is chosen because of its large photon yield, relatively weak hygroscopicity, mechanical stability and moderate price. An overall configuration of the ECL is shown in Fig. 2.17. Each CsI(Tl) crystal has a tower-like shape with 30 cm length (corresponds to 16.2 X_0) and is assembled to point toward the interaction point. The transverse dimensions of a crystal vary depending on their polar angle positions. Typical dimensions of a crystal are 55 mm $\times$ 55 mm (front surface) and

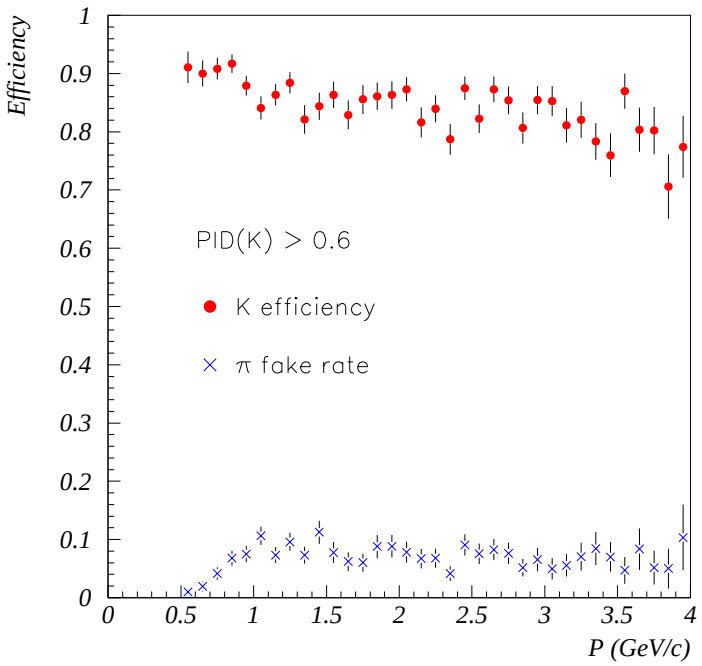

Figure 2.16: Kaon identification efficiency and π fake rate as a function of momentum.

65 mm $\times$ 65 mm (rear surface) for the barrel part, and 44.5 mm $\times$ 70.8 mm (front surface) and 54 mm $\times$ 82 mm (rear surface) for the end-cap part. The geometrical configuration of these crystals are summarized in Table 2.5. Each crystal is read out by two 2 cm $\times$ 1 cm photodiodes.

The photon energy resolution is measured to be

$$\frac{\sigma_E}{E} = 1.34 \oplus \frac{0.066}{E} \oplus \frac{0.81}{E^{1/4}}\% \tag{2.19}$$

from the beam test before installation into the Belle structure. Fig. 2.18 shows the energy resolution measured from Bhabha events. The energy resolution of photon was achieved to be 1.7% for the barrel ECL, and 1.74% and 2.85% for the forward and backward ECL, respectively.

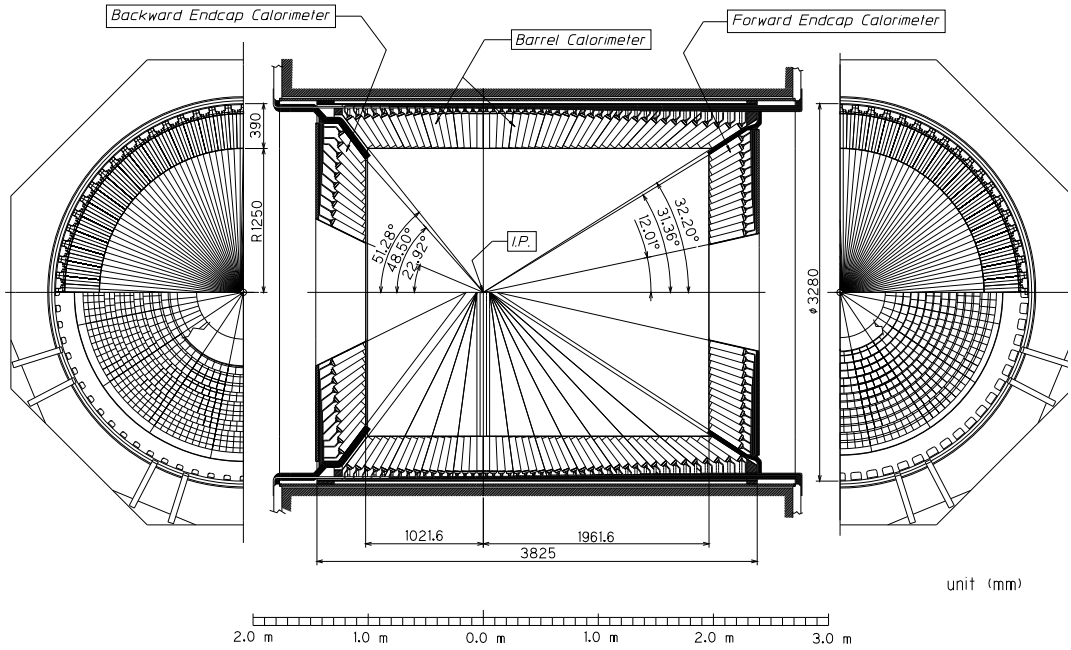

Figure 2.17: Configuration of the ECL.

Electron Identification (EID)

EID in Belle primarily relies on a comparison of the charged particle momentum measured by the CDC and the energy deposit in the ECL. Electrons lose all their energies in the ECL crystals with electromagnetic showers, while hadrons and muons deposit only part of their energies in the ECL. Thus, E/p, the ratio of the cluster energy measured by the ECL to the charged track momentum measured by the CDC is close to one for an electron or positron and tends to be lower for the other charged particles. Because electromagnetic shower evolves faster than hadronic shower, the shape of a shower detected at the ECL is different both in transverse and longitudinal direction between an electron or positron and hadron. To evaluate the shower shape in transverse direction quantitatively, $E9/E25$ is defined as a ratio of energy summed in 3×3 crystals to that in 5×5 crystals. The dE/dx measurement from the CDC is also an effective tool to identify an electron especially for the low momentum region where E/p is unreliable for electron or positron identification because they lose fair amount of their energy before they reach the ECL. In low momentum region the

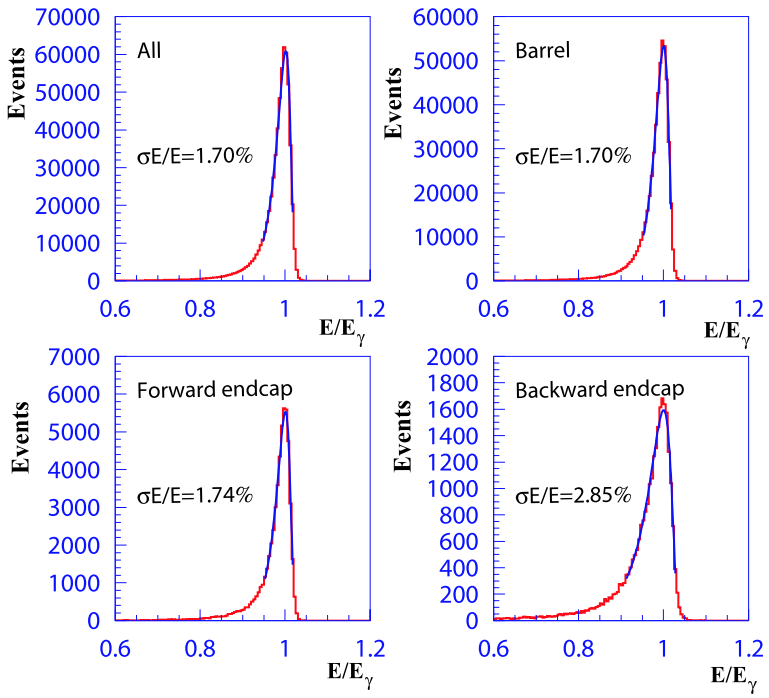

Figure 2.18: Energy resolutions measured from $e^+e^- \to \gamma\gamma$ event samples for overall, barrel, forward-endcap, and backward-endcap. E and E_γ are measured and calculated γ energies, respectively.

ACC information is used for hadron rejection as well.

The probability density functions (PDF's) for electrons and non-electrons are calculated for each of above discriminants by track-basis, and unified into a final likelihood output $\mathcal{R}_e$ taking into account the momentum and angular dependencies [40].

The efficiency of electron identification is greater than 90% and a hadron fake rate (the probability to misidentify hadron as electron) is $\sim 0.3\%$ for a track with $p > 1$ GeV/c. Fig. 2.19 shows the electron identification efficiency as a function of momentum.

2.3.7 Superconducting Solenoid

A charged particle with a momentum vector at an angle λ with respect to the magnetic field direction, will have a trajectory which is described by a helix. The magnitude of the momentum can be determined from the measured radius of cur-

Table 2.5: Geometrical parameters of the ECL

Item	θ coverage	θ segment	φ segment	No.of crystals
Forward end-cap	$12.4^\circ - 31.4^\circ$	13	48-144	1152
Barrel	$32.2^\circ - 128.7^\circ$	46	144	6624
Backward end-cap	$130.7^\circ - 155.1^\circ$	10	64-144	960

vature of the helix using the relation

$$p = 0.3 \times \frac{qBR}{\cos\lambda}, \tag{2.20}$$

where $q = \pm 1$ is the charge of the particle, B is magnetic field, R is radius of curvature and p is the momentum of particle. A superconducting solenoid provides a magnetic field of 1.5 T parallel to the beam pipe. The superconducting coil consists of a single layer of a niobium-titanium-copper alloy embedded in a high purity aluminum stabilizer. It is wound around the inner surface of an aluminum support cylinder with 3.4 m in diameter and 4.4 m length.

2.3.8 K_L and Muon Detection System (KLM)

KLM.is the only detector which is outside the solenoid magnetic field. It has two major parts, namely barrel KLM and endcaps (backward and forward) KLM. The KLM system [41] is designed to identify K_L's and muons with high efficiency over a broad momentum range greater than 600 MeV/c. The KLM system consists of alternating layers of charged particle detectors and 4.7 cm thick iron plates. The barrel-shaped region around the interaction point covers an angular range in $45^\circ < \theta < 125^\circ$ and endcaps in forward and backward directions extend this to $20^\circ < \theta < 125^\circ$. There are 15 detector layers and 14 iron layers in the octagonal barrel region and 14 detector layers and 14 iron layers in each of forward and backward endcaps. The longitudinal scale of hadron shower is determined by the nuclear interaction length. The iron plates provide a total of 3.9 interaction lengths of material for a particle traveling normal to the detector planes. In addition, the electromagnetic calorimeter (ECL) provides another 0.8 interaction length of material to convert K_L's. The K_L which interacts in the iron or in the ECL produces a cascade shower of ionizing particles. The location of this shower determines the direction of K_L, however fluctuations in the size of the shower discourage a useful measurement of the K_L energy. The multiple layers of charged particle detectors and iron allow the discrimination between muons and charged hadrons based upon their range and transverse scattering. Muons travel much farther with smaller deflections than strongly interacting hadrons.

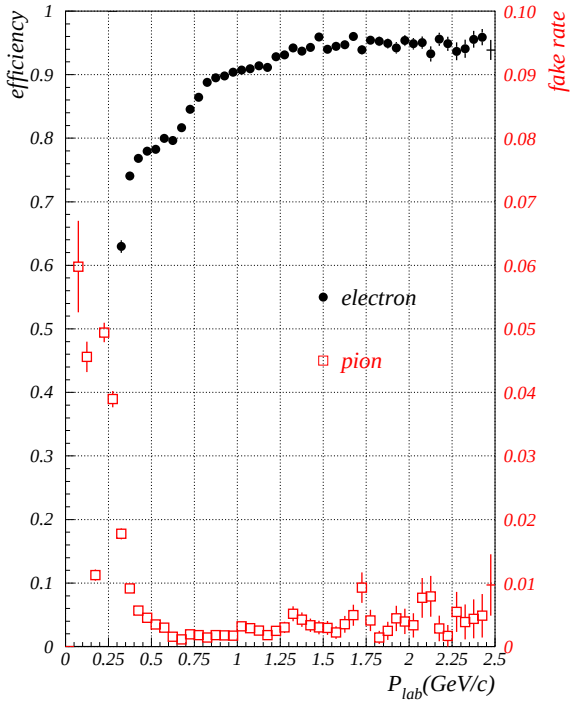

Figure 2.19: Electron identification efficiency (circles) and fake rate for $\pi^{\pm}$ (rectangles) as a function of momentum. Note that the scales for the efficiency and fake rate are different.

The detection of charged particles is provided by glass-electrode-resistive plate counters (RPCs) [42]. RPCs have two parallel plate electrodes with high bulk resistivity ($> 10^{10}\Omega$cm) separated by a gas-filled gap. We have chosen a non-flammable mixture of 62% CH_2FCF_3 (HFC-134a), 30% argon, and 8% butane-silver. The butane-silver is a mixture of approximately 70% n-butane and 30% iso-butane. In the streamer mode, an ionizing particle traversing the gap initiates a streamer in the gas that results in a local discharge of the plates. This discharge is limited by the high resistivity of the plates and the quenching characteristics of the gas. The discharge induces a signal on external pickup strips, which can be used to record the location and time of the ionization.

Fig. 2.20 shows the cross section of a superlayer for the barrel region, in which two RPCs are sandwiched between the orthogonal θ and φ pickup-strips with the ground planes for signal reference and proper impedance. This unit structure of the RPCs and two readout-planes is enclosed in an aluminum box and is less than 3.7 cm thick. Each PRC is electrically insulated with a double layer of 0.125 mm thick

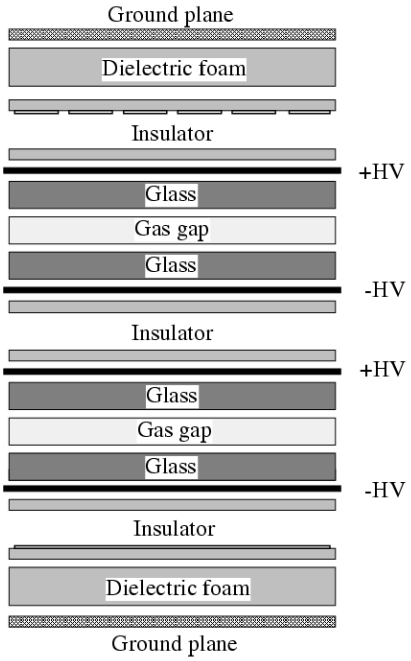

Figure 2.20: Cross section of a KLM superlayer.

mylar. Signals from both RPCs are picked up by copper strips above and below the pair of RPCs, providing a three-dimensional space point for particle tracking. Each barrel module has two rectangular RPCs with 48 z pickup strips perpendicular to the beam direction. The smaller seven superlayers closest to IP have 36 φ strips and the outer eight superlayers have 48 φ strips orthogonal to the z strips. Each end-cap superlayer module contains 10 π-shaped RPCs and have the 96 φ and 46 θ pickup-strips.

Fig. 2.21 shows the difference between the direction of the K_L cluster candidate and the missing momentum direction in data. The missing momentum vector is calculated using all the other measured particles in the event. The direction of the neutral cluster measured in the KLM is consistent with that of the missing momentum. A large deviation of the missing momentum direction from the neutral cluster direction is mainly due to undetected neutrinos and particles escaping the detector acceptance.

For muon identification [43], following two quantities are used to test the hypothesis that a track is a muon rather than a hadron.

- ΔR

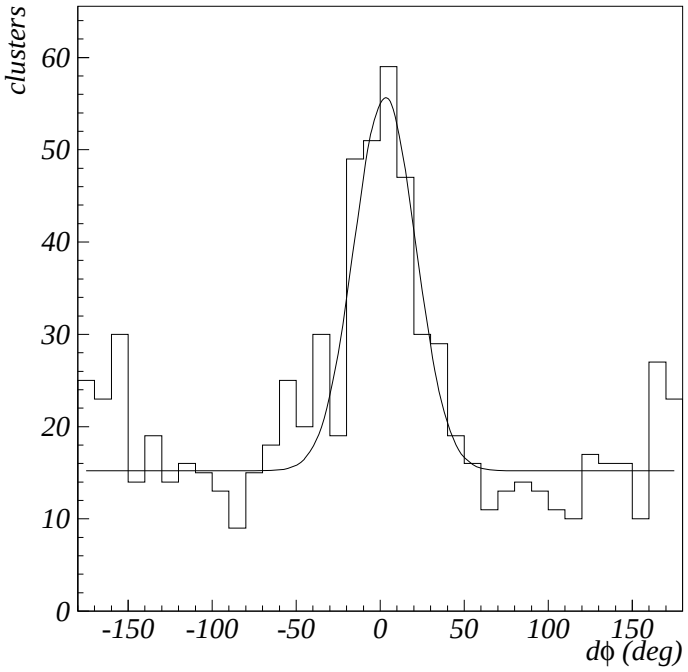

Figure 2.21: Difference between the neutral cluster and the direction of missing momentum in the KLM.

difference between the measured and expected range of the track in KLM.

- χ^2_r
  normalized transverse deviations of all hits associated with the track.

Based on above quantities, a simple product of the probability densities for each particle species i, $\mathcal{L}_i(\Delta R, \chi^2_r) = p^1_i(\Delta R) \cdot p^2_i(\chi^2_r)$ is constructed using the distributions of 100,000 single track events containing muons, pions, or kaons. The muon likelihood ratio is defined then as

$$\mathcal{R}_\mu = \frac{\mathcal{L}_\mu}{\mathcal{L}_\mu + \mathcal{L}_\pi + \mathcal{L}_K}. \tag{2.21}$$

Muon identification efficiency for criteria $\mathcal{R}_\mu > 0.1$ and $\mathcal{R}_\mu > 0.9$ for an experiment $e^+e^- \to e^+e^-\mu^+\mu^-$ sample is shown in Fig. 2.22. Typical efficiency for $\mathcal{R}_\mu > 0.9$ is $80 - 90\%$ for a muon track with 1.0 GeV/$c < p <$ 2.0 GeV/c.

The muon identification fake rate, depending on polar angle θ, is $2 - 7\%$ ($\mathcal{R}_\mu > 0.1$) and $1 - 3\%$ ($\mathcal{R}_\mu > 0.9$) for a track with 1.0 GeV/$c < p <$ 2.0 GeV/c, by using an experimental $K_S \to \pi^+\pi^-$ sample with 98% purity, as shown in Fig. 2.23.

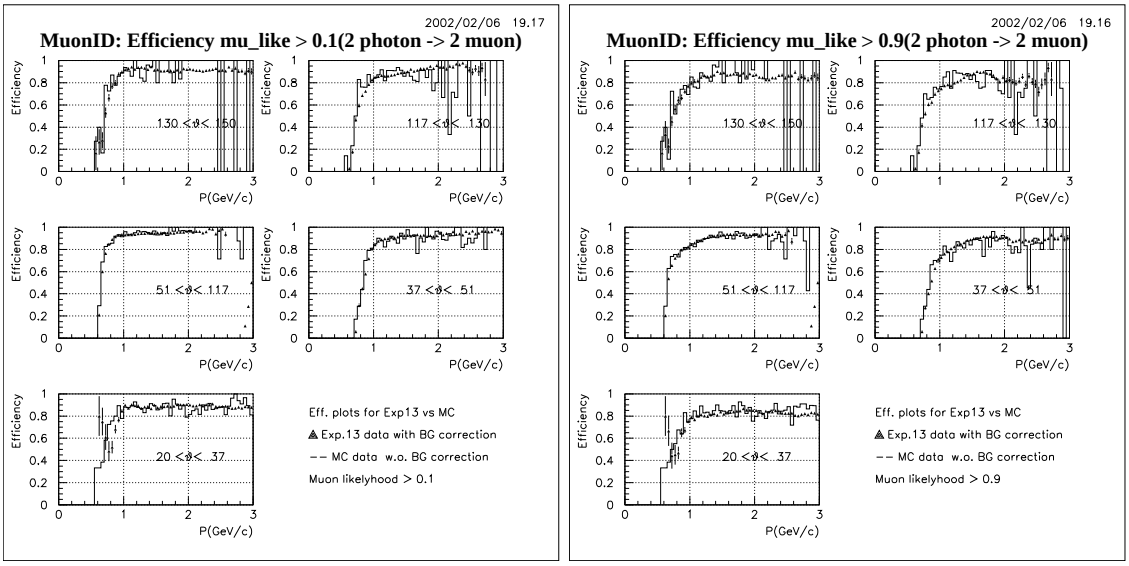

Figure 2.22: Muon identification efficiency for different polar angle regions for $\mathcal{R}_\mu > 0.1$ (left) and $\mathcal{R}_\mu > 0.9$ (right), using $e^+e^- \to e^+e^-\mu^+\mu^-$ sample.

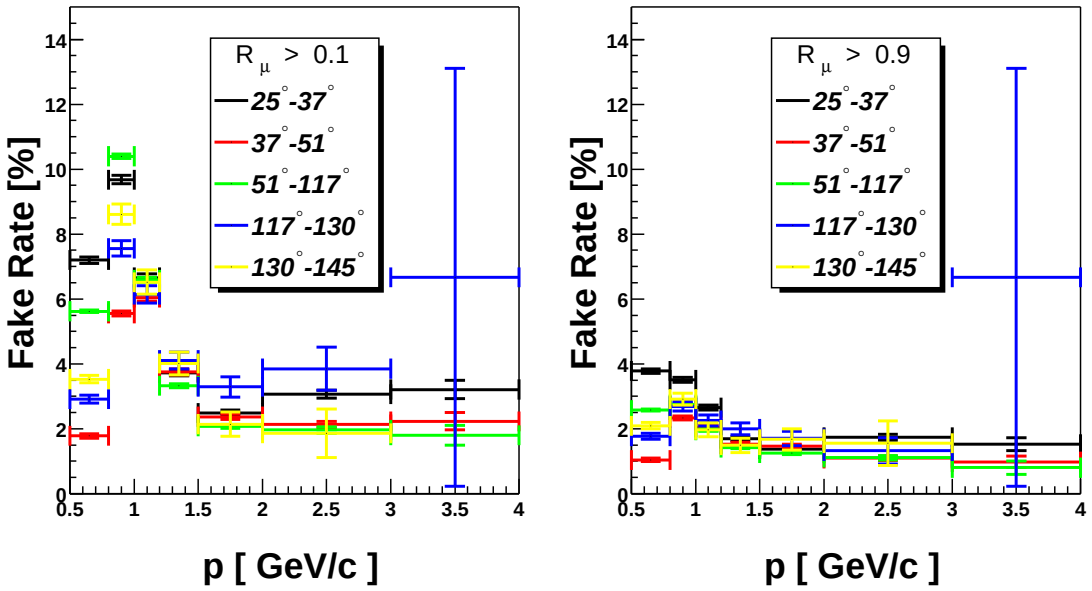

Figure 2.23: Muon identification fake rate for different polar angle regions for $\mathcal{R}_\mu > 0.1$ (left) and $\mathcal{R}_\mu > 0.9$ (right), using an experimental $K_S \to \pi^+\pi^-$ sample.

2.3.9 Extreme Forward Calorimeter (EFC)

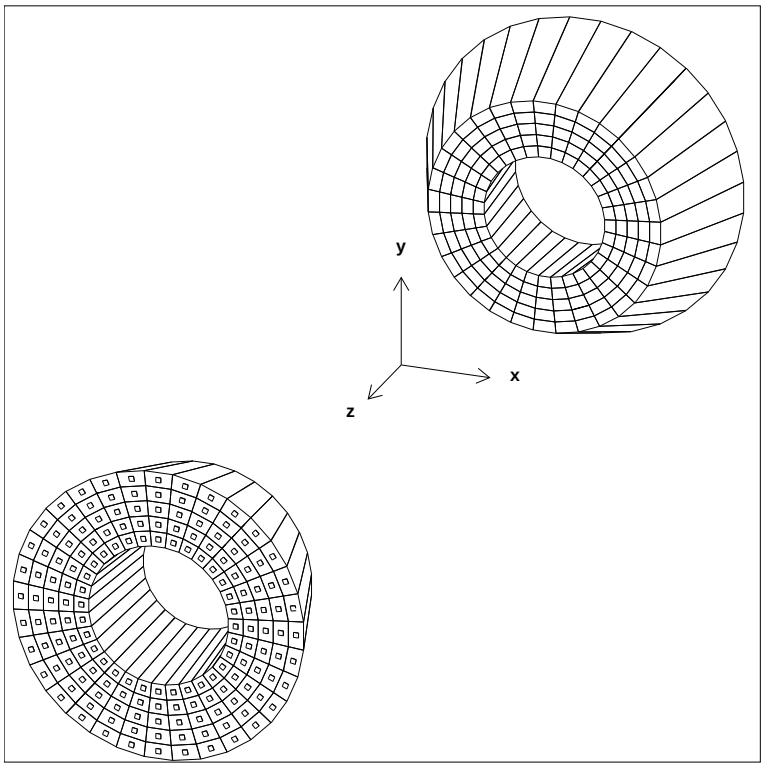

Figure 2.24: Configuration of the EFC.

EFC [44] is a calorimeter which further extends the polar angle coverage by ECL of $17^\circ < \theta < 150^\circ$. EFC covers the angular range from 6.4° to 11.5° in the forward direction and 163.3° to 171.2° in the backward direction (Fig. 2.24). EFC is also required to function as a beam mask to reduce backgrounds for CDC. In addition, EFC is used for a beam monitor for the KEKB control and a luminosity monitor for the Belle experiment. It also can be used as a tagging device for two-photon physics.

Since EFC is placed in the very high radiation-level area around the beam pipe near IP, it is required to be radiation-hard. Therefore, a radiation-hard BGO (Bismuth Germanate, $Bi_4Ge_3O_{12}$) crystal calorimeter is used for EFC. The detector is segmented into 32 in φ and 5 in θ for both the forward and backward detectors. The radiation lengths of the forward and backward crystals are 12 and 11, respectively.

The energy sum spectra for Bhabha events show a correlation between the forward and backward EFC detectors. A clear peak at 8 GeV with a resolution of 7.3% (rms) is seen for the forward EFC, while a clear peak at 3.5 GeV with a resolution

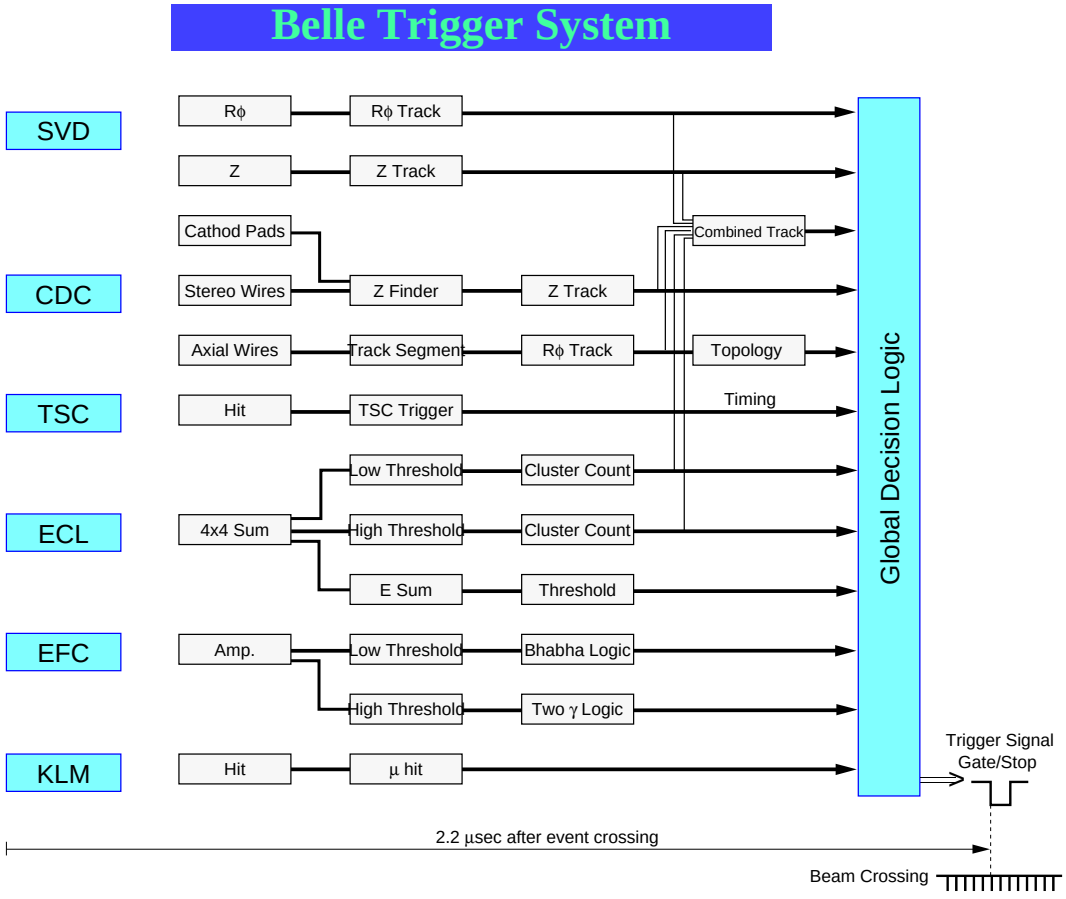

Figure 2.25: Sub-trigger system and the Global Decision Logic (GDL).

of 5.8% (rms) is seen in the backward EFC. These results are compatible with the beam test results.

2.3.10 Trigger System

The trigger system in Belle experiment records or discards the hit signals on each sub-detector. Since at higher luminosity, the physics events including $B\bar{B}$ events are produced at a very high rate, but also expect a large beam background due to the high beam current. Therefore, the trigger system which selects useful events from many unnecessary events in the online level plays an important role.

Fig. 2.25 shows a schematic view of the Belle Level 1 trigger system which is composed of the sub-trigger system and the central trigger system called the Global Decision Logic (GDL). The sub-trigger system is based on two categories, track

triggers and energy triggers. The CDC and TOF/TSC provide the trigger signals from charged particles, while the ECL trigger system provides triggers based on total energy deposit and cluster counting of crystal hits. The KLM and EFC trigger systems provide additional trigger information and the EFC triggers are used for tagging two-photon events as well as Bhabha events. The sub-triggers process event signals in parallel and provide trigger information to the GDL, where all information are combined to distinguish physics and background events and to characterize an physics event type. Information from the SVD is not implemented in the present trigger arrangement. The trigger system provides the trigger signal with the fixed time of 2.2 μs after the event occurrence, which used to be restricted by buffer size of the obsolete SVD module. Since process time of the GDL is 350 ns, the sub-triggers are required to issue the signal within 1.85 μs of the event occurrence. The Belle trigger system, including the sub-trigger system, is operated in a pipelined manner with clocks synchronized to the KEKB accelerator RF signal. Fig.2.26 shows a schematic view of the GDL, which consists of ITD (Input Trigger Delay), FTDL (Final Trigger Decision Logic) and TMDL(TiMing Decission Logic) modules. Timing of the sub-trigger signals is adjusted to overlap each other, by the ITD module, which therefore assigns larger delay to faster signal. Using thus adjusted signals the FTDL judges event occurrence or the type of the physics event with 32 MHz frequency. We use PSNM (Pre-Scaled aNd Mask) modules to prescale or mask the input signals. We define some 40 logics which express physics events, for example, if CDC nearly back-to-back tracks and KLM hit signals are detected at the same time, the FTDL identifies $e^+e^- \rightarrow \mu^+\mu^-$ event occurrence and send a signal to the next stage. Each of the multitrack, total energy, and isolated cluster counting trigger provides more than 95% efficiency for multi-hadronic data sample. As a result the combined efficiency is more than 99.5%.

2.3.11 Data Acquisition (DAQ)

The distributed-parallel system is devised for the Belle Data Acquisition System in order to satisfy the requirements so that it works at 500 Hz with a deadtime fraction of less than 10%. The global scheme of the system is shown in Fig. 2.27. The entire system is segmented into seven subsystems running in parallel, each handling the data from a sub-detector. Data from each subsystem are combined into a single event record by an event builder, which converts "detector-by-detector" parallel data streams to an "event-by-event" data river. The event builder output is transferred to an online computer farm, where another level of event filtering is done after the fast event reconstruction. The data are then sent to a mass storage system located at the computer center via optical fibers.

A typical data size of a hadronic event by $B\overline{B}$ or $q\bar{q}$ production is measured to be about 30 kB, which corresponds to the maximum data transfer rate of 15 MB/s.

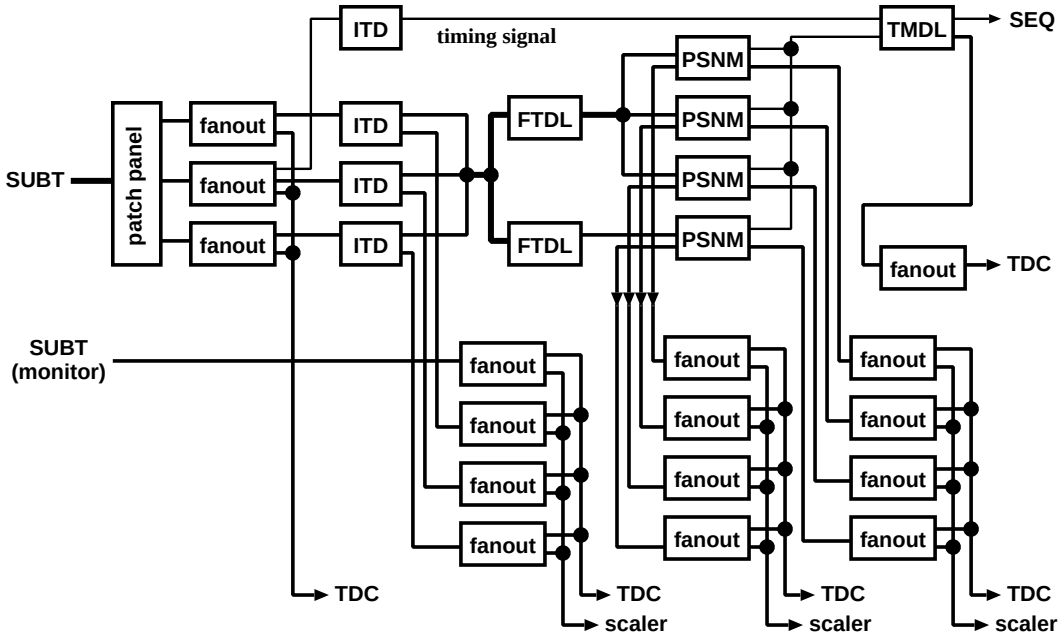

Figure 2.26: Schematic view of the GDL.

2.3.12 Offline Software and Computing

The computing and software system is of great importance to the Belle experiment as very complex analysis techniques using a large amount of data are required for physics discoveries. A traditional high energy physics (HEP) computing model is adopted by the Belle collaboration. Namely, the Belle collaboration choose to use tape library systems with the sequential access method for the input and output of experimental data as the mass storage system.

All software, except for a few HEP-specific and non-HEP-specific free software packages, are developed by the members of the Belle collaboration. In particular, the mechanisms to handle event structure and input and output formatting and to process events in parallel on a large Symmetric Multiple Processor (SMP) compute server are developed locally using C and C++ programming languages.

2.4 Analysis Framework

The event processing framework, called Belle AnalysiS Framework (BASF), takes users' reconstruction and analysis codes as modules which are dynamically linked at the run time. A module is written as an object on a class of C++. The class, inherited from the module class of BASF which has virtual functions for events,

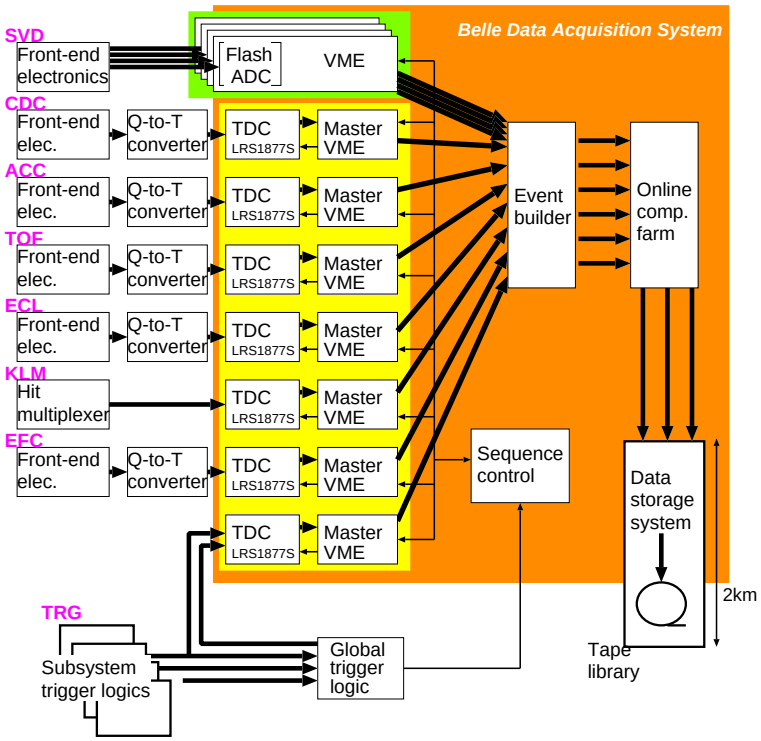

Figure 2.27: Belle DAQ system overview.

begins and ends run processing and other utility functions such as initialization, termination, and histogram definitions. Modules written in Fortran and C can also be linked using wrapper functions.

The data transfer between modules is managed by PANTHER, and event and I/O management package developed by the Belle collaboration. PANTHER describes the logical structure and inter-relationships of the data using an entity relationship model. In order to store data (structure) in the event structure one writes a description file as an ASCII text file. A PANTHER utility converts the description file into C and C++ header files and source code. The user will include the header files in his/her code and the source code is compiled and linked into the user module to have access to the data structure in the module.

The standard reconstruction module for subdetectors and global reconstruction of four momenta, production vertices, and likelihoods for being specific species such as electrons, muons, pions, kaons, protons, and gammas of charged and neutral particles are prepared and used to produce physics results as well as detector performance results described in this thesis.

2.5 DST Production and Skimming

The data obtained by sub-detectors are in the form of direct logs (Raw Data). They are converted into physics objects, for example, 4-vectors of x_μ and p_μ or timing information.

The most downstream of the reconstruction flow is the event classification and skimming. Here, all events are examined in such a way that certain selection criteria are applied to select events of our interest. Once events are satisfied with our selection, they are recorded into not only DST (Data Summary Tape) but also specific data files on the disk as skimmed data. Based on those data, detector calibrations are carried out in detail and the offline luminosity is computed.

In physics analyses, one does not need complete information available in DST. Instead, easy access to experimental data is highly demanded because we must process a large amount of data. For this purpose, minimal sets of DST (MDST), which is compact but sufficient to study physics events, are created for all runs.

2.5.1 Hadronic event selection

To suppress uninteresting events such as μ pair production, τ pair production, QED processes referring to Bhabha and radiative Bhabha processes and two photon processes, and select hadronic events we applied following cuts,

- The number of good charged track is required to be more than two. The good charged track defined to satisfy $|dr| < 2.0$ cm, $|dz| < 4.0$ cm and $P_t > 0.1$ GeV/c where dr, dz, and P_t represents the impact paramter to the nominal interaction point in the x, y plane along the z-axis and the transverse momentum respectively. This requirement suppress QED process and μ pair production effectively.

- At least one good ECL cluster should be within the fiducial volume of $-0.7 < \cos\theta < 0.9$. The good ECL cluster is defined as the cluster having the energy more than 100MeV.

- The total visible energy $E_{\rm vis}$ calculated from the good tracks assuming the pion mass and good photons in an event has to satisfy,
  $E_{\rm vis} \geq 0.2\sqrt{s}$,
  where $\sqrt{s}$ represents the cms energy. The good photon is defined as the good ECL cluster within the CDC acceptance($17^0 < \theta < 180^0$) with no associated tracks from the CDC.

- The energy sum of the good ECL clusters within the CDC acceptance, $E_{\rm sum}$ is required to satisfy

$0.1 < E_{\rm sum}/\sqrt{s} < 0.8$
This requirement reduces the QED process. To suppress the QED events which falls in the gap of the calorimeter, we apply an additional cut to the above,
$E'_{\rm sum}/(\#$ good ECL cluster$) < 1.0$GeV,
where $E'_{\rm sum}$ is the energy sum of all good ECL clusters including the ones outside the CDC acceptance.

- The momenta sum of the good tracks and good photons is required to be balanced in the z direction to eliminate the beam background,
$|P_z| < 0.5\sqrt{s}$

- We require a cut on the position of the primary vertex, that is formed by all good tracks, is required to satisfy
$|r_{\rm vertex}| < 1.5$ cm and $|z_{\rm vertex}| < 3.5$ cm,
where $r_{\rm vertex}$ and $z_{\rm vertex}$ represent the positions of the primary vertex in the $r-\phi$ plane and in the z-axis respectively.

- The event is split into two hemispheres by a plane perpendicular to the event thrust axis. The invariant mass of tracks in each hemisphere is calculated assuming a pion mass. This invariant mass is basically equivalent to the invariant mass of τ in τ pair production processes. In the event, we regard the larger invariant mass as heavy jet mass, $M_{\rm jet}$. The events are required to satisfy
$M_{\rm jet} > 1.8{\rm GeV}/c^2$ *or* $\left\{ \begin{array}{c} E'_{\rm sum}/\sqrt{s} > 0.18 \\ M_{\rm jet}/E_{\rm vis} > 0.25. \end{array} \right\}$

  The efficiency of the hadronic event selection is estimated using Monte Carlo simulation. The selection retains 99.1% of $B\bar{B}$ events and 79.5% of the continuum processes while reducing the contamination of the non-hadronic components to be less than 5%.

2.5.2 Crab crossing

The e^+ and e^- beams have finite crossing angle of $\pm 11m$rad at KEKB. This non-zero crossing angle is a unique feature of KEKB, that provides effective beam separation at the collision point, without high level of background. The achieved luminosity in this design can be further increased by tilting the electron and positron beam bunches to allow head-on collisions, without altering the crossing angle. This requirement can be accomplished by the implementation of superconducting radio-frequency cavities called "crab cavities".

The concept of crab cavities was first suggested by R. Palmer almost 30 years ago for linear electron-positron colliders. It was used in storage rings in 1989 by K. Oide and K. Yokoya. In 1992, prototype models of crab-cavities were done by K. Akai as part of a collaboration between KEK and Cornell laboratories. At KEKB, detailed engineering and prototyping were done by K.Hosoyama's team. In January 2007, first full-size cavities were built and installed at KEK accelerator center. Commissioning at KEKB started in February 2007 and continued until the end of June. Crab cavities were operated successfully for the first time at KEKB.

The parameter that defines the performance of crab cavities is called "tune shift". This quantity is proportional to the luminosity divided by the product of beam currents. At low beam currents, the crab cavities achieved a tune-shift comparable to the world record. Recently, at high beam currents (1300 mA in e^+ beam and 700 mA in e^- beam, KEKB accelerator team was able to operate at a luminosity above $10^{34}/cm^2/sec$. These were the results of first round of commissioning and will improve further. According to simulations, the crab-cavities may eventually enhance the luminosity by a factor of two.

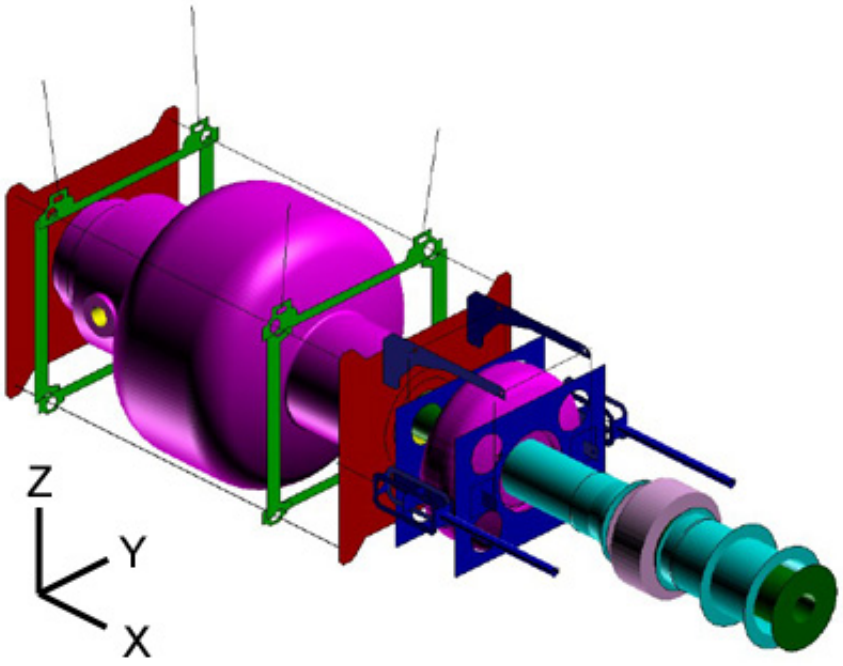

Figure 2.28: A CAD drawing of a crab cavity

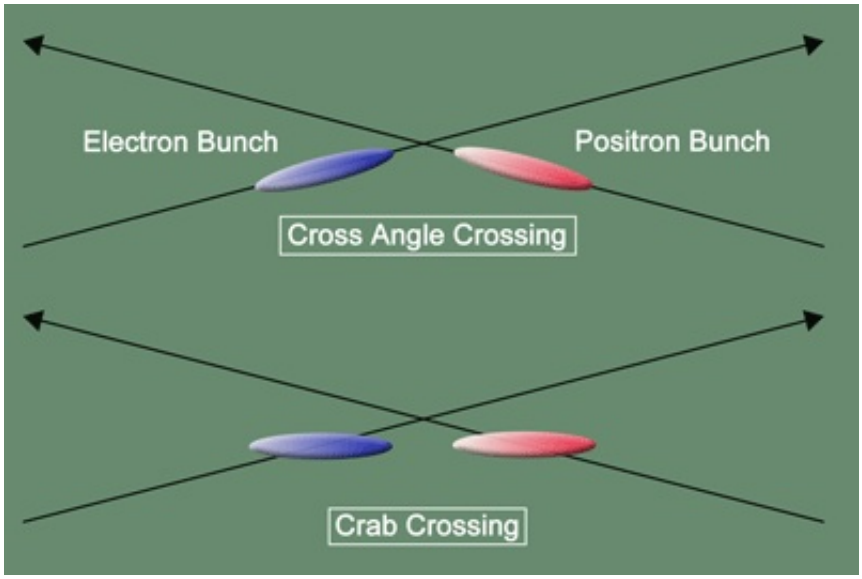

Figure 2.29: Crab cavity enables the tilted collisions of electron and positron beam bunches

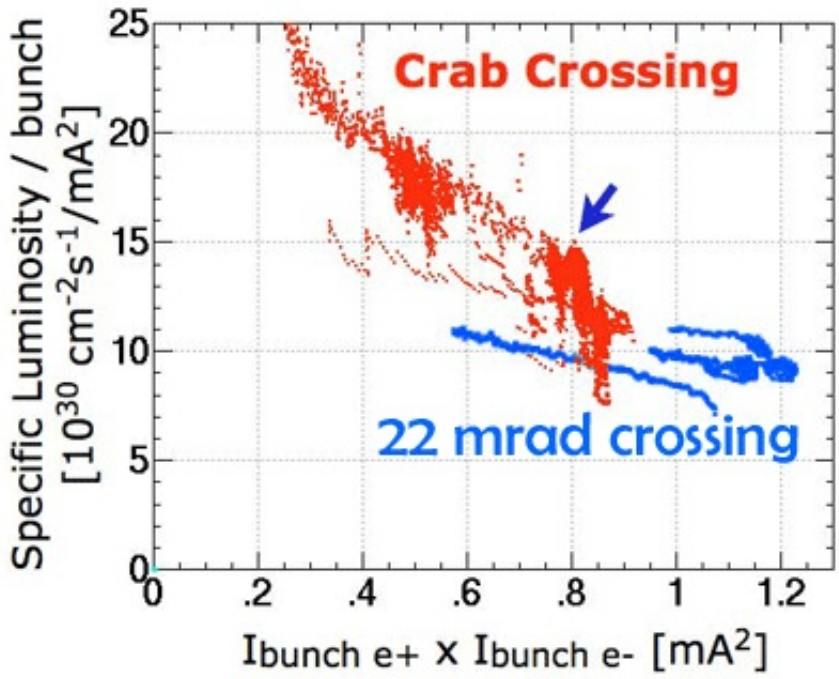

Figure 2.30: This figure shows the luminosity per bunch divided by the product of bunch currents. The red points show the results with crab cavities while the turquoise points show collisions without the crab cavities. A clear improvement is visible, especially at low bunch currents. The beam-beam tune shift reached a record value of 0.088 near the location of the arrow.

Chapter 3

Partial reconstruction tags for $B \to D^*\pi$ decays

We reconstruct $B \to D^*\pi$ decays using a technique called partial reconstruction. This technique along with its advantages and prior usage is described in this chapter. The B-candidate thus obtained is called 'CP-side' B. B mesons are produced in pairs from the decay of the $\Upsilon(4S)$ resonance. We determine the flavor of the other B, also called the tag-side B using the charge of the lepton or kaon tags and obtain $D^*\pi$ signal yields with these tags separately. The flavor tagging technique is described in Chapter 4. The partially reconstructed $D^*\pi$ signal candidates with lepton tag are used to obtain time-dependent CP violation parameters, $S^{\pm}$ in Chapter 5.

3.1 Partial reconstruction technique in $B \to D^*\pi$ decays

The $\bar{B}^0 \to D^{*+}\pi^-$ decay can be studied by both full and partial reconstruction methods. In the full reconstruction method, B is reconstructed from the decay products from the subsequent D decays. However, in partial reconstruction method, the D is not reconstructed from its decay products. Only the momentum of the hard pion from initial B decay and soft pion momentum from the subsequent D^* decay, $D^* \to D^0\pi^+$, are used. Since the D is not reconstructed from its decay products, we have an improvement in efficiency in the partial reconstruction, compared to the full reconstruction method. Considering only the CP-side efficiency, the typical gain is ≈ 12.5 (Appendix 1). We do not use the flavour tagging information and the signal to noise ratio for full and partial reconstruction to estimate the typical gain.

3.2 History of CP asymmetry measurements in $B \to D^*\pi$ decays

This decay has been studied by both Belle and BaBar using full and partial reconstruction techniques. The summary of the results for parameters, a and c from the previous Belle and BaBar are shown in Fig. 3.1. The most recent Belle and BaBar results are based on studies made using 386 and 232 million $B\bar{B}$ pairs respectively. Table 3.1 summarizes the different updates of Belle and BaBar results for a and c using lepton tag. Table 3.2 illustrates the different updates of BaBar results for a and c using kaon tag.

The statistical error on a with partial reconstruction from BaBar is lower than that of Belle. The BaBar result includes both lepton and kaon tags, whereas Belle uses lepton tag only. Furthermore, the lower bound on the lepton momentum used by BaBar is lower than that used by Belle. We will reduce the statistical error in the present analysis since we use about twice the data sample used by the previous Belle analysis. The statistical error will be further reduced by adding the kaon-tagged sample to the data-sample. We will also try to improve the tagging efficiency and the fitting procedure used to determine the CP violation parameters.

The systematic errors on the parameters a and c from BaBar are also smaller than Belle. The errors on a measured by BaBar with kaon tag dominates the world average. We would like to improve the systematic error estimation and thus, reduce the systematic uncertainty.

Expt.	$B\bar{B}$ pairs ($\times 10^6$)	a	c	Ref.
BaBar	178	-0.048±0.022±0.010	-0.015±0.036±0.019	[21]
BaBar	232	-0.042±0.014±0.010	-0.019±0.022±0.013	[19]
Belle	152	-0.030±0.028±0.018	-0.005±0.028±0.018	[22]
Belle	386	-0.041±0.019±0.017	-0.007±0.019±0.017	[23]

Table 3.1: Summary of the different updates of the BaBar and Belle results for the lepton tag.

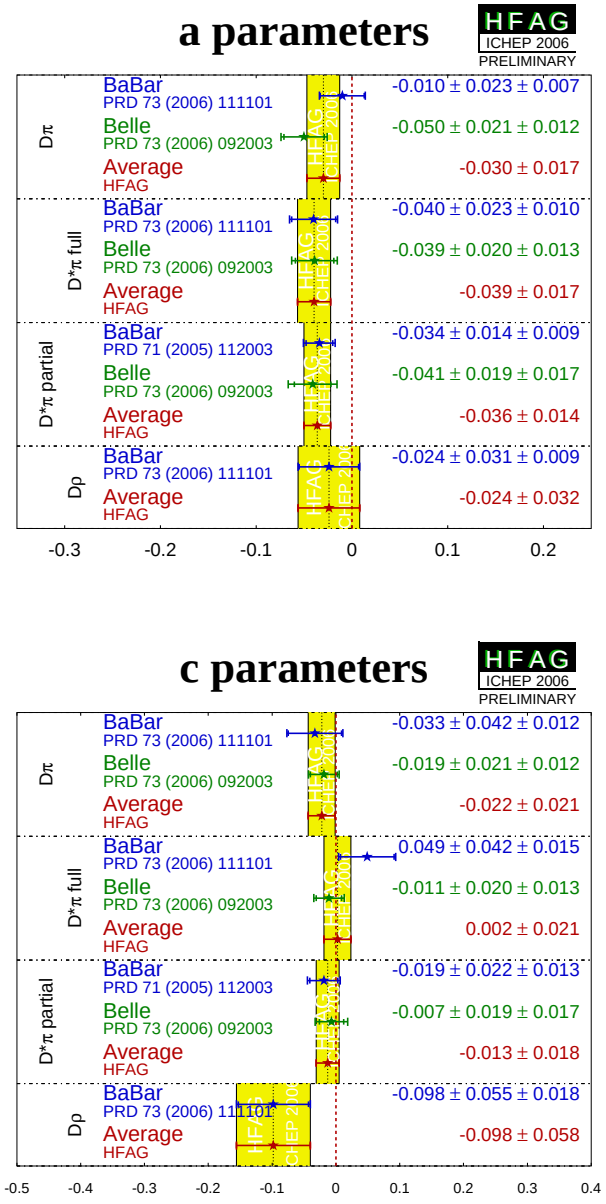

Figure 3.1: HFAG plots for a and c in $D\pi$, $D^*\pi$ and $D\rho$ decays

$B\bar{B}$ pairs ($\times 10^6$)	a	b	c	Ref.
82	-0.054±0.032±0.019	-0.009±0.019±0.011	+0.005±0.031±0.020	[20]
178	-0.033±0.023±0.015	-0.004±0.012±0.011	+0.019±0.023±0.016	[21]
232	-0.025±0.020±0.013	-0.004±0.010±0.010	-0.003±0.020±0.015	[19]

Table 3.2: Summary of the previous BaBar results for kaon tag.

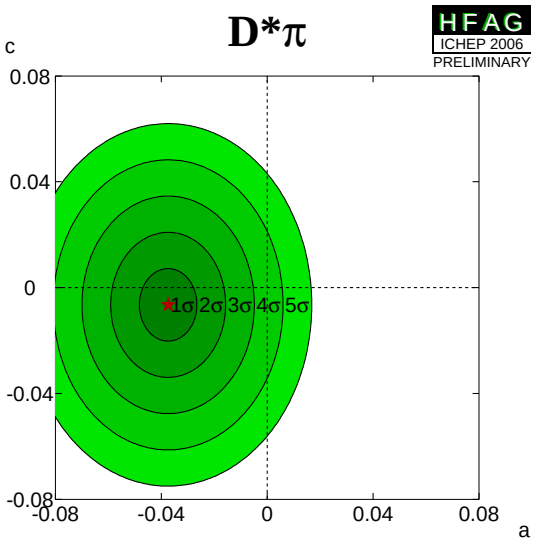

Figure 3.2: HFAG plot showing the current values of a and c in $B \to D^*\pi$ decays

Fig. 3.2 shows the latest HFAG [1] plot for the amount of CP violation in $B \to D^*\pi$ decay, combining the results from both partial and full reconstruction. The value of CP violation deviates from zero by ≈ 3.5 standard deviations. We would like to improve the precision on a and c in $D^*\pi$ system, using higher statistics and both lepton and kaon tag. We expect to observe CP violation in this mode using a huge data-set of $B\bar{B}$ pairs.

3.3 Data set

The time-dependent CP violation study is done using 387 million $B\bar{B}$ pairs, out of the available data-set of 687 million $B\bar{B}$ pairs collected with the Belle detector at the KEKB asymmetric-energy e^+e^- (3.5 GeV on 8 GeV) collider, operating at the

$\Upsilon(4S)$ resonance ($\sqrt{s} = 10.58$ GeV). These events are tagged using leptons only for the "tag-side " B. We also have the sample using kaons for tagging the "tag-side" B. The data-sets using lepton and kaon tags are different data-sets. Table 3.3 shows the number of $B\bar{B}$ pairs collected in each experiment collected with the Belle detector. Monte-Carlo simulation using proper detector conditions is done to simulate at least thrice the size of the collected data sample for each experiment. We use a Monte-Carlo set corresponding to 3$\times$ 577 million $B\bar{B}$ pairs in this analysis.

Experiment number	Number of $B\bar{B}$ pairs (in 10^6)
7	$6.4587 + 0.1615 - 0.0976$
9	$4.7597 + 0.0286 - 0.0473$
11	$8.8509 + 0.0517 - 0.0518$
13	$11.6998 + 0.2393 - 0.2392$
15	$13.5679 + 0.0963 - 0.1055$
17	$12.4588 + 0.3301 - 0.3301$
19	$27.1705 + 0.1676 - 0.1676$
21	$4.3371 + 0.0540 - 0.0676$
23	$6.4755 + 0.0675 - 0.0989$
25	$28.0008 + 0.3329 - 0.1605$
27	$28.1814 + 0.2110 - 0.1516$
31	$19.6587 + 0.3045 - 0.3031$
33	$19.3022 + 0.3000 - 0.2987$
35	$18.5262 + 0.2861 - 0.2855$
37	$67.1819 + 1.0326 - 1.0319$
39	$47.0818 + 0.7265 - 0.7246$
41	$64.0134 + 0.9863 - 0.9857$
43	$61.5614 + 0.9493 - 0.9474$
45	$14.3538 + 0.2218 - 0.2215$
47	$41.2186 + 0.6406 - 0.6393$
49	$29.7271 + 0.4648 - 0.4634$
51	$41.8919 + 0.6605 - 0.6590$
55	$80.2472 + 1.2462 - 1.2439$
$7 - 55$	656.725 ± 8.940
$7 - 51$	576.478 ± 7.699

Table 3.3: Number of $B\bar{B}$ pairs available in each experiment

3.4 Analysis technique

In the reconstruction of the CP-side tags, we study: $\bar{B}^0 \to D^{*+}\pi^-$; $D^* \to D^0\pi^+$. We use the π from initial B decay and π coming from the subsequent D^* decay , without reconstructing the D candidates at all. The momentum of the pion from the B-decay is ≈ 2 GeV/c in the B rest frame, hence called 'hard pion' (π_h). In the $\Upsilon(4S)$ rest frame, it is smeared due to the B motion. There is a small energy release (~ 0.146 GeV) in the D^{*+} decay compared to D^*, D masses, hence the charged pion from D^{*+} will maintain the direction of the D^{*+} approximately. This pion carries 0.039 GeV/c momentum in the D^* frame and less than 0.25 GeV/c in $\Upsilon(4S)$ rest frame and is hence called the 'soft pion' (π_s). In the $\Upsilon(4S)$ rest frame, the boost of the D^* is large enough to ensure the soft pion to be almost along the direction of its parent particle D^*. The D^{*+} travels in a path nearly opposite to π_h, since B moves slowly in the $\Upsilon(4S)$ rest frame, with $\beta = 0.06$. Thus, π_h and π_s are almost back-to-back in $\Upsilon(4S)$ rest frame.

We construct a partially reconstructed D^* frame using energy-momentum conservation:

$$\begin{aligned} E_{D^*} &= E_{\bar{B}^0} - E_h, \\ \boldsymbol{p}_h + \boldsymbol{p}_{D^*} &= \boldsymbol{p}_B. \end{aligned} \tag{3.1}$$

Using E_{D^*}, the momentum of D^{*+} can be obtained in $\Upsilon(4S)$ rest frame as: $p^*_D = \sqrt{E^2_{D^*} - m^2_{D^*}}$. We construct a partially reconstructed D^{*+} frame (Fig. 3.3), using p_{D^*} and E_{D^*} and points opposite to p_h with magnitude p^*_D.

We define a variable, p_δ, which is calculated from the hard pion momentum, p_h. p_δ is defined as: $||p_h| - |p_{D^*}||$ and from Eqn. 3.1, it follows:
$|p_\delta| \leq |\boldsymbol{p}_B|$ (≈ 0.3 GeV/c).

The magnitude of p^*_D is known based on Eqn. 3.1 but the azimuthal angle of this vector about the π_h direction can not be determined as shown in Fig. 3.3. The actual D^{*+} frame lies on a circle in three-momentum space. We boost the charged soft pions into the partially reconstructed D^* frame. In a true D^* frame, the soft pion is mono-energetic. However, in the partially reconstructed D^{*+} frame, the soft pion momentum will have a limited spread. We study the parallel and the transverse components of the momentum of the soft pion, π_s along the opposite direction to h, which are denoted as $p_\parallel$ and $p_\perp$ respectively. The parallel component will have a smaller spread than the transverse one, as the D^* momentum has very little uncertainty in the longitudinal direction.

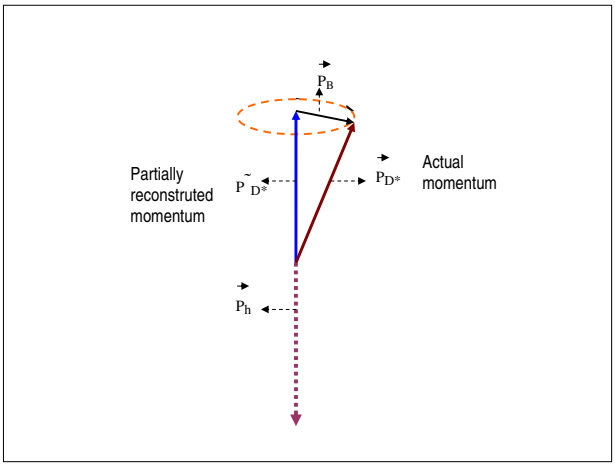

Figure 3.3: Schematic diagram showing relation between partially reconstructed and actual D^* momentum

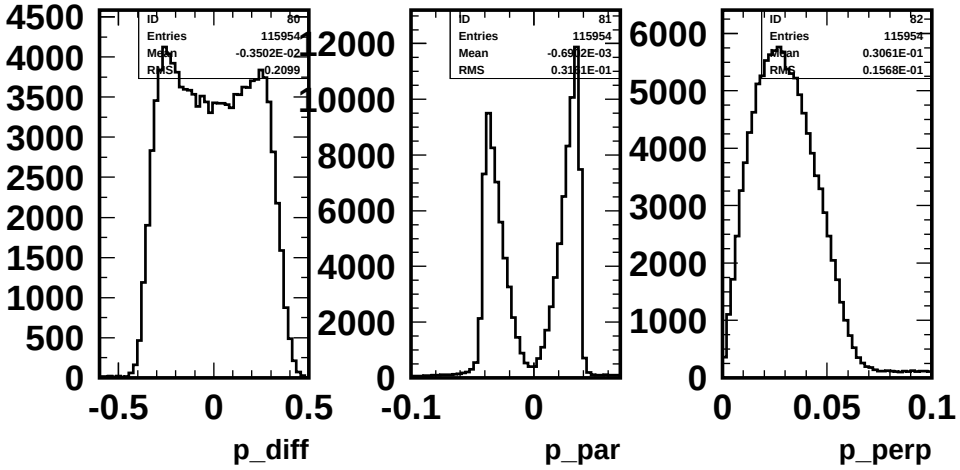

Figure 3.4: Distributions of p_δ, $p_\parallel$ and $p_\perp$ using 0.2 million signal Monte Carlo events.

The three kinematic variables, p_δ, $p_\parallel$ and $p_\perp$ (Fig. 3.4) can be used for signal to background discrimination. Table 3.4 shows the entire fitting region and the signal region in these three variables.

Quantity	Entire region	Signal region
$p_\parallel$	$-0.1 < p_\parallel/\mathrm{GeV}/c < 0.07$	$-0.05 < p_\parallel/\mathrm{GeV}/c < -0.01$
		$0.01 < p_\parallel/\mathrm{GeV}/c < 0.04$
p_δ	$-0.6 < p_\delta/\mathrm{GeV}/c < 0.5$	$-0.4 < p_\delta/\mathrm{GeV}/c < 0.4$
$p_\perp$	$p_\perp/\mathrm{GeV}/c < 0.1$	$p_\perp/\mathrm{GeV}/c < 0.05$

Table 3.4: Signal region in the kinematic variables, p_δ, $p_\parallel$ and $p_\perp$

3.5 Skimming selection

We skim the on-resonance, generic Monte Carlo and off-resonance data, using the cuts listed in Table 3.5. We apply a loose selection cut on $p_\parallel$ and $p_\perp$ variables, as these do not affect our signal region (Table 3.4). The skimming selection selects 1.6% of Hadron B events.

Quantity	Requirement
Fast pion momentum	$1.93 < p_h/\mathrm{GeV}/c < 2.5$
Closest approach to IP (r) for fast pion (dr_h)	< 0.1 cm
Closest approach to IP (z) for fast pion (dz_h)	< 2.0 cm
Slow pion momentum	$0.0 < p_s/\mathrm{GeV}/c < 0.5$
Charge of hard and soft pion	opposite
$\lvert p_\parallel \rvert$	$< 0.2/\mathrm{GeV}/c$
$p_\perp$	$< 0.1/\mathrm{GeV}/c$

Table 3.5: Skimming selection criteria

3.6 Hard pion selection

Table 3.6 shows a list of the hard pion selection cuts and the number of hard pions selected from a real $D^*\pi$ (true hard pions) and selection efficiency due to each of them in a sample Monte-Carlo simulated events containing $\bar{B}^0 \to D^{*+}\pi^-$; $D^* \to D^0\pi^+$. We select tracks within the allowed momentum range for the hard pions. The hard pion tracks must be consistent with having originated from the interaction profile (IP).

Event selection	Requirement	Number	Efficiency (in %)
At least 1 hard pion (no cut)		177111	100.0
Momentum	$1.93 < p_h/\mathrm{GeV}/c < 2.5$	170643	96.4
Muon probability	< 0.80	167991	94.9
Electron probability	< 0.80	167654	94.7
Pion probability	> 0.30	162609	91.8
Closest approach to IP (r) (dr_h)	< 0.1 cm		
Closest approach to IP (z) (dz_h)	< 2.0 cm	150609	90.3
SVD hits in layers 2 to 4 (SVD2 data)	≥ 2		
SVD hits (r - ϕ plane)	≥ 2		
SVD hits (z plane)	≥ 2	150609	85.0
Lab polar angle (θ_{lab})	$23^\circ < \theta_{lab} < 139^\circ$ (SVD1)		
	$17^\circ < \theta_{lab} < 150^\circ$ (SVD2)	149742	84.6

Table 3.6: Summary of hard pion cuts along with the number of hard pion candidates left and reduction in hard pion selection efficiency after each cut done using 0.2 million simulated signal events containing $\bar{B}^0 \to D^{*+}\pi^-$; $D^* \to D^0\pi^+$

Fig. 3.5 shows the momentum distribution in $\Upsilon(4S)$ rest frame and the impact parameters, dr and dz for the hard pions. We apply lepton veto cuts to reduce contamination from the lepton tracks. We also apply pion probability cut to remove kaons from the hard pion tracks. We use the range of the polar angle (θ_{lab}) cut, according to each version of SVD [32]. Efficiency of a cut is the ratio of number of candidates remaining after the cut to the number without any cut. The hard pion selection efficiency is 85% after all the cuts are applied.

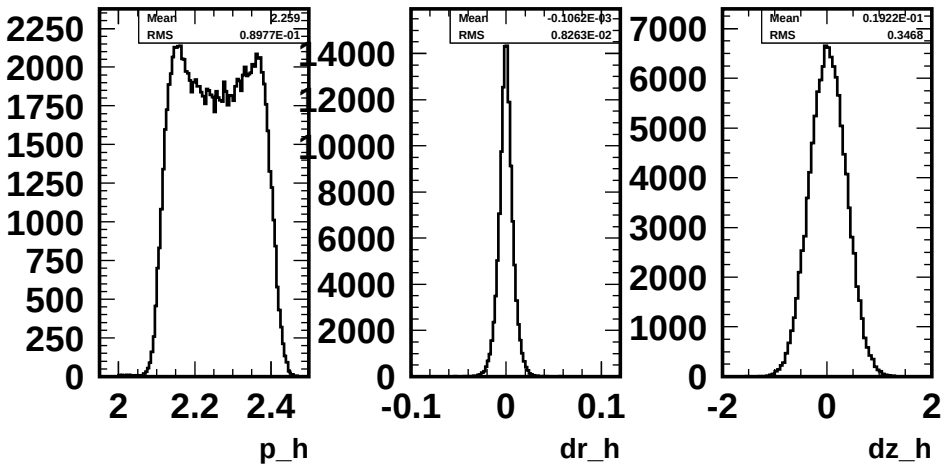

Figure 3.5: Momentum and impact parameters dr, dz of hard pion in $\Upsilon(4S)$ rest frame, using 0.2 million signal Monte Carlo events with cuts: $1.93 < p_h/\mathrm{GeV}/c < 2.5$, $muid_h < 0.80$, $eid_h < 0.80$, $pid_h > 0.30$, $dr_h < 0.1$ cm, $dz_h < 2.0$ cm, SVD hits in layers 2 to 4 (SVD2 data) ≥ 2, $23^\circ < \theta_{lab} < 139^\circ$ (SVD1), $17^\circ < \theta_{lab} < 150^\circ$ (SVD2)

3.7 Soft pion selection

Table 3.7 shows the the list of soft pion selection cuts and the number of soft pions selected from a real $D^*\pi$ (true soft pions) and soft pion selection efficiency due to each cut. For soft pions, we apply a momentum cut, allowed by the decay kinematics. The track must be consistent with having originated from the interaction point (IP). We apply loose impact parameter cuts on the soft pion tracks. Since these tracks do not always reach the particle identification (PID) system, no PID requirements are made. Fig. 3.6 shows the momentum distribution in the $\Upsilon(4S)$ rest frame and the impact parameters, dr and dz for the soft pions. The soft pion selection efficiency is 63% after all the soft pion selection cuts are applied.

Event selection	Requirement	Number	Efficiency (in %)
No cut		218869	100.0
Momentum	$0.05 < p_s/\mathrm{GeV}/c < 0.30$	2046431	93.5
Closest approach to IP (r) (dr_s)	< 1.0 cm	167294	76.4
Closest approach to IP (z) (dr_z)	< 4.0 cm	137962	63.0

Table 3.7: Summary of soft pion cuts along with the number of soft pion candidates left and reduction in soft pion selection efficiency after each cut done using 0.2 million signal events

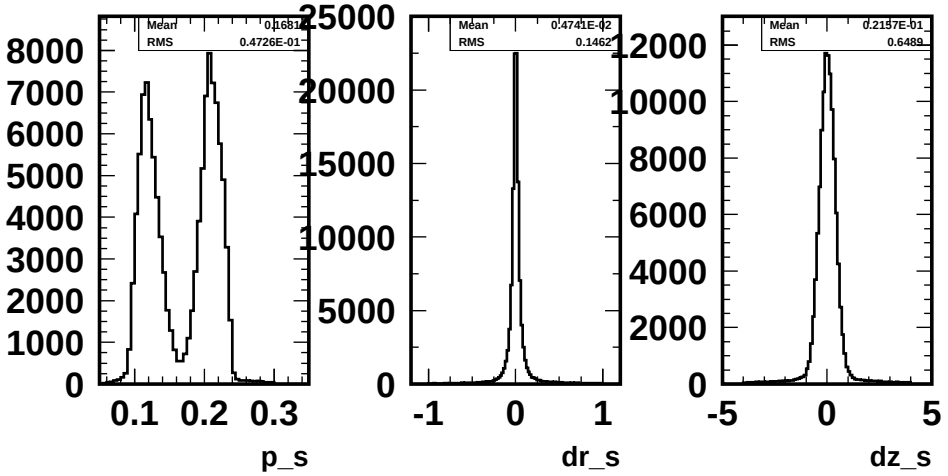

Figure 3.6: Momentum and impact parameters dr, dz of soft pion in $\Upsilon(4S)$ rest frame, using 0.2 million signal Monte Carlo events, with cuts: $0.05 < p_s/\mathrm{GeV}/c < 0.30$, $dr_s < 1.0$, $dr_z < 4.0$

3.8 B candidate selection

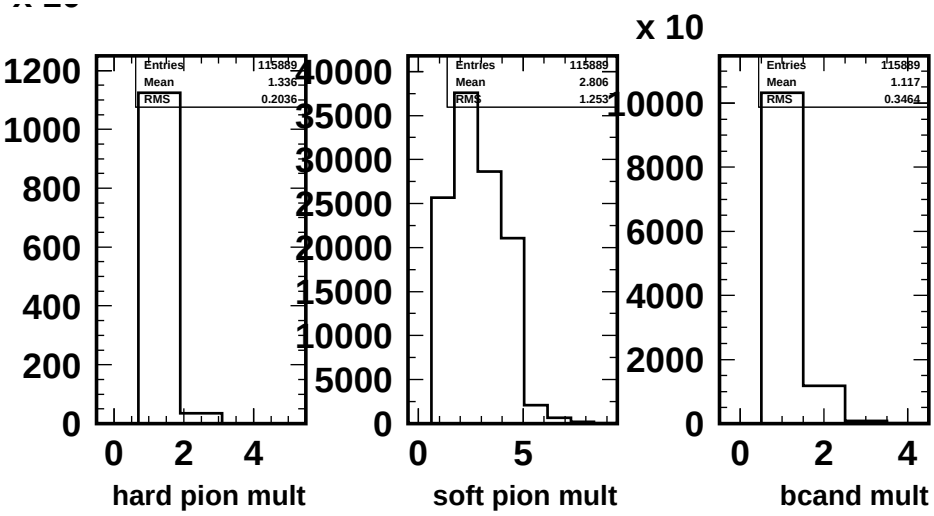

Figure 3.7: Multiplicities of hard pion, soft pion and B candidate, using 0.2 million signal Monte Carlo events.

The average multiplicity of hard and soft pion lists after the selection cuts are applied are 1.3 and 2.8 respectively (shown in Fig. 3.7). We construct B candidates using the hard and soft pion candidates. For the signal case, the hard pion and soft pions must have opposite charge. A loose requirement on R_2, the normalized second Fox-Wolfram moment ($R_2 < 0.6$, rejecting $\approx 0.9\%$ signal events) is made to reduce continuum background events.

Quantity	Requirement
Charge of hard and soft pion	opposite
R_2	< 0.6
$p_\parallel$	$-0.1 < p_\parallel/\mathrm{GeV}/c < 0.07$
$p_\perp$	$0.0 < p_\perp/\mathrm{GeV}/c < 0.1$
p_δ	$-0.6 < p_\delta/\mathrm{GeV}/c < 0.5$
Multiple $D^*\pi$	Largest δ_{fs}

Table 3.8: B candidate selection criteria

The B candidate selection requirement is listed in Table 3.8. An efficiency of

55% for B candidate reconstruction is obtained. The multiplicity of B candidate is 1.1 (Fig. 3.7). If there are multiple $D^*\pi$ candidates, the one with the largest value of δ_{fs}, the angle between hard and soft pion direction in the $\Upsilon(4S)$ rest frame, is selected. This is based on the fact that for the signal candidate, the hard and soft pions must be almost back-to-back in the $\Upsilon(4S)$ rest frame.

3.9 Discriminating variables

One of the major aims of our analysis is to develop variables to efficiently discriminate signal from background. $D^{*+}\rho^-$ is a major background mode for our decay mode. Events of the type $e^+e^- \rightarrow q\bar{q}(q = u, d, s, c)$, also referred as continuum events, are another major background for our signal. Other backgrounds include generic B decay modes, other than $D^{*+}\rho^-$. We developed variables to improve signal to background ratio and obtain cleaner partially reconstructed tags for $B \rightarrow D^*\pi$ decays.

3.9.1 Likelihood ratio using variables obtained using particles coming from D^0

Our signal decay mode is $\bar{B}^0 \rightarrow D^{*+}h^-(h = \pi^-)$; $(D^{*+} \rightarrow D^0\pi_s^+)$. We look for evidence of D^0 opposite to π_h. Hence, we look for particles coming from D^0, such as kaons, leptons in partially reconstructed (PR) D^{*+} frame ($\sim D^0$ frame). The kaons and leptons come from $b \rightarrow c \rightarrow s$ decay ($D^0 \rightarrow K^-X$) and $D^0 \rightarrow l^+X$ decays respectively. We study the momentum (p) and helicity ($cos\theta_H$) distributions of these particles for two cases, namely "same sign" (π_h and K or l are of same sign) and "opposite sign" (π_h and K or l are of opposite sign). The "same sign" events are called "same B" and the "opposite sign" events are called "opposite B". We use $\sim$ 5 million generic neutral B events,(with $\bar{B}^0 \rightarrow D^{*+}\pi^-$ and $\bar{B}^0 \rightarrow D^{*+}\rho^-$ removed), $\sim$ 5 million events generic charged B events, $\sim$ 9 million continuum events background events for this study. We do not remove $B^\pm \rightarrow D^{*\pm}h^0$ from generic charged B background. Fig. 3.8, Fig. 3.9 and Fig. 3.10 show the momentum (p) and helicity ($cos\theta_H$) distributions for the cases where we use kaons, electrons and muons from D^0 respectively.

In case of both electrons and muons from D^0, p <1.4 GeV in $\Upsilon(4S)$ centre-of-mass frame is applied to exclude leptons coming from semi-leptonic B-decays of the other B. An additional cut of $p_e > 0.5$ GeV in $\Upsilon(4S)$ centre-of-mass frame is applied.

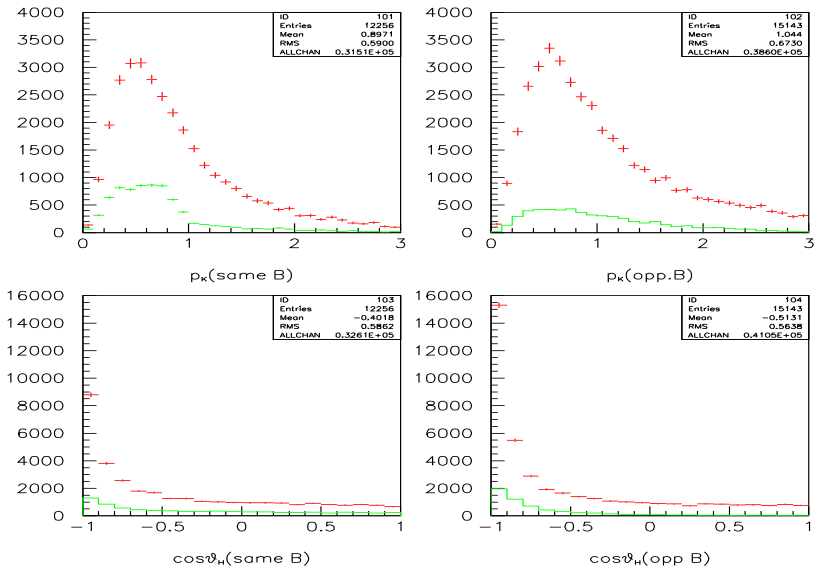

Figure 3.8: p_K, $cos\theta_H$ distributions in PR D^* frame; Points with error bars: Combined bkg., scaled to 8.2 fb^{-1}; Solid: Signal MC, scaled to 8.2 fb^{-1}; Cuts: $p_K < 0.8$ GeV, $cos\theta_H >$ -0.5 : "K flag"

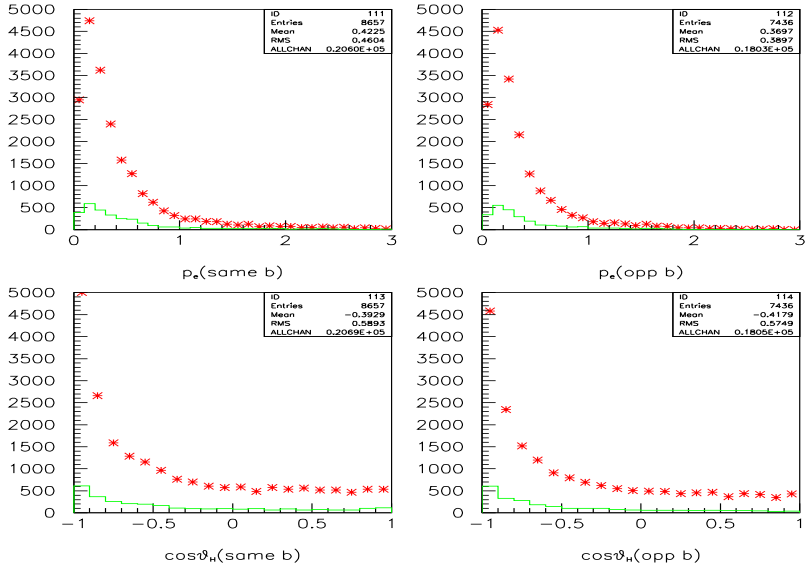

Figure 3.9: p_e, $cos\theta_H$ distributions in PR D^* frame; Points with error bars: Combined bkg., scaled to 8.2 fb^{-1}; Solid: Signal MC, scaled to 8.2 fb^{-1}; Cuts: $p_e < 0.8$ GeV, $cos\theta_H >$ -0.5 : "e flag"

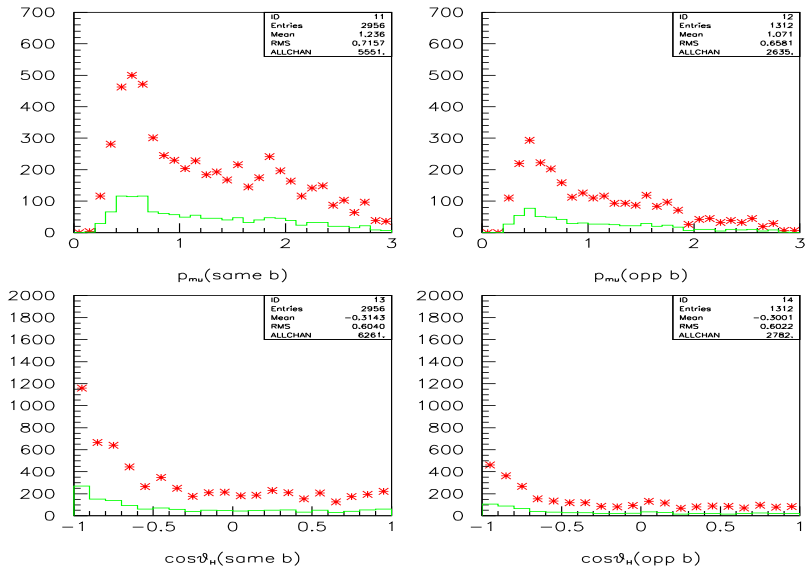

Figure 3.10: $p_{/mu}$, $cos\theta_H$ distributions in PR D^* frame; Points with error bars: Combined bkg., scaled to 8.2 fb^{-1}; Solid: Signal MC, scaled to 8.2 fb^{-1}; Cuts: $p_{/mu} < 0.8$ GeV, $cos\theta_H >$ -0.5 : "$/mu$ flag"

Table 3.9 summarizes the efficiencies of the tagging kaon and lepton cases, with "same B" type events and cuts $p_{PR} < 0.8$ GeV, $cos\theta_H >$ - 0.5. We define a quantity called "rejection ratio" as the ratio of the efficiency for the signal to that of the background. Table 3.10 shows the rejection ratio for the lepton and kaon cases.

	Sig. MC	Gen. neu.	Gen. chg.	Cont.	tot. bkg.
eff. K same B	0.277	0.075	0.160	0.081	0.085
eff. e same B	0.0394	0.0344	0.02985	0.01203	0.0138
eff. μ same B	0.0356	0.0328	0.0265	0.0129	0.0153

Table 3.9: Efficiencies of the tagging kaon and lepton cases with "same B" type events and cuts $p_{PR} < 0.8$ GeV, $cos\theta_H >$ - 0.5

	Kaons	electrons	muons
Rejection ratio, same B	3.225	2.851	2.464

Table 3.10: Rejection ratio for the tagging kaon and lepton cases

We develop other variables to discriminate signal from continuum background events. In each event where we select a π_h candidate we look in the remainder of the events. We defined:
$R_{hl}= \Sigma P_l(cos\theta_i)|E_i|/\Sigma|E_i|$, where,
P_l is the lth order for Legendre polynomial (l = 2,3),
θ is the angle between h and ith particle the Υ(4S) centre-of-mass frame,
E_i is the energy of the ith particle in the Υ(4S) centre-of-mass frame
and i runs over all particles except h.

The following event selection criteria were used:
$p_{h_{cms}} > 2.0$ GeV
$p_{s_{cms}} < 0.25$ GeV
$R_2 < 0.4$.

We look at the distributions for R_{h2} and R_{h3} for the 3 sets in both signal and background, using three sets of particles, $\{i\}$
1) all particles, excluding h (R_{h2} and R_{h3})
2) charged only, excluding h (R_{h2c} and R_{h3c})
3) neutral only (R_{h2n} and R_{h3n}).

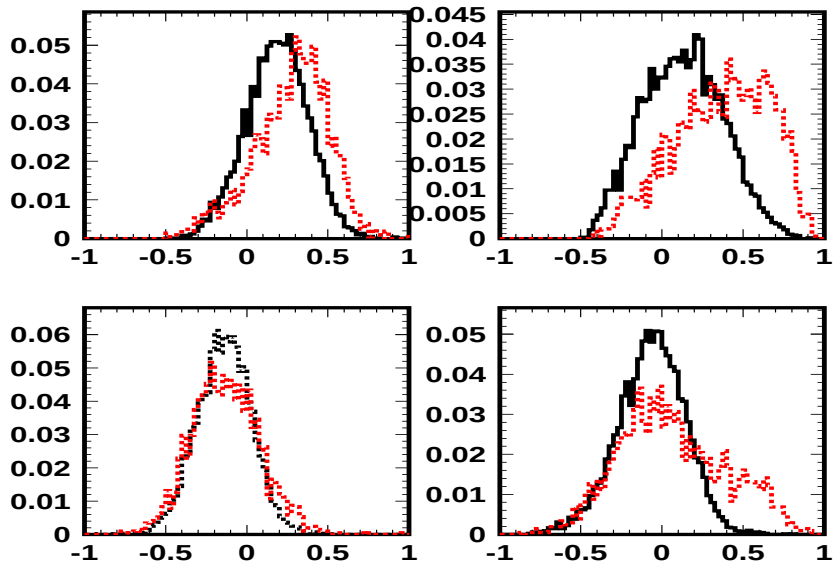

Figure 3.11: R_{h2c} and R_{h3c}; R_{h2n} and R_{h3n} distributions; signal Monte-Carlo (10000 events with $R_2 < 0.4$): black and continuum (50000 continuum events with $R_2 < 0.4$): red

We observe moderate signal to background separation for R_{h2c}, R_{h2n} and R_{h3n}. 2-d plots of various combinations are made. No correlations are observed. Hence, 3-d PDF can be obtained by multiplying the 1-d PDF's and thus, 3-d likelihood ratio can be made using these variables.

We calculate tagging probabilities of K or l by selecting events which have at least 1 K or l with the cuts kaon likelihood ratio > 0.7 and electron likelihood ratio > 0.6 , muon likelihood ratio > 0.9 for K or l respectively. Following additional cuts are also made for these events:
right sign (h and π_s opposite sign) with $p < 0.8$ GeV, $\cos\theta_H > -0.5$
where p is the momentum and θ_H is the helicity angle in partially reconstructed D^* frame. These tagging probabilities are summarized in Table 3.11.

Then, we make 4-D likelihood ratio using pdf's of R_{h2c}, R_{h2n} and R_{h3n} (fitted) and K/l Table 3.11. Figure-of-merit plots are made for this likelihood ratio. Figure-of-merit is defined as:
Figure-of-merit $= \epsilon_{sig}/\sqrt{\epsilon_{bkg}}$. Fig 3.12 shows the 4-D likelihood ratio distribution and the figure-of-merit distribution for the same. Fig 3.13 shows the signal efficiency (ϵ_{sig}) and the background efficiency (ϵ_{bkg}) used to obtain the figure-of-merit distri-

	K.and.not l	l.and.not K	K.and.l	not K.and.not l
signal	0.14689	0.09287	0.0178	0.7424
continuum	0.0438	0.0487	0.0053	0.902

Table 3.11: Tagging probabilities for various cases with tagging kaons and leptons

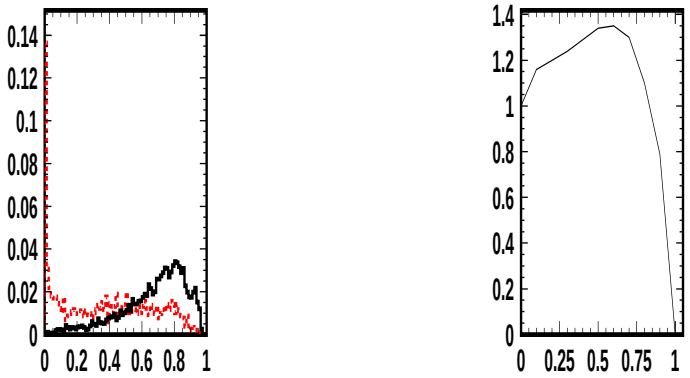

Figure 3.12: Left: 4-d L.R with signal Monte-Carlo (10000 events with $R_2 < 0.4$) in black and continuum (50000 continuum events with $R_2 < 0.4$)in red; right: Figure-of-merit ($\epsilon_{sig}/\sqrt{\epsilon_{bkg}}$) for 4-d L.R

bution for 4-D likelihood ratio. Slightly higher figure-of-merit is obtained for 4-d case than 3-d case. Hence, a cut of 4-d L.R > 0.4 is made. According to MC, $\epsilon_{sig} = 0.88$; $\epsilon_{bkg} = 0.45$.

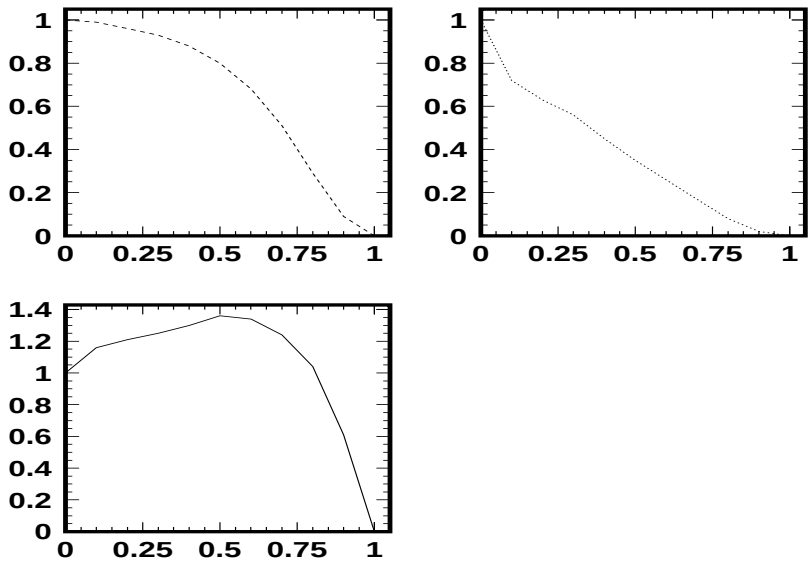

Figure 3.13: Top row: ϵ_{sig} (left), ϵ_{bkg} (right); bottom row: Figure-of-merit ($\epsilon_{sig}/\sqrt{\epsilon_{bkg}}$ for 4-d L.R

We fit to $p_{\|}$ with cuts: $|p_{\delta}| < 0.4GeV$, $R_2 < 0.4$ and $\tilde{p}_{\perp} < 0.05GeV$, 4-d LR$> 0.4$ using ≈ 2.727 fb^{-1} $\Upsilon(4S)$ data with 1.199 fb^{-1} continuum data, scaled to $\Upsilon(4S)$ data), 4.70 fb^{-1} generic charged Monte-Carlo (scaled to $\Upsilon(4S)$ data, $B \rightarrow D^{*+}h^0$ removed), 4.7308 fb^{-1} generic neutral Monte-Carlo (scaled to $\Upsilon(4S)$ data), $D^*\rho$ and signal Monte-Carlo. We observe that the signal to background discrimination is better with the 4-d LR cut.

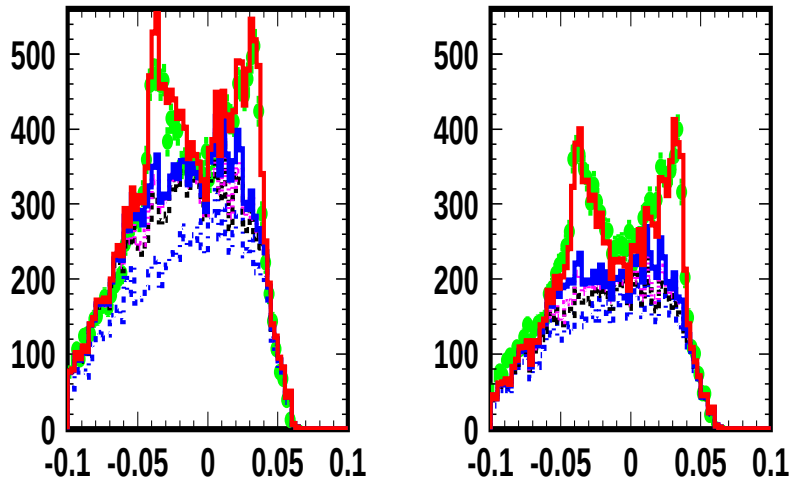

Figure 3.14: Fit to $p_{\|}$ without LR cut (left) and with LR cut (right) using ≈ 2.727 fb^{-1} data using continuum data(dotted line)(1.199 fb^{-1}, scaled to $\Upsilon(4S)$ data) (blue dotted), continuum data + generic charged Monte-Carlo(4.70 fb^{-1}, scaled to $\Upsilon(4S)$ data, $B \rightarrow D^{*+}h^0$ removed) (black), continuum data + generic charged + generic neutral Monte-Carlo (4.7308 fb^{-1}, scaled to $\Upsilon(4S)$ data) (magenta), continuum data + generic charged + generic neutral + $D^*\rho$ Monte-Carlo (blue solid), continuum data + generic charged + generic neutral + $D^*\rho$ + signal Monte-Carlo (red)

3.9.2 Invariant mass variable made using particles coming from D^0

We investigate invariant mass using the particles coming from D^0 in PR D^* frame as a possible way to improve our selection criteria.

We consider 3 sets of particles in "partially reconstructed"(PR) D* frame, with momentum p <0.9 GeV:
all particles, charged particles only and neutral particles only. In PR D* frame, plots for invariant mass (M_{inv}), total momentum (P_{tot}), total charge (Q_{tot}) and total number of particles making the invariant mass (N_{tot}) are made for these sets of particles. The particles are ordered in increasing order of momentum in PR D^* frame. We tag particles coming from D^0 and make the above-mentioned plots with and without the tag in signal MC. We observed the following:

- Mean number of particles making M_{inv} = 16.97
  Mean number of particles from D^0 making M_{inv} = 2.957
  Mean number of charged particles making M_{inv} = 7.616
  Mean number of charged particles from D^0 making M_{inv} = 1.710

- We observe a lot of neutral particles not from D^0 contributed to M_{inv}.

Then, we calculate likelihood ratio (LR) for charged and neutral particles separately, defining

LR_{chg} = likelihood of charged particle coming from D^0/(likelihood of charged particle coming from D^0 + likelihood of charged particle not coming from D^0)
and LR_{neu} = likelihood of neutral particle coming from D^0/(likelihood of neutral particle coming from D^0 + likelihood of neutral particle not coming from D^0) in signal MC.

However, the potential improvements to the signal to background discrimination are small.

3.9.3 Shape variables R_l obtained using particles in Υ(4S) frame

We look at the variable: $R_l = \Sigma P_l(cos\theta_i)|p_i||p_h|/\Sigma|p_i||p_h|$ where,
P_l stands for Legendre poynomials (l = 2,3)
θ is the angle between h and ith particle the Υ(4S) centre-of-mass frame,
p_h is the energy of the hard pion in the Υ(4S) centre-of-mass frame,
p_i is the energy of the ith particle in the Υ(4S) centre-of-mass frame
and i runs over all particles except h. We looked at three cases, namely:
R_l : all particle case;
R_{lc}: charged particles only;
R_{ln}: neutral particles only.

We make R_l variables, using charged particles only and neutral particles only, separately, like R_{hl} case. These distributions are shown in Fig 3.15. R_l and R_{lc} variables show better signal to background discrimination then R_{ln} variables. We checked correlation between the variables R_{2c}, R_{3c}; R_{2n}, R_{3n} and R_2, R_3 in case of signal (Fig 3.16) and continuum (Fig 3.17).

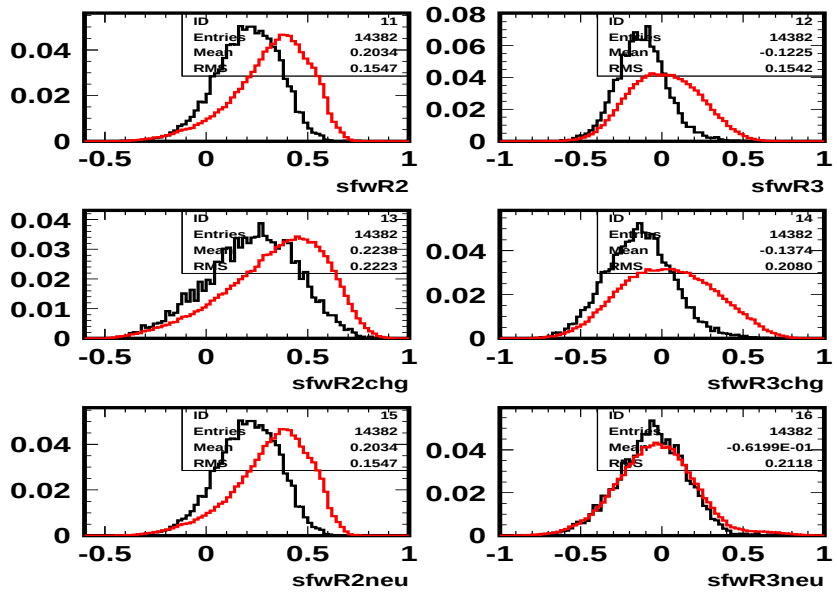

Figure 3.15: R_l, R_{lc} and R_{ln}, l =1,2 distributions; black: signal, red: continuum

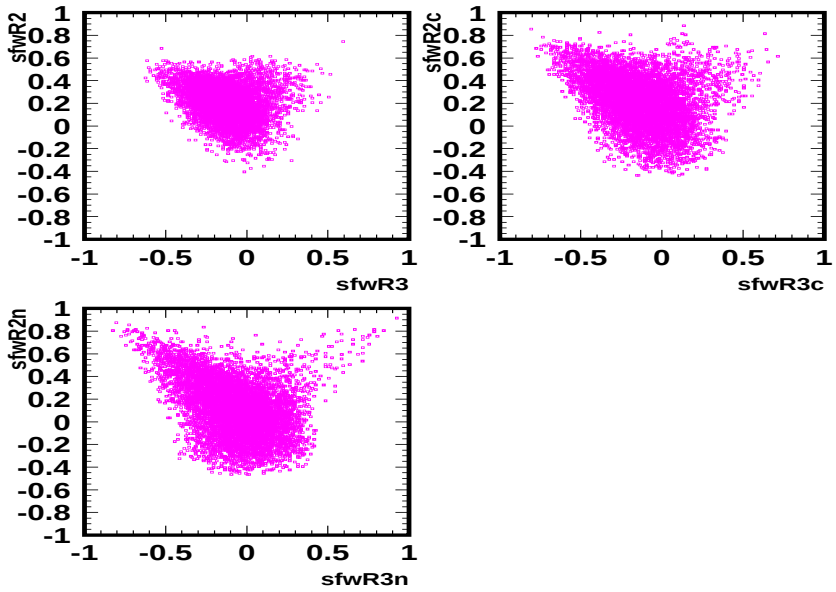

Figure 3.16: Correlation between the variables R_{2c}, R_{3c}; R_{2n}, R_{3n} and R_2, R_3 in case of signal

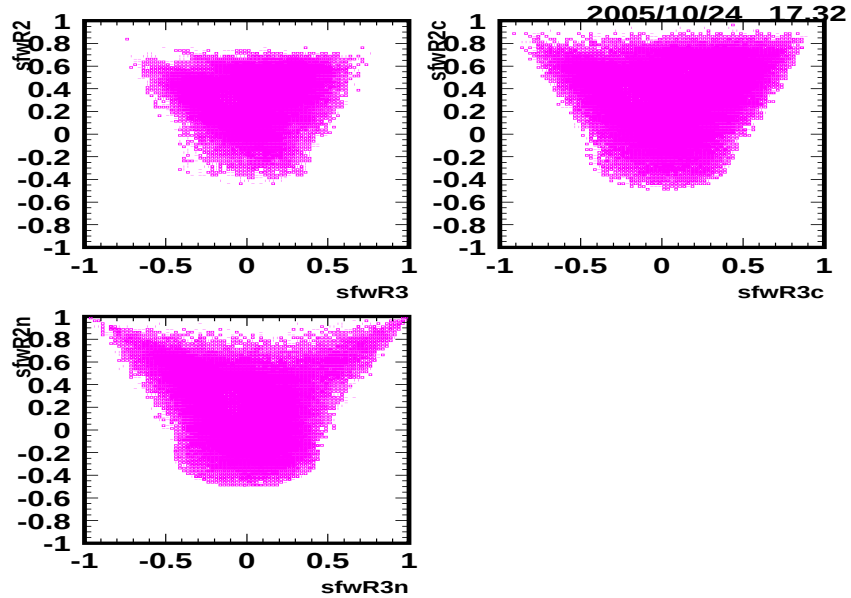

Figure 3.17: correlation between the variables R_{2c}, R_{3c}; R_{2n}, R_{3n} and R_2, R_3 in case of continuum

3.9.4 Fisher discriminant made using shape variables R_l

Then, Fisher discriminants F_{hc23}, F_{hn23} and F_{h23} are constructed, using variables R_{h2c} and R_{h3c} (F_{hc23}); R_{h2n} and R_{h3n} (F_{hn23}); R_{h2} and R_{h3} (F_{h23}). The Fisher discriminant shows visible separation between signal and continuum (Fig 3.18).

Figure of merit plots (Fig 3.19) are made for F_{23} and F_{c23}. The figure of merit value of F_{23} variable is slightly higher than that of F_{c23}.

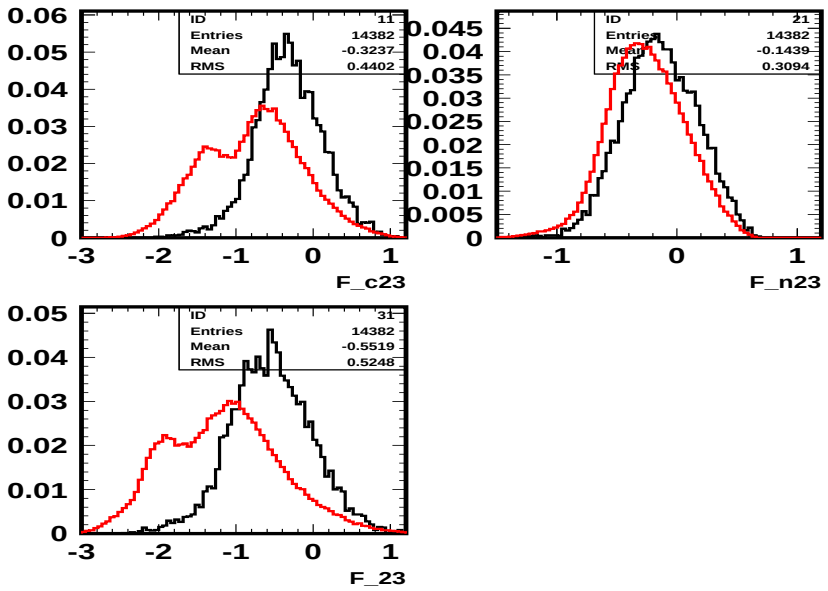

Figure 3.18: Distributions for Fisher discriminants F_{c23}, F_{n23} and F_{23}; black: signal, red: continuum

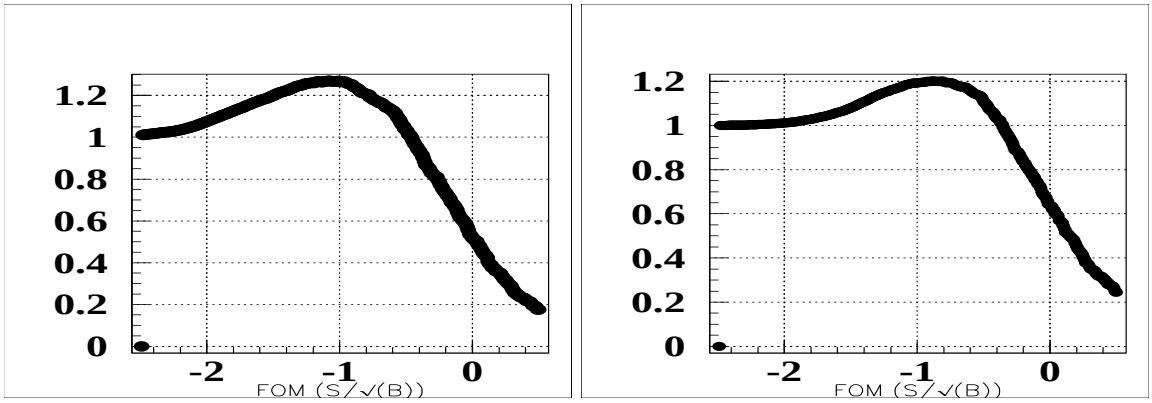

Figure 3.19: Figure of merit plots made for F_{23} (left), F_{c23} (right)

3.9.5 Variables involving photons in Υ(4S) frame

We develop new variables, involving photons to improve signal to background ratio. The definitions of these variables are:

$R_\gamma = \Sigma p_{\gamma_\parallel}/\sqrt{(s)} - E_h$; and
$r_\gamma = \Sigma p_{\gamma_\parallel}/\Sigma E_\gamma$, where
p_γ, E_γ and E_h are in Υ(4S) centre-of-mass frame;
$p_{\gamma_\parallel}$ is the parallel component of p_γ with respect to hard pion, h The distributions of these variables in same and opposite hemisphere with respect to h are studied. The notations used for these variables are listed below:
$R_{\gamma_{sh}} = R_\gamma$, same hemisphere;
$R_{\gamma_{oh}} = R_\gamma$, opposite hemisphere;
$R_{\gamma_{diff}} = R_{\gamma_{sh}}$ - $R_{\gamma_{oh}}$;
$r_{\gamma_{sh}} = r_\gamma$, same hemisphere;
$r_{\gamma_{oh}} = r_\gamma$, opposite hemisphere;
$r_{\gamma_{diff}} = r_{\gamma_{sh}}$ - $r_{\gamma_{oh}}$.
We use photons, with $E_\gamma > 0.05$ GeV in lab frame and distributions for R_γ, $R_{\gamma_{sh}}$, $R_{\gamma_{oh}}$, $R_{\gamma_{diff}}$, r_γ, $r_{\gamma_{sh}}$, $r_{\gamma_{oh}}$, $r_{\gamma_{diff}}$ using signal Monte-Carlo (100,000 events) (Fig. 3.20) and continuum data ($\approx$ 5.6 million events) (Fig. 3.21) are made. Figure-of-merit plots for $R_{\gamma_{sh}}$ and $R_{\gamma_{diff}}$ are shown in Fig. 3.22 and for $r_{\gamma_{sh}}$ and $r_{\gamma_{diff}}$ are shown in Fig. 3.23.

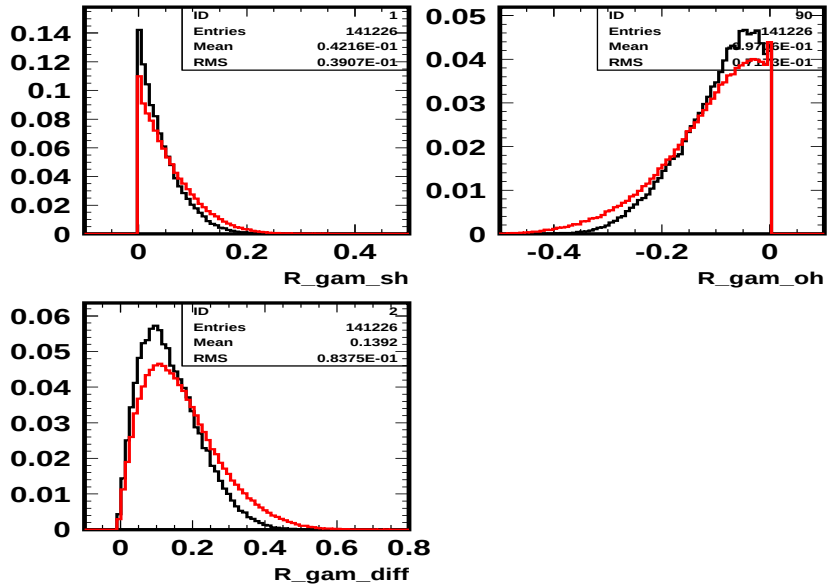

Figure 3.20: $R_{\gamma_{sh}}$, $R_{\gamma_{oh}}$, $R_{\gamma_{diff}}$ for signal Monte-Carlo (100,000 events) (black), continuum data ($\approx$ 5.6 million events) (red)

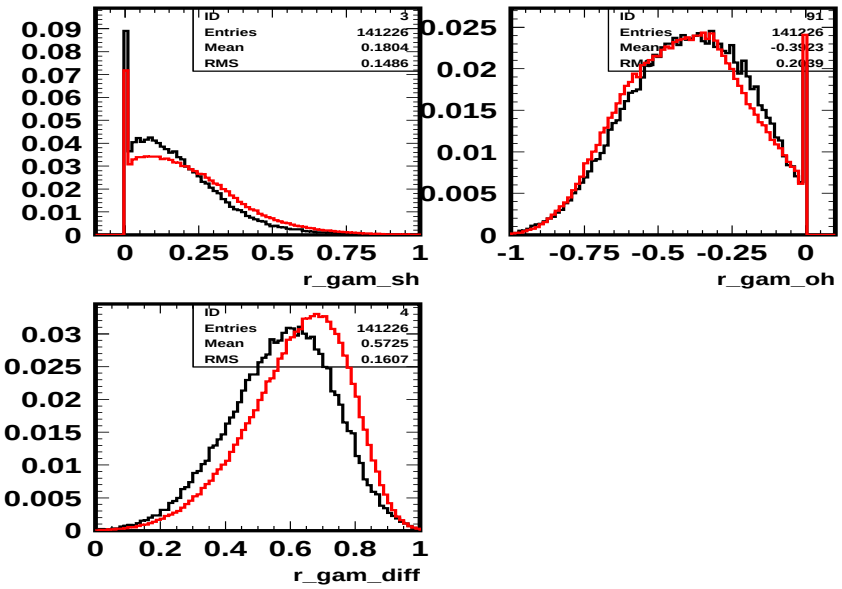

Figure 3.21: $r_{\gamma_{sh}}$, $r_{\gamma_{oh}}$, $r_{\gamma_{diff}}$ for signal Monte-Carlo (100,000 events) (black), continuum data ($\approx$ 5.6 million events) (red)

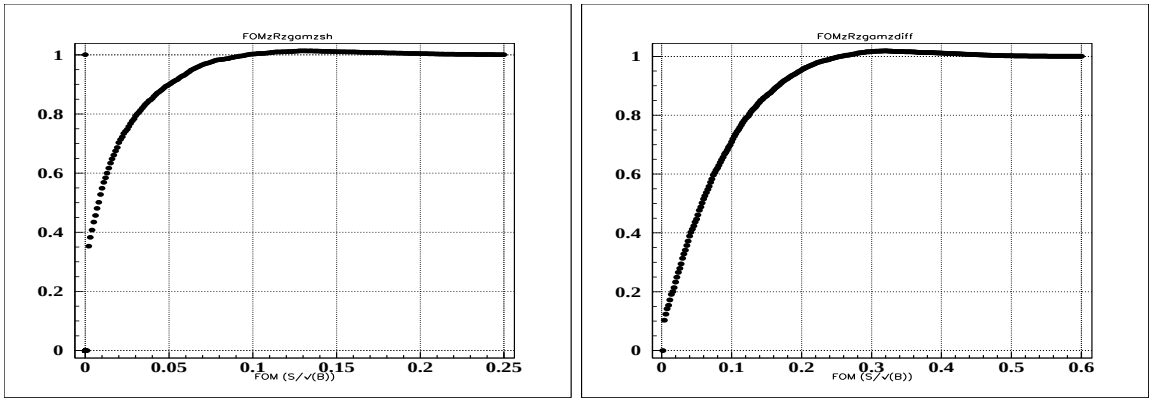

Figure 3.22: Figure-of-merit plots for likelihood ratio plots for $R_{\gamma_{sh}}$ (left), $R_{\gamma_{diff}}$ (right)

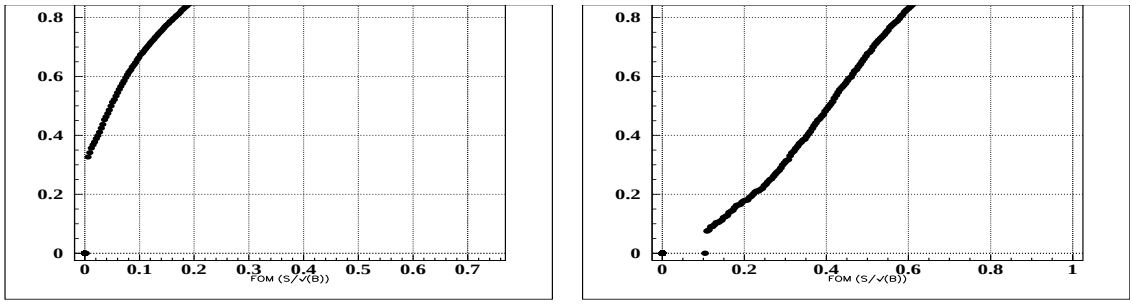

Figure 3.23: Figure-of-merit plots for likelihood ratio plots for $r_{\gamma_{sh}}$ (left), $r_{\gamma_{diff}}$ (right)

3.9.6 Shape variables R_{hl} using particles in Υ(4S) frame

We improve the continuum suppression techniques by developing the following shape variables R_{hl} , defined as:
R_{hl}= $\Sigma P_l(cos\theta_i)|p_i||p_h|/\Sigma|p_i||p_h|$ where,
P_l = lth Legendre poynomials
θ = angle between h and ith particle the Υ(4S) CM frame,
p_h = energy of the hard pion in the Υ(4S) CM frame,
p_i = energy of the ith particle in the Υ(4S) CM frame
and i runs over all particles except h.

We look at the distributions of R_{hl}, (l =2,3) (Fig. 3.24) using 100,000 signal Monte-Carlo events and $\approx$ 0.6 fb^{-1} data for following three cases:
R_{hl} : all particle case;
R_{hlc}: charged particles only;
R_{hln}: neutral particles only.

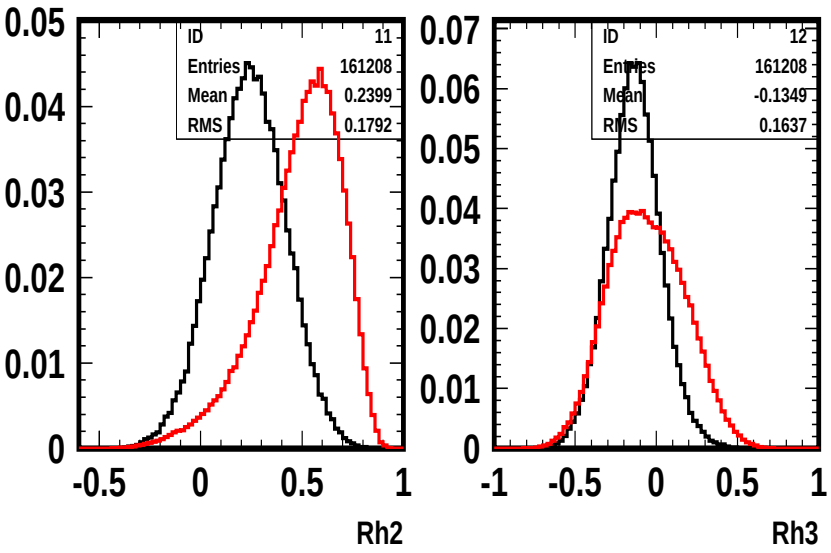

Figure 3.24: R_{hl2} and R_{hl3} distributions (black: signal MC (100000 events), red: continuum data (0.6 fb^{-1})

The continuum suppression variable, R_2 is shown in Fig. 3.25.

There exists correlation between the R_{hl}, (l = 2,3) and R_2 variables. The correlation plots are shown in Figs. 3.26 and 3.27. Hence, R_2 cut is not used in

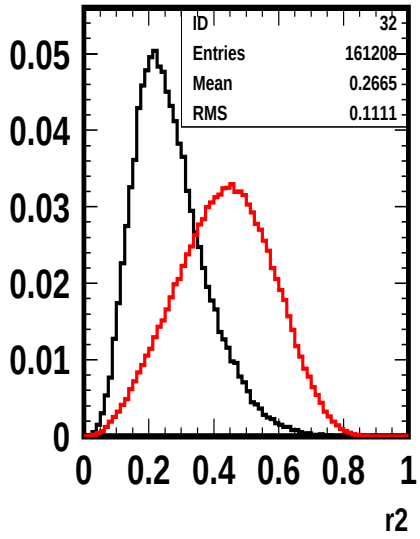

Figure 3.25: R_2 distribution (black: signal MC (100000 events), red: continuum data (0.6 fb^{-1})

the selection criteria. Correlation also exists between the R_{hl}, (l = 2,3) Fig. 3.28. Hence, multi-dimensional PDFs are constructed using these variables in order to build a likelihood ratio using them.

Likelihood ratio (LR) distributions are done using R_2, R_{h2} and R_2, R_{h3} and R_2 and R_{h2}, R_{h3} and R_2. We use normalized signal (S) and background (B) distributions to make the LR distributions (Fig. 3.29) using the definition:
$LR = S/(S + B)$.

LR $R_2 = R_2$;
$LR1 = R_{h2}$ and R_2;
$LR2 = R_{h3}$ and R_2;
$LR3 = R_{h2}$, R_{h3} and R_2.
We use a standard Belle software package called Brutus to make LR.

$S/\sqrt{B}$ plots are done for LR's using 100,000 signal Monte-Carlo events and about 0.6 fb^{-1} continuum data. Likelihood ratio using R_{h2} and R_2 ($LR2$) gives higher $S/\sqrt{B}$ than that of 1d LR for R_2 and is slightly higher than that of LR_3.

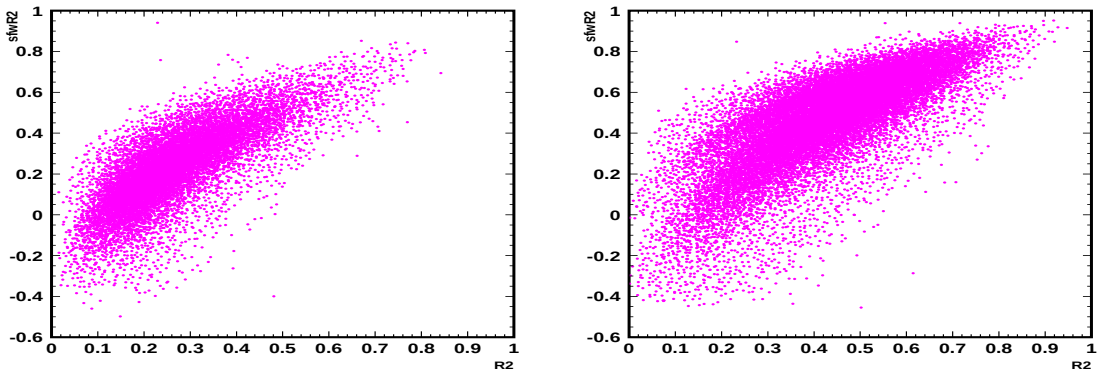

Figure 3.26: Correlation between R_{hl2} and R_2 (left: signal MC (100000 events), right: continuum data (0.6 fb^{-1})

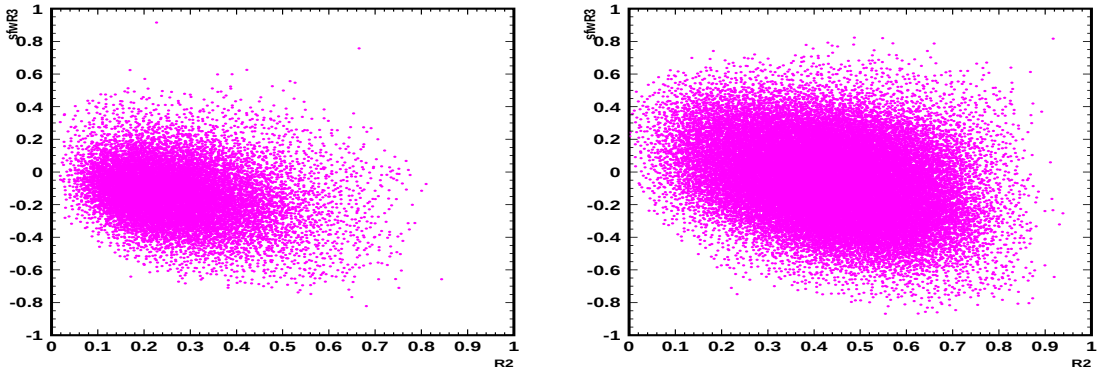

Figure 3.27: Correlation between R_{hl3} and R_2 (left: signal MC (100000 events), right: continuum data (0.6 fb^{-1})

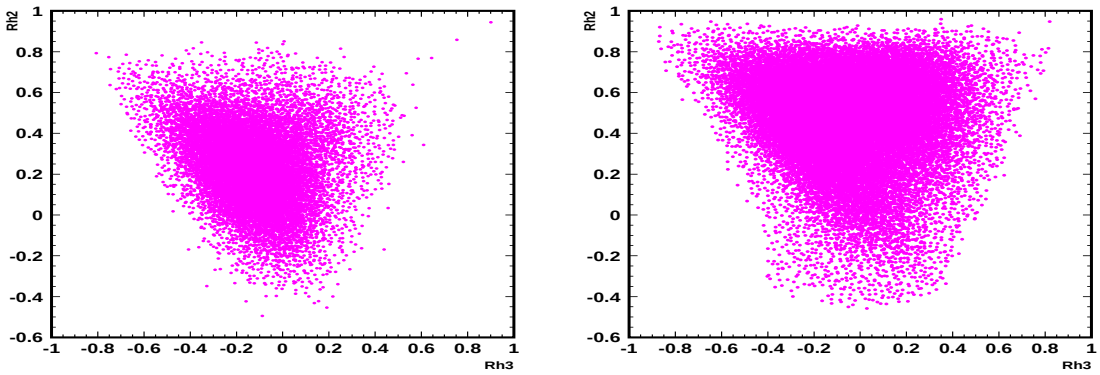

Figure 3.28: Correlation between R_{hl2}, R_{hl3} (left: MC, right: data)

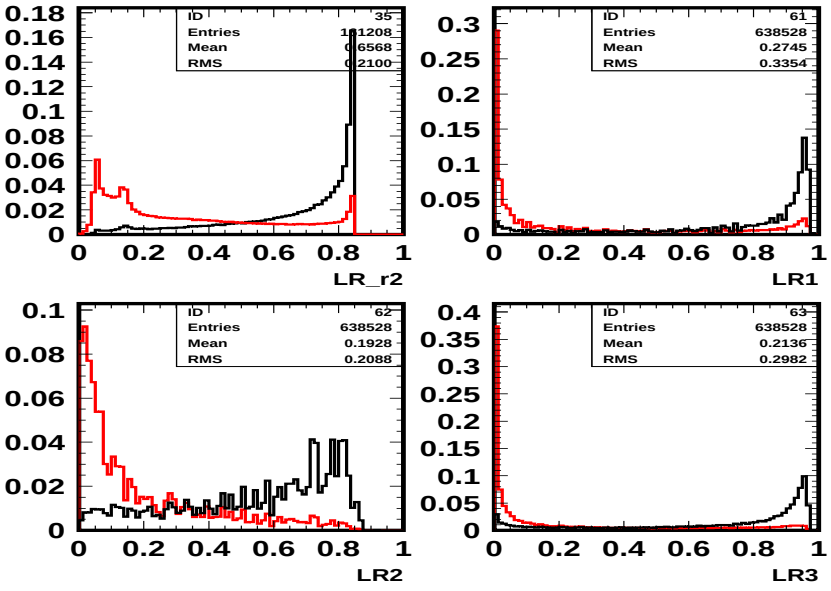

Figure 3.29: Likelihood ratio plots, top left (R_2), top right (R_{hl2} and R_2), bottom left (R_{hl3} and R_2), bottom right (R_{hl2}, R_{hl3} and R_2)

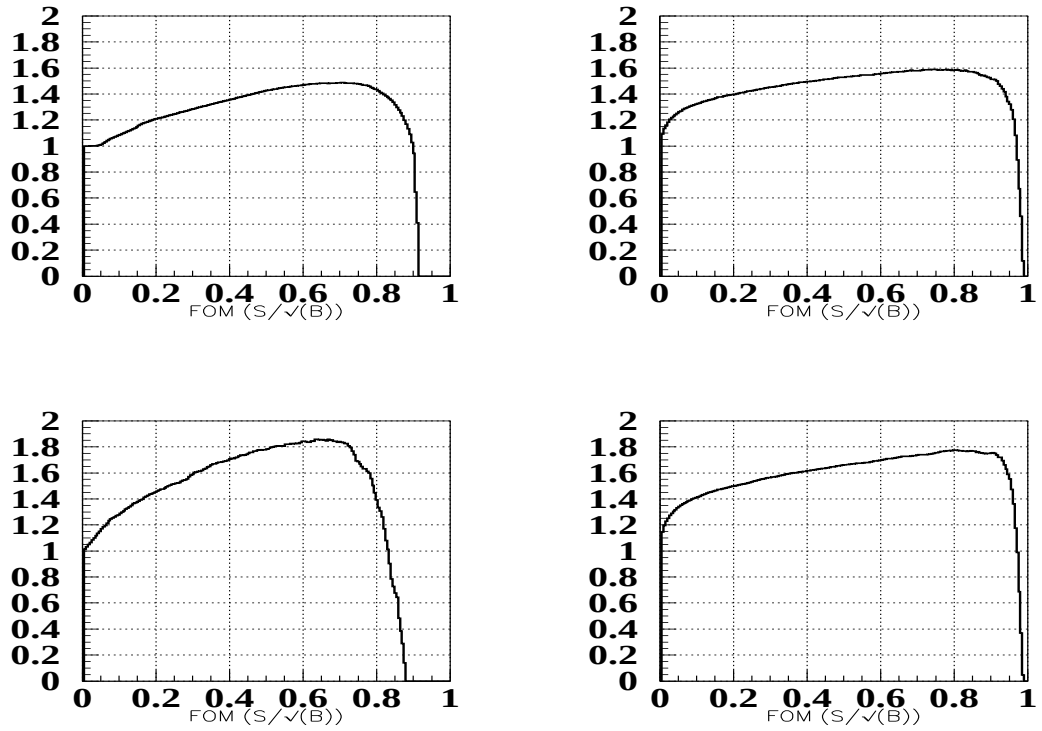

Figure 3.30: Figure-of-merit plots for likelihood ratio plots, top left (R_2), top right (R_{hl2} and R_2), bottom left (R_{hl3} and R_2), bottom right (R_{hl2}, R_{hl3} and R_2)

3.10 Developing fit algorithm for kinematic variables

We use the kinematic variables in the following range:
p_δ ($|\boldsymbol{p}_h| - |\boldsymbol{p}_{D^*}|$) : -0.5 - 0.5 GeV
$\tilde{p}_\parallel$ ("$\parallel$" component of π_s boosted into P.R. D^* frame) : -0.1 - 0.1 GeV
$\tilde{p}_\perp$ ("$\perp$" component of π_s boosted into P.R. D^* frame) : 0.0 - 0.1 GeV, using the following cuts:
Right sign combination: π_h and π_s opposite sign
$|\tilde{p}_\parallel| < 0.1$ GeV,
$|\tilde{p}_\perp| < 0.1$ GeV,
$|p_\delta| < 0.5$ GeV,
$LR_2 > 0.6$
LR_2: 2d likelihood ratio using R_{h3} and R_2.

The components in the fit are selected from generic Monte-Carlo, and are categorized into the following types:

- $D^*\pi$: The hard pion is required to originate from a real $B \to D^*\pi$ decay.
- $D^*\rho$: The hard pion is required to originate from a real $B \to D^*\rho$ decay.
- $B\bar{B}$ background: The event is taken from generic Monte-Carlo, but is neither a $D^*\pi$ nor $D^*\rho$.
- Continuum background: Only Continuum events are taken into account for this background type.

We fit $p_\parallel$ variable using a data sample $\approx 17.2\ fb^{-1}$ using the following signal and background components: signal MC: $\approx 67.9\ fb^{-1}$ (generated: 2×10^5 events), $D^{*+}\rho$ MC: $\approx 26.9\ fb^{-1}$ (generated: 2×10^5 events), generic MC: $\approx 17\ fb^{-1}$ and continuum MC: $\approx 6.3\ fb^{-1}$. Fig. 3.32 shows the fit projection. We check the 1d, 2d and 3d fits in the kinematic variables, which will be described in detail below, using a fake data-set, with the signal and background components taken in their relative ratio from this 1d fit in $p_\parallel$.

Since continuum Monte-Carlo has much higher statistics compared to continuum data, we use continuum Monte-Carlo, instead of continuum data for fitting. Fig. 3.32 shows the distributions of the kinematic variables $p_\parallel$, $p_\perp$ and p_δ using continuum data ($\approx 2.374\ fb^{-1}$) fitted with the variable shapes obtained using continuum Monte-Carlo ($\approx 28.81\ fb^{-1}$).

1d fit in the variables $p_\parallel$, $p_\perp$ and p_δ; 2d fit using $p_\parallel$ and $p_\perp$ and 3d fit using $p_\parallel$, $p_\perp$ and p_δ with no correlation assumed between the variables are made using a fake data-set using extended unbinned maximum likelihood method. In all the fits in

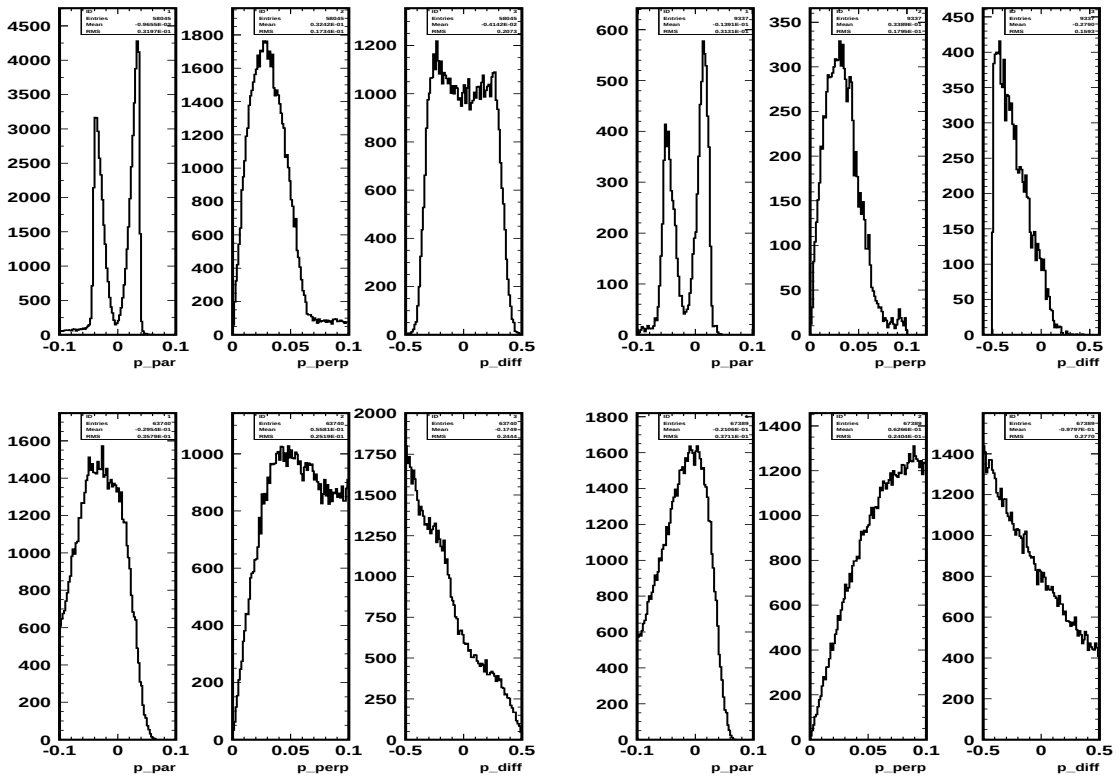

Figure 3.31: Kinematic variable ($p_\parallel$, $p_\perp$), p_δ) distributions for signal (top left), $D^*\rho$ (top right), generic (bottom left)and continuum (bottom right) Monte-Carlo

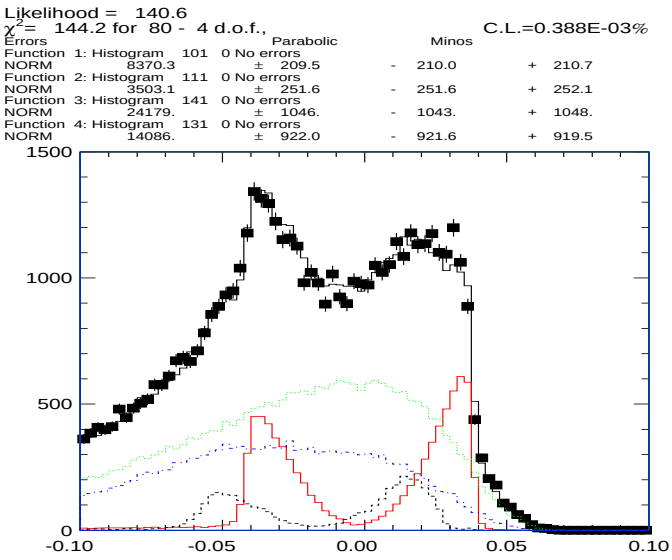

Figure 3.32: 1d-fit in $p_{\|}$ using $\approx 17.2\ fb^{-1}$ data (black solid dots with error bars) using signal MC: $\approx 67.9\ fb^{-1}$ (red), $D^{*+}\rho$ MC: $\approx 26.9\ fb^{-1}$ (dotted black), generic MC: $\approx 17\ fb^{-1}$ (dotted blue) and continuum MC: $\approx 6.3\ fb^{-1}$ (dotted green)

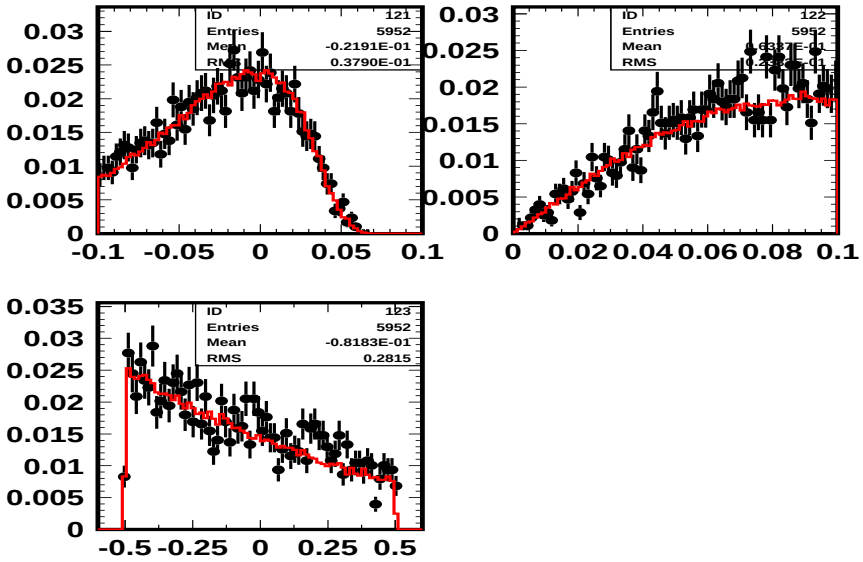

Figure 3.33: Kinematic variable distributions between continuum Monte-Carlo (red curve) and continuum data (points with error bars); top (left): $p_{\|}$, top (right): $p_{\perp}$, bottom: p_{δ}

this section, $D^*\pi$ signal, $D^*\rho$, generic and continuum Monte-Carlo are shown in red, green, cyan and magenta colours respectively.
2d PDF = 2d PDF ($p_{\|}$, $p_{\perp}$) (no correlation assumed in the fit between the 2 variables)

3d PDF = 2d PDF ($p_{\|}$, $p_{\perp}$) $\times$ 1d PDF for p_{δ} (no correlation assumed in the fit between p_{δ} and other 2 variables).

We look at 1d distribution for p_{δ} to check its correlation with other 2 variables, before making the 3d fit. To check the fit quality we make 4 regions, with cuts on $p_{\|}$ and $p_{\perp}$ and use smoothed histogram as PDF (Table 3.14).

The PDF almost describes the distribution in the 4 contributions for 4 regions. Correlation exists between the 3 variables for some cases, but is mostly okay for others. We use 1d histogram shape for p_{δ}, with 2d PDF obtained earlier to make 3d fit, using product of PDF's, without taking into account any correlation between the three variables, $p_{\|}$ and $p_{\perp}$ and p_{δ}.

An additional check is done by varying the number of bins used for the fit to kinematic variables using the 2d-fit case. Table 3.16 shows the results with number of bins 30 and 50. The fit results using these 2 different number of bins are consistent with each other within error bars.

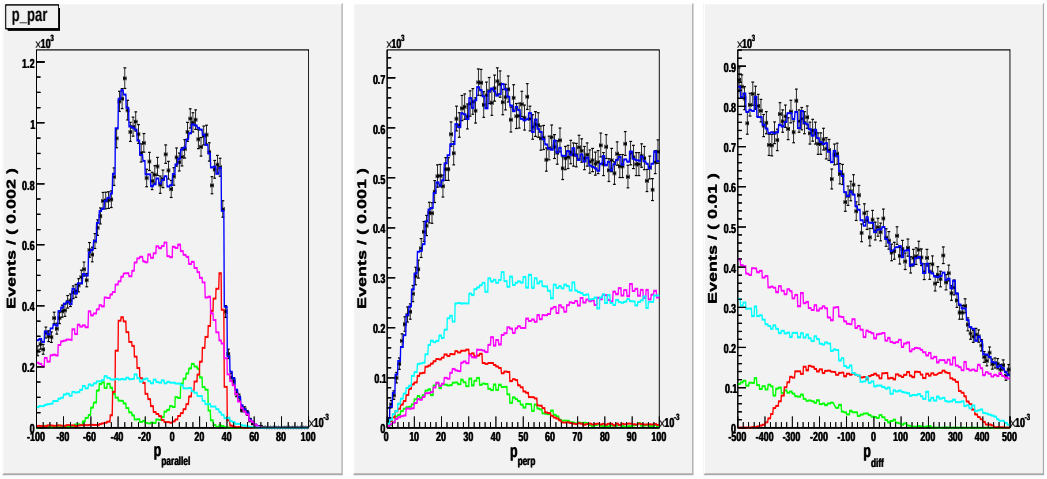

Figure 3.34: 1d-fit projection onto $p_{\parallel}$, $p_{\perp}$ and p_{δ} using fake data-sets. $D^*\pi$ signal, $D^*\rho$, generic and continuum Monte-Carlo backgrounds are shown in red, green, cyan and magenta colours respectively.

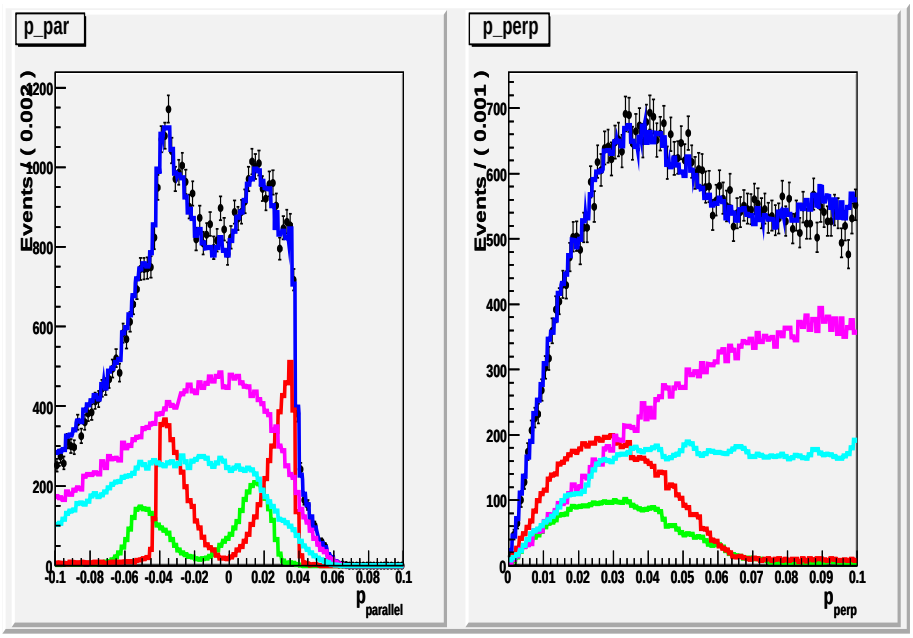

Figure 3.35: 2d-fit projections onto $p_{\parallel}$ (right) and $p_{\perp}$ (left) using fake data-set. $D^*\pi$ signal, $D^*\rho$, generic and continuum Monte-Carlo backgrounds are shown in red, green, cyan and magenta colours respectively.

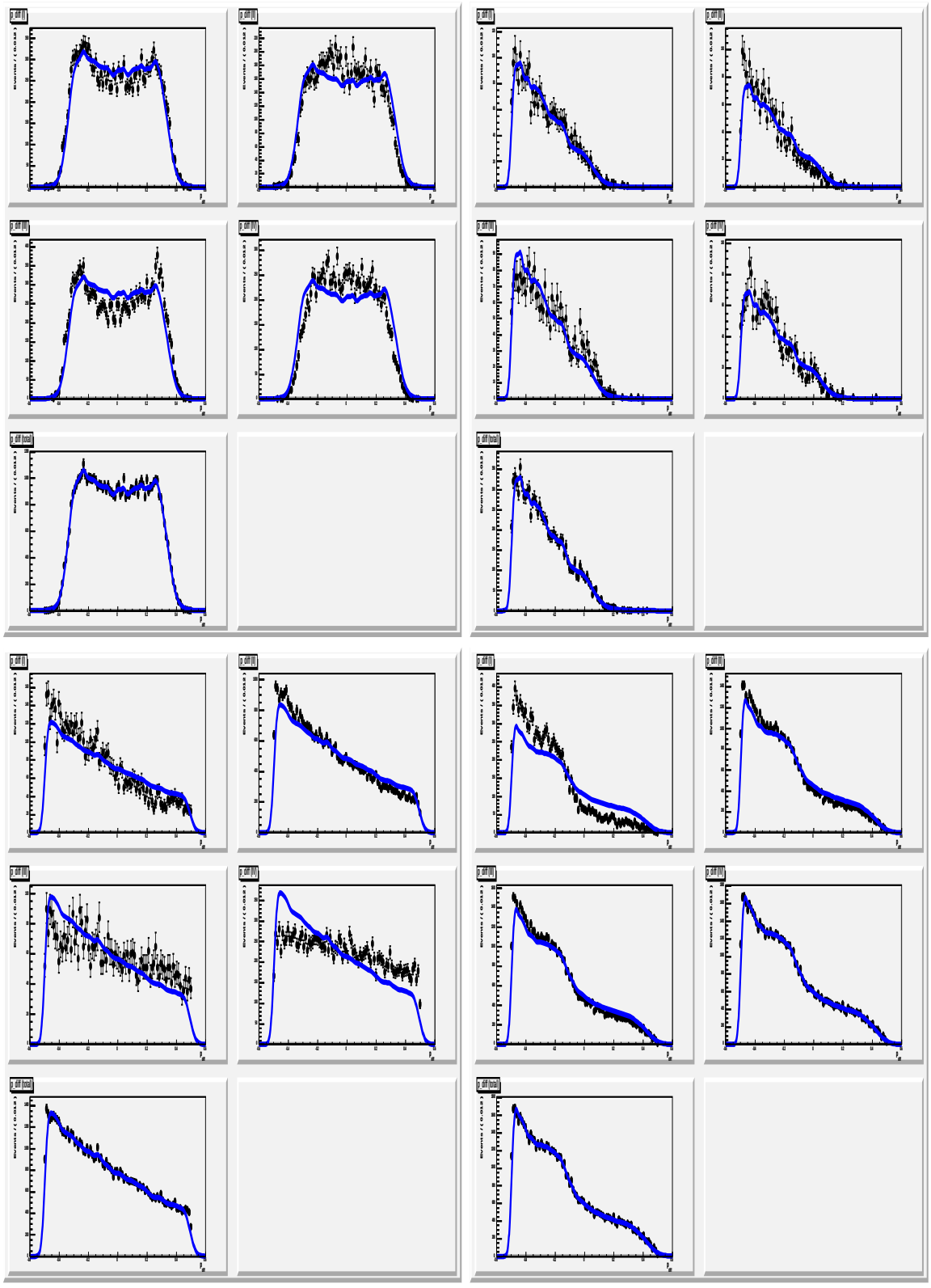

Figure 3.36: 1d-fit projections onto p_δ for signal, $D^*\rho$, generic and continuum Monte-Carlo in 4 regions of ($p_\parallel$, $p_\perp$).

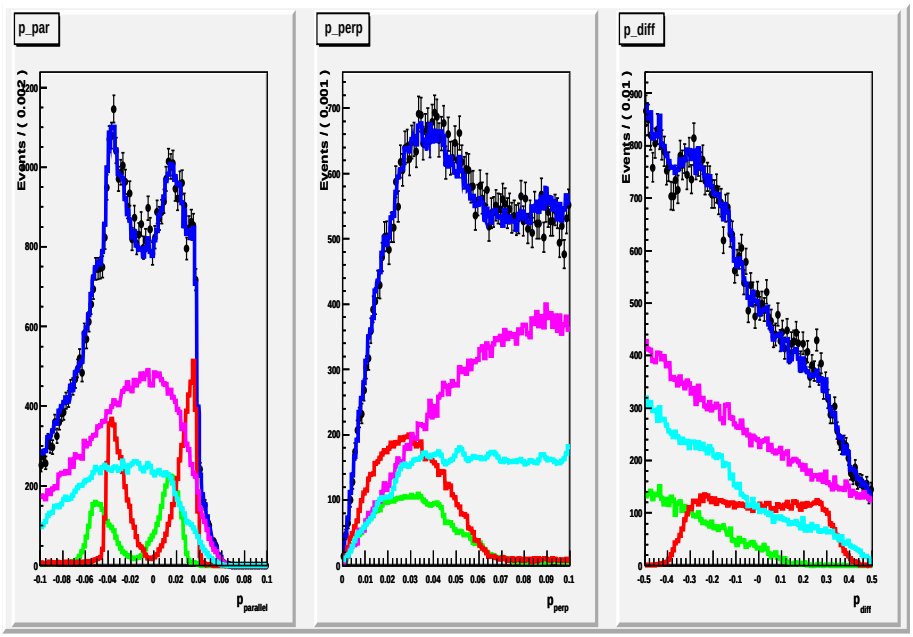

Figure 3.37: 3d-fit projections onto $p_{\parallel}$ (left), $p_{\perp}$ (middle) and p_{δ} (right) using fake data-set. $D^*\pi$ signal, $D^*\rho$, generic and continuum Monte-Carlo backgrounds are shown in red, green, cyan and magenta colours respectively.

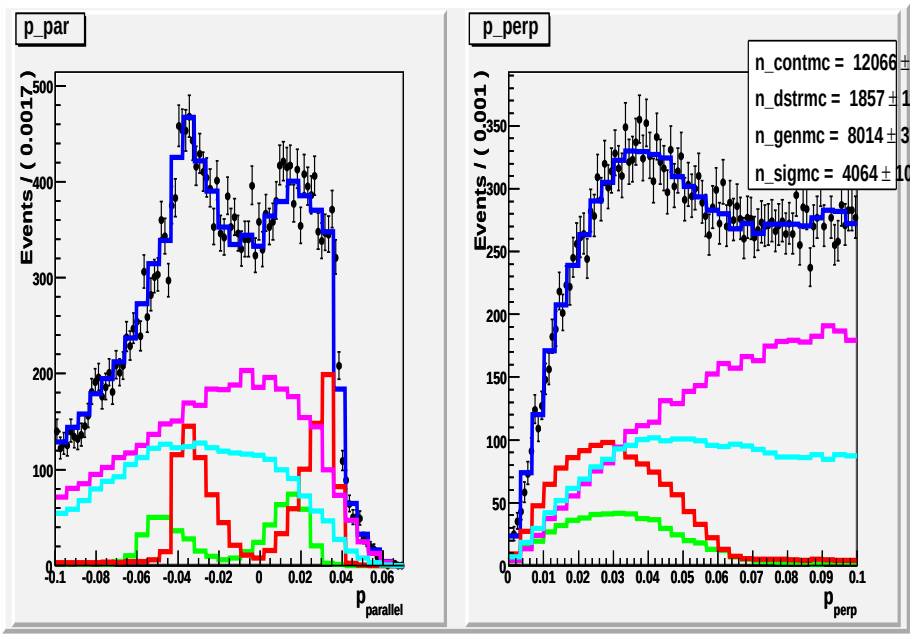

Figure 3.38: 2d-fit projections onto $p_{\|}$ (left), $p_{\perp}$ (right) with lesser bins (30 bins) in fake data-set. $D^*\pi$ signal, $D^*\rho$, generic and continuum Monte-Carlo backgrounds are shown in red, green, cyan and magenta colours respectively.

	Signal MC	$D^*\rho$ MC	cont. MC	generic MC
sample	8000	4000	26000	14000
1d fit ($p_\parallel$)	8083 ±210	4302±258	30800±1072	8814 ±950
1d fit ($p_\perp$)	6403± 1967	4110±2253	18040±1719	23449±2269
1d fit (p_δ)	9402±502	3920±1239	24544 ±1052	14137±2380

Table 3.12: Fit yields for signal and background components using 1d fit in $p_\parallel$, $p_\perp$ and p_δ using fake data-sets. $D^*\pi$ signal, $D^*\rho$, generic and continuum Monte-Carlo backgrounds are shown in red, green, cyan and magenta colours respectively.

	Signal MC	$D^*\rho$ MC	cont. MC	generic MC
sample	8000	4000	26000	14000
1d fit (p_δ)	9402±502	3920±1239	24544 ±1052	14137±2380
2d fit ($p_\parallel$, $p_\perp$)	8145±141	4391±151	24683 ±424	14781±450

Table 3.13: Fit yields for signal and background components using 1d fit in p_δ and 2d fit using $p_\parallel$, $p_\perp$ using fake data-sets

Toy Monte-Carlo study is done to check fit stability. The algorithm for this Toy Monte-Carlo study is described below:

- Step 1: PDFs for signal and three background components are made: pdf1, pdf2, pdf3, pdf4 and are added to get final pdf.
- Step 2: We then generate samples for each contribution, with N_{true} number of events from the respective pdfs (taken in ratio as expected in real data). These samples are added to obtain one Toy MC experiment.
- Step 3: We fit theToy MC with the final pdf and obtain respective yields with error, $N_i \pm \sigma_i$ for signal and background components.
- Step 4: Steps 2 and 3 are done several times to generate several toy MC experiments.

We observed that the statistics of the sample used to build the PDF doesn't affect, as Toy MC is generated from the PDF and we fit it with the same PDF. Then, we check the pull distributions for all 4 parameters. We define pull (P):

$$P = (Y - N_{true})/\sigma, \tag{3.2}$$

Region	$p_\parallel$	$p_\perp$	Region	$p_\parallel$	$p_\perp$
I	< 0 GeV	<0.035 GeV	II	< 0 GeV	>0.035 GeV
III	> 0 GeV	<0.035 GeV	IV	> 0 GeV	>0.035 GeV

Table 3.14: Four regions made using $p_\parallel$ and $p_\perp$ variables

	Signal MC	$D^*\rho$ MC	cont. MC	generic MC
sample	8000	4000	26000	14000
1d fit (p_δ)	9402±502	3920±1239	24544 ±1052	14137±2380
2d fit ($p_\parallel$, $p_\perp$)	8145±141	4391±151	24683 ±424	14781±450
3d fit	8173±126	4745 ± 134	24998 ±367	14083±386

Table 3.15: Fit yields for signal and background components using 1d fit in p_δ and 2d fit using $p_\parallel$, $p_\perp$ and 3d fit using $p_\parallel$, $p_\perp$, p_δ variables

where Y, N_{true} and σ are the fit yield, expected yield and error on the fit yield respectively. The difference $Y - N_{true}$ is called the residual value. The fit is unbiased if the pull distribution has a mean equal to 0 and sigma equal to 1.

We check Toy MC with 2d fit, using correlation of $p_\parallel$, $p_\perp$ variables and fitted the Toy MC ensembles with PDF, without correlation (Fig. 3.39) between them. However, the fit is biased if correlation is not taken into account. Fig. 3.40 shows the residual and pull distributions for 2d-fit with correlation between $p_\parallel$ and $p_\perp$. The fit is unbiased if correlation between variables is properly taken into account.

We conclude the following from the 2d fit using PDF, without correlation between the variables using Toy MC:

- Toy MC study indicates fit is not biased if PDF's provided are "perfect", not limited by statistics and all correlations between variables are taken into account correctly.
- PDF's used for fake data set are limited by statistics. Poor fit yields for 2-d case may be due to low statistics for PDF's.

The fake data-set is made from the same data-sample that is used to build the PDFs to fit. This could cause a bias in the fit result. Hence, the fake data-set and the data-set to build PDFs are made mutually exclusive. Table 3.18 shows the number of events used to make fake data-set and PDF from the initial data-set of signal and background components.

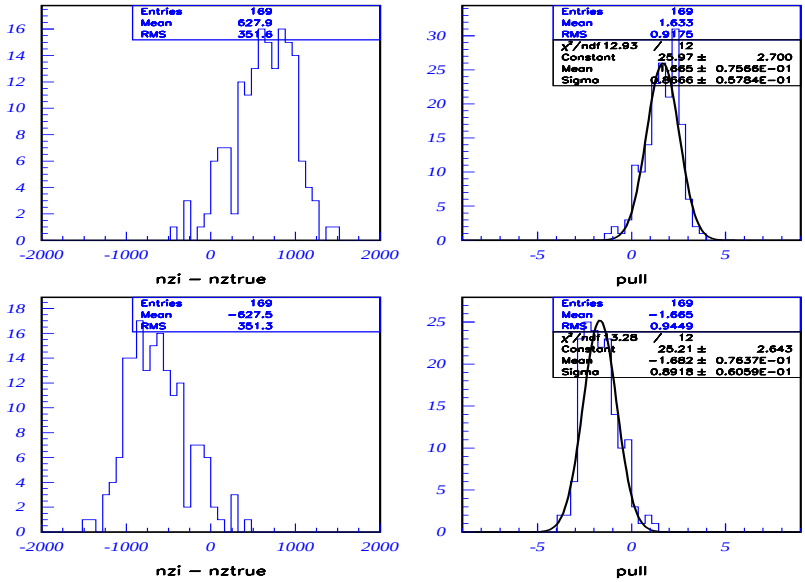

Figure 3.39: Residual (left) and pull (right) (fitted with a single Gaussian) distribution for 2d-fit (without correlation); rows from top to bottom: $D^*\pi$ signal, $D^*\rho$ background

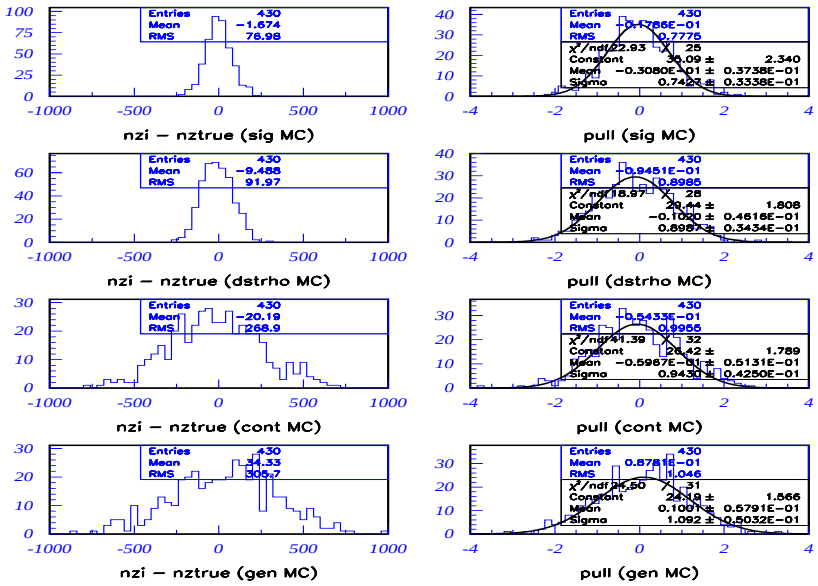

Figure 3.40: Residual (left) and pull (right) (fitted with a single Gaussian) distribution for 2d-fit (with correlation between $p_\parallel$, $p_\perp$); rows from top to bottom: $D^*\pi$ signal, $D^*\rho$, continuum and generic Monte-Carlo background

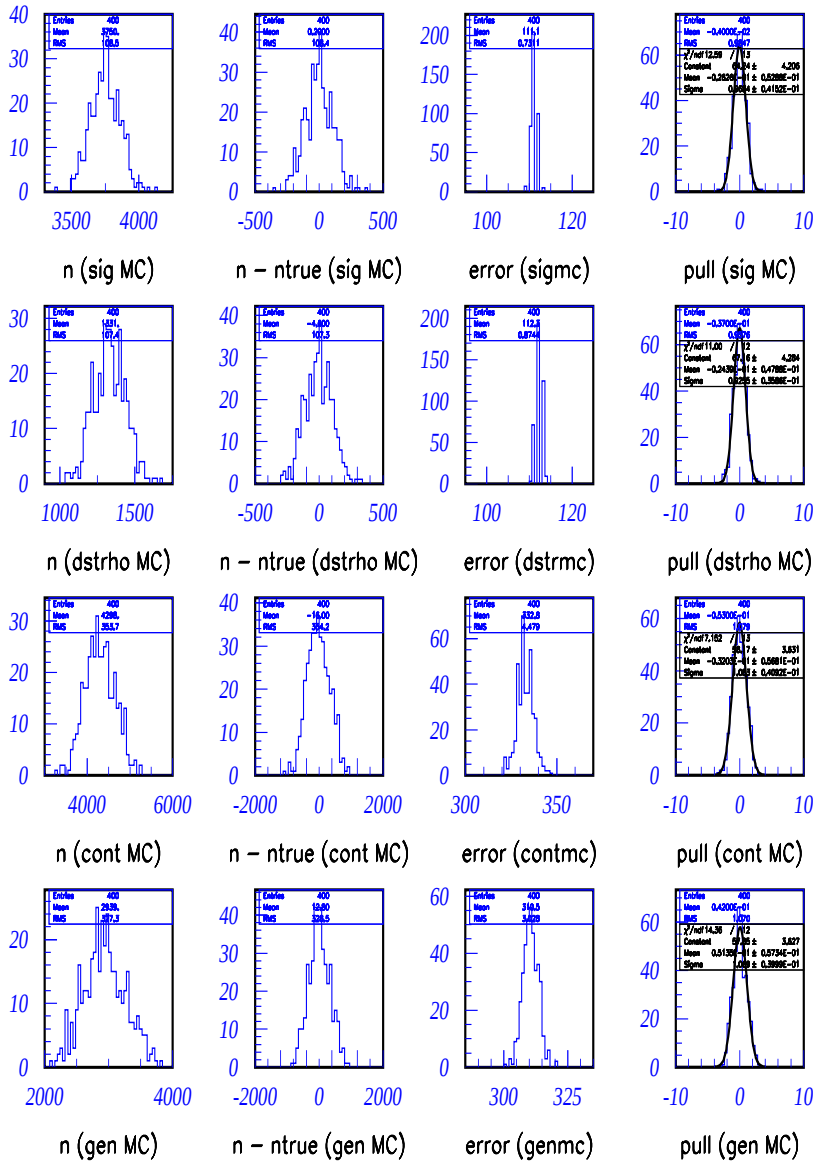

Figure 3.41: Left to right: yield, residual, error and pull distribution for 1d fit in $p_{\|}$ using 400 Toy MC samples. Top to bottom rows: Signal MC, $D^*\rho$ MC, cont. MC, generic MC

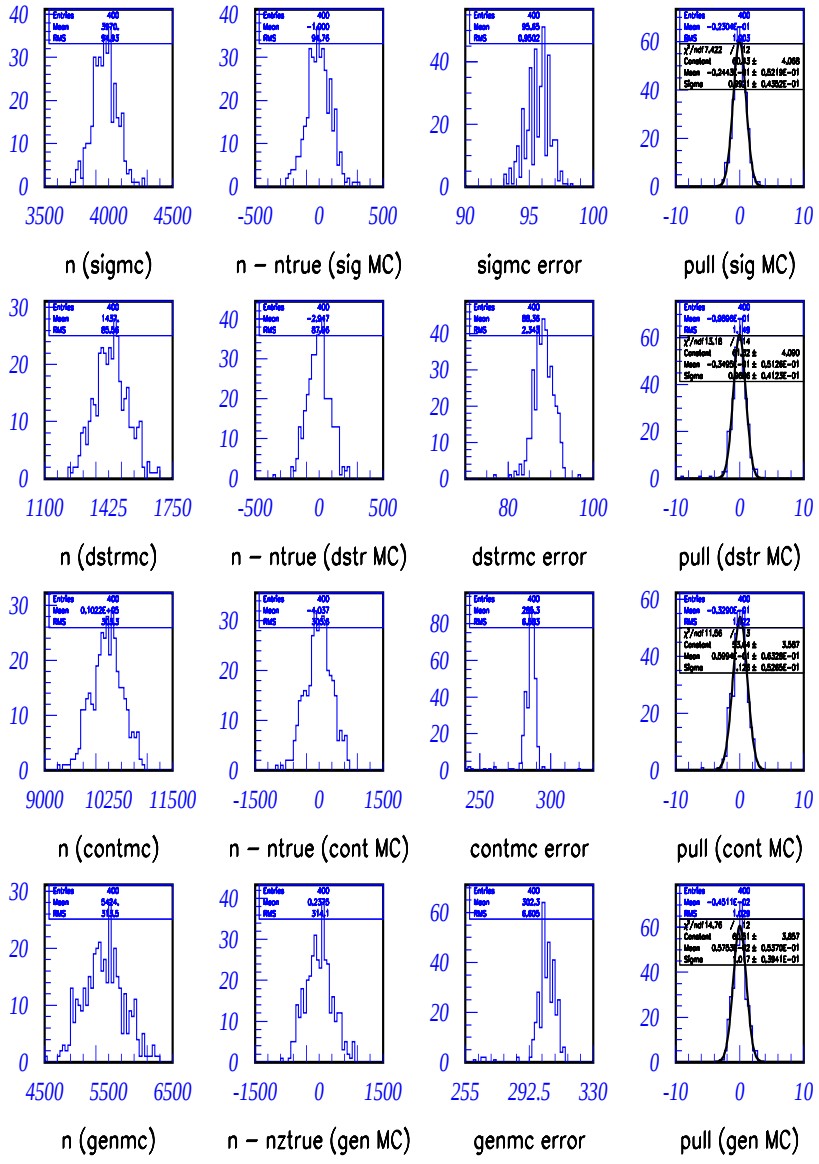

Figure 3.42: Left to right: yield, residual, error and pull distribution for 2d-fit in ($p_{\|}$, $p_{\perp}$) using 400 Toy MC samples. Top to bottom rows: Signal MC, $D^*\rho$ MC, cont. MC, generic MC

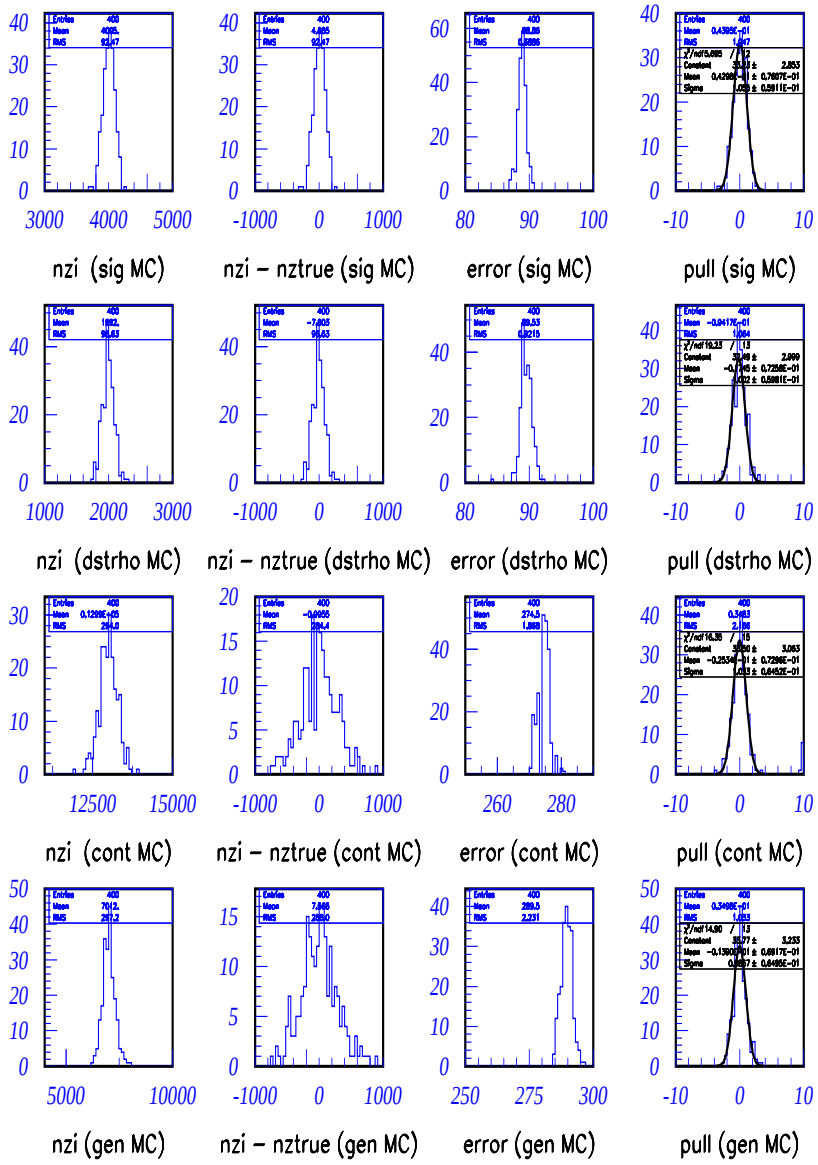

Figure 3.43: Left to right: yield, residual, error and pull distribution for 3d-fit in $((p_{\|},\ p_{\perp}),\ p_{\delta})$ using 400 Toy MC samples. Top to bottom rows: Signal MC, $D^{*}\rho$ MC, cont. MC, generic MC

	bins	Signal MC	$D^*\rho$ MC	cont. MC	generic MC
sample		4000	2000	13000	7000
2d fit	50	4105±100	1759 ± 102	11358 ±305	8779±330
2d fit	30	4064±101	1857 ± 108	12066 ±343	8014±373

Table 3.16: Fit yields for signal and background components for 2d fit using $p_{\parallel}$, $p_{\perp}$ using fake data-set with different binning

		Signal MC	$D^*\rho$ MC	cont. MC	generic MC
N_{true}	2d-fit	4000	2000	13000	7000

Table 3.17: N_{true} values for signal and background components

Toy MC study suggests that 1d, 2d, 3d fits are not biased. Errors decrease by $\approx$ 14 % from 1d fit $\rightarrow$ 2d fit and by $\approx$ 7 % from 2d fit $\rightarrow$ 3d fit. We use 2d fit to obtain yield of $D^*\pi$ using p_δ and $p_{\parallel}$, with a cut in the signal region on the third variable, $p_{\perp}$ since the variable that we use for our best candidate selection (δ_{fs}) is correlated with the third variable $p_{\perp}$.

A Toy MC study with 400 samples is done to study the effect of statistical fluctuation of PDF in the fit. In both 1d and 2d Toy MC case, statistical fluctuation introduced of PDF does not affect the yield significantly and affects the error only by a few percent.

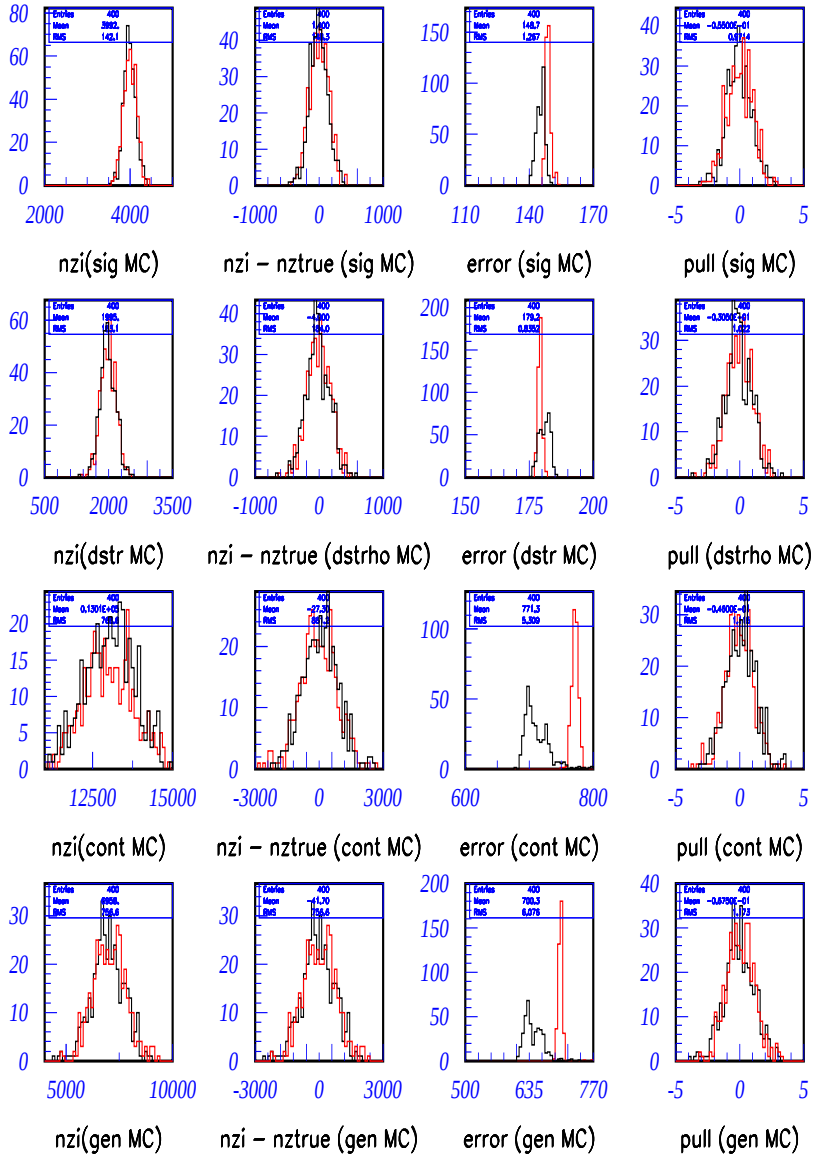

Figure 3.44: Left to right: yield, residual, error and pull distribution for 1d-fit in $p_{\|}$ using 400 Toy MC samples, with true MC pdf (red) and pdf with statistical fluctuation introduced in it (black). Top to bottom rows: Signal MC, $D^*\rho$ MC, cont. MC, generic MC

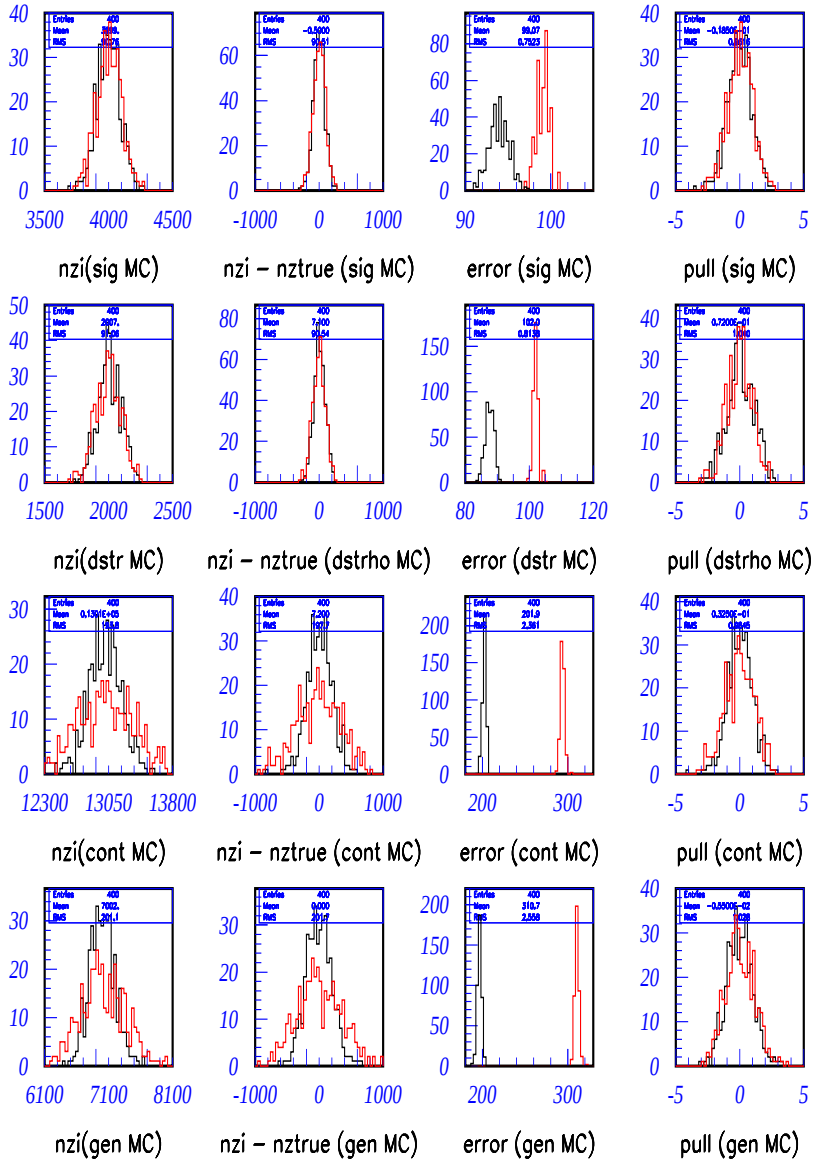

Figure 3.45: Left to right: yield, residual, error and pull distribution for 2d-fit in $((p_{\|}, p_{\perp})$ using 400 Toy MC samples, with true MC pdf (red) and pdf with statistical fluctuation introduced in it (black). Top to bottom rows: Signal MC, $D^*\rho$ MC, cont. MC, generic MC

	total	fake data	pdf
Signal MC	56357	4000	52357
$D^*\rho$ MC	9574	2000	7574
cont. MC	75095	13000	62095
generic MC	78035	7000	71035

Table 3.18: Number of events of signal and background used to make fake data-set and PDF

	Signal MC	$D^*\rho$ MC	cont. MC	generic MC
1d(in $p_\parallel$)				
N_{true}	3754	1330	4325	2921
Y	3750 ± 109	1331 ± 107	4298 ± 354	2939 ± 327
σ	111.1 ± 0.7	112.3 ± 0.9	332.8 ± 4.5	319.5 ± 3.0
2d ($p_\parallel$), $p_\perp$)				
N_{true}	3961	1442	10180	5479
Y	3970 ± 92	1437 ± 86	10220 ± 303	5424 ± 314
σ	95.7 ± 1.0	88.4 ± 2.3	285.3 ± 6.7	302.3 ± 5.6
3d (($p_\parallel$, $p_\perp$), p_δ)				
N_{true}	8000	4000	26000	14000
Y	4095 ± 92	1992 ± 97	12990 ± 294	7012 ± 297
σ	88.9 ± 0.7	89.5 ± 0.9	274.5 ± 1.9	289.5 ± 2.2

Table 3.19: Fit yields for signal and background components 1d fit in $p_\parallel$, 2d fit using ($p_\parallel$, $p_\perp$), 3d fit using (($p_\parallel$, $p_\perp$), p_δ)

	Signal MC	$D^*\rho$ MC	cont. MC	generic MC
1d $\rightarrow$ 2d				
change in σ (in %)	-13.86	-21.28	-14.27	-5.38
2d $\rightarrow$ 3d				
change in σ (in %)	-7.11	1.24	-3.79	-4.23

Table 3.20: Change in σ for signal and background components for 1d $\rightarrow$ 2d fit and 2d $\rightarrow$ 3d

Chapter 4

Flavor tagging in $B \to D^*\pi$ decays

4.1 Components and signal region for the fit to obtain $D^*\pi$ yield

The fit to obtain the yield for $D^*\pi$ signal is done using the following two variables: p_δ and $p_\parallel$, with a cut in the signal region on the third variable, $p_\perp$ ($p_\perp < 0.05$ GeV/c). We use unbinned maximum likelihood method to perform the two-dimensional fit, taking into account the correlation between the two variables. The full fitting range is summarized in Table 4.1.

The components in the fit are selected from generic Monte Carlo, and are categorized into the following types:

- $D^*\pi$: The hard pion is required to originate from a real $B \to D^*\pi$ decay.
- $D^*\rho$: The hard pion is required to originate from a real $B \to D^*\rho$ decay.
- correlated background: The event is neither a $D^*\pi$ nor $D^*\rho$, but the slow pion originates from a D^* decay, which in turn originates from the same B as the fast pion. Decays, such as $D^{*+}l^+\nu_l$, $B \to D^{**}\pi$, $B \to D^*a_1$ are major contributions to this background. Only 30% of the neutral type correlated background are 2-body decays. The amount of the major 2-body and 3-body decays in the neutral type correlated background are :
  $B \to D^{**}\pi$ (7.1%), $B \to D^*a_1$ (9.3 %), $D^{*+}l^+\nu_l$ (50%) .
- uncorrelated background: Everything that remains including the continuum events are taken into account for this background type. $B \to D\pi$ is the largest source of this background.

Quantity	Entire fit region	Signal region
$p_{\parallel}$	$-0.10 < p_{\parallel}/\mathrm{GeV}/c < 0.07$	$-0.05 < p_{\parallel}/\mathrm{GeV}/c < -0.01$
		$0.01 < p_{\parallel}/\mathrm{GeV}/c < 0.04$
p_{δ}	$-0.60 < p_{\delta}/\mathrm{GeV}/c < 0.50$	$-0.40 < p_{\delta}/\mathrm{GeV}/c < 0.40$

Table 4.1: Fit region

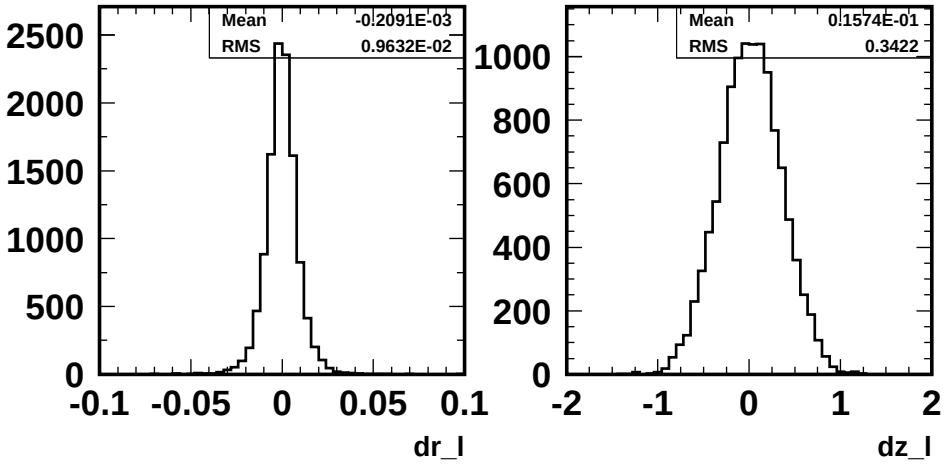

Figure 4.1: Impact parameters dr, dz of lepton from the tag side in $\Upsilon(4S)$ rest frame, using 0.2 million signal Monte Carlo events.

4.2 Flavour tagging

The flavour of the tag-side B is determined from the charge of the lepton and kaon candidate in the remainder of the event. A detailed description of the requirements of tagging leptons and kaons is given in the next two sections. If both lepton and kaon are identified in an event, it is tagged using the lepton track only.

4.3 Tagging lepton selection

The probability of the existence of a lepton from the tag side is $\approx 21\%$, from the branching fraction (BR) of semi-leptonic B-decay, $\mathrm{BR}(B^0 \to Xl^+\nu_l) = 2 \times (10.4 \pm 0.4)\%$, where the factor of two arises since the lepton can be either an electron or a muon. These leptons are primary leptons, originating mainly from the

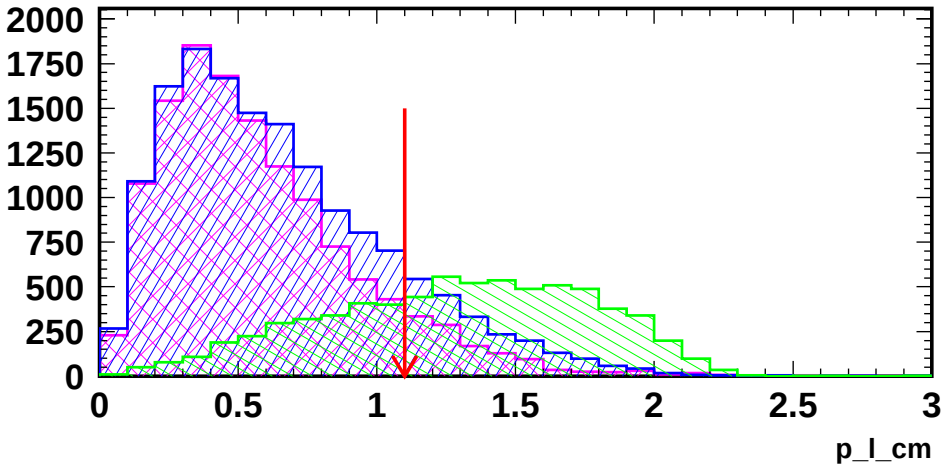

Figure 4.2: Momentum of CP-side (magenta) and tag-side (primary: green, secondary: blue) leptons in $\Upsilon(4S)$ rest frame, using 0.2 million signal Monte Carlo events.

$B^0 \to D^{*+} l^+ \nu_l$ (5.35%), $B^0 \to D^+ l^+ \nu_l$) (2.12%) decays. We obtain an efficiency of $\approx 19\%$ for selecting a true tag-side lepton.

We apply the tagging selection criteria (Table 4.2) and provide the loss in the number of leptons for each of them. Fig. 4.3 shows the impact parameters, dr and dz for these leptons. For the leptons that are used to tag the flavour of B, the momentum is required to be greater than 1.1 GeV/c to reject secondary leptons (leptons coming from an intermediate D). Fig. 4.3 shows the momentum distribution for CP-side (magenta) and tag-side (blue) leptons in $\Upsilon(4S)$ rest frame.

In order to reduce contamination from leptons of the CP-side (leptons originating from the D of the CP-side), we make a requirement on the cosine of the angle between the lepton and hard pion ($\cos\delta_{fl}$). The hard pion and lepton will be almost back-to-back in $\Upsilon(4S)$ rest frame, as the lepton originates from the D of the CP-side. The $\cos\delta_{fl}$ distribution peaks at -1. On the other hand, since the leptons (primary or secondary) from the tag-side are not correlated with the hard pion direction, we should have a flat distribution in $\cos\delta_{fl}$ for such leptons. Thus, the $\cos\delta_{fl}$ distribution (Fig. 4.3) helps distinguish the CP-side and tag-side leptons.

The leptons from the CP-side are secondary leptons. Such leptons are reduced

Quantity	Requirement	Number	Efficiency (in %)
No cut		1071	100.0
More than 1 lepton	reject	1066	99.5
Momentum	$1.1 < p_l/\mathrm{GeV}/c < 2.3$	660	61.6
Muon probability	> 0.90		
Muon χ^2/ndf	< 3.5		
Electron probability	> 0.90	579	54.1
Closest approach to IP (r) (dr_l)	< 0.1 cm		
Closest approach to IP (z) (dz_l)	< 2.0 cm	577	53.9
SVD hits in layers 2 to 4 (SVD2 data)	≥ 2		
SVD hits (r - ϕ plane)	≥ 2		
SVD hits (z plane)	≥ 2	560	52.3
Lab polar angle	$23^\circ < \theta_{lab} < 139^\circ$ (SVD1)		
	$17^\circ < \theta_{lab} < 150^\circ$ (SVD2)	560	52.3
Angle between lepton and fast pion	$\cos\delta_{fl} > -0.75$	483	45.1

Table 4.2: Summary of tagging lepton cuts along with the number of lepton candidates left and the reduction in lepton candidate selection efficiency after each cut done using 0.2 million signal Monte Carlo events

by both the lepton momentum cut and the cut on $\cos\delta_{fl}$. The multiplicity of the lepton candidates is 1.02 (Fig. 4.3). Since there are very few ($\approx 2\%$) events, with more than one lepton, we reject such events.

Finally, the efficiency of selecting a tagging lepton is estimated to be 45% (Table 4.2). We do not use the variables described in Sec. 3.9 for signal to background discrimination for the lepton tagged sample since it is a very clean sample itself due to the requirement of a high-momentum lepton on the tag-side. We use a loose continuum suppression cut of $R_2 < 0.6$ to reduce the continuum background.

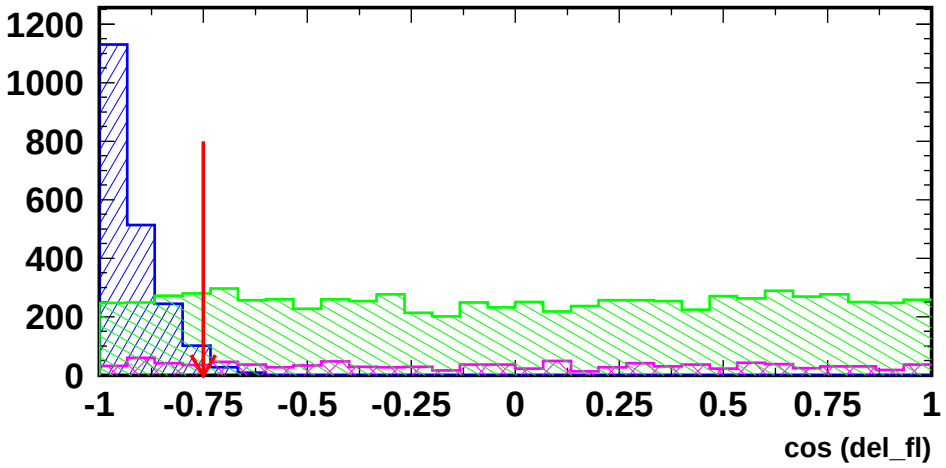

Figure 4.3: Cosine of the angle between the lepton and hard pion in $\Upsilon(4S)$ rest frame ($\cos\delta_{fl}$) distribution for tag-side (primary: green, secondary: magenta) and CP-side (secondary: blue) leptons, using 0.2 million signal Monte Carlo events.

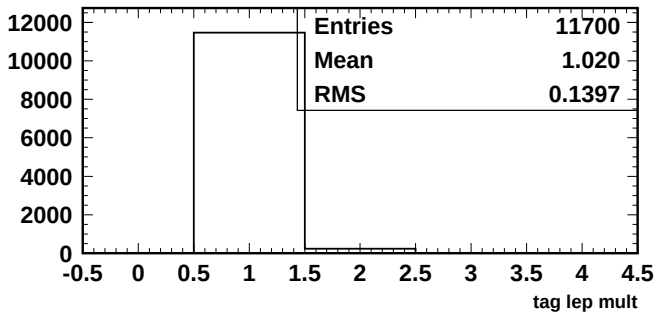

Figure 4.4: Multiplicity of the tag lepton candidate, using 0.2 million signal Monte Carlo events.

4.4 Yields with lepton tag

The probability to reconstruct a $D^*\pi$ candidate accompanied by a 'true' lepton that passes the tagging lepton selection criteria is 5 %. [1] The expected signal yield (Y) with lepton tag, quoted in Table 4.3 is obtained by using the expected efficiency (ϵ) of this tag as:

$$Y = \epsilon \times N_{B\bar{B}} \times BR(B \to D^*\pi) \times BR(D^* \to D^0\pi). \tag{4.1}$$

Purity (P) is defined as:

$$P = \frac{S}{S+B},$$

where S and B are the signal and total background yields in the signal box respectively.

The branching fractions of the decays, $B \to D^*\pi$ and $D^* \to D^0\pi$ are taken from PDG 2006 [25]. The major contribution to the uncertainty on the expected signal yield comes from the error on BR ($B \to D^{*+}\pi^-$), which is 0.21 ($\approx 7.6\%$). The error on the expected yield (σ_Y) is calculated as follows:

$$\sigma_Y = Y \times \sqrt{\left(\frac{\sigma(N_{B\bar{B}})}{N_{B\bar{B}}}\right)^2 + \left(\frac{\sigma(BR(B \to D^{*+}\pi^-))}{BR(B \to D^{*+}\pi^-)}\right)^2 + \left(\frac{\sigma(BR(D^{*+} \to D^0\pi^+))}{BR(D^{*+} \to D^0\pi^+)}\right)^2} \tag{4.2}$$

The branching fraction (BR) of $B^0 \to D^{*+}\pi^-$ is calculated using the following equation:

$$BR(B^0 \to D^{*+}\pi^-) = \frac{Y}{\epsilon \times N_{B\bar{B}} \times BR(D^* \to D^0\pi)}. \tag{4.3}$$

Statistical error (σ_{stat}) on this branching ratio is:

$$\sigma_{stat} = BR(B^0 \to D^{*+}\pi^-) \times \frac{\sigma_Y}{Y}. \tag{4.4}$$

where its systematic error (σ_{syst}) is:

$$\sigma_{syst} = BR(B^0 \to D^{*+}\pi^-) \times \sqrt{\left(\frac{\sigma(N_{B\bar{B}})}{N_{B\bar{B}}}\right)^2 + \left(\frac{\sigma(BR(D^{*+} \to D^0\pi^-))}{BR(D^{*+} \to D^0\pi^-)}\right)^2} \tag{4.5}$$

[1] A 'true' lepton means a real lepton from the tag side, but that does not necessarily mean that it gives correct flavour tag. Probability (B candidate exists in $B \to D^*\pi$; $D^* \to D^0\pi$) $\times$ probability (lepton exists in the tag side) $\times$ probability (lepton passes the tagging lepton selection criteria) $= 0.55 \times 0.208 \times 0.45 = 0.05$

4.4.1 Fit results with lepton tag using $D^*\pi$ signal, $D^*\rho$, correlated and correlated background

We use the background classification into $D^*\rho$, correlated and uncorrelated background to obtain the fit yield. Table 4.3 summarizes the fit results using SVD1, SVD2 and SVD1 + SVD2 data sets with lepton tag. Fig. 4.4.1 shows the projections in the signal region of the variables used in the yield fit for the three SVD samples using this tag.

From the signal MC study, the expected signal efficiencies in the entire fit region and the signal region (Table 4.1) with lepton tag for SVD1 are 3.9% and 3.8% respectively and for SVD2 are 4.5% and 4.3% respectively.
We obtain the branching fraction for $B^0 \to D^{*+}\pi^-$ to be $(2.51 \pm 0.02 \pm 0.04) \times 10^{-3}$ using 656.7 million $B\bar{B}$ pairs with lepton tag. Only the error in the number of $B\bar{B}$ pairs and the one in the branching fraction of $D^* \to D^0\pi$ are used in the systematic estimation of this BR. The branching fraction quoted by PDG, 2006 [25] for $B^0 \to D^{*+}\pi^-$ is $(2.76 \pm 0.21) \times 10^{-3}$. The purity obtained in the signal window using lepton tag is 59%.

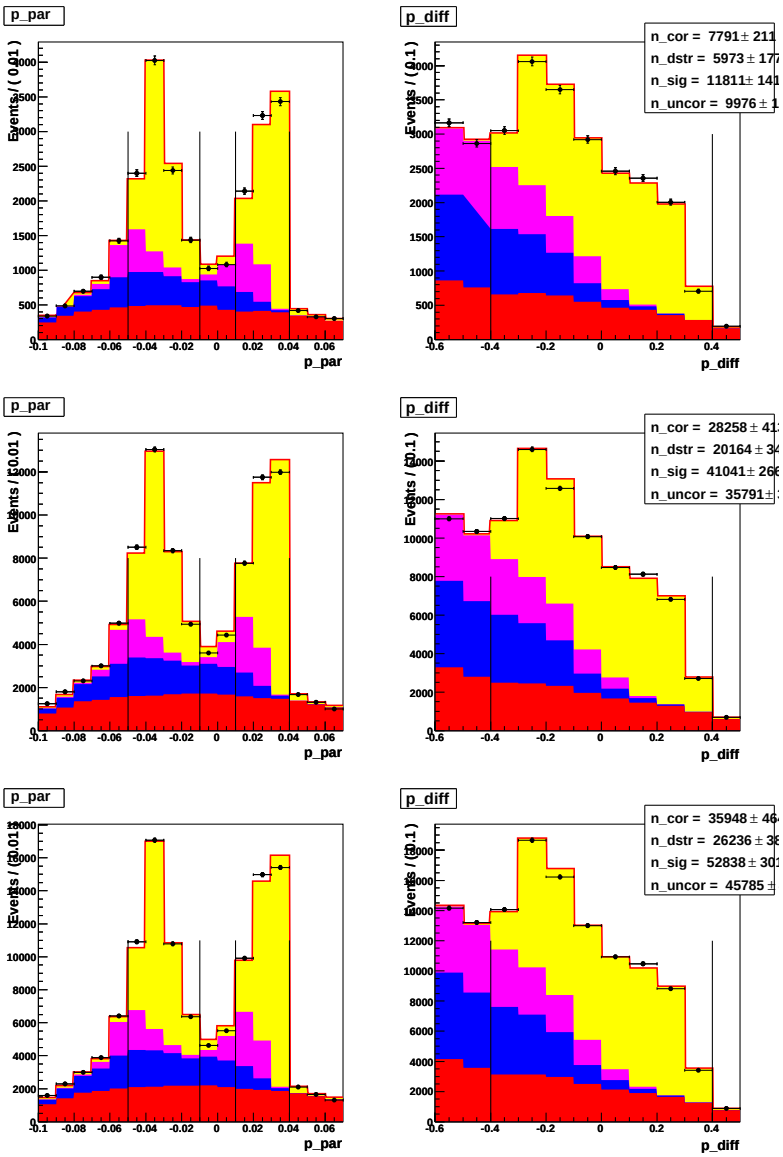

Figure 4.5: Results of fit yields to SVD1 (top), SVD2 (middle) and SVD1 + SVD2 (bottom) data, using lepton tag, projected onto the $p_{\|}$ (left) and p_{δ} (right) axes in the signal region of these variables. The contributions are: $D^*\pi$ (yellow), $D^*\rho$ (magenta), correlated background (blue) and uncorrelated background (red).

Component type	SVD1	SVD2	SVD1 + SVD2
Exp. range	7 - 27	31 - 55	7 - 55
Million $B\bar{B}$ pairs	152.0 ± 1.2	504.8 ± 8.9	656.7 ± 7.8
Entire fitting region			
Expected $D^*\pi$ signal	11094 ± 853	42251 ± 3295	51521 ± 3997
$D^*\pi$ signal	11811 ± 141	41041 ± 266	52838 ± 301
$D^*\rho$ background	5973 ± 177	20164 ± 342	26236 ± 385
Correlated background	7791 ± 211	28258 ± 413	35948 ± 464
Uncorrelated background	9976 ± 192	412379 ± 366	45785 ± 414
Signal region			
Expected $D^*\pi$ signal	10866 ± 835	40641 ± 3169	49918 ± 3872
$D^*\pi$ signal	11275 ± 135	38989 ± 253	50196 ± 286
$D^*\rho$ background	2370 ± 70	7864 ± 133	10232 ± 150
Correlated background	2201 ± 60	8195 ± 120	10425 ± 135
Uncorrelated background	3167 ± 61	11095 ± 113	14193 ± 128
Purity (in %)	59.3 ± 0.7	58.9 ± 0.5	59.0 ± 0.4
BR($D^*\pi$)($\times 10^{-3}$)	$2.74 \pm 0.04 \pm 0.03$	$2.48 \pm 0.02 \pm 0.05$	$2.51 \pm 0.02 \pm 0.04$

Table 4.3: Yields in SVD1, SVD2 and SVD1 + SVD2 data using lepton tag. Only the error in the number of $B\bar{B}$ pairs and the one in the branching fraction of $D^* \to D^0\pi$ are used in the systematic error calculation of the BR ($B \to D^*\pi$).

4.4.2 Yields with lepton tag using $D^*\pi$ signal, $D^*\rho$, generic and continuum Monte-Carlo background

In this subsection, we obtain the $D^*\pi$ signal yield using the background classification into $D^*\rho$, generic and continuum Monte-Carlo background. This is done in order to compare the fit yields using the background classification into $D^*\rho$, correlated and uncorrelated background with the current one.

Table 4.4 summarizes the fit results using SVD1, SVD2 and SVD1 + SVD2 data sets with lepton tag. Fig. 4.4.2 shows the projections in the signal region of the variables used in the yield fit for the three SVD samples using this tag.

We obtain the branching fraction for $B^0 \to D^{*+}\pi^-$ to be $(2.54\pm0.01\pm0.04)\times10^{-3}$ using 534.59 million $B\bar{B}$ pairs with lepton. Only the error in the number of $B\bar{B}$ pairs and the one in the branching fraction (BR) of $D^* \to D^0\pi$ are used in the systematic estimation of this BR. The branching fraction quoted by PDG, 2006 [25] for $B^0 \to D^{*+}\pi^-$ is $(2.76 \pm 0.21) \times 10^{-3}$. The purity obtained in the signal window using lepton tag is 59%.

We observe that we obtain similar signal yields and purity using both the background classifications yield, as expected. We use the signal yield obtained using the background classification in previous subsection for our time-dependent analysis because the discrimination between the three background components in the kinematic variables is better in this case.

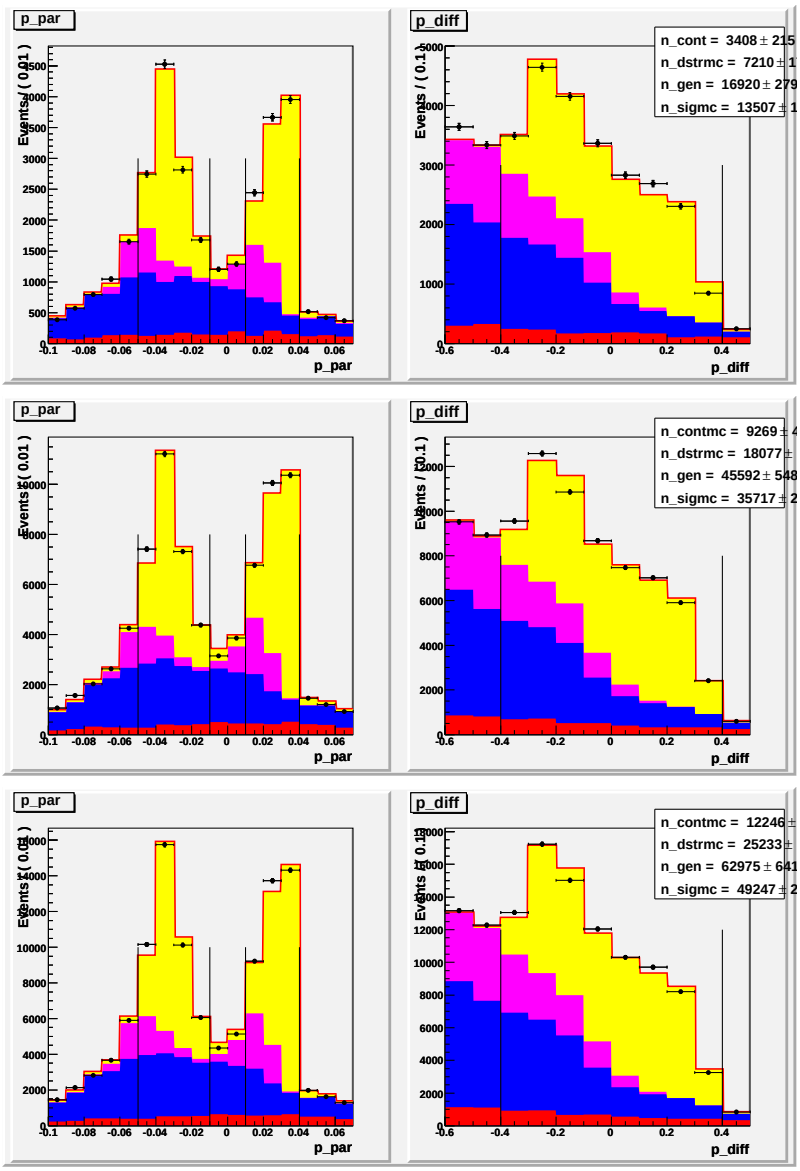

Figure 4.6: Results of kinematic fits to SVD1 (top) and SVD1 + SVD2 (bottom) data, using lepton tag, projected onto the $p_{\parallel}$ (left) and p_{δ} (right) axes in the signal region of these variables. The contributions are: $D^*\pi$ (yellow), $D^*\rho$ (magenta), $B\bar{B}$ background (blue) and continuum background (red).

Component type	SVD1	SVD2	SVD1 + SVD2
Exp. range	7 - 27	31 - 49	7 - 49
Million $B\bar{B}$ pairs	152.0 ± 1.2	382.6 ± 5.6	534.6 ± 7.0
Entire fitting region			
Expected $D^*\pi$ signal	13690 ± 1052	39497 ± 3080	53186 ± 4126
$D^*\pi$ signal	13507 ± 156	35717 ± 248	49247 ± 288
$D^*\rho$ background	7211 ± 191	18077 ± 308	25233 ± 347
$B\bar{B}$ background	16920 ± 287	45592 ± 548	62975 ± 600
Continuum background	3408 ± 232	9269 ± 405	12246 ± 448
Signal region			
Expected $D^*\pi$ signal	13404 ± 1031	38060 ± 2968	51465 ± 3992
$D^*\pi$ signal	12832 ± 147	33574 ± 233	46292 ± 273
$D^*\rho$ background	2884 ± 80	6689 ± 114	9589 ± 136
$B\bar{B}$ background	5076 ± 98	14134 ± 170	18893 ± 192
Continuum background	1091 ± 84	2873 ± 126	3919 ± 155
Purity (in %)	58.6 ± 0.8	58.6 ± 0.5	58.8 ± 0.4
BR($D^*\pi$)($\times 10^{-3}$)	$2.71 \pm 0.03 \pm 0.03$	$2.49 \pm 0.02 \pm 0.04$	$2.54 \pm 0.01 \pm 0.04$

Table 4.4: Yields in SVD1, SVD2 and SVD1 + SVD2 data using lepton tag. Only the error in the number of $B\bar{B}$ pairs and the one in the branching fraction of $D^* \to D^0\pi$ are used in the systematic error calculation of the BR ($B \to D^*\pi$).

4.5 Tagging kaon

The probability that a 'true' charged kaon [2] exists in the tag side is $\approx 40\%$ (Appendix 2). The tagging selection criteria are listed in Table 4.5.

Fig. 4.7 shows the momentum distribution in $\Upsilon(4S)$ rest frame and the impact

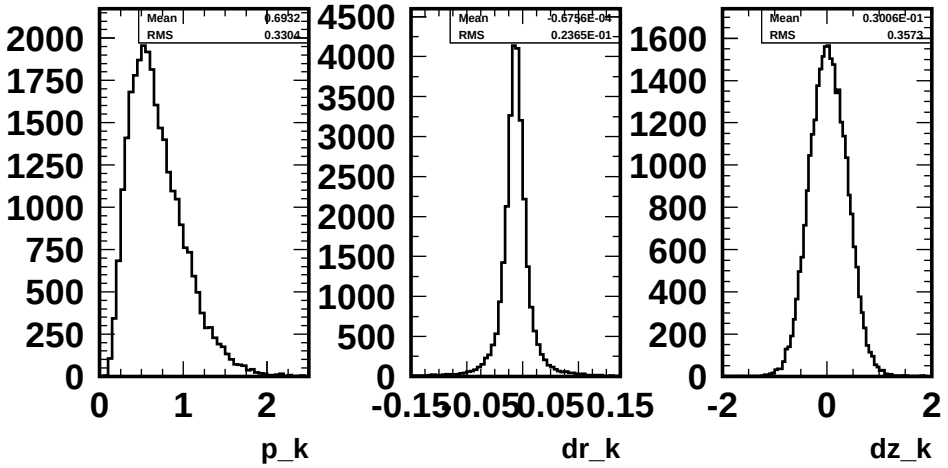

Figure 4.7: Momentum and impact parameters dr, dz of kaon from the tag side in $\Upsilon(4S)$ rest frame, using 0.2 million signal Monte Carlo events.

parameters, dr and dz for the true tagged kaons.

A cut on the cosine of the angle between the kaon and hard pion ($\cos\delta_{fk}$) is made to reduce contamination from CP-side, similar to lepton case. This variable is the best handle to discriminate between kaons from tag-side and those from CP-side but does not help to distinguish between the pions and kaons from the tag-side.

Table 4.6 shows the true origin of the kaon candidate selected after the flavour tagging selection. The purity of the true tag-side kaons, defined as the ratio of the number of true tag-side kaons and the total number of kaons is $\approx 80\%$. About 10% of the kaons are fake kaons, which mainly consists of pions, electrons, muons or protons from either the CP-side or the tag-side, but mainly tag-side. We veto the muons, electrons and protons to reduce the number of fake kaon candidates by

[2] A 'true' kaon means a real kaon from the tag side, but that does not necessarily mean that it gives correct flavour tag.

Quantity	Requirement	Number	Efficiency (in %)
No cuts		2140	100.0
R_2	< 0.4	1932	90.3
Momentum	$0.0 < p_k/\mathrm{GeV}/c$	1932	90.3
Muon probability	< 0.80	1905	89.04
Electron probability	< 0.80	1884	88.1
Proton probability	< 0.80	1849	86.4
Kaon probability	> 0.80	1658	77.5
SVD hits in layers 2 to 4 (SVD2 data)	≥ 2		
SVD hits (r - ϕ plane)	≥ 2		
SVD hits (z plane)	≥ 2	1491	69.7
Closest approach to IP (r) (dr_k)	< 0.15 cm		
Closest approach to IP (z) (dz_k)	< 2.0 cm	171	68.8
Lab polar angle (θ_{lab})	$23^\circ < \theta_{lab} < 139^\circ$ (SVD1)		
	$17^\circ < \theta_{lab} < 150^\circ$ (SVD2)	1467	68.6
Angle between kaon and fast pion	$\cos\delta_{fk} > -0.5$	1108	51.8

Table 4.5: Summary of tagging kaon cuts along with the number of kaon candidates left and the reduction in kaon candidate selection efficiency after each cut done using 0.2 million signal Monte Carlo events

requiring a cut on their probabilities to be smaller than 0.8. The muon veto rejects $\approx 44\%$ muons, electron veto rejects $\approx 69\%$ electrons and the proton veto rejects $\approx 97\%$ protons. These three cuts affect the tag-side kaons (secondary kaons from the tag-side) by less than a percent only.

We require a tight cut on the kaon probability (> 0.80) in order to reduce the number of pions, that fake as kaon candidates. We lose $\approx 11\%$ of the kaon candidates by this cut.

In Fig. 4.8, we show the contributions from the kaons from tag-side and CP-side separately. The kaons from CP-side peak at -1 in $\cos\delta_{fk}$, since the hard pion and kaon will be nearly back-to-back in $\Upsilon(4S)$ rest frame. On the contrary, since the kaons from tag-side can be in any direction with respect to the hard pion, $\cos\delta_{fk}$ is flat for such kaons. We reduce the secondary kaons from CP-side by the $\cos\delta_{fk}$ cut.

For 14% of the events, we have more than one kaon candidate (Fig. 4.9). For events, that have multiple kaon candidates, we choose the candidate that has the largest $\cos\delta_{fk}$ as the kaons from the CP-side peak at -1 in the $\cos\delta_{fk}$ distribution. The probability to select the true tag-kaon with this best candidate selection proce-

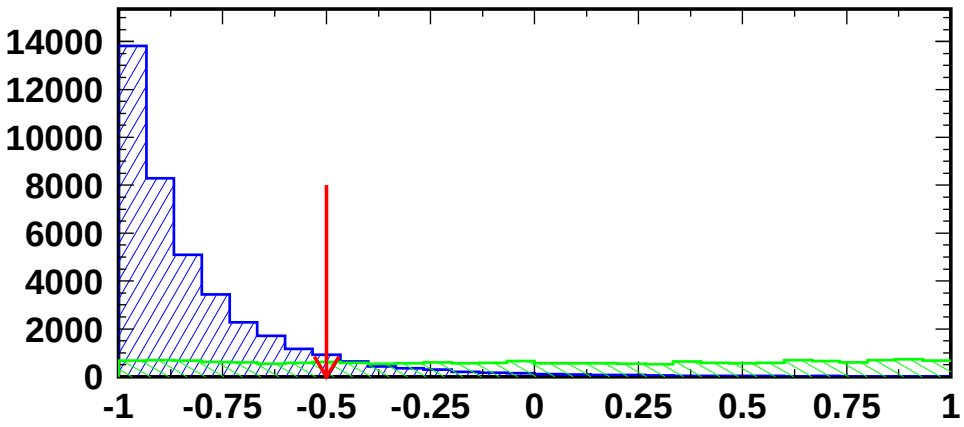

Figure 4.8: Cosine of the angle between the kaon and hard pion in $\Upsilon(4S)$ rest frame ($\cos\delta_{fk}$) distribution for kaons from both tag-side and CP-side (blue: CP-side, green: tag-side), using 0.2 million signal Monte Carlo events.

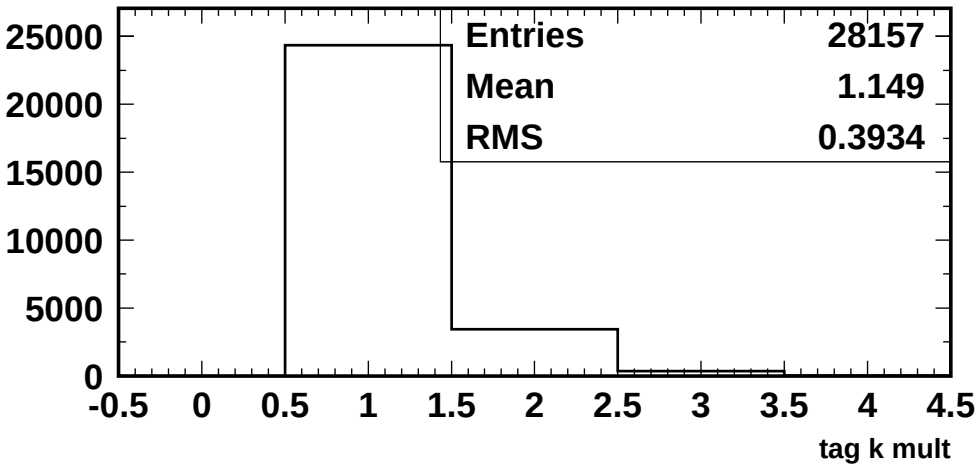

Figure 4.9: Multiplicity of the tag kaon candidate, using 0.2 million signal Monte Carlo events.

True origin	Amount (in %)
Tag-side kaons	80.4
CP-side kaons	9.7
Tag-side pions	7.6
CP-side pions	0.4
Others	1.8

Table 4.6: True origin of the kaon candidate selected for the flavour tagging

dure is $\approx 95\%$.

The efficiency of selecting correctly a tagging kaon is then estimated to be $\sim 52\%$ after all the tagging kaon selection cuts are applied. In the kaon-tagged sample, we can use the variables that we developed for signal to background discrimination. However, we use a tighter continuum suppression cut of $R_2 < 0.4$ to reduce the continuum background and hence, the requirements on the other discriminating variables are not used.

4.6 Yields with kaon tag

4.6.1 Yields with kaon tag using $D^*\pi$ signal, $D^*\rho$, correlated and correlated background

We use the background classification into $D^*\rho$, correlated and uncorrelated background to obtain the fit yield. Table 4.7 summarizes the fit results using SVD1, SVD2 and SVD1 + SVD2 data sets with kaon tag. Fig. 4.10 shows the projections in the signal region of the variables used in the fit for obtaining $D^*\pi$ yield for the three SVD samples, using kaon tag.

From the signal MC study, the expected signal efficiencies in the entire fit region and the signal region (Table 4.1) with kaon tag in SVD1 sample are 10.8% and 10.3% respectively and in SVD2 sample are 12.3% and 11.8% respectively.

The probability that a true tag-side kaon is selected is 11.2%.[3]

The purity obtained in the signal window using kaon tag is 38%. We obtain a branching ratio of $(3.11 \pm 0.01 \pm 0.04) \times 10^{-3}$ for $B \to D^*\pi$ with kaon using 656.7

[3]Probability (B candidate exists) $\times$ probability (kaon exists in the tag side) $\times$ probability (kaon passes the tagging kaon selection criteria) $= 0.55 \times 0.40 \times 0.51 = 0.112$.

million $B\bar{B}$ pairs.

Component type	SVD1	SVD2	SVD1 + SVD2
Exp. range	7 - 27	31 - 55	7 - 55
Million $B\bar{B}$ pairs	152.0 ± 1.2	504.8 ± 8.9	656.7 ± 7.8
Entire fitting region			
Expected $D^*\pi$ signal	30801 ± 2368	116522 ± 9087	142360 ± 11043
$D^*\pi$ signal	32700 ± 291	116523 ± 563	148866 ± 633
$D^*\rho$ background	17327 ± 393	57634 ± 760	74984 ± 858
Correlated background	19475 ± 492	75670 ± 952	94274 ± 1073
Uncorrelated background	111034 ± 580	412379 ± 1117	523567 ± 1258
Signal region			
Expected $D^*\pi$ signal	29375 ± 2258	111785 ± 8717	136197 ± 10565
$D^*\pi$ signal	31009 ± 276	110406 ± 533	141110 ± 600
$D^*\rho$ background	6775 ± 154	22339 ± 295	28149 ± 322
Correlated background	5461 ± 138	21959 ± 276	27104 ± 308
Uncorrelated background	37596 ± 196	134898 ± 365	11095 ± 423
Purity (in %)	38.4 ± 0.4	38.1 ± 0.3	37.9 ± 0.2
BR($D^*\pi$)($\times 10^{-3}$)	$3.28 \pm 0.03 \pm 0.04$	$3.08 \pm 0.01 \pm 0.05$	$3.11 \pm 0.01 \pm 0.04$

Table 4.7: Yields in SVD1, SVD2 and SVD1 + SVD2 data using kaon tag. Only the error in the number of $B\bar{B}$ pairs and the one in the branching fraction of $D^* \to D^0\pi$ are used in the systematic error calculation of the BR ($B \to D^*\pi$).

4.6.2 Yields with kaon tag using $D^*\pi$ signal, $D^*\rho$, generic and continuum Monte-Carlo background

In this subsection, we obtain the $D^*\pi$ signal yield using the background classification into $D^*\rho$, generic and continuum Monte-Carlo background.
Table 4.8 summarizes the fit results using SVD1, SVD2 and SVD1 + SVD2 data sets with kaon tag. Fig. 4.8 shows the projections in the signal region of the variables used in the kinematic fit for the three SVD samples, using kaon tag.

We observe that we obtain similar signal yields and purity using both the background classifications yield, as expected.

The purity obtained in the signal window using kaon tag is 39%. We obtain a branching ratio of $(2.84 \pm 0.01 \pm 0.04) \times 10^{-3}$ for $B \to D^*\pi$ with kaon using 534.59

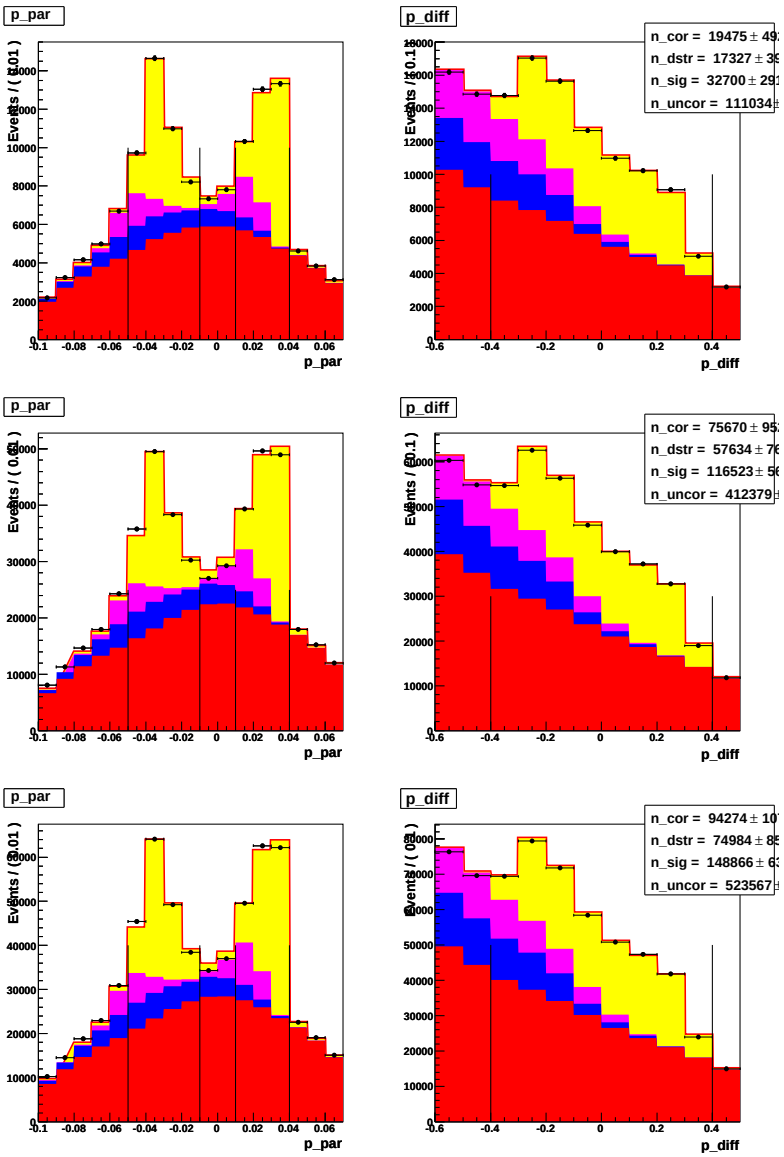

Figure 4.10: Results of yield fits to SVD1 (top), SVD2 (middle) and SVD1 + SVD2 (bottom) data, using kaon tag, projected onto the $p_{\|}$ (left) and p_{δ} (right) axes in the signal region of these variables. The contributions are: $D^*\pi$ (yellow), $D^*\rho$ (magenta), correlated background (blue) and uncorrelated background (red).

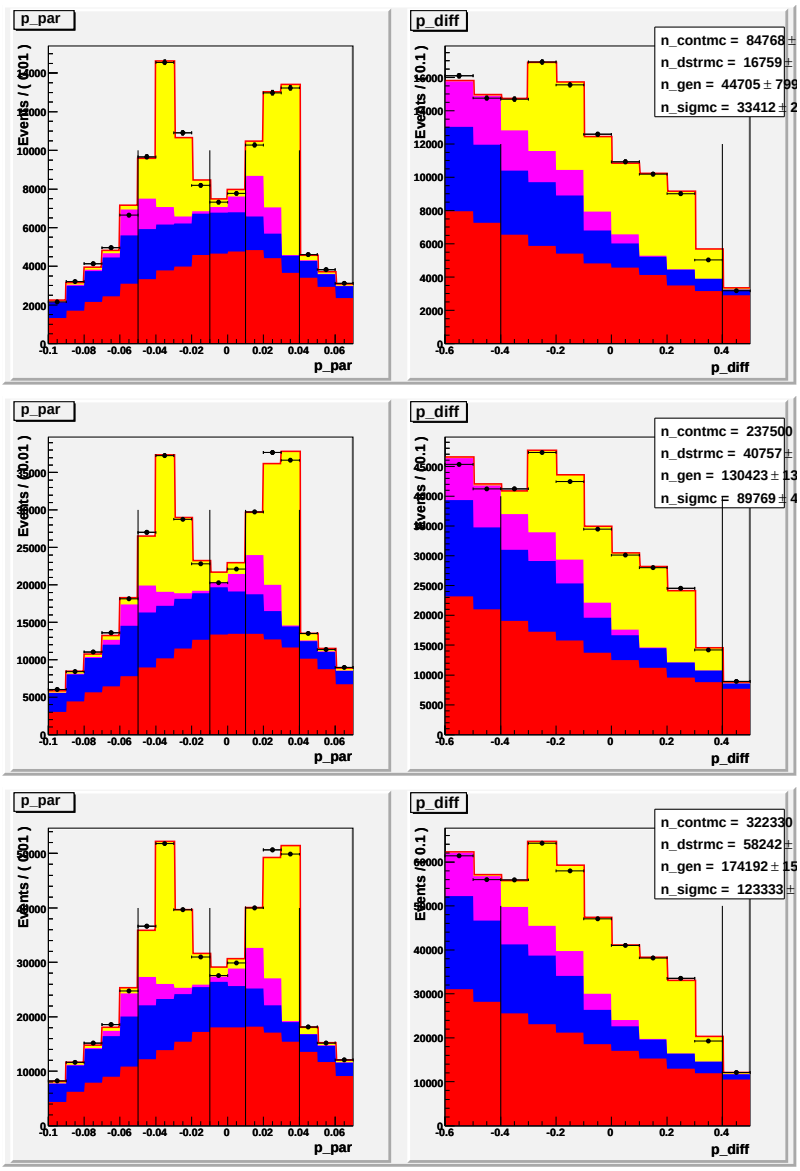

Figure 4.11: Results of kinematic fits to SVD1 (top) and SVD1 + SVD2 (bottom) data, using kaon tag, projected onto the $p_{\|}$ (left) and p_{δ} (right) axes in the signal region of these variables. The contributions are: $D^*\pi$ (yellow), $D^*\rho$ (magenta), $B\bar{B}$ background (blue) and continuum background (red).

Component type	SVD1	SVD2	SVD1 + SVD2
Exp. range	7 - 27	31 - 49	7 - 49
Million $B\bar{B}$ pairs	152.0 ± 1.2	382.6 ± 5.6	534.6 ± 7.0
Entire fitting region			
Expected $D^*\pi$ signal	30801 ± 2368	88329 ± 6888	119130 ± 9241
$D^*\pi$ signal	33412 ± 291	89769 ± 500	123333 ± 576
$D^*\rho$ background	16759 ± 373	40757 ± 593	58242 ± 716
$B\bar{B}$ background	44705 ± 799	130423 ± 1282	174192 ± 1537
Continuum background	84768 ± 789	237500 ± 1299	322330 ± 1531
Signal region			
Expected $D^*\pi$ signal	29375 ± 2258	84738 ± 6608	114114 ± 8852
$D^*\pi$ signal	31741 ± 276	82485 ± 465	115933 ± 541
$D^*\rho$ background	6536 ± 145	15488 ± 225	22132 ± 272
$B\bar{B}$ background	13412 ± 240	39127 ± 385	52258 ± 461
Continuum background	28821 ± 268	83125 ± 455	109592 ± 521
Purity (in %)	39.4 ± 0.4	37.7 ± 0.2	38.7 ± 0.2
BR($D^*\pi$)($\times 10^{-3}$)	$3.03 \pm 0.03 \pm 0.03$	$2.76 \pm 0.02 \pm 0.05$	$2.84 \pm 0.01 \pm 0.04$

Table 4.8: Yields in SVD1, SVD2 and SVD1 + SVD2 data using kaon tag. Only the error in the number of $B\bar{B}$ pairs and the one in the branching fraction of $D^* \to D^0\pi$ are used in the systematic error calculation of the BR ($B \to D^*\pi$).

million $B\bar{B}$ pairs.

4.7 Summary on $D^*\pi$ signal yield using lepton and kaon tag

Tables 4.9 summarizes the signal yields obtained by previous Belle [23] (using lepton tag only), BaBar [19] (using both lepton and kaon tag) and current Belle analyses respectively. The $D^*\pi$ signal yields are quoted in the table.

Tag type	Expt.	$B\bar{B}$ pairs	Signal yield	Purity (in signal region)
Lepton	Belle	386	21773 ± 214	66%
Lepton	BaBar	232	18710 ± 270	54%
Kaon	BaBar	232	70580 ± 660	31%
Lepton	Belle	657	50196 ± 286	59%
Kaon	Belle	657	141110 ± 600	38%

Table 4.9: Summary of previous Belle and BaBar (top) and current Belle (bottom) signal yields, using lepton and kaon tag

The signal yield per $N_{B\bar{B}}$ obtained by the current analysis with lepton tag is $\approx$ 35% more than the previous Belle analysis. We use looser cuts on polar angle (θ_{lab}) for hard pions (Table 3.6) and tagging leptons (Table 4.2) and dr_s (Table 3.7), and gain $\approx$ 20% due to it. We gain another $\approx$ 10% due to looser selection of signal window. Our signal yield per $N_{B\bar{B}}$ and purity in $D^*\pi$ with lepton tag are similar to those obtained by BaBar.

The signal yield per $N_{B\bar{B}}$ obtained by the current analysis with kaon tag is $\approx$ 29% less than the previous BaBar analysis.[4] The purity in $D^*\pi$ with kaon tag is higher than that obtained by BaBar.

[4]This could be due to the fact that BaBar has better kaon identification than Belle. Also, the kaon selection criteria used by BaBar may be looser than Belle.

Chapter 5

Time dependent analysis of $B \to D^*\pi$ decays

5.1 Fit procedure to measure CP violation parameters $S^{\pm}$

We perform a maximum likelihood fit in Δz distribution using the lepton tagged candidates, which are in signal region of the variables p_δ and $p_\parallel$ on the third variable, $p_\perp$ ($p_\perp < 0.05$ GeV/c) in order to measure the CP violation parameters in the $D^*\pi$ sample. We minimize the following likelihood function in this fit in order to obtain the CP violation parameters $S^{\pm}$:

$$-2\ln\mathcal{L} = -2\sum_{\mathrm{i}} \ln\mathcal{L}_{\mathrm{i}},$$

$$\mathcal{L}_i = f_{D^*\pi}P_{D^*\pi} + f_{D^*\rho}P_{D^*\rho} + f_{unco}P_{unco} + f_{corr}P_{corr} \tag{5.1}$$

Here, $f_{D^*\pi}$, $f_{D^*\rho}$, f_{unco}, f_{corr} are the event-by-event fractions of $D^*\pi$ signal, $D^*\rho$, uncorrelated and correlated backgrounds respectively, that are obtained using the two-dimensional yield fit done with the variables p_δ and $p_\parallel$ such that $f_{D^*\pi} + f_{D^*\rho} + f_{unco} + f_{corr} = 1$. $P_{D^*\pi}$, $P_{D^*\rho}$, P_{unco}, P_{corr} are the probability distribution functions (PDF) for $D^*\pi$ signal, $D^*\rho$, uncorrelated and correlated backgrounds respectively. In these PDFs, the experimental effects are taken into account by the shapes of the resolution functions, R_k, R_{det}, R_{np} are the shapes of the resolution functions due to the kinematic smearing, detector resolution and the finite lifetime of non-primary tracks in the tag-side such as D-meson respectively. The resolution functions are described in detail in the next three sections.

The signal and background PDFs (Eq. 5.1) have two parts, one for the correctly tagged $D^*\pi$ events and the other for incorrectly tagged or wrong tagged $D^*\pi$ events.

A $D^*\pi$ event is correctly tagged when the flavour of tag-side B is measured correctly and incorrectly tagged when it is not, based on the charge of the high-momentum tagging lepton. If the charge of the tagging lepton is positive, the tag-side B is a B^0 and it is $\bar{B}^0$ otherwise. The wrong-tag fractions w^+ and w^- are the probabilities to incorrectly measure the flavour of tagging B^0 and $\bar{B}^0$ mesons respectively. The quantity $w^\pm$ is called the wrong-tag fraction for the tagging leptons.

We define two quantities w_{Loss} and w_{Gain} related to $w^\pm$ as follows:

$$\begin{aligned} w_{Loss} &= w^+, q_l > 0 \\ &= w^-, q_l < 0 \\ w_{Gain} &= w^-, q_l > 0 \\ &= w^+, q_l < 0 \end{aligned} \tag{5.2}$$

where q_l is the charge of the tagging lepton.

Mistagging is taken into account the PDFs of $B \to D^*\pi$ signal using negatively-charged (${l_{tag}}^-$) and positively-charged (${l_{tag}}^+$) leptons, called $P(l^-_{tag}, \pi^\pm_f)$ and $P(l^+_{tag}, \pi^\pm_f)$ respectively as:

$$\begin{aligned} P(l^-_{tag}, \pi^\pm_f) &= (1 - w^-)P(B^0 \to D^{(*)\mp}\pi^\pm) + w^+ P(\bar{B}^0 \to D^{(*)\mp}\pi^\pm) \\ P(l^+_{tag}, \pi^\pm_f) &= (1 - w^+)P(B^0 \to D^{(*)\mp}\pi^\pm) + w^- P(\bar{B}^0 \to D^{(*)\mp}\pi^\pm) \end{aligned} \tag{5.3}$$

where w^+ and w^- are the 'wrong-tag fractions' and $P(B^0 \to D^{(*)\mp}\pi^\pm)$ is the PDF for $B \to D^*\pi$ signal.

The signal and background PDF's are defined below:

- Probability distribution function for $D^*\pi$ ($P_{D^*\pi}$)

  The signal PDF is given by the following equation:

$$P_{D^*\pi} = (1 - w_{Loss})P^{CT}_{mix} + w_{Gain}P^{WT}_{mix} \tag{5.4}$$

  w_{Loss} and w_{Gain} are defined in Eq. 5.2. P^{CT}_{mix} and P^{WT}_{mix} are defined as:

$$P^{CT}_{mix} = \frac{e^{-|\Delta z/\beta\gamma c|}/\tau_{B^0}}{8\tau_{B^0}}[1 - q_f q_l cos(\Delta m \frac{\Delta z}{\beta\gamma c}) + q_l S^{-q_f} sin(\Delta m \frac{\Delta z}{\beta\gamma c})] \otimes \mathcal{R}_{det} \otimes \mathcal{R}_k \tag{5.5}$$

The symbol $\otimes$ in Eqn. 5.5 stands for a mathematical operator called "convolution" that expresses the amount of overlap of one function as it is shifted over another function.[1]

$$P_{mix}^{WT} = P_{mix}^{CT} \otimes \mathcal{R}_{np} \tag{5.6}$$

In the nomenclature of P_{mix}^{CT} and P_{mix}^{WT}, CT and WT stands for correctly and incorrectly or wrong tagged $D^*\pi$ events.

We obtain the definition of P_{mix}^{CT} from the probability that a state produced at time 0 as a B^0 or $\bar{B}^0$ decays into the final state $D^{(*)\mp}\pi^{\pm}$ at a given time t (given by Eq. 1) taking into account the experimental effects by using the resolution functions. This decay probability can be summarized as:

$$\begin{aligned}
\Gamma(B^0 \to D^{(*)\pm}\pi^{\mp}) &= \tfrac{(e^{-|\Delta t|/\tau_{B^0}})}{8\tau_{B^0}}[1 \mp \cos(\Delta m \Delta t) - S^{\pm}\sin(\Delta m \Delta t)], \\
\Gamma(\bar{B}^0 \to D^{(*)\pm}\pi^{\mp}) &= \tfrac{(e^{-|\Delta t|/\tau_{B^0}})}{8\tau_{B^0}}[1 \pm \cos(\Delta m \Delta t) + S^{\pm}\sin(\Delta m \Delta t)],
\end{aligned} \tag{5.7}$$

where Δm is the B^0-$\bar{B}^0$ mixing frequency ,
Δt $(= \Delta z/\beta\gamma c)$ is the difference between the times of the decays of the CP-side B meson and the tag-side B meson,
$S^{\pm} = -(2R/1+R^2)\sin(2\phi_1 + \phi_3 \pm \delta)$.
R and δ are the ratio of the magnitudes and the strong phase difference of the DCSD and CFD amplitudes, respectively.

- Probability distribution function for $D^*\rho$ $(P_{D^*\rho})$

The $D^*\rho$ background PDF is given by the following equation:

$$P_{D^*\rho} = (1 - w_{Loss})P_{mix}^{CT} + w_{Gain}P_{mix}^{WT} \tag{5.8}$$

w_{Loss}, w_{Gain}, P_{mix}^{CT} and P_{mix}^{WT} are defined in Eqs. 5.2, 5.7 and 5.5. These quantities are similar to the ones used for signal PDF.

In $P_{D^*\rho}$, CP violation parameters, $S^{\pm}$ are constrained to be zero. Hence, for $P_{D^*\rho}$, P_{mix}^{CT} reduces to:

$$P_{mix}^{CT} = \frac{e^{-|\Delta z/\beta\gamma c|}/\tau_{B^0}}{8\tau_{B^0}}[1 - q_f q_l cos(\Delta m_d \frac{\Delta z}{\beta\gamma c})] \otimes \mathcal{R}_{det} \otimes \mathcal{R}_k \tag{5.9}$$

[1] A convolution is defined as a product of functions a and b over a finite range $[0, x]$ is given by:

- Probability distribution function for correlated background (P_{corr})

  The correlated background PDF is given by the following equation:

$$P_{corr} = (1 - w_{Loss})(f_{mix}P^{CT}_{mix} + (1 - f_{mix})P^{CT}_{chg}) + w_{Gain}(f_{mix}P^{WT}_{mix} + (1 - f_{mix})P^{WT}_{chg}) \quad (5.10)$$

  Here, P stands for PDF; f_{BB} is the fraction of $B\bar{B}$ events; f_{mix} is the fraction of neutral B events in the $B\bar{B}$ contributions; CT and WT denote the correct-tag and wrong-tag contributions respectively.
  The wrong-tag fractions w_{Loss}, w_{Gain} and the PDF's for the mixed-type events in the correlated background P^{CT}_{mix} and P^{WT}_{mix} are defined in Eqs. 5.2, 5.7 and 5.5. P^{CT}_{chg} and P^{WT}_{chg} are the PDFs for the charged-type events in the correlated background and are defined as:

$$P^{CT}_{chg} = \frac{e^{-|\Delta z/\beta\gamma c|}/\tau_{B^+}}{2\tau_{B^+}} \otimes \mathcal{R}_{det} \otimes \mathcal{R}_k \quad (5.11)$$

$$P^{WT}_{chg} = P^{CT}_{chg} \otimes \mathcal{R}_{np} \quad (5.12)$$

- Probability distribution function for uncorrelated background (P_{unco})

  The uncorrelated background PDF is given by the following equation:

$$P_{unco} = (1 - f_{BB})P_{cont} + f_{BB}[(1 - w_{Loss})(f_{mix}P^{CT}_{mix} + (1 - f_{mix}) P^{CT}_{chg})] + f_{BB}[w_{Gain}(f_{mix}P^{WT}_{mix} + (1 - f_{mix})P^{WT}_{chg})] \quad (5.13)$$

$$P_{cont} = \frac{1 + q_f q_l A_{qq}}{4}[f_\delta\delta + (1 - f_\delta)\frac{1}{\beta\gamma c\tau_{qq}}e^{-|\Delta z|/\beta\gamma c\tau_{qq}}] \otimes \mathcal{R}_{det} \quad (5.14)$$

  Here, the event variables q_f and q_l are the charges of the fast pion and the tagging lepton respectively; A_{qq} accounts for possible asymmetry in the continuum contribution to the same-sign and opposite-sign events; τ_{qq} is the average lifetime of the charm contribution in the continuum (close to the average D mesons lifetime); R_{det} is the resolution functions due to the detector resolution.

The time-difference Δt is related to the measured quantity Δz, with additional consideration to possible offsets in the mean value of Δz,

$$\Delta t \approx (\Delta z + \epsilon_{\Delta z})/\beta\gamma c \tag{5.15}$$

It is necessary to allow non-zero values of offsets $\epsilon_{\Delta z \pm\pm}$ in the PDFs:

$$\Delta z_{true} = (\Delta z_{CP} + \epsilon_{\Delta z \pm\pm}) \otimes \mathcal{R} \tag{5.16}$$

because a small bias can mimic the effect of CP violation:

$$cos(\Delta m \Delta t) \rightarrow cos(\Delta m \Delta t) - \Delta m \epsilon_{\Delta t} sin(\Delta m \Delta t) \tag{5.17}$$

Even a bias as small as $\epsilon_{\Delta t} \sim 1\mu m$ can lead to sine-like terms as large as 0.01, of the order of expected CP violation effect. Furthermore, since in this partial reconstruction method, both the vertex positions are obtained from single tracks, the analysis is more susceptible to such vertexing biases. Hence, we apply a small correction to each vertex position to correct for a known bias due to the relative misalignment of the SVD and the CDC in SVD1 data. Since the alignment in SVD2 data was found to be comparable to the corrected SVD1 data, no additional corrections are applied to SVD2 data. We allow separate offsets for each combination of fast pion and tagging lepton track.

In order to test the fitting procedure, fits are performed with Δm and τ_{B^0} floated and $S^{\pm}$ fixed to zero. We determine B^0 lifetime, τ_{B^0} and $B^0\bar{B}^0$ mixing frequency, Δm and the mixing asymmetry, defined as:

$$A^{mix} = \frac{N^{OF} - N^{SF}}{N^{OF} + N^{SF}} \tag{5.18}$$

Here, N^{SF} and N^{OF} are the number of same-flavour and opposite-flavour candidates.

To display the CP violation effect, we define same-flavour (SF) and opposite-flavour (OF) (Table 5.1) asymmetries as:

$$A^{SF} = \frac{N^{--} - N^{++}}{N^{--} + N^{++}}, A^{OF} = \frac{N^{+-} - N^{-+}}{N^{+-} + N^{-+}} \tag{5.19}$$

Here, N^{--} and N^{++} are the number of same-flavour candidates and N^{+-} and N^{+-} are the number of opposite-flavour candidates. (We use the following convention: $N^{q_f q_l}$.) Same-flavor and opposite-flavor candidates are the candidates where the charges of the fast pion track and the tagging lepton track are same and opposite respectively (Table 5.1).

Type	q_f	q_l
SF	-	-
OF	+	-
OF	-	+
SF	+	+

Table 5.1: Four possible charge-flavour combination using q_f and q_l. q_f and q_l are the charges of the fast pion track and the tagging lepton track respectively. The charge of the tagging lepton determines the flavour of the B.

5.2 Resolution functions

We want to obtain $S^{\pm}$ using the lepton-tagged sample. Hence, we use the lepton-tagged events for the determination of the shapes of the resolution function parameters, R_k, R_{det}, R_{np} due to the kinematic smearing, detector resolution and the finite lifetime of non-primary tracks in the tag-side such as D-meson respectively.

5.2.1 Determination of $\mathcal{R}_k$ parameters

We use the standard Belle package for vertex resolution, "tatami", to describe the kinematic smearing effect. This smearing is due to the fact that we use the approximation: $\Delta t \approx \Delta z/\beta\gamma c$. Hence, this parametrization is, as a function of x = $\Delta z_{gen}/\beta\gamma c - \Delta t_{gen}$, which is the difference between Δt obtained using the above approximation and the true Δt.

$$\mathcal{R}_k(x) = \int [(1-f_k)E_{np}(x', \tau^1_{kp}, \tau^1_{kn}) + f_k E_{np}(x', \tau^2_{kp}, \tau^2_{kn})] \frac{e^{-(x-x')^2/2\sigma_k^2}}{\sqrt{2\pi\sigma_k^2}} dx' \quad (5.20)$$

$$\begin{aligned} E_{np}(x; \tau_p, \tau_n) &= \frac{1}{\tau_p + \tau_n} exp(-\frac{x}{\tau_n}), t < 0 \\ &= \frac{1}{\tau_p + \tau_n} exp(-\frac{x}{\tau_p}), t \geq 0 \end{aligned} \quad (5.21)$$

and $\tau^{\{1,2\}}_{k\{p,n\}}$ and σ_k depend linearly on $|\Delta t|$,

$$\begin{aligned} \tau^{\{1,2\}}_{k\{p,n\}} &= \tau^{\{1,2\}0}_{k\{p,n\}} + \tau^{\{1,2\}1}_{k\{p,n\}} |\Delta t|, \\ \sigma_k &= \sigma^0_k + \sigma^1_k |\Delta t| \end{aligned} \quad (5.22)$$

In this analysis, R_k is made to be a symmetric function, that is,

$$\tau_{kn}^{\{1,2\}\{0,1\}} = \tau_{kp}^{\{1,2\}\{0,1\}} \tag{5.23}$$

So, there are seven free parameters of $\mathcal{R}_k$, $\tau_{k1}^p[0]$, $\tau_{k1}^p[1]$, $\tau_{k2}^p[0]$, $\tau_{k2}^p[1]$, $\sigma_k[0]$, $\sigma_k[1]$ and f_k, which are obtained from a fit to the Monte Carlo information for correctly tagged true signal events. Fig. 5.1 shows the $\mathcal{R}_k$ fit projections onto x = $\Delta z_{gen}/\beta\gamma c - \Delta t_{gen}$ using Monte Carlo simulation. Table 19 summarizes the results of $\mathcal{R}_k$ fit parameters.

Parameter	This analysis
Exp. range	7 - 51
Million $B\bar{B}$ pairs	$3 \times (576.5 \pm 7.7)$
$\tau_{k1}^p[0]$	$+0.183 \pm 0.003$
$\tau_{k1}^p[1]$	$+0.011 \pm 0.002$
$\tau_{k2}^p[0]$	$+0.074 \pm 0.001$
$\tau_{k2}^p[1]$	$+0.035 \pm 0.001$
$\sigma_k[0]$	-0.011 ± 0.002
$\sigma_k[1]$	$+0.046 \pm 0.001$
f_k	$+0.719 \pm 0.007$

Table 5.2: R_k parameters determined using Monte Carlo simulation

5.2.2 Determination of $\mathcal{R}_{det}$ parameters

The detector resolution is measured using $J/\psi \to \mu^+\mu^-$ sample. The muons are selected using the selection criteria listed in Table 5.3. The signal region and lower and upper sideband regions are defined in terms of the invariant mass of J/ψ ($M_{\mu^+\mu^-}$) as: $3.085 < M_{\mu^+\mu^-}/\mathrm{GeV}/c^2 < 3.109$, $2.830 < M_{\mu^+\mu^-}/\mathrm{GeV}/c^2 < 2.848$ and $3.322 < M_{\mu^+\mu^-}/\mathrm{GeV}/c^2 < 3.367$ respectively (Fig. 5.2).

A vertex position is obtained for each muon track by fits of these tracks to the IP. Then, we have

$$\delta(\Delta z) = z_{CP} - z_{gen} \tag{5.24}$$

Here, z_{CP} is CP-side (reconstructed side) vertex and z_{gen} is the true z.

Since $z_{gen} = 0$ for $J/\psi \to \mu^+\mu^-$ decays, as both the muons tracks originate from the same vertex,

$$\begin{aligned} \delta(\Delta z) &= z_{CP} \\ &= z_{\mu^+} - z_{\mu^-} \end{aligned} \tag{5.25}$$

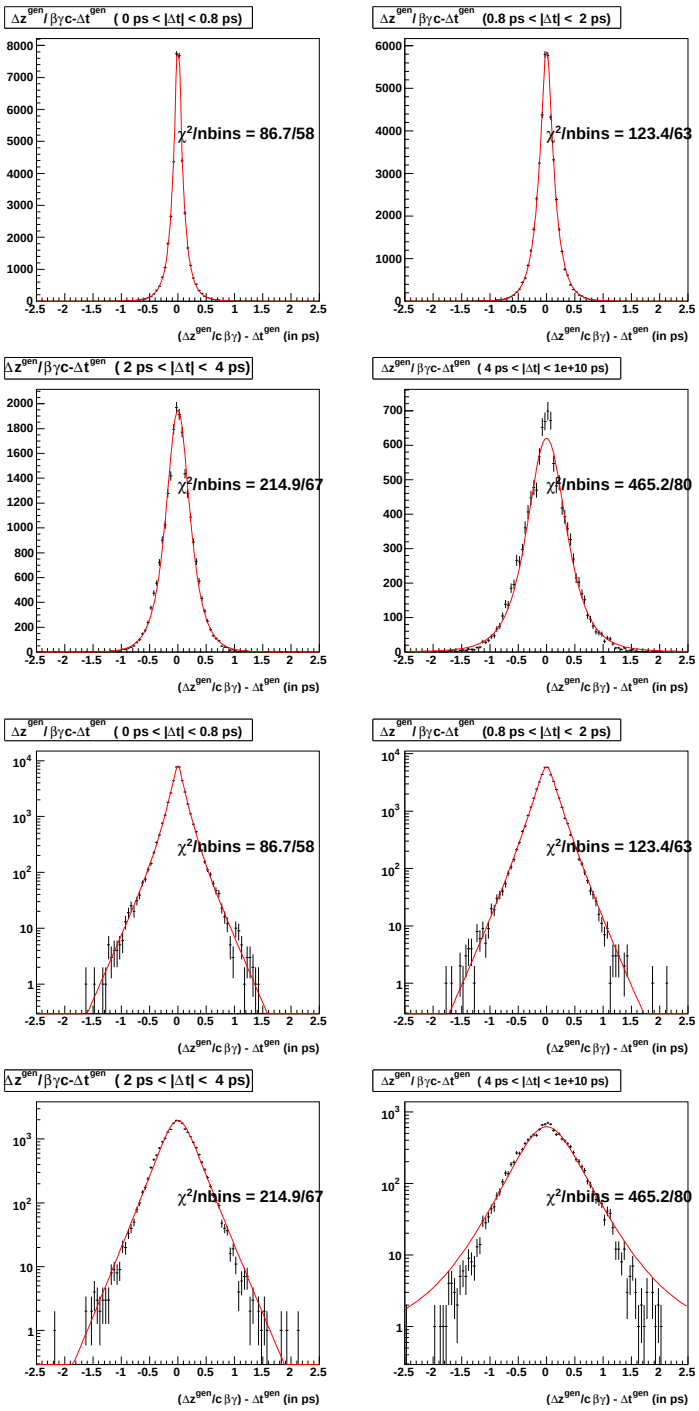

Figure 5.1: Results of the fits to extract R_k parameters projected onto x = $\Delta z_{gen}/\beta\gamma c - \Delta t_{gen}$, using SVD1 + SVD2 Monte Carlo in linear (top) and logarithmic scale (bottom) in four bins of Δt

Quantity	Requirement
Momentum	$1.1 < p_l/\mathrm{GeV}/c < 2.3$
Muon probability	> 0.90
Muon χ^2/ndf	< 3.5
Electron probability	> 0.90
Closest approach to IP (r) (dr_l)	< 0.1 cm
Closest approach to IP (z) (dz_l)	< 2.0 cm
SVD hits (r - ϕ plane)	≥ 2
SVD hits (z plane)	≥ 2
Lab polar angle	$23^\circ < \theta_{lab} < 139^\circ$ (SVD1)
	$17^\circ < \theta_{lab} < 150^\circ$ (SVD2)
$M_{\mu^+\mu^-}$	$2.8 < M_{\mu^+\mu^-}/\mathrm{GeV}/c^2 < 3.4$

Table 5.3: Summary of muon selection cuts

We do not use $J/\psi \to e^+e^-$ because the radiative tail in the J/ψ invariant mass makes the background treatment complicated.

Previous studies on single-track resolution suggest that the resolution of each track can be written as the sum of three Gaussians (R_{track}) with a common mean $< \Delta z > = 0$.

$$R_{track} = (1 - f_{tail})\mathcal{G}(\delta(\Delta z); \sigma_{\delta(\Delta z)} s_{main}) + f_{tail}((1 - f_{tata})\mathcal{G}(\delta(\Delta z); \sigma_{\delta(\Delta z)} s_{tail}) + f_{tata}\mathcal{G}(\delta(\Delta z); \sigma_{\delta(\Delta z)} s_{tata})) \quad (5.26)$$

where s_{main}, s_{tail}, s_{tata} are error scale factors for the three Gaussians and f_{tail} and f_{tata} are the fraction of the distribution in the tail and in the tail part of the tail respectively. This form for detector resolution is called 'triple Gaussian'. As described earlier, $\delta(\Delta z)$ is the difference between the measured and the true z-vertex positions of the track and $\sigma_{\delta(\Delta z)}$ is the error on this quantity.

The five free parameters of $\mathcal{R}_{det}$ are s_{main}, s_{tail}, s_{tata}, f_{tail} and f_{tata} are determined from an unbinned maximum likelihood fit to the J/ψ candidates. We determine two sets of five parameters from a simultaneous fit to the full dataset as we analyse data taken with two different vertex detectors. We determine the $\mathcal{R}_{det}$ parameters for both $J/\psi \to \mu^+\mu^-$ Monte Carlo and data. The procedure is outlined below:

- We fit the J/ψ invariant mass sideband with a second-order polynomial using a binned likelihood fit. The background fractions are assumed to be the same for SVD1 and SVD2.

- The background $|\Delta t|$ shape is assumed to be

$$P_{bkg} = (f_\delta \delta(\Delta z) + (1 - f_\delta)\frac{1}{2\beta\gamma c\tau_{bkg}} e^{-|\Delta z|/\beta\gamma c\tau bkg}) \otimes \mathcal{R}_{det} \tag{5.27}$$

- The signal $|\Delta t|$ shape is assumed to be

$$P_{sig} = \mathcal{R}_{det} \tag{5.28}$$

- We perform a simultaneous unbinned maximum likelihood fit to the signal and the sideband regions to extract the R_{det} parameters. The PDF used is

$$P = (1 - f_{bkg})P_{sig} + f_{bkg}P_{bkg} \tag{5.29}$$

  Here, $f_{bkg} = 1$ for the sideband regions and is calculated as the ratio of the fit result in the bin containing a particular event and the number of events in data in that bin for the signal region.

- Since Δz biases can also appear in $J/\psi \to \mu^+\mu^-$ sample, the offset $\epsilon_{\Delta z\pm}$ is introduced: $\Delta z \to \Delta z + \epsilon_{\Delta z\pm}$. The definition

$$\delta(\Delta z) = (\Delta z)_{\mu^+} - (\Delta z)_{\mu^-} \tag{5.30}$$

  is used, and so only one offset is needed. Two different offsets are set for SVD1 and SVD2.

Figs. 5.2, 5.3, 5.4 and 5.5 shows the $\mathcal{R}_{det}$ fit projections onto Δz using SVD1, SVD2 Monte Carlo and SVD1, SVD2 data respectively. Table 5.4 summarizes the results of $\mathcal{R}_{det}$ fit parameters for both Monte Carlo and data.

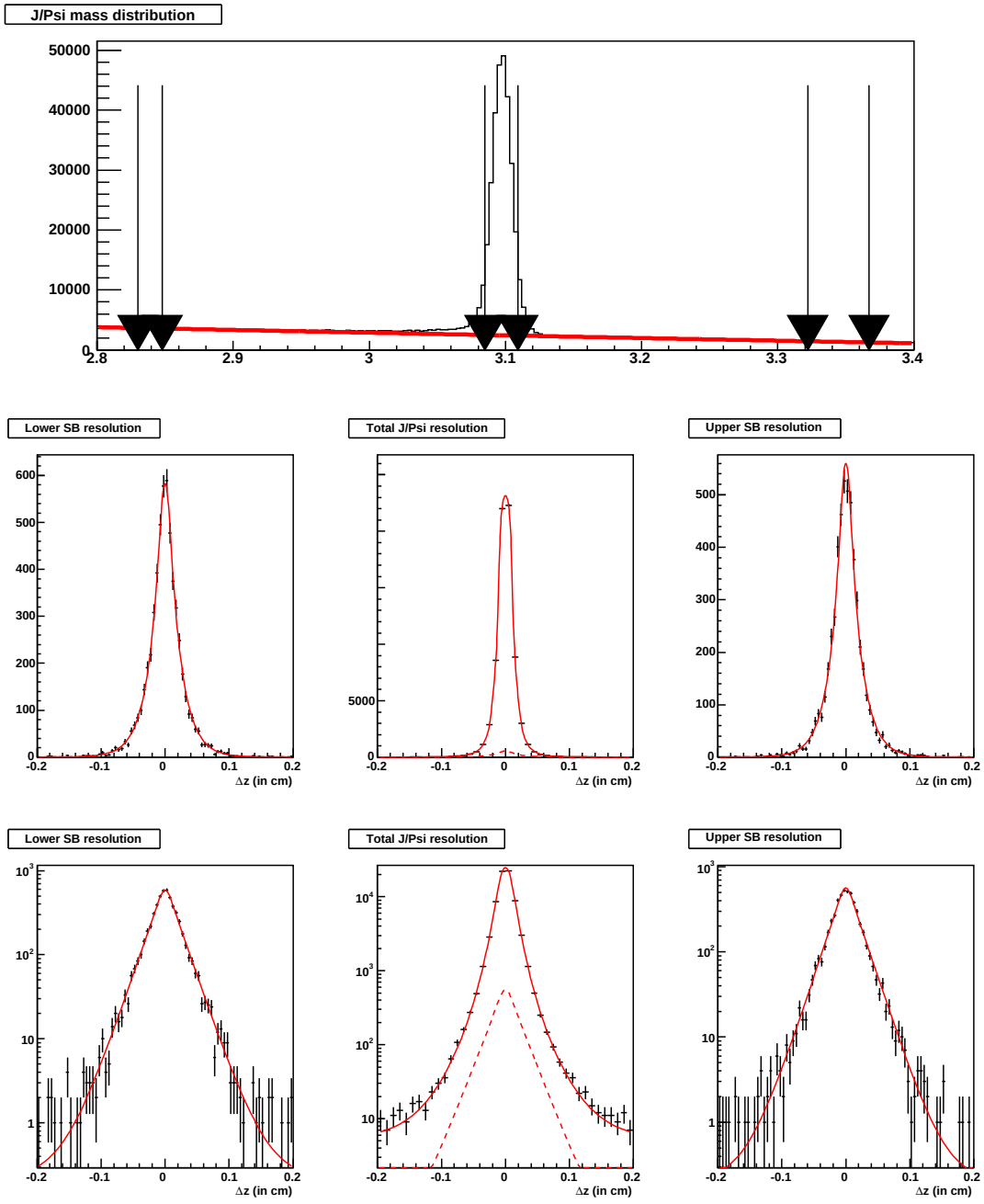

Figure 5.2: Results of the fits to extract R_{det} parameters using SVD1 Monte Carlo. Top plot: J/ψ invariant mass ($M_{\mu^+\mu^-}$) distribution; middle row: projection onto Δz in linear scale and bottom row: projection onto $|\Delta z|$ in logarithmic scale.

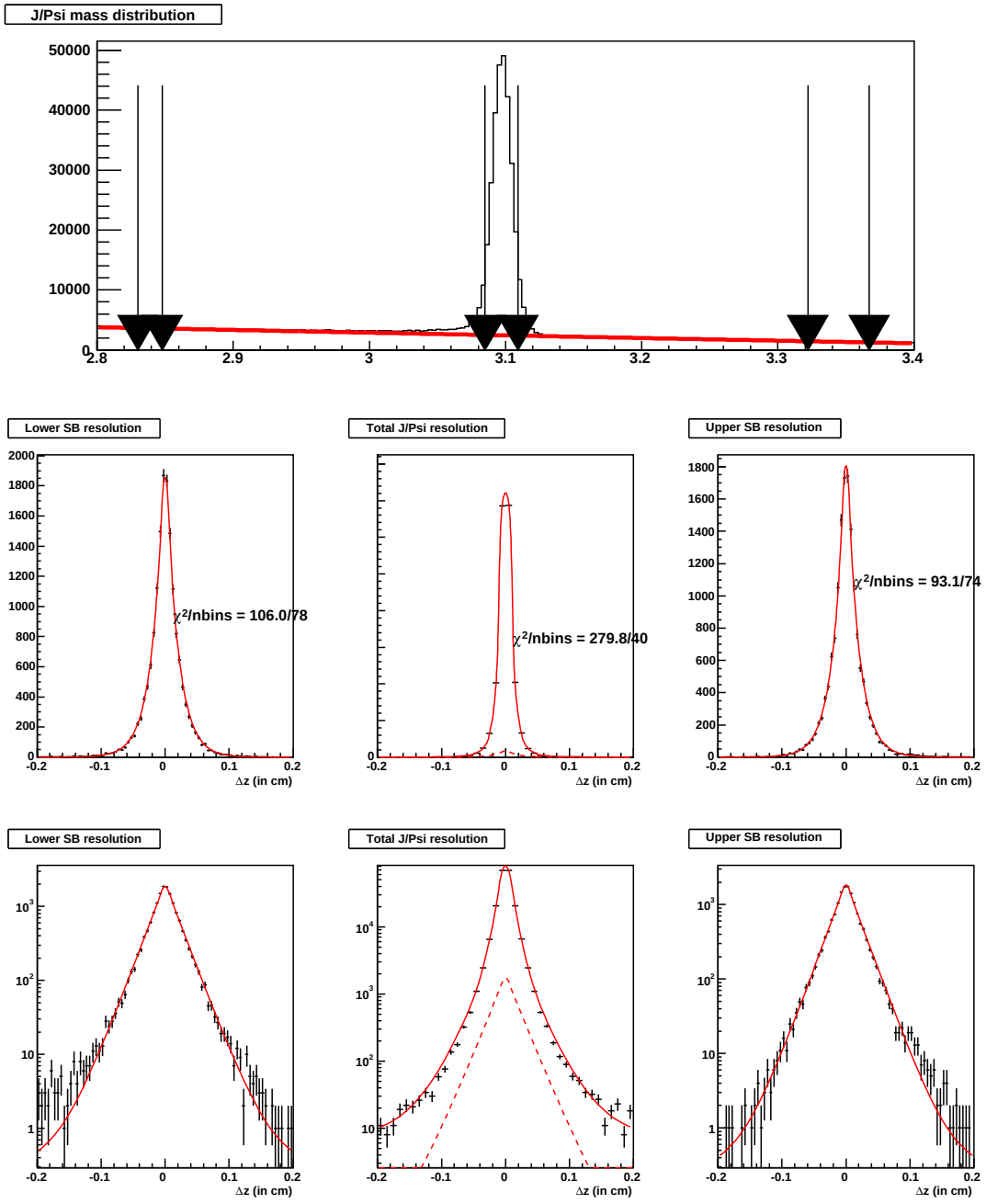

Figure 5.3: Results of the fits to extract R_{det} parameters using SVD2 Monte Carlo. Top plot: J/ψ invariant mass ($M_{\mu^+\mu^-}$) distribution; middle row: projection onto Δz in linear scale and bottom row: projection onto $|\Delta z|$ in logarithmic scale.

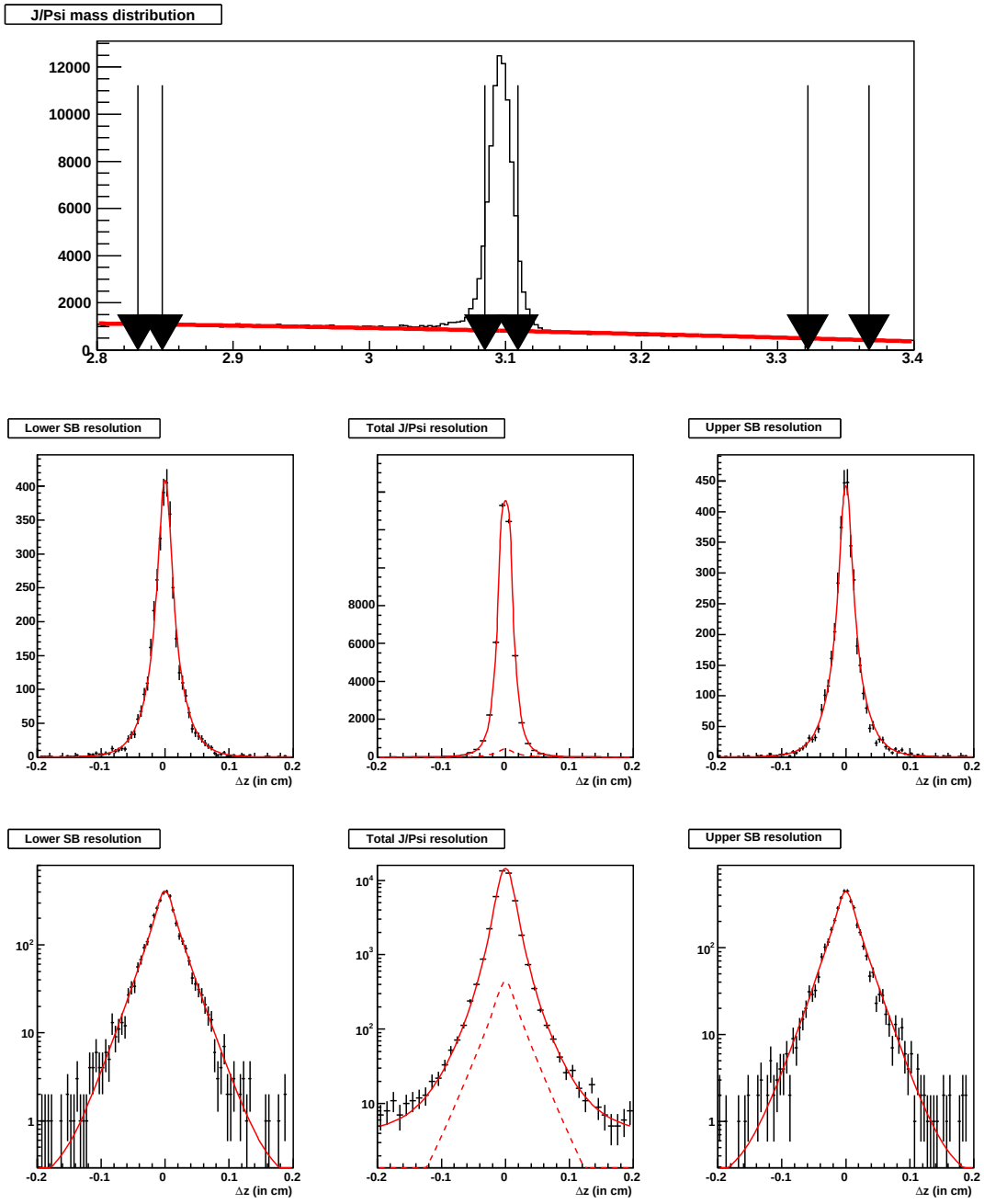

Figure 5.4: Results of the fits to extract R_{det} parameters using SVD1 data. Top plot: J/ψ invariant mass ($M_{\mu^+\mu^-}$) distribution; middle row: projection onto Δz in linear scale and bottom row: projection onto $|\Delta z|$ in logarithmic scale.

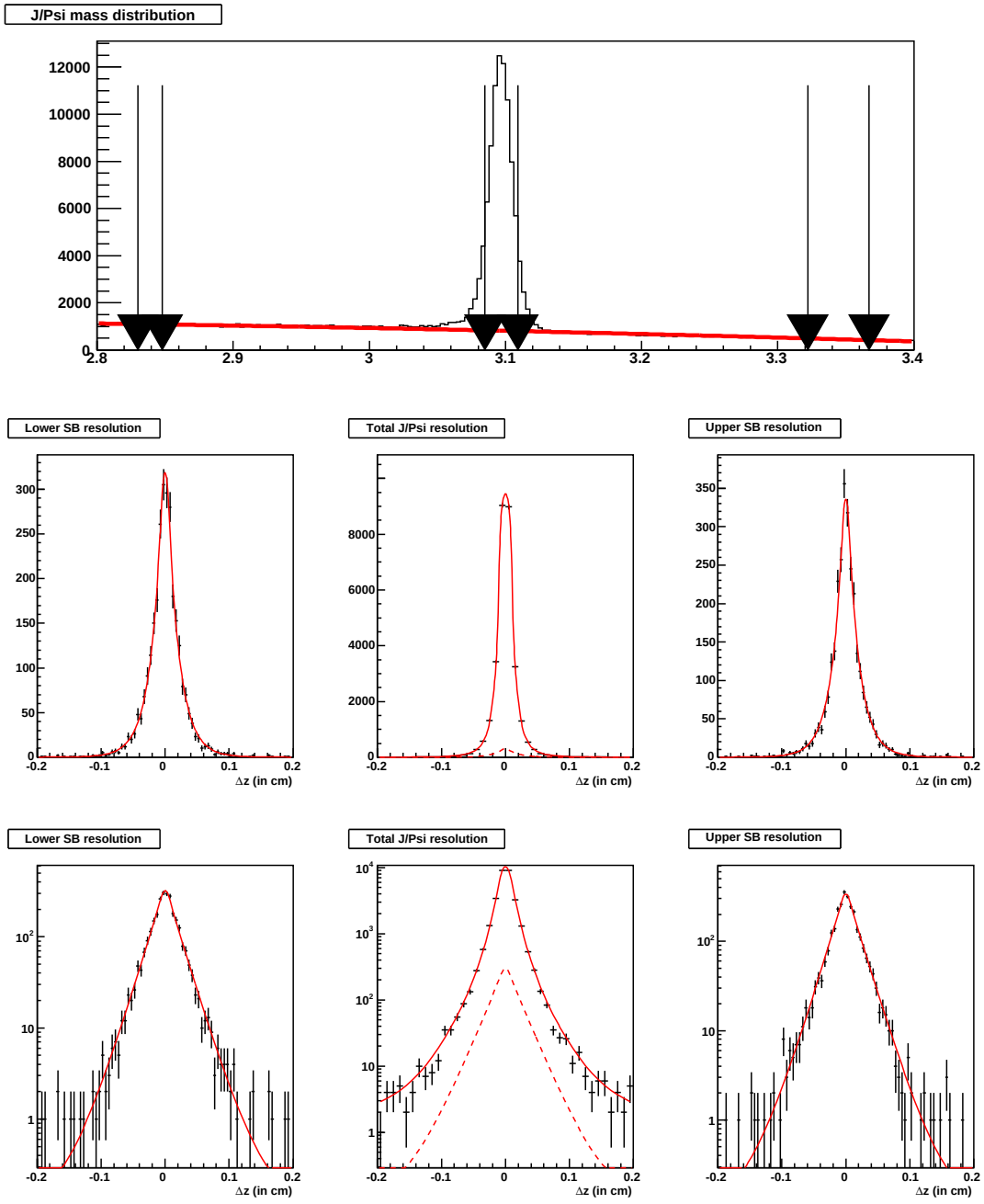

Figure 5.5: Results of the fits to extract R_{det} parameters using SVD2 data. Top plot: J/ψ invariant mass ($M_{\mu^+\mu^-}$) distribution; middle row: projection onto Δz in linear scale and bottom row: projection onto $|\Delta z|$ in logarithmic scale.

Parameter	Monte Carlo	Data
SVD1		
Exp. range	7 - 27	7 - 27
Million $B\bar{B}$ pairs	$3 \times (152.0 \pm 1.0)$	152.0 ± 1.0
s_{main}	0.997 ± 0.005	1.005 ± 0.010
f_{tail}	0.091 ± 0.005	0.123 ± 0.010
s_{tail}	2.629 ± 0.067	2.527 ± 0.084
f_{tata}	0.056 ± 0.003	0.060 ± 0.005
s_{tata}	76.843 ± 1.378	82.839 ± 1.970
$\epsilon_{\Delta z \pm}$	-0.876 ± 0.231	5.766 ± 0.043
SVD2		
Exp. range	31 - 51	31 - 51
Million $B\bar{B}$ pairs	$3 \times (352.9 \pm 6.6)$	352.9 ± 6.6
s_{main}	1.058 ± 0.002	1.072 ± 0.004
f_{tail}	0.084 ± 0.001	0.139 ± 0.003
s_{tail}	3.961 ± 0.035	3.675 ± 0.038
f_{tata}	0.028 ± 0.001	0.025 ± 0.001
s_{tata}	78.892 ± 1.338	85.253 ± 1.830
$\epsilon_{\Delta z \pm}$	0.066 ± 0.105	0.096 ± 0.217

Table 5.4: $\mathcal{R}_{det}$ parameters obtained from the fit to SVD1 (Expt. 7 -27) and SVD2 (Expt. 31 -51) $J/\psi \to \mu^+\mu^-$ candidates using Monte Carlo and data separately.

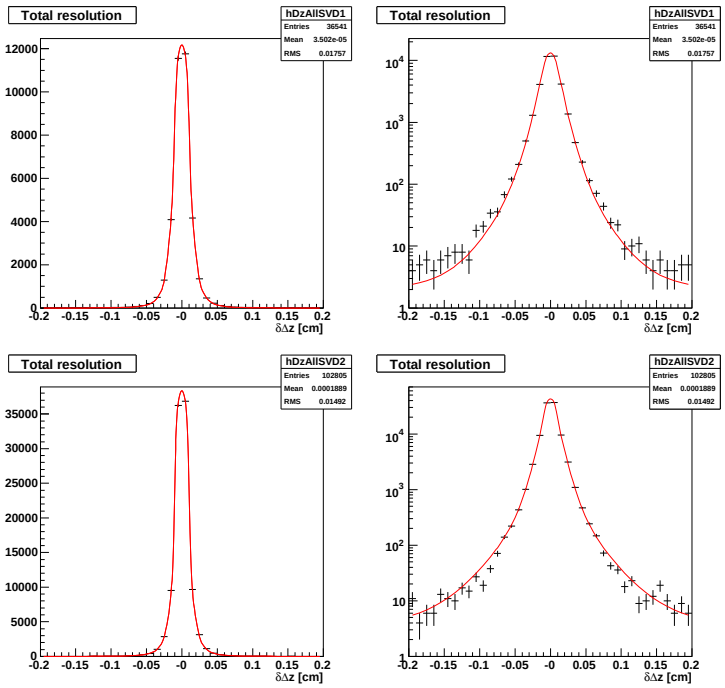

Figure 5.6: Results of the fits to extract R_{det} parameters projected onto $\delta(\Delta z)$ using SVD1 (top) and SVD2 (bottom) Monte Carlo in linear (left) and logarithmic (right) scales).

We obtain the $\mathcal{R}_{det}$ parameters from a fit to the Monte Carlo information for correctly tagged signal events ($D^*\pi$ events that have a real fast pion and a real primary lepton in the tag-side) using the triple Gaussian function as done for the $J/\psi \to \mu^+\mu^-$ sample. A vertex position is obtained for the fast pion track and the tagging lepton as described earlier. Then, we have

$$\delta(\Delta z) = (\Delta z)_{CP} - (\Delta z)_{gen} \tag{5.31}$$

We determine two sets of the five parameters of $\mathcal{R}_{det}$ (s_{main}, s_{tail}, s_{tata}, f_{tail} and f_{tata}) from a simultaneous fit to the full dataset as we analyse data taken with two different vertex detectors. Fig. 5.6 shows the $\mathcal{R}_{det}$ fit projections onto $\delta(\Delta z)$ using SVD1 and SVD2 Monte Carlo respectively. Table 5.5 summarizes the results of $\mathcal{R}_{det}$ fit parameters for SVD1 and SVD2 Monte Carlo. There is a good agreement between the $\mathcal{R}_{det}$ parameters obtained using the correctly tagged $D^*\pi$ events and those obtained using the $J/\psi \to \mu^+\mu^-$ candidates (Table 5.4) in Monte Carlo. This suggests that we can use the parameters obtained uisng the $J/\psi \to \mu^+\mu^-$ candidates to do the CP fit.

Parameter	SVD1	SVD2
Exp. range		
Million $B\bar{B}$ pairs	$3 \times (152.0 \pm 1.0)$	$3 \times (352.9 \pm 6.6)$
s_{main}	$+1.113 \pm 0.005$	$+1.082 \pm 0.003$
f_{tail}	$+0.054 \pm 0.002$	$+0.066 \pm 0.001$
s_{tail}	$+3.592 \pm 0.069$	$+4.361 \pm 0.042$
f_{tata}	$+0.078 \pm 0.005$	$+0.033 \pm 0.002$
s_{tata}	$+105.927 \pm 4.886$	$+83.405 \pm 3.516$

Table 5.5: $\mathcal{R}_{det}$ parameters obtained using $\bar{B}^0 \to D^{*+}\pi^-$ candidates in SVD1 and SVD2 Monte Carlo.

5.2.3 Determination of $\mathcal{R}_{np}$ parameters

When the lepton candidate used to measure Δz does not originate from the decay vertex of the corresponding B, the Δz measurement is smeared by a quantity that can be taken into account by this resolution function.

The detector resolution is convolved with the following parametrization, as a function of y = $\Delta z_{CP} - \Delta z_{gen} = \delta(\Delta z)$, where $(\Delta z)_{CP}$ is CP-side (reconstructed side) vertex and $(\Delta z)_{gen}$ is the true Δz.

$$\mathcal{R}_{np}(y;\tau_n,\tau_p) = f_p E_p(y;\tau_p) + (1-f_p)E_n(y;\tau_n) \tag{5.32}$$

$$\begin{aligned} E_p(y;\tau) &= \frac{1}{\tau} exp(-\frac{y}{\tau}), y > 0 \\ &= 0, y \leq 0 \\ E_n(y;\tau) &= \frac{1}{\tau} exp(+\frac{y}{\tau}), y \leq 0 \\ &= 0, y > 0 \end{aligned} \tag{5.33}$$

and f_p is the positive skewness of the smearing.

$$\begin{aligned} \tau_p &= \tau_p^0 + \tau_p^1 s\sigma_z \\ \tau_n &= \tau_n^0 + \tau_n^1 s\sigma_z \end{aligned} \tag{5.34}$$

where s are the same error scale factors as in $\mathcal{R}_{det}$.

The seven free parameters of $\mathcal{R}_{np}$ are ${f_p}^{UC}$, ${f_p}^{UU}$, ${f_p}^{NU}$, τ_p^0, τ_p^1, τ_n^0 and τ_n^1. These parameters are obtained by a fit of $R_{det} \otimes R_{np}$ to the Monte Carlo simulation. We do a simultaneous fit in three regions, namely, uncorrelated background in the correlated background sideband (UC), the uncorrelated background in the other regions (UU) and all other event types (NU). A single set of parameters is fitted for the SVD1 and SVD2 data since this phenomenon is related to the physics of the decay, and not the vertex detector.

Table 5.6 illustrates the signal, correlated and uncorrelated sideband regions. Fig. 5.7 shows the $p_\parallel$, p_δ and $p_\perp$ distributions for these components along with $D^*\rho$ background component.

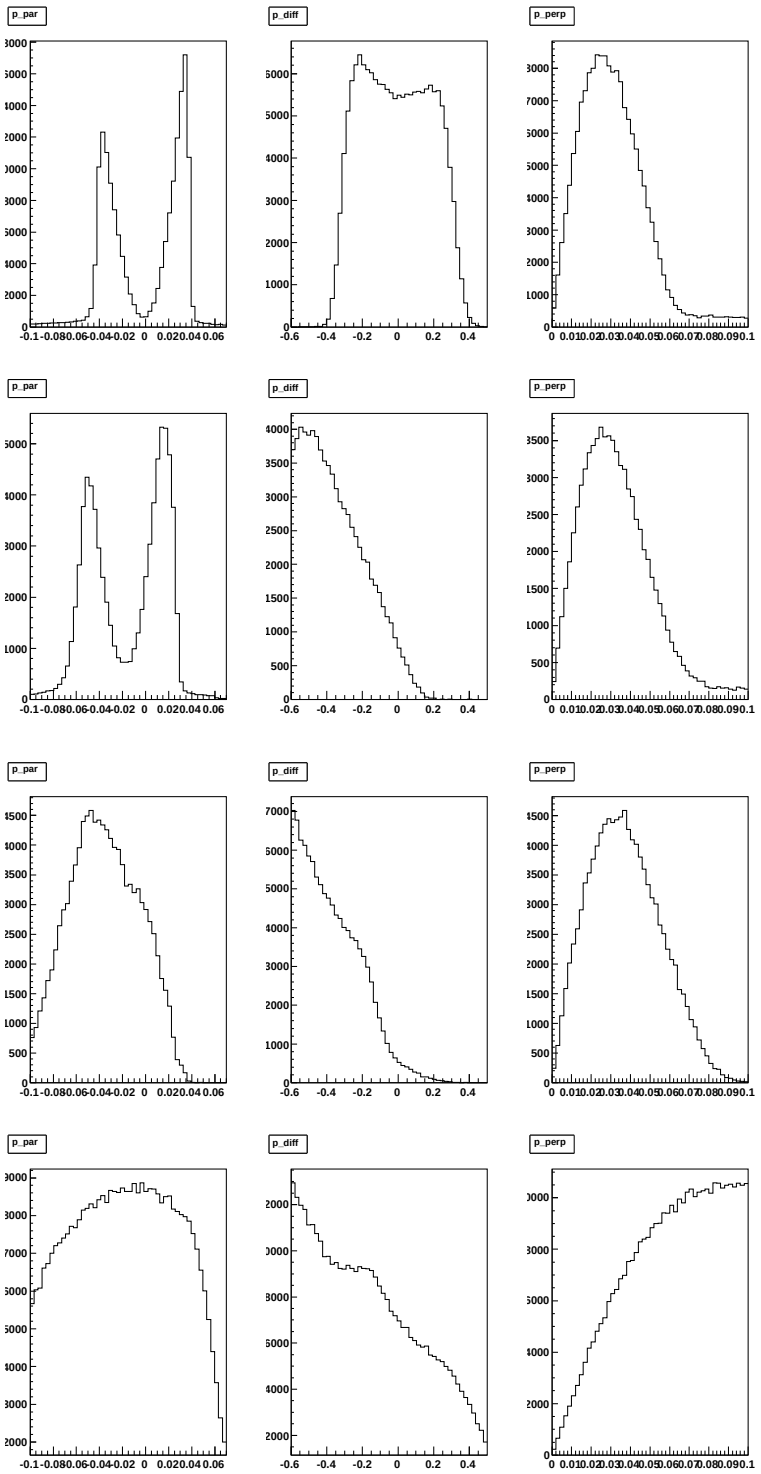

Figure 5.7: $p_{\|}$ (left), p_{δ} (middle) and $p_{\perp}$ (right) distributions for $D^*\pi$ (1st row), $D^*\rho$(2nd row), correlated (3rd row) and uncorrelated (4th row) backgrounds obtained from Monte Carlo simulation

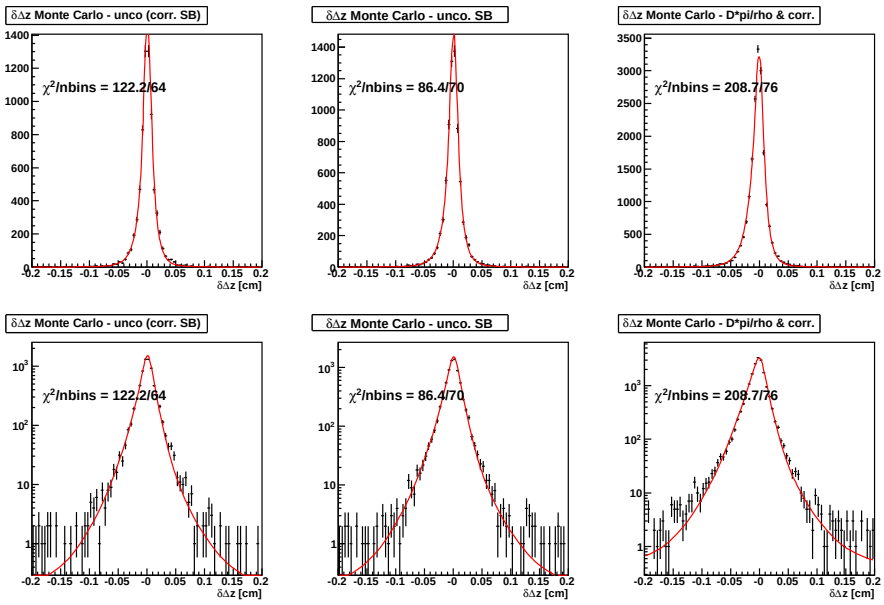

Figure 5.8: Results of the fits to extract R_{np} parameters projected onto y = $\Delta z_{CP} - \Delta z_{gen} = \delta(\Delta z)$ using SVD1 + SVD2 Monte Carlo in linear (top) and logarithmic scale (bottom)

Fig. 5.8 shows the $\mathcal{R}_{np}$ fit projections onto $\delta(\Delta z)$ using Monte Carlo simulation. Table 5.7 summarizes the results of $\mathcal{R}_{np}$ fit parameters.

Quantity	Entire region	Signal region	Corr. bkgd.	Unco. bkgd.
$p_{\|}$	$-0.10 < p_{\|} < 0.07$	$-0.05 < p_{\|} < -0.01$ $0.01 < p_{\|} < 0.04$	$-0.10 < p_{\|} < -0.07$	$-0.10 < p_{\|} < 0.07$
p_δ	$-0.60 < p_\delta < 0.50$	$-0.40 < p_\delta < 0.40$	$-0.60 < p_\delta < 0.00$	$-0.60 < p_\delta < 0.50$
$p_\perp$	$0.00 < p_\perp < 0.05$	$0.00 < p_\perp < 0.05$	$0.00 < p_\perp < 0.05$	$0.08 < p_\perp < 0.10$

Table 5.6: Signal region, correlated and uncorrelated sideband regions in the kinematic variables, p_δ, $p_{\|}$ and $p_\perp$, in GeV/c.

Parameter	This analysis
Exp. range	
Million $B\bar{B}$ pairs	$3 \times (576.5 \pm 7.7)$
f_p^{UU}	$+0.221 \pm 0.014$
f_p^{UC}	$+0.193 \pm 0.013$
f_p^{NU}	$+0.468 \pm 0.015$
τ_p^0	$+0.590 \pm 0.031$
τ_p^1	$+0.768 \pm 0.076$
τ_n^0	$+0.031 \pm 0.014$
τ_n^1	$+0.333 \pm 0.036$

Table 5.7: R_{np} parameters determined using Monte Carlo simulation. Three different values of f_p are used for the uncorrelated background in the correlated background sideband (UC), the uncorrelated background in the other regions (UU) and all other event types (NU) respectively

5.3 Determination of the uncorrelated and correlated background fit parameters

The background fit parameters for uncorrelated and correlated backgrounds are obtained from separate fits to respective sideband regions. The procedure is described in detail in this section. Since there is no CP in background, the CP violation parameters are fixed to 0 for the background fits and float them for estimation of systematic errors. The fit is further simplified by fixing the biases in Δz to zero ($\epsilon = 0$).

5.3.1 Determination of the uncorrelated background fit parameters

In order to obtain the uncorrelated background parameters, the events in the uncorrelated background sideband are used. The sideband used for this fit is given in Table 5.6. The amount of various components in this sideband region is given in Table 5.8. This region is populated by uncorrelated background events ($\sim 95\%$) mostly.

Hence, the PDF used to do this fit is:

$$P_{bkg} = P_{unco} \tag{5.35}$$

We neglect all the components other than uncorrelated to do the uncorrelated background fit. The uncorrelated background PDF is defined in Eq. 5.13. Thus, the

Component	fraction(in %) Monte-Carlo	fraction(in %) Data
$D^*\pi$ signal	3.0	3.2
$D^*\rho$ background	1.4	3.1
Correlated background	1.1	2.9
Uncorrelated background	94.5	90.8

Table 5.8: Amount of signal and background components in uncorrelated background sideband in Monte-Carlo and data

parameters that are obtained from the uncorrelated background fit are f_{BB}, f_{mix}, f_δ, τ_{qq}, A_{qq} and $w^\pm$. Table 5.9 summarizes the results of the fits to extract the uncorrelated background parameters. Fig. 5.9 shows the fit results projected onto Δz in the four charge and flavour combinations.

Parameter	Monte Carlo	Data
Exp. range	7-51	7 - 55
Million $B\bar{B}$ pairs	$3 \times (576.5 \pm 7.7)$	656.7 ± 7.8
f_{BB}	$+0.809 \pm 0.004$	$+0.764 \pm 0.006$
f_{mix}	$+0.415 \pm 0.012$	$+0.331 \pm 0.027$
f_δ	$+0.965 \pm 0.003$	$+0.968 \pm 0.004$
τ_{qq}	$+24.589 \pm 1.719$	$+23.348 \pm 2.742$
A_{qq}	$+0.331 \pm 0.020$	$+0.346 \pm 0.031$
w^-	$+0.177 \pm 0.004$	$+0.220 \pm 0.008$
w^+	$+0.166 \pm 0.004$	$+0.208 \pm 0.008$

Table 5.9: Results of fits to extract uncorrelated background parameters for both Monte Carlo and data ($\epsilon = 0$)

5.3.2 Determination of the correlated background fit parameters

To obtain the correlated background parameters, the events in the correlated background sideband are used. This region is populated by correlated and uncorrelated background events mostly. Hence, the PDF used to do this fit is:

$$P_{bkg} = (1 - f_{unco})P_{corr} + f_{unco}P_{unco} \tag{5.36}$$

where f_{unco} is obtained from the result of the event-by-event yield fit, after renormalizing the events neglecting $D^*\pi$ and $D^*\rho$ events, and $P_{corr} = P_{BB}$.
The uncorrelated and correlated background PDFs are given by Eqs. 5.10 and 5.13 respectively. The sideband used for this fit is given in Table5.6. The amount of various components in this sideband region is given in Table 5.10.:

	fraction(in %)	fraction(in %)
Component	Monte-Carlo	Data
$D^*\pi$ signal	2.0	2.0
$D^*\rho$ background	6.0	4.0
Correlated background	52.0	41.0
Uncorrelated background	40.0	53.0

Table 5.10: Amount of signal and background components in correlated background sideband in Monte-Carlo and data

The parameters that are obtained from the correlated background fit are f_{mix} and $w^{\pm}$ for correlated events.

The correlated background parameters are obtained using the correlated events in the correlated sideband region and signal region in Monte-Carlo. The parameters obtained from the two cases are summarized in Table 5.11 and Fig. 5.10 shows the fits in the correlated sideband region and signal regions respectively. The parameters obtained in the two cases are consistent with each other within error bars. Hence, we can use the correlated background parameters obtained in the correlated sideband region while fitting in signal region.

Parameter	correlated sideband	signal region
f_{mix}	$+0.450 \pm 0.020$	$+0.443 \pm 0.013$
w^-	$+0.054 \pm 0.005$	$+0.048 \pm 0.003$
w^+	$+0.058 \pm 0.005$	$+0.049 \pm 0.003$

Table 5.11: Results of fits to extract correlated background parameters for using $3 \times (576.5 \pm 7.7)$ million $B\bar{B}$ pairs Monte-Carlo events

A fit to the uncorrelated events in the correlated sideband region is done in Monte-Carlo (Fig. 5.11) and the parameters thus, obtained are listed in Table 5.12. Table 5.12 also shows the uncorrelated background parameters obtained in uncorrelated background sideband. The parameters in both the cases seem to be in good

agreement with eachother. The wrong-tags for uncorrelated background obtained in this fit should be higher than those obtained from the fit to the uncorrelated background sideband. The reason is that fast pion momentum looser in correlated sideband than uncorrelated sideband, hence, there should be more non-primary tracks in correlated sideband.

Parameter	correlated sideband	uncorrelated sideband
f_{BB}	$+0.853 \pm 0.010$	$+0.809 \pm 0.004$
f_{mix}	$+0.473 \pm 0.045$	$+0.415 \pm 0.012$
f_{δ}	$+0.934 \pm 0.018$	$+0.965 \pm 0.003$
τ_{qq}	$+14.893 \pm 4.991$	$+24.589 \pm 1.719$
A_{qq}	$+0.425 \pm 0.071$	$+0.331 \pm 0.020$
w^{-}	$+0.267 \pm 0.012$	$+0.177 \pm 0.004$
w^{+}	$+0.263 \pm 0.012$	$+0.166 \pm 0.004$

Table 5.12: Results of fits to extract uncorrelated background parameters using uncorrelated events in correlated sideband and uncorrelated sideband in Monte Carlo

The parameters obtained from the fit to both uncorrelated and correlated events separately in the correlated sideband region in Monte-Carlo are fixed and a fit projection (not actual fit) using both uncorrelated and correlated events in correlated sideband region is done. This projection is shown in Fig. 5.12 and seems to be good. This confirms that the correlated background distribution is properly described.

Unlike the uncorrelated sideband, the correlated sideband contains both uncorrelated and correlated events and both types of events are taken into account in the background PDF used to fit in this region. Hence, in principle, the parameters that can be obtained from fit in this region are f_{mix} and $w^{\pm}$ for correlated events and f_{BB}, f_{mix} , f_{δ} , τ_{qq}, A_{qq} and $w^{\pm}$ for uncorrelated events. However, we fix most of the uncorrelated background parameters, such as, f_{BB}, f_{mix} , f_{δ} , τ_{qq} and A_{qq} from the uncorrelated background fit done earlier in Monte-Carlo and data respectively while fitting in Monte-Carlo and data respectively in correlated sideband. Thus, we have only 5 free parameters now, namely, f_{mix} and $w^{\pm}$ for correlated events and $w^{\pm}$ for uncorrelated events.

We considered two cases for the correlated sideband fit, namely,

- with 5 free parameters f_{mix} and $w^{\pm}$ for correlated events and
- $w^{\pm}$ for uncorrelated events and with 3 free parameters f_{mix} and $w^{\pm}$ for correlated events with $w^{\pm}$ for uncorrelated events fixed from the fit done using

uncorrelated events only in the correlated sideband in Monte-Carlo.

Tables 5.13 summarizes the fit results for the two cases in Monte-Carlo and Figs. 5.13 show the fit projection plots for the two cases. $w^{\pm}$ for correlated events is expected to be of the same order at that of signal (~ 6 %). $w^{\pm}$ for correlated events in first case are quite different from the expected ones, whereas those obtained in second case seem consistent with expected values. Hence, we use the second case to obtain correlated background parameters in Monte-Carlo.

Parameter	Case1	Case2
f_{mix}	$+0.615 \pm 0.034$	$+0.573 \pm 0.027$
w^-	$+0.152 \pm 0.018$	$+0.052 \pm 0.010$
w^+	$+0.130 \pm 0.017$	$+0.047 \pm 0.010$
w^-_{unco}	$+0.144 \pm 0.017$	$+0.267$ (fixed)
w^+_{unco}	$+0.161 \pm 0.017$	$+0.263$ (fixed)

Table 5.13: Results of fits to extract correlated background parameters for Monte Carlo using $3 \times (576.5 \pm 7.7)$ million $B\bar{B}$ pairs in cases 1 and 2

The correlated background parameters in data are obtained using case 2. Table 5.14 summarizes the fit results in data and Fig. 5.14 shows the fit projection plots.

Parameter	Data
Exp. range	7 - 55
Million $B\bar{B}$ pairs	656.7 ± 7.8
f_{mix}	$+0.603 \pm 0.047$
w^-	$+0.099 \pm 0.015$
w^+	$+0.080 \pm 0.015$
$w^-_{unco}(fixed)$	$+0.267$
$w^+_{unco}(fixed)$	$+0.263$

Table 5.14: Results of fits to extract correlated background parameters in data

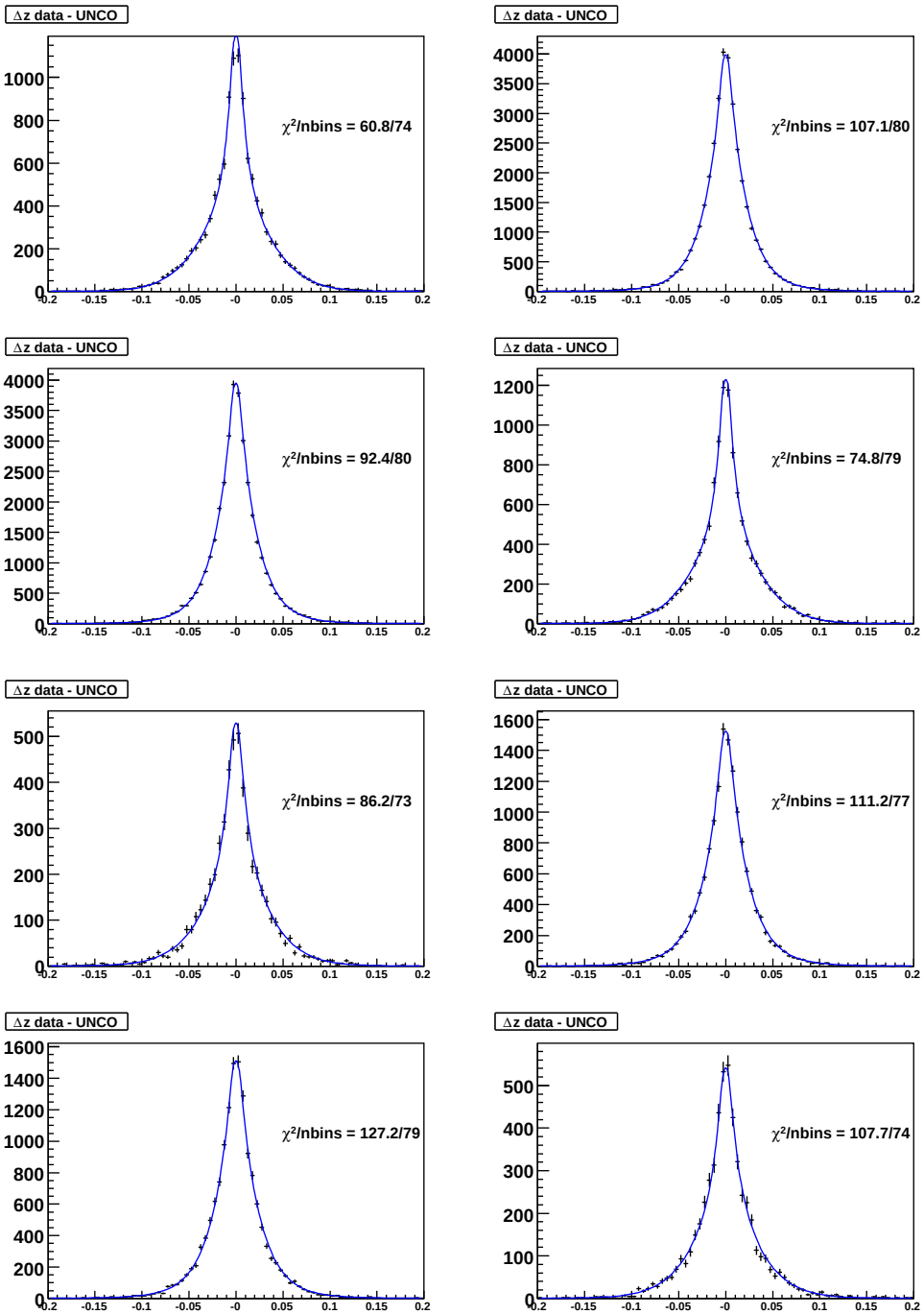

Figure 5.9: Results of the fits to extract uncorrelated background Δt shape projected onto Δz in the four charge and flavour combinations for SVD1 + SVD2 Monte Carlo(top) and SVD1 + SVD2 data (bottom)

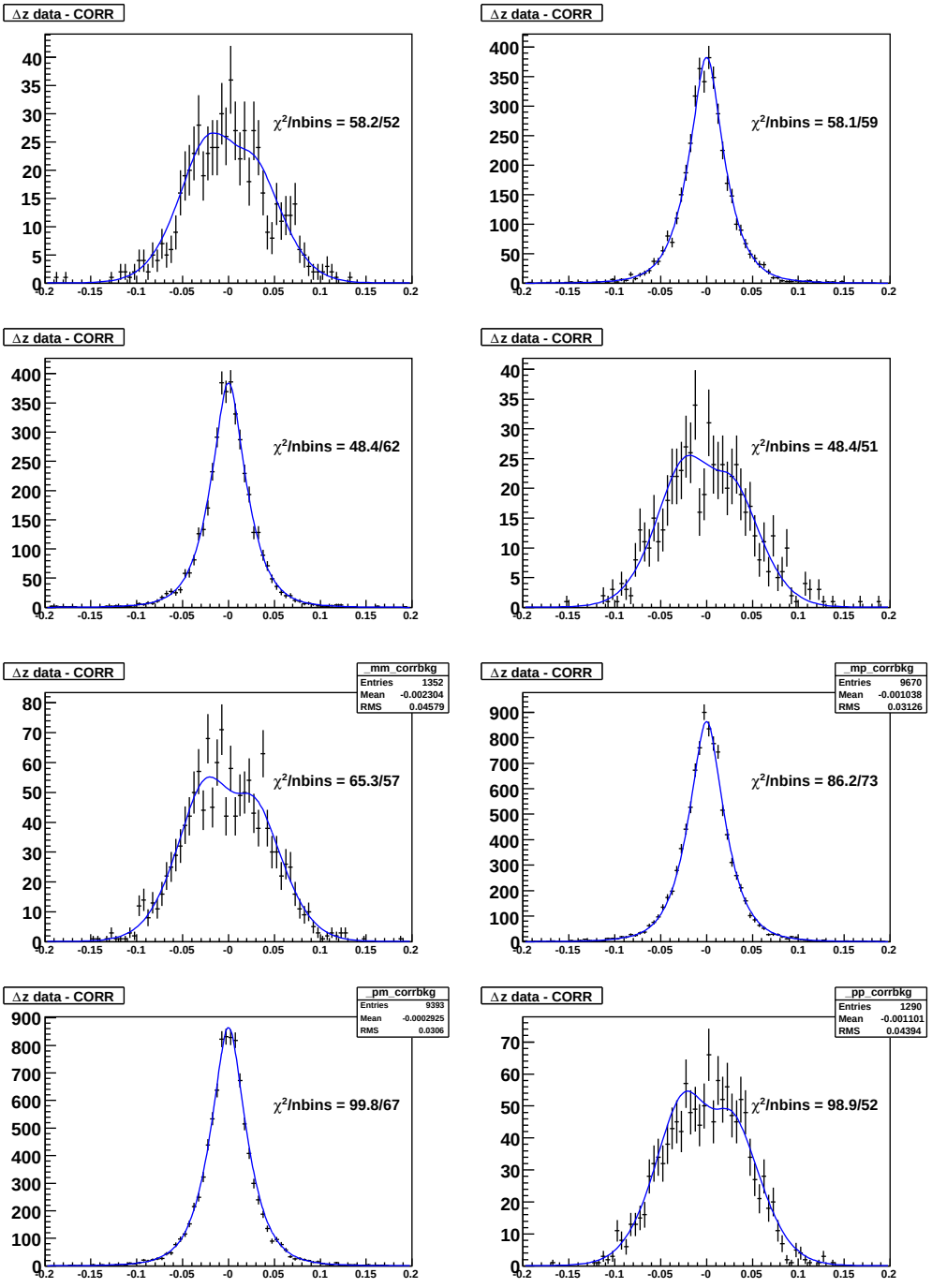

Figure 5.10: Fit to correlated events in correlated sideband (top) and signal region (bottom) in Monte-Carlo

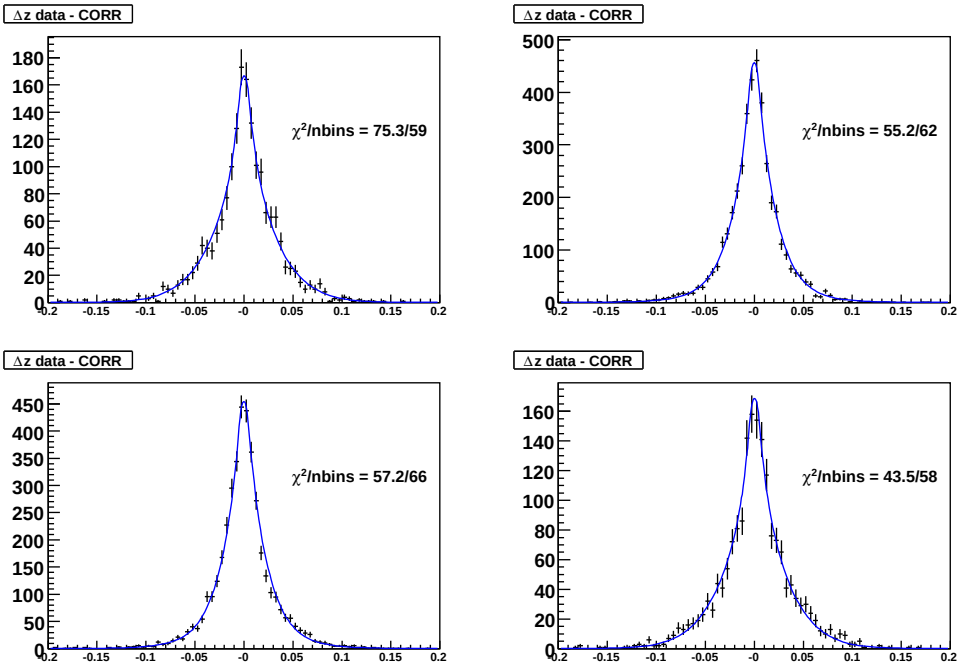

Figure 5.11: Fit to the uncorrelated events in the correlated sideband region in Monte-Carlo

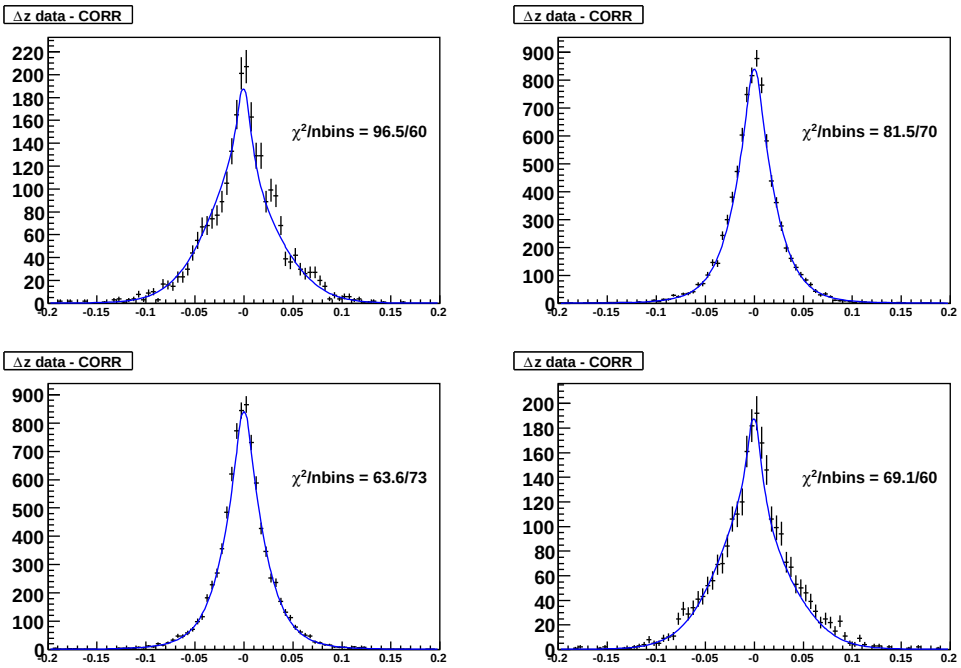

Figure 5.12: Projection of fit to correlated sideband with all parameters fixed from fit to uncorrelated and correlated events separately in the correlated sideband region in Monte-Carlo

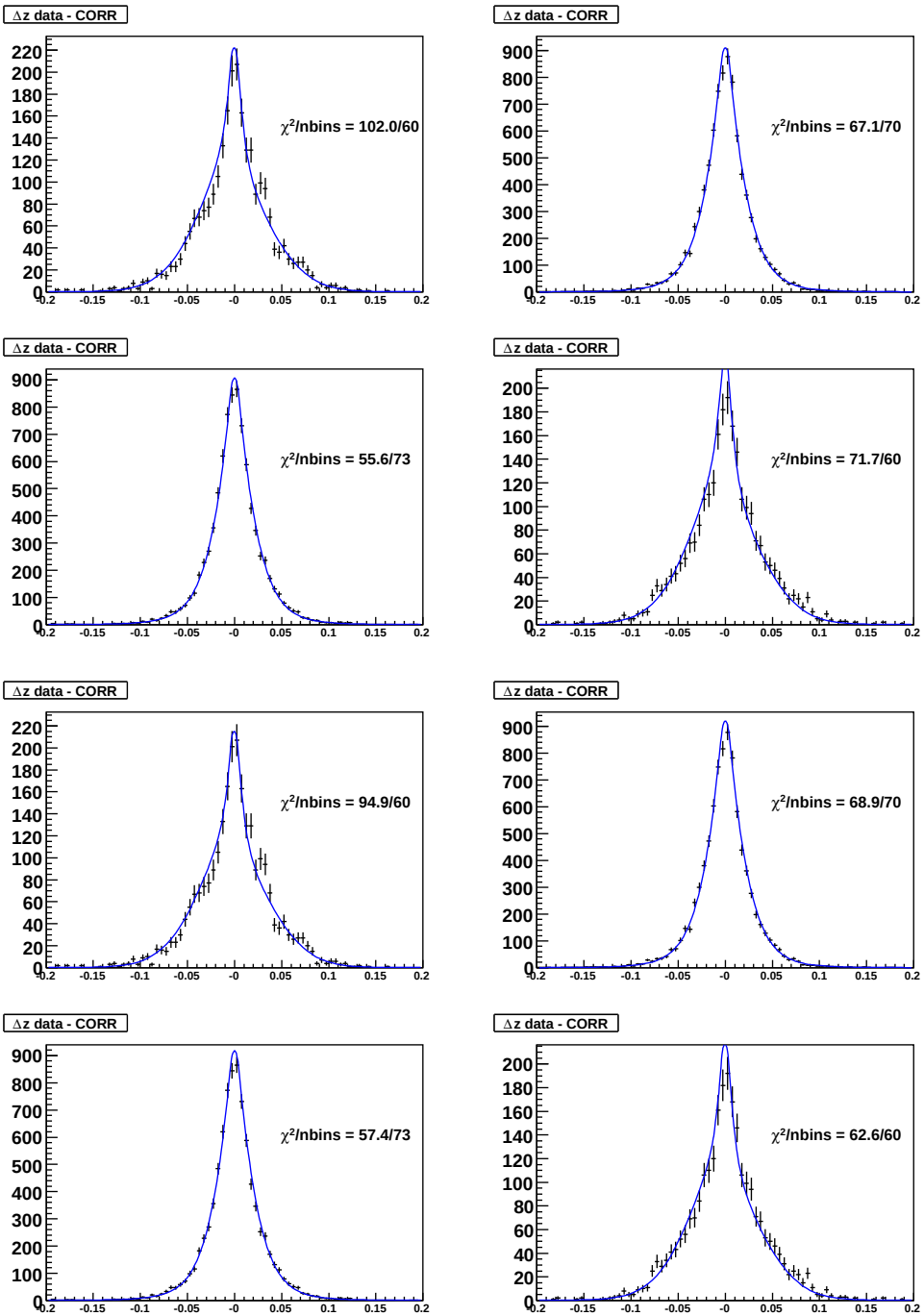

Figure 5.13: Results of the fits to extract correlated background Δt shape projected onto Δz in the four charge and flavour combinations for SVD1 + SVD2 Monte Carlo in case 1(top) and case 2 (bottom)

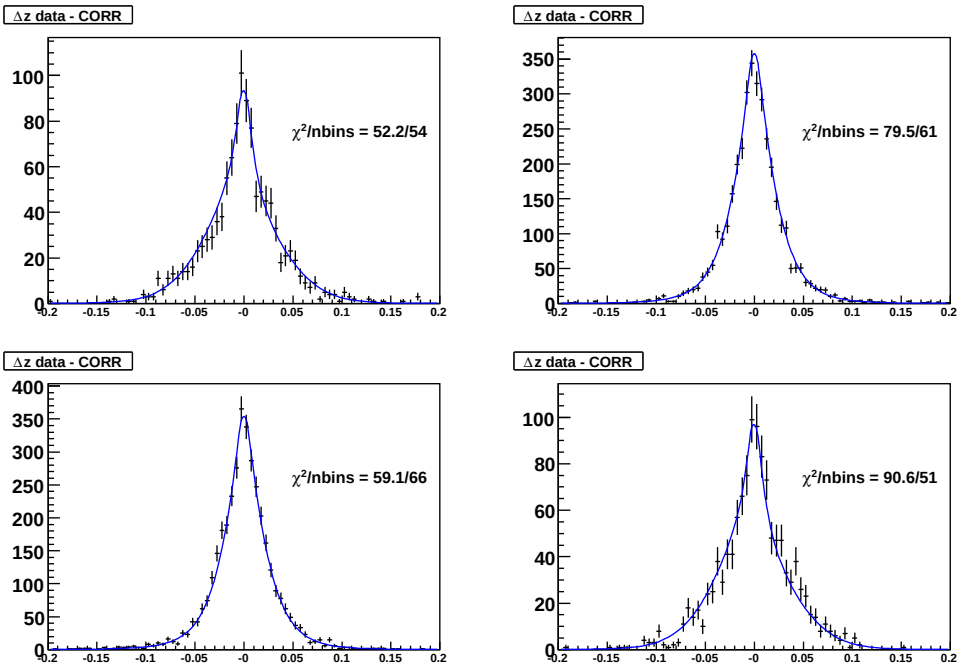

Figure 5.14: Results of the fits to extract correlated background Δt shape projected onto Δz in the four charge and flavour combinations for SVD1 + SVD2 data

	τ_{B^0}	Δm	w^-	
Generator value	1.534	0.507		
SVD1 MC	1.539 ± 0.009	0.488 ± 0.004	0.064 ± 0.003	0.066
SVD2 MC	1.495 ± 0.005	0.506 ± 0.002	0.060 ± 0.002	0.059
SVD1 + SVD2 MC	$+1.506 \pm 0.005$	$+0.502 \pm 0.002$	0.061 ± 0.002	0.061
SVD1 + SVD2 MC(signal only)	1.514 ± 0.005	0.508 ± 0.002	0.061 ± 0.002	0.062
SVD1 + SVD2 MC(signal, primary tracks)	1.510 ± 0.005	0.508 ± 0.002	0.003 ± 0.001	0.003
SVD1 MC*	1.513 ± 0.009	0.503 ± 0.004	0.059 ± 0.002	0.061
SVD2 MC*	1.497 ± 0.005	0.505 ± 0.002	0.060 ± 0.003	0.060
SVD1 + SVD2 MC*	1.501 ± 0.005	0.504 ± 0.002	0.060 ± 0.002	0.060
SVD1 + SVD2 MC(signal only*)	1.510 ± 0.005	0.511 ± 0.002	0.060 ± 0.002	0.061

Table 5.15: Summary of Δm and τ_{B^0} in various SVD samples.(*) stands for the case where $\mathcal{R}_{det}$ parameters from a fit to the Monte Carlo information for correctly tagged signal events ($D^*\pi$ events that have a real fast pion and a real primary lepton in the tag-side.)

5.4 Determination of the B^0-$\bar{B}^0$ mixing frequency Δm and the B^0 lifetime τ_{B^0}

In order to test the fitting procedure, fits are performed with Δm and τ_{B^0} floated and $S^{\pm}$ fixed to zero. We obtain $\Delta m = +0.503 \pm 0.004$ ps^{-1} and $\tau_{B^0} = +1.479 \pm 0.008$ ps, using a data-set of about 657 million $B\bar{B}$ pairs and $\Delta m = +0.502 \pm 0.002$ ps^{-1} and $\tau_{B^0} = +1.506 \pm 0.005$ ps using Monte Carlo corresponding to about 3 times the data sample when both τ_{B^0} and Δm are floated. Figs. 5.15 and 5.16 show the fits projected onto Δz in the four charge and flavour combinations and the mixing asymmetry respectively for both Monte Carlo and data.

The values of Δm and τ_{B^0} from PDG 2006 are:
$\Delta m = 0.507 \pm 0.005$ ps^{-1} and $\tau_{B^0} = 1.530 \pm 0.009$ ps
and the ones used in the Monte-Carlo generation are:
$\Delta m = 0.507$ and $\tau_{B^0} = 1.534$ ps.

In Monte-Carlo, Δm and τ_{B^0} are also obtained for signal only case, using all tracks and using only primary tracks. The results of lifetime-mixing results are summarized in Table 5.15.

The wrong-tag fractions and the mixing values obtained in the signal only case and signal with background case are consistent with each other. Δm is in agreement

	τ_{B^0}	Δm
PDG 2006	1.530 ± 0.009	0.507 ± 0.005
SVD1 data	1.499 ± 0.016	0.501 ± 0.007
SVD2 data	1.473 ± 0.009	0.504 ± 0.004
SVD1 + SVD2 data	1.479 ± 0.008	0.503 ± 0.004

Table 5.16: Summary of Δm and τ_{B^0} in data in various SVD samples.

with the generator value in all the cases. τ_{B^0} is low in the signal only case itself. The $\mathcal{R}_{det}$ parameters obtained using may be the cause of the bias in the neutral B lifetime. In order to check if we recover the correct lifetime with $\mathcal{R}_{det}$ parameters obtained using $D^*\pi$ sample itself, τ_{B^0} is obtained in this case. However, the value is still low. The reason behind this is not properly understood.

In summary, athough Δm is in agreement with the generator value in all the cases, τ_{B^0} obtained from the fit using Monte-Carlo (Table 5.15) is significantly lower than the generator value. However, it will be shown below that τ_{B^0} is not correlated with the CP violation parameters, $S^{\pm}$.

Expt.	Million $B\bar{B}$ pairs	τ_{B^0}	Δm	Ref.
Belle	386	1.493 ± 0.020	0.504 ± 0.006	[23]
BaBar	232	1.480 ± 0.020	0.518 ± 0.010	[19]

Table 5.17: Summary of Δm and τ_{B^0} measurements by previous studies on this mode

We observe low τ_{B^0} in data (Table 5.16) also. The measured lifetime of neutral B^0 in the previous results on this mode (Table 5.17) has been observed to be lower than the world average. However, as demonstrated in Monte-Carlo, the lifetime bias does not affect the CP violation parameters. This is further demonstrated by an ensemble test, described in the next section.

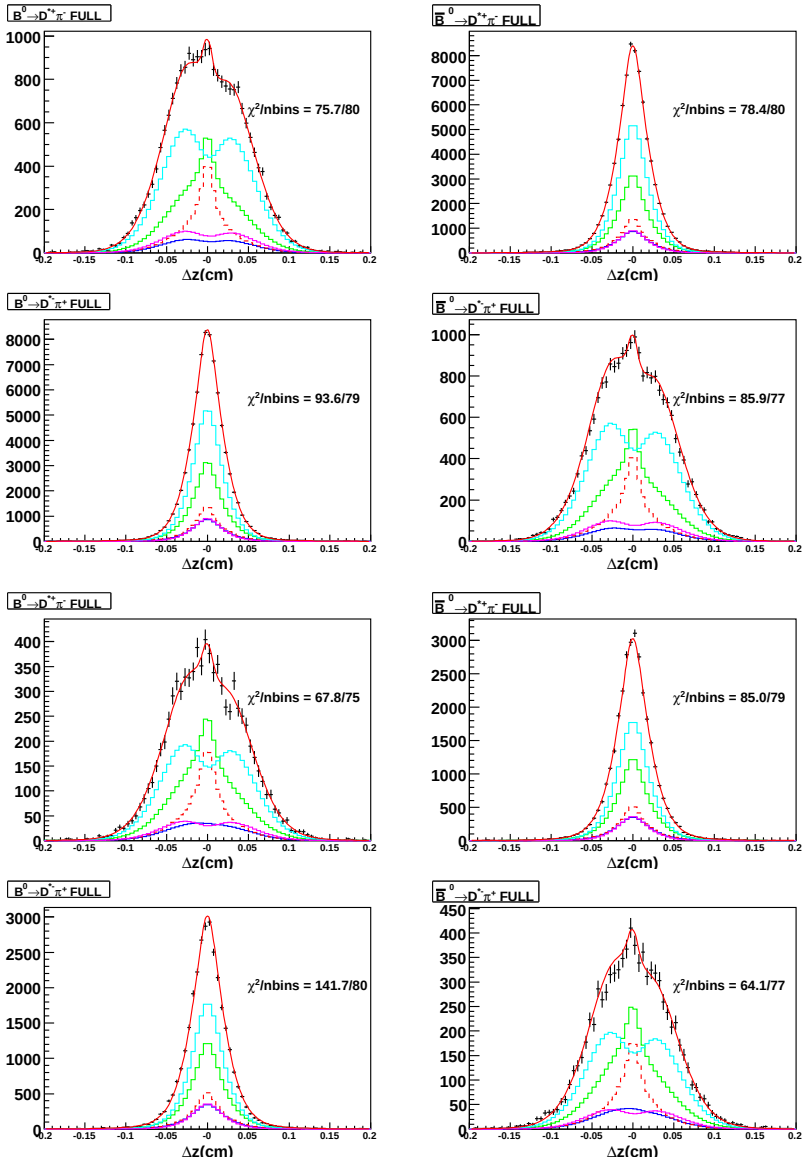

Figure 5.15: Results of the fits to obtain τ_{B^0} and Δm projected onto Δz in the four charge and flavour combinations for SVD1 + SVD2 Monte Carlo (top four) and SVD1 + SVD2 data (bottom four). Total background fraction is shown in green in the Δz projection plots. The contributions are: $D^*\pi$ (light blue), $D^*\rho$ (magenta), correlated background (blue) and uncorrelated background (red).

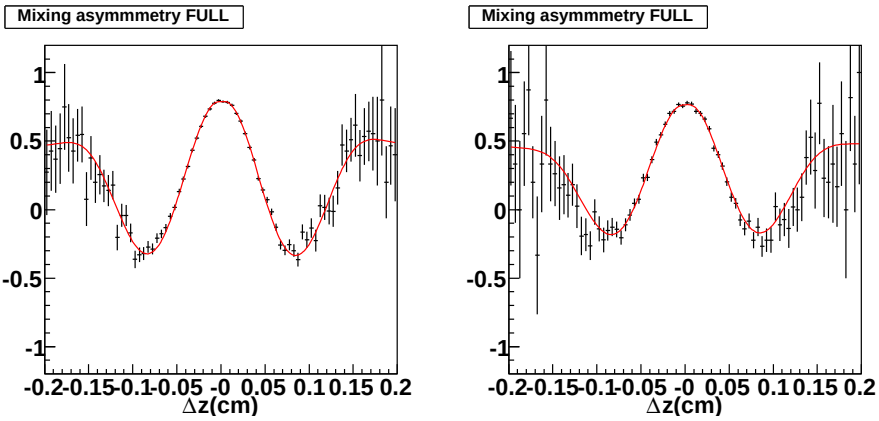

Figure 5.16: Mixing asymmetry for SVD1 + SVD2 Monte Carlo (left) and SVD1 + SVD2 data (right)

Fixed:	None	τ_{B^0}	τ_{B^0}, Δm
S^+	$+0.006 \pm 0.010$	$+0.007 \pm 0.010$	$+0.009 \pm 0.010$
S^-	$+0.014 \pm 0.011$	$+0.013 \pm 0.011$	$+0.011 \pm 0.011$
Δm	$+0.502 \pm 0.002$	$+0.500 \pm 0.002$	$fixed$
τ_{B^0}	$+1.506 \pm 0.005$	$fixed$	$fixed$
w^-	$+0.061 \pm 0.002$	$+0.061 \pm 0.002$	$+0.059 \pm 0.002$
w^+	$+0.061 \pm 0.002$	$+0.061 \pm 0.002$	$+0.059 \pm 0.002$
$\epsilon^{(1)}_{--}$	-3.885 ± 5.706	-4.079 ± 5.766	-4.074 ± 5.742
$\epsilon^{(1)}_{-+}$	-0.237 ± 1.581	-0.191 ± 1.582	-0.117 ± 1.578
$\epsilon^{(1)}_{+-}$	$+1.150 \pm 1.580$	$+1.183 \pm 1.589$	$+1.244 \pm 1.585$
$\epsilon^{(1)}_{++}$	$+5.976 \pm 5.836$	$+5.899 \pm 5.899$	$+5.853 \pm 5.883$
$\epsilon^{(2)}_{--}$	-0.641 ± 3.331	-0.929 ± 3.364	-1.164 ± 3.343
$\epsilon^{(2)}_{-+}$	$+0.197 \pm 0.952$	$+0.239 \pm 0.958$	$+0.307 \pm 0.955$
$\epsilon^{(2)}_{+-}$	$+1.470 \pm 0.968$	$+1.503 \pm 0.973$	$+1.568 \pm 0.971$
$\epsilon^{(2)}_{++}$	-2.734 ± 3.255	-2.882 ± 3.285	-3.002 ± 3.269

Table 5.18: Results of fits to check correlation between $S^{\pm}$, τ_{B^0} and Δm using Monte-Carlo

Fits to the MC with $S^{\pm}$ floated give results consistent with zero, as expected. Results of such fits are shown in Fig. 5.18. These fits are done for 3 cases:

- Δm and τ_{B^0} floated,
- Δm floated and τ_{B^0} fixed (to PDG'06 value) and
- Δm and τ_{B^0} fixed (to PDG'06 values) .

The same-flavour (SF) and opposite-flavour (OF) asymmetries for these 3 cases are shown in Fig. 5.17 to display the CP violation effect. We observe that these asymmetries are very small and consistent with zeto, as expected, in MC.

The fit results are summarized in Table 5.18. All the three cases give similar result for $S^{\pm}$. Hence, we conclude that the correlations between $S^{\pm}$, Δm and τ_{B^0} are small.

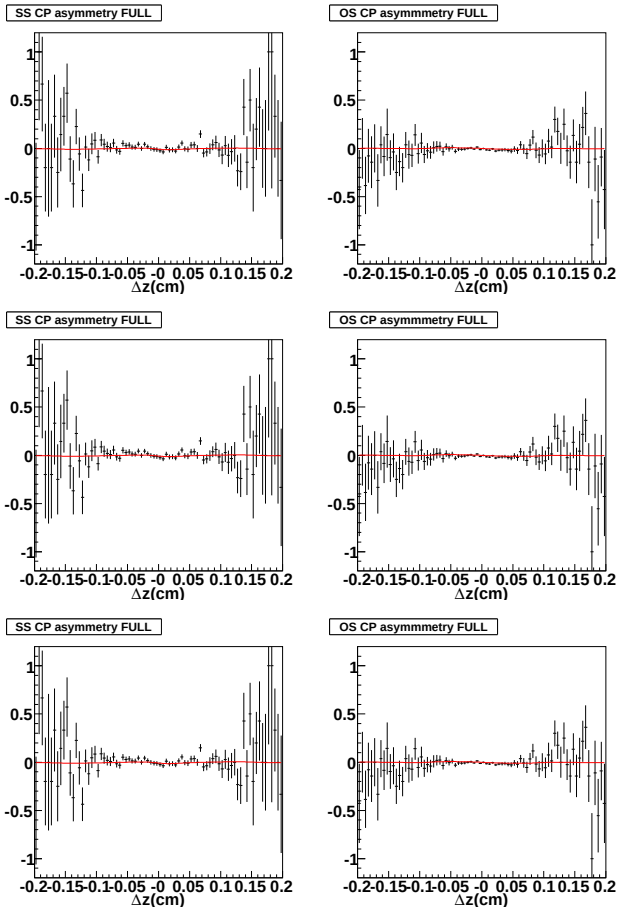

Figure 5.17: Same-flavour (SF) and opposite-flavour (OF) asymmetry plots with Δm and τ_{B^0} floated (top), Δm floated and τ_{B^0} fixed (middle) and Δm and τ_{B^0} fixed (bottom) using MC.

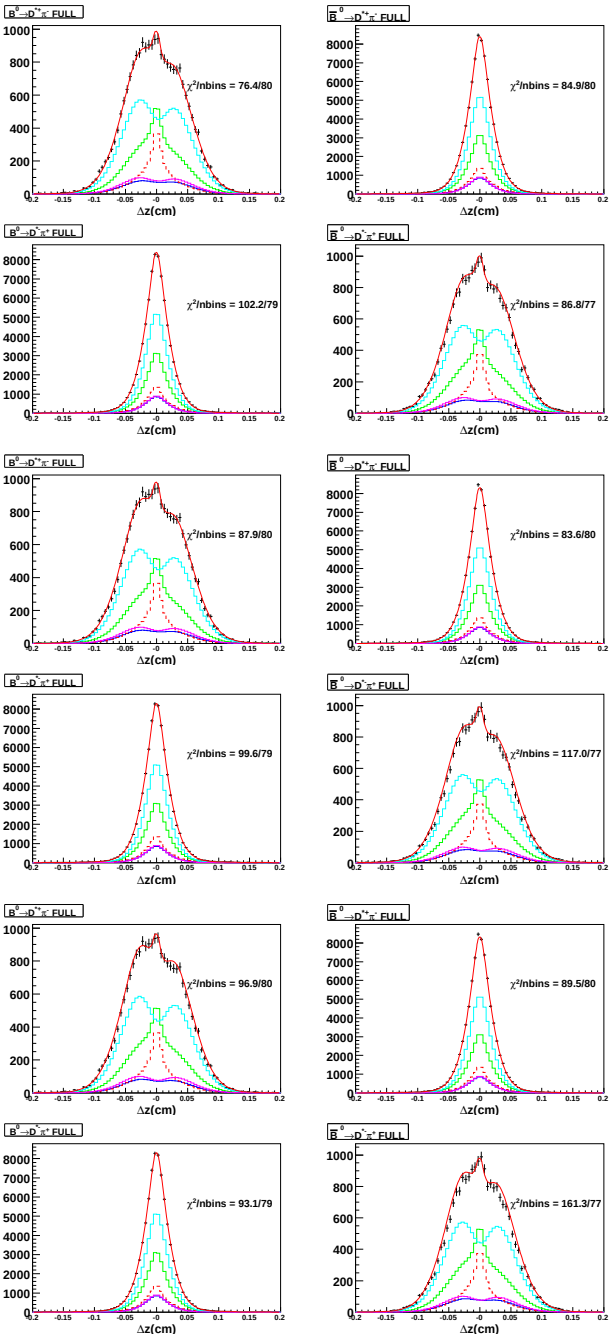

Figure 5.18: Fit plots to obtain $S^{\pm}$ with Δm and τ_{B^0} floated (top), Δm floated and τ_{B^0} fixed (middle) and Δm and τ_{B^0} fixed (bottom) using MC.

5.5 Ensemble tests

We generate several signal samples in order to check if there is any possible bias in the fitter, where we use only a single $D^*\pi$ sample. We generate 100 $D^*\pi$ samples with 5.2 million events each ($\approx 3 \times$ data), using a pre-skim that requires at least 1 lepton with $p_l > 0.8$ GeV. This enables us to simulate and reconstruct using $\approx$ 933,000 events, instead of 5.2 million events. The decays of the D^* and its daughters are generic, while the other B in the event is required to decay generically. The events are simulated with experiment 25 condition.

Fits to obtain $S^{\pm}$ are performed, using the resolution parameters measured from the generic MC with this ensemble is done, with both Δm and τ_{B^0} floated. $\mathcal{R}_{np}$ effect is properly taken into account in the PDF. Fig 5.19 shows the average $S^{\pm}$ and $S^{\pm}/\sigma_{S^+}$ for these cases. Table 5.19 summarizes the $< S^{\pm} >$ and $< S^{\pm} > /\sigma_{S^{\pm}}$ values obtained. The deviations on $S^{\pm}$ ($S^{\pm}/\sigma_{S^{\pm}}$) are fitted with a single Gaussian (Fig. 5.20) and the fit output is summarized in Table 5.20. No significant bias is seen for this ensemble. Thus, this ensemble test confirms that there is no bias in the fit algorithm for the signal only case.

Parameter	value
$< S^+ >$	$+0.003$
$< S^- >$	-0.002
$< S^+ > /\sigma_{S^+}$	$+0.319$
$< S^- > /\sigma_{S^-}$	-0.224

Table 5.19: $< S^{\pm} >$ and $< S^{\pm} > /\sigma_{S^{\pm}}$ values obtained from the fit done with 100 generated signal samples with no CP

Parameter	mean	sigma
S^+/σ_{S^+}	$+0.32 \pm 0.21$	2.13 ± 0.15
S^-/σ_{S^-}	-0.22 ± 0.20	2.04 ± 0.15

Table 5.20: Results of $S^{\pm}$ and $S^{\pm}/\sigma_{S^{\pm}}$ fit with a single Gaussian for the ensemble generated for signal with no CP

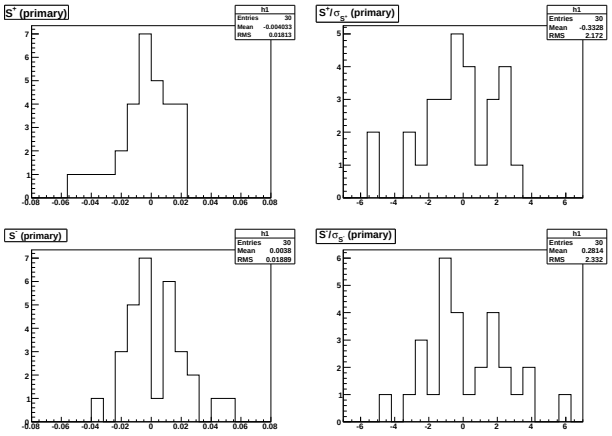

Figure 5.19: $S^{\pm}$ and $S^{\pm}/\sigma_{S^{\pm}}$ distributions obtained from the fit done with 100 generated signal samples with no CP

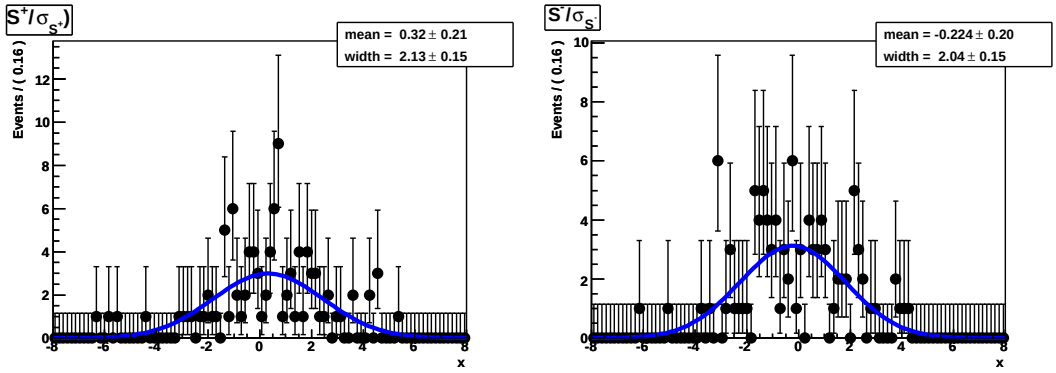

Figure 5.20: $S^{\pm}/\sigma_{S^{\pm}}$ distributions obtained from the fit done with 100 generated signal samples with no CP fitted with a single Gaussian

Fits to obtain $S^{\pm}$ are also performed, using the 100 generated signal samples with no CP with Δm and τ_{B^0} fixed to the PDG'06 values. $\mathcal{R}_{np}$ effect is properly taken into account in the PDF.

Parameter	value
$< S^{+} >$	$+0.004$
$< S^{-} >$	-0.003
$< S^{+} > /\sigma_{S^{+}}$	$+0.485$
$< S^{-} > /\sigma_{S^{-}}$	-0.409

Table 5.21: $< S^{\pm} >$ and $< S^{\pm} > /\sigma_{S^{\pm}}$ obtained from the fit done with 100 generated signal samples with no CP

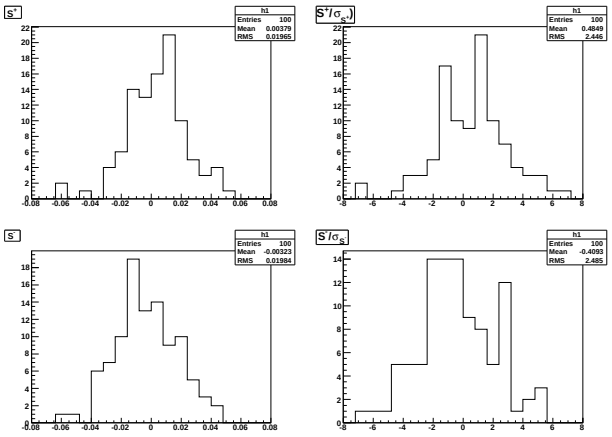

Figure 5.21: $S^{\pm}$ and $S^{\pm}/\sigma_{S^{\pm}}$ plots obtained from the fit done with 100 generated signal samples with no CP

Fig. 5.21 shows the $S^{\pm}$ and $S^{\pm}/\sigma_{S^{\pm}}$ distributions obtained and the results are summarized in Table 5.21.

5.6 Linearity check

In order to check the accuracy of the fitter, a linearity check is performed. Fits to obtain $S^{\pm}$ are done using 11 different Evtgen Monte-Carlo samples, generated with non-zero values of $S^{\pm}$ ($= -2R\sin(2\phi_1 + \phi_3 \pm \delta)$). These samples are generated using SVS_NONCPEIGEN model, with different combinations of R, weak phase w ($= \phi_1 + \frac{\phi_3}{2}$) and strong phase δ. We generate 5.2 million events ($\approx 3 \times$ data) for each case, using a pre-skim that requires at least 1 lepton with $p_l > 0.8$ GeV. This enables us to simulate and reconstruct using $\approx$ 933,000 events, instead of 5.2 million events. The details of the cases generated and the corresponding fit results are given in Table 5.22 and the fit plots for 2 cases are shown in Fig 5.22.

Since there are sign differences between Evtgen and the PDFs used in the analysis, the values of $S^{\pm}$ are calculated from the input values of R, weak phase w and δ as $S^{\pm} = -2R\sin(2w \pm \delta)$. Input values of $\tau_{B^0} = 1.53$ ps (Evtgen default) and $\Delta m = 0.507$ ps^{-1} (PDG 2006) are used. The decays of the D^* and its daughters are generic, while the other B in the event is required to decay semileptonically. The events are simulated with experiment 25 condition. The resolution parameters measured from the generic MC are used for the fit.

The result of the linearity check is summarized in Table 5.22. No significant bias is found.

R	w	δ	S^+ Input	S^+ Output	S^- Input	S^- Output
0.05	+0.785	0.00	-0.10	-0.091 ± 0.009	-0.10	-0.108 ± 0.009
0.05	−0.785	0.00	+0.10	$+0.117 \pm 0.009$	+0.10	$+0.114 \pm 0.009$
0.05	0.00	+1.57	-0.10	-0.09 ± 0.009	+0.10	$+0.101 \pm 0.009$
0.05	0.00	−1.57	+0.10	$+0.108 \pm 0.009$	-0.10	-0.107 ± 0.009
0.05	+1.57	0.00	0.00	$+0.006 \pm 0.009$	0.00	-0.017 ± 0.009
0.05	−1.57	0.00	0.00	-0.007 ± 0.009	0.00	$+0.001 \pm 0.009$
0.05	0.00	0.00	0.00	$+0.007 \pm 0.009$	0.00	-0.008 ± 0.009
0.025	−0.393	−0.785	+0.05	$+0.067 \pm 0.009$	0.00	-0.011 ± 0.009
0.025	−0.393	+0.785	0.00	-0.006 ± 0.009	+0.05	$+0.044 \pm 0.009$
0.025	+0.393	+0.785	-0.05	-0.039 ± 0.009	0.00	$+0.003 \pm 0.009$
0.025	+0.393	−0.785	0.00	-0.006 ± 0.009	-0.05	-0.049 ± 0.009

Table 5.22: Results of fits of linearity check using various $D^{*-}\pi^+$ Evtgen samples, with 5.2 million events generated for each case

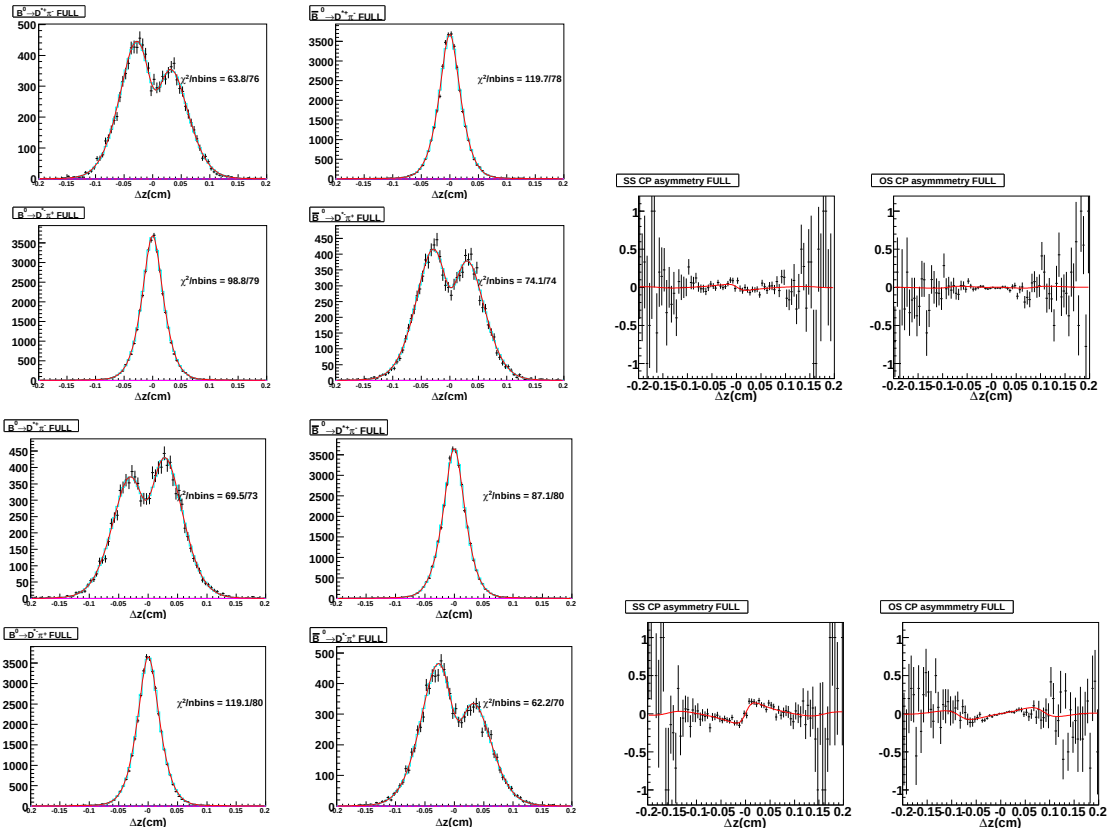

Figure 5.22: Results of the fits to obtain $S^{\pm}$ projected onto Δz in the four charge and flavour combinations and CP asymmetry plots for $R = 0.025$, $w = 0.393$, $\delta = 0.785$ (top) and $R = 0.05$, $w = 0.785$, $\delta = 0.00$ (bottom)

A linearity check is also performed with the generated signal samples, with CP. Fits to obtain $S^{\pm}$ are also done with Δm and τ_{B^0} floated. Figs. 5.23 and 5.24 show the linearity and residual plots for the various cases with $R = 0.05$ and $R = 0.025$ respectively. The inset shows results of a first order polynomial fit in both linearity and residual plots. No significant bias is observed in this case also, when Δm and τ_{B^0} are also floated alongwith $S^{\pm}$. This implies that the lifetime bias does not affect $S^{\pm}$.

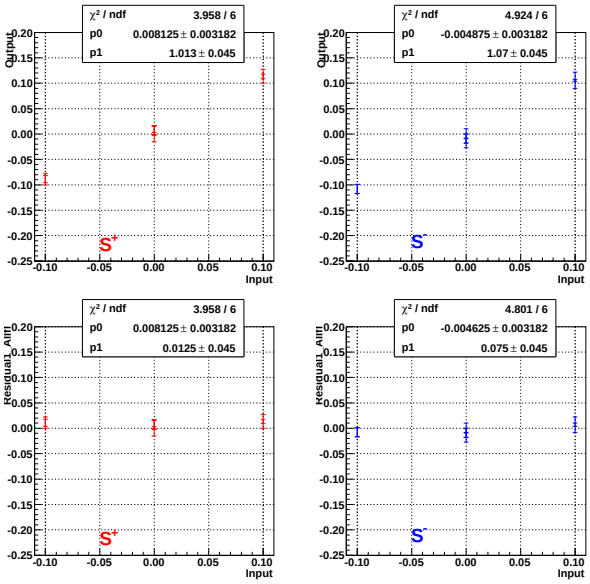

Figure 5.23: Linearity plots (top) for $S^{\pm}$ and residual plots (bottom) for $S^{\pm}$ with Δm and τ_{B^0} floated using the signal samples generated with CP for $R = 0.05$. The inset shows results of a first order polynomial fit in both linearity and residual plots.

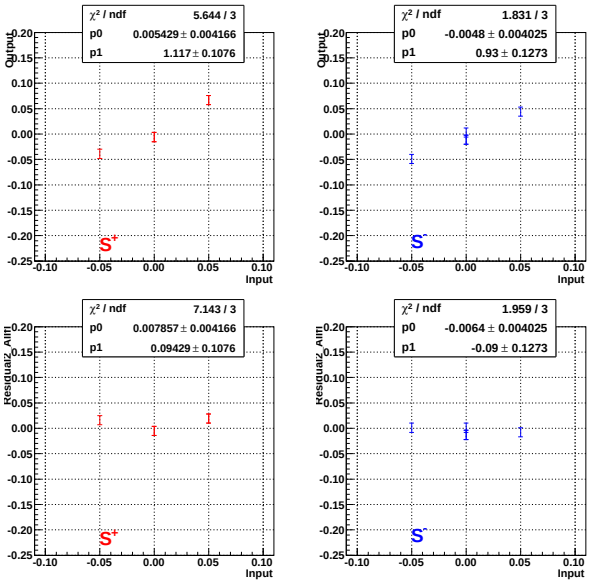

Figure 5.24: Linearity plots (top) for $S^{\pm}$ and residual plots (bottom) for $S^{\pm}$ with Δm and τ_{B^0} floated using the signal samples generated with CP for $R = 0.025$. The inset shows results of a first order polynomial fit in both linearity and residual plots.

5.7 Comparision of $S^{\pm}$ values obtained by previous and our analysis

Analysis	Parameter	Monte-Carlo	Data
Previous [23]	S^+	$+0.028 \pm 0.018$	$+0.048 \pm 0.028$
	S^-	-0.007 ± 0.019	$+0.034 \pm 0.027$
Our(with ϵ_z fixed to 0	S^+	$+0.009 \pm 0.010$	$+0.034 \pm 0.025$
in corr. and unco. bkg. PDFs)	S^-	$+0.011 \pm 0.011$	$+0.060 \pm 0.025$
Our(with non-zero ϵ_z	S^+	$+0.010 \pm 0.010$	$+0.034 \pm 0.025$
in corr. and unco. bkg. PDFs)	S^-	$+0.008 \pm 0.011$	$+0.056 \pm 0.025$

Table 5.23: Comparision of $S^{\pm}$ values obtained by previous and our analysis. We use the case with ϵ_z fixed to 0 in the background PDFs to obtain $S^{\pm}$ values in our analysis.

Table 5.23 shows the $S^{\pm}$ values obtained by previous analyses and ours. In the previous analysis, ϵ_z in the correlated and uncorrelated background PDFs was fixed to non-zero values, obtained from the respective background fit. However, we fix all the ϵ_z in the correlated and uncorrelated background PDFs to 0 in our analysis. So, we checked our results in two cases, namely, with ϵ_z fixed to 0 in the correlated and uncorrelated background PDFs and with non-zero ϵ_z in the correlated and uncorrelated background PDFs, as done in the previous analysis. Comparing our results for the two cases, we observe that $S^{\pm}$ values are consistent with each other both in Monte-Carlo and data. Thus, fixing ϵ_z to 0 in the background PDF's does not affect the $S^{\pm}$ values.

Comparing the results obtained by previous analysis and ours in Table 5.23, we observe that S^+ value is more negative and S^- is more positive in our result. The reason behind it is explained later in this section. The errors on $S^{\pm}$ in data is lesser in our result than in the previous one, because our yield is $\approx 35\%$ higher than the previous analysis due to looser selection criteria. The errors on $S^{\pm}$ in Monte-Carlo is lesser in our case than the previous case due to the looser selection criteria and larger sample. The Monte-Carlo sample used in the previous analysis is about 2×357 fb^{-1} whereas that used in our analysis is 3×531 fb^{-1}. The same data sample of 357 fb^{-1} is used for both previous and our analysis.

In the previous analysis, the non-primary component ($\mathcal{R}_{np}$) in the signal and background PDFs was artificially switched off. We fix this problem in our analysis and properly include the non-primary component in the PDFs. Table 5.24 shows

Analysis	Parameter	without R_{np}	with R_{np}
Previous [23]	S^+	$+0.028 \pm 0.018$	-0.007 ± 0.018
	S^-	-0.007 ± 0.019	$+0.026 \pm 0.019$
Our	S^+	$+0.046 \pm 0.011$	$+0.009 \pm 0.010$
	S^-	-0.026 ± 0.011	$+0.011 \pm 0.011$

Table 5.24: Comparision of $S^{\pm}$ values obtained by previous and our analysis in Monte-Carlo with and without taking non-primary effect properly in PDFs

the $S^{\pm}$ values obtained by the previous analysis and our analysis in both the cases, namely, without and with including the non-primary component in the PDFs in Monte-Carlo. We observe a 4σ deviation from 0 in S^+ in the former case. Similar shift from 0 is also seen in S^+ in the previous analysis in the former case but the shift is not so prominent due to lower statistics used in Monte-Carlo. We observe that S^+ value is more negative and S^- is more positive when $\mathcal{R}_{np}$ effect in the PDFs is properly taken into account. Also, both $S^{\pm}$ values are consistent with 0 in Monte-Carlo, as expected in this case.

Analysis	Parameter	without $\mathcal{R}_{np}$	with $\mathcal{R}_{np}$
Previous [23]	S^+	$+0.048 \pm 0.028$	$+0.015 \pm 0.028$
	S^-	$+0.034 \pm 0.027$	$+0.067 \pm 0.027$
Our	S^+	$+0.075 \pm 0.025$	$+0.034 \pm 0.025$
	S^-	$+0.032 \pm 0.025$	$+0.060 \pm 0.025$

Table 5.25: Comparision of $S^{\pm}$ values obtained by previous and our analysis in data with and without taking non-primary effect properly in PDFs

We observe that S^+ value is more negative and S^- is more positive when $\mathcal{R}_{np}$ effect in the PDFs is properly taken into account in data also for both previous and our analysis (Table 5.25). So, we conclude that the reason behind S^+ becoming more negative and S^- more positive in our result is the fact that we take into account $\mathcal{R}_{np}$ effect in the PDFs is properly.

Table 5.26 shows the $S^{\pm}$ values obtained by our analysis in three cases. The first case is the one used to obtain the $S^{\pm}$ values in our analysis. The second case has tighter polar angle cuts on the hard pion (h) and the tagging lepton (l) as used by the previous analysis including the non-primary component in the PDFs properly. S^+ becomes more positive and S^- more negative as we tighten our selection criteria on the polar angles. However, we do not impose the exact selection criteria (tighter

Parameter	Our selection with $\mathcal{R}_{np}$	Our selection, except tight polar angle cut on h, l with $\mathcal{R}_{np}$	Our selection, except tight polar angle cut on h, l without $\mathcal{R}_{np}$
S^+	$+0.034 \pm 0.025$	$+0.042 \pm 0.025$	$+0.073 \pm 0.025$
S^-	$+0.060 \pm 0.025$	$+0.066 \pm 0.025$	$+0.033 \pm 0.025$

Table 5.26: Comparision of $S^{\pm}$ values obtained by our analysis in data with and without taking non-primary effect properly in PDFs and with and without using the tight polar angle cuts on hard pion h and tagging lepton l (as in previous analysis)

dr cut on soft pion and tighter selection of signal window) used by the previous analysis. Hence, our statistical errors are still higher than that obtained by the previous analysis, using the same data sample. In the third case, where we use the tight polar angle cuts but do not include the R_{np} effect in the PDFs properly, we observe that S^+ value becomes more positive and S^- is more negative.

In summary, the primary reason behind the difference in the $S^{\pm}$ values obtained by the previous analysis and our analysis (Table 5.23) is that we include the non-primary component in the signal and background PDFs properly. An ensemble test to check the effect of $\mathcal{R}_{np}$ on the $S^{\pm}$ values is also performed.

The ensemble test to check the effect of $\mathcal{R}_{np}$ is done using 100 generated signal samples. Fits to obtain $S^{\pm}$ are performed, using 100 generated signal samples with no CP, with Δm and τ_{B^0} fixed to the PDG'06 values in order to check the effect on the $S^{\pm}$ values if $\mathcal{R}_{np}$ effect is not taken into account properly in the PDF.

Parameter	value
$< S^+ >$	$+0.026$
$< S^- >$	-0.026
$< S^+ > / \sigma_{S^+}$	$+2.615$
$< S^- > / \sigma_{S^-}$	-2.523

Table 5.27: $< S^{\pm} >$ and $< S^{\pm} > / \sigma_{S^{\pm}}$ obtained from the fit done with 100 generated signal samples with no CP without $\mathcal{R}_{np}$ effect

Fig. 5.25 shows the $S^{\pm}$ and $S^{\pm}/\sigma_{S^{\pm}}$ distributions obtained from the fit done without taking into account the with $\mathcal{R}_{np}$ effect in the PDF and the results are summarized in Table 5.27.

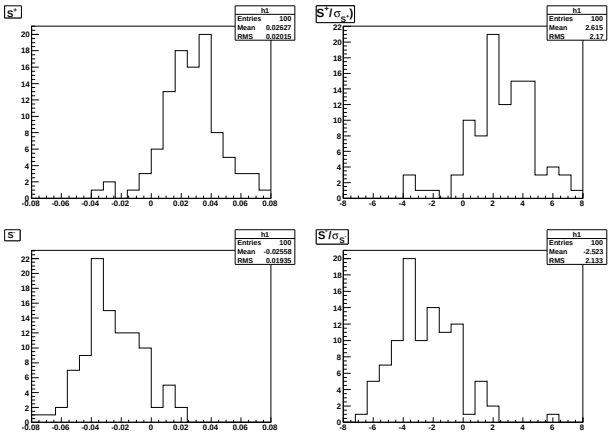

Figure 5.25: $S^{\pm}$ and $S^{\pm}/\sigma_{S^{\pm}}$ plots obtained from the fit done with 100 generated signal samples with no CP without $\mathcal{R}_{np}$ effect

Tables 5.21 and 5.27 show that shift on S^{+} ($S^{+}/\sigma_{S^{+}}$) becomes more positive and shift on S^{-} ($S^{-}/\sigma_{S^{-}}$) becomes more negative when the $\mathcal{R}_{np}$ effect is not taken into account. Thus, we can conclude that if $\mathcal{R}_{np}$ effect is properly taken into account in the signal and background PDF's, shift on S^{+} ($S^{+}/\sigma_{S^{+}}$) becomes more negative and shift on S^{-} ($S^{-}/\sigma_{S^{-}}$) becomes more positive. The inference of the ensemble is in agreement with the observation from the comparision study of the previous result with our result.

5.8 Systematic errors

This analysis is very sensitive to the vertexing bias. We have used Δz offsets in the fits to take care of this bias. In order to estimate the systematic effect of these offsets, we do the CP fit with and without the offsets (Fig. 5.26) using 100 generated $D^*\pi$ signal samples. Tables 5.28, shows the difference between the two results and is quoted as the systematic error due to the vertexing bias.

	S^+	S^-
Difference	$+0.0022$	-0.0007

Table 5.28: CP fit results in MC with and without offset (Δm and τ_{B^0} fixed)

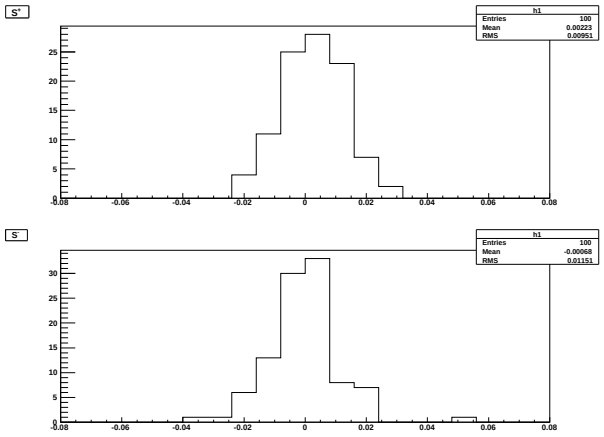

Figure 5.26: Difference between $S^{\pm}$ with and without offset (Δm and τ_{B^0} fixed) obtained from the fit done with 100 generated signal samples with no CP

Other sources of systematic error are the parameters of resolution functions, $\mathcal{R}_k$, $\mathcal{R}_{det}$ and $\mathcal{R}_{np}$, the parameters of uncorrelated and correlated background and physics parameters, Δm, τ_{B^0}, τ_{B^+}, $S^{\pm}_{D^*\rho}$ and $S^{\pm}_{corr}$ that are fixed in the CP fit. Additional systematic errors can result from the fixing of number of bins for the kinematic variables, p_δ and $p_{\|}$ in the yield fit.

Bkg. param.	S^+ $+1\sigma$	S^+ -1σ	S^- $+1\sigma$	S^- -1σ
$(f_{BB})_{unco}$	$+0.0003$	$+0.0000$	$+0.0013$	$+0.0008$
$(f_{mix})_{unco}$	$+0.0002$	$+0.0001$	$+0.0010$	$+0.0010$
$(f_{\delta})_{unco}$	$+0.0001$	$+0.0002$	$+0.0010$	$+0.0011$
$(\tau_{qq})_{unco}$	$+0.0001$	$+0.0002$	$+0.0010$	$+0.0010$
$(A_{qq})_{unco}$	$+0.0004$	$+0.0000$	$+0.0014$	$+0.0007$
$(w^-)_{unco}$	$+0.0002$	$+0.0001$	$+0.0007$	$+0.0014$
$(w^+)_{unco}$	$+0.0002$	$+0.0010$	$+0.0009$	$+0.0012$
$(f_{mix})_{corr}$	$+0.0004$	-0.0004	$+0.0001$	$+0.0006$
$(w^-)_{corr}$	-0.0001	$+0.0000$	-0.0008	$+0.0015$
$(w^+)_{corr}$	$+0.0001$	-0.0002	$+0.0002$	$+0.0005$

Table 5.29: Shifts in S^+ and S^+ when background parameters are varied by $\pm 1\sigma$ (Δm and τ_{B^0} fixed)

Systematic error	S^+	S^-
Varying bkg. parameters by $\pm 1\sigma$	$+0.0007$	$+0.0040$
Floating biases	-0.0118	-0.0052
Total	$+0.0118$	$+0.0065$

Table 5.30: Summary of systematic error due to background parameters

Systematic error	S^+	S^-
Default	0.0344	0.0598
Double $p_{\parallel}$ bins	0.0319	0.0652
Double $p_{\perp}$	0.0315	0.0606

Table 5.31: Summary of systematic error due to varying binning in yield fit

Bkg. param.	S^+ $+1\sigma$	S^+ -1σ	S^- $+1\sigma$	S^- -1σ
${S^{\pm}}_{D^*\rho}$	-0.0058	-0.0005	-0.0028	$+0.0020$
${S^{\pm}}_{corr.}$	-0.0045	-0.0018	-0.0016	$+0.0008$
Δm	-0.0014	-0.0036	-0.0036	-0.0011
τ_{B^0}	-0.0024	-0.0025	-0.0024	-0.0022
τ_{B^+}	-0.0020	-0.0030	-0.0027	-0.0024

Table 5.32: Summary of systematic error due to physics parameters

Systematic error source	S^+	S^-
$\mathcal{R}_{det}$ parameters	0.0015	0.0113
Kinematic smearing	0.0011	0.0075
Non-primary tracks	0.0039	0.0084
Background parameters	0.0118	0.0065
Physics parameters	0.0099	0.0071
Yield fit	0.0038	0.0055
Total without offset	0.0164	0.0194
Δz offset	0.0022	0.0007
Total with offset	0.0166	0.0194

Table 5.33: Summary of possible sources of systematic error

5.9 Conclusion

The CP violation parameters $S^{\pm}$ obtained using 357 fb^{-1} data (when both τ_{B^0} and Δm are fixed to PDG'06 value) are:
$S^{+} = +0.034 \pm 0.027(stat) \pm 0.017(syst)$ and
$S^{-} = +0.060 \pm 0.025(stat) \pm 0.019(syst)$.
Fig. 5.27 shows the fit projections onto Δz in the four charge and flavour combinations and Fig. 5.28 shows the same-flavor and opposite-flavor asymmetry plots for this fit. Monte Carlo sample of about 3 $\times$ 357 fb^{-1} is used for the fit.

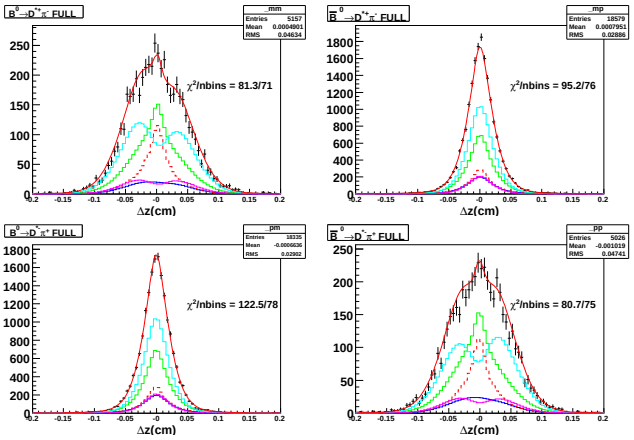

Figure 5.27: Fit projections to obtain $S^{\pm}$ onto Δz in the four charge and flavour combinations with Δm and τ_{B^0} fixed using 357 fb^{-1} data

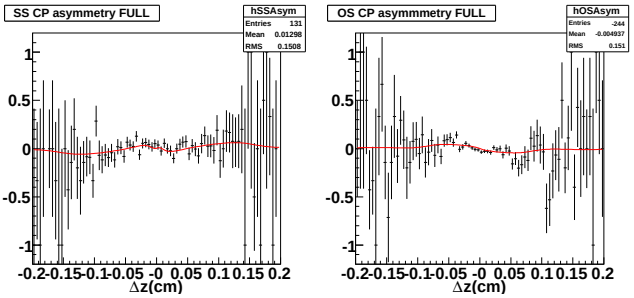

Figure 5.28: Same-flavor (left) and opposite-flavor (right) asymmetry plots o obtain $S^{\pm}$ with Δm and τ_{B^0} fixed using 357 fb^{-1} data

Our plan is to obtain CP violation parameters $S^{\pm}$ using the entire available

data-set of 657 million $B\bar{B}$ pairs and use the kaon-tagged sample along with the lepton-tagged sample to reduce the statistical error. We aim for a publication with this larger data-sample.

Chapter 6

Appendices

6.1 Appendix 1

Gain = $(\epsilon_{D^*\pi(PR)} \times A)/((\epsilon_1 \times A \times BR(D^0 \rightarrow K^-\pi^+)) + (\epsilon_2 \times A \times BR(D^0 \rightarrow K^-\pi^+\pi^0)) + (\epsilon_3 \times A \times BR(D^0 \rightarrow K^-\pi^+\pi^+\pi^-)) + (\epsilon_4 \times B \times BR(D^- \rightarrow K^-\pi^+\pi^+)))$ Here, $\epsilon_{D^*\pi(PR)}$ stands for B candidate reconstruction efficiency using partial reconstruction, A = BR($B \rightarrow D^*\pi$) $\times$ BR($D^* \rightarrow D^0\pi$), B = BR($B \rightarrow D^*\pi$) $\times$ BR($D^* \rightarrow D^+\pi$) and ϵ_1, ϵ_2, ϵ_3, ϵ_4 are the reconstruction efficiencies of $D^0 \rightarrow K^-\pi^+$, $D^0 \rightarrow K^-\pi^+\pi^0$, $D^0 \rightarrow K^-\pi^+\pi^+\pi^-$ and $D^+ \rightarrow K^-\pi^+\pi^+$ decay modes respectively [26].

Decay mode		Efficiency
$D^0 \rightarrow K^-\pi^+$	ϵ_1	0.350
$D^0 \rightarrow K^-\pi^+\pi^0$	ϵ_2	0.115
$D^0 \rightarrow K^-\pi^+\pi^+\pi^-$	ϵ_3	0.160
$D^+ \rightarrow K^-\pi^+\pi^+$	ϵ_4	0.320

Table 6.1: Reconstruction efficiency in three different decay modes of D^0 and one D^+ decay mode

6.2 Appendix 2

Main contributions to the probability that a charged kaon exists in the tag side are:
BR($B^0 \rightarrow D^{*+}X$) $\times$ BR($D^{*+} \rightarrow D^0\pi$) $\times$ BR($D^0 \rightarrow K^+X$) $\approx$ 15%
BR($B^0 \rightarrow D^{*+}X$) $\times$ BR($D^{*+} \rightarrow D^+X$) $\times$ BR($D^+ \rightarrow K^+X$) $\approx$ 4%
BR($B^0 \rightarrow D^{\pm}X$) $\times$ BR($D^{\pm} \rightarrow K^+X$) $\approx$ 3%

$\mathrm{BR}(B^0 \to D^{*0}X\ ) \times \mathrm{BR}(D^{*0} \to D^0X) \times \mathrm{BR}(D^0 \to KX) \approx 1\%$

6.3 Appendix 3

We summarize the results of the fits to determine the resolution function parameters obtained by the previous analysis below. Tables 6.2, 6.3 and 6.4 summarizes the results of $\mathcal{R}_k$ fit parameters.

Parameter	This analysis
Exp. range	7 - 37
Luminosity (in fb^{-1})	≈ 657
$\tau^p_{k1}[0]$	$+0.182 \pm 0.007$
$\tau^p_{k1}[1]$	$+0.012 \pm 0.004$
$\tau^p_{k2}[0]$	$+0.075 \pm 0.002$
$\tau^p_{k2}[1]$	$+0.038 \pm 0.002$
$\sigma_k[0]$	-0.009 ± 0.004
$\sigma_k[1]$	$+0.043 \pm 0.002$
f_k	$+0.718 \pm 0.015$

Table 6.2: R_k parameters determined using Monte Carlo simulation

Parameter	Monte Carlo	Data
SVD1		
Exp. range	7 - 27	7 - 27
Luminosity (in fb^{-1})	$\approx 2 \times 140$	$\approx 2 \times 217$
s_{main}	$+1.001 \pm 0.005$	$+1.016 \pm 0.010$
s_{tail}	$+2.628 \pm 0.067$	$+2.628 \pm 0.097$
f_{tail}	$+0.085 \pm 0.005$	$+0.114 \pm 0.010$
s_{tata}	$+85.220 \pm 1.585$	$+92.834 \pm 2.287$
f_{tata}	$+0.059 \pm 0.004$	$+0.064 \pm 0.006$
sig_{ol}	N/A	N/A
fol_{sgl}	N/A	N/A
$\epsilon_{\Delta z \pm}$	-0.808 ± 0.236	$+5.532 \pm 0.439$
SVD2		
Exp. range	31 - 37	31 - 37
Luminosity (in fb^{-1})	≈ 140	≈ 217
s_{main}	1.054 ± 0.006	1.071 ± 0.006
s_{tail}	3.804 ± 0.077	3.747 ± 0.064
f_{tail}	0.097 ± 0.003	0.135 ± 0.004
s_{tata}	101.881 ± 3.904	159.854 ± 4.8
f_{tata}	0.026 ± 0.001	0.026 ± 0.001
sig_{ol}	N/A	N/A
fol_{sgl}	N/A	N/A
$\epsilon_{\Delta z \pm}$	$+0.563 \pm 0.274$	$+0.287 \pm 0.33$

Table 6.3: R_{det} parameters obtained from the fit to SVD1 and SVD2 $J/\psi \to \mu^+\mu^-$ candidates using Monte Carlo and data separately

Parameter	This analysis
Exp. range	7 - 37
Luminosity (in fb^{-1})	≈ 657
f_p^{UU}	$+0.301 \pm 0.020$
f_p^{UC}	$+0.215 \pm 0.025$
f_p^{NU}	$+0.548 \pm 0.026$
τ_p^0	$+0.628 \pm 0.049$
τ_p^1	$+0.426 \pm 0.100$
τ_n^0	$+0.193 \pm 0.025$
τ_n^1	$+0.039 \pm 0.047$

Table 6.4: R_{np} parameters determined using Monte Carlo simulation. Three different values of f_p are used for the uncorrelated background in the correlated background sideband (UC), the uncorrelated background in the other regions (UU) and all other event types (NU) respectively

6.4 Appendix 4

The CP violation parameters $S^{\pm}$, the B^0-$\bar{B}^0$ mixing frequency Δm and the B^0 lifetime τ_{B^0} obtained by the previous Belle analysis using 357 fb^{-1} data and Monte Carlo corresponding to about 2 times the data sample are summarized below.

Using 357 fb^{-1} data
$\Delta m = 0.503 \pm 0.006$ ps^{-1} when τ_{B^0} is fixed and Δm is floated. $\Delta m = 0.506 \pm 0.006$ ps^{-1} and $\tau_{B^0} = 1.495 \pm 0.012$ ps when both τ_{B^0} and Δm are floated.

Using Monte Carlo corresponding to about 2×357 fb^{-1}
$\Delta m = 0.507 \pm 0.004$ ps^{-1} and $\tau_{B^0} = 1.494 \pm 0.009$ ps when both τ_{B^0} and Δm are floated.

The CP violation parameters $S^{\pm}$ obtained using 357 fb^{-1} data are:
$S^{+} = 0.048 \pm 0.028(stat) \pm 0.017(syst)$ and
$S^{-} = 0.034 \pm 0.027(stat) \pm 0.017(syst)$.

Fits to Monte Carlo using about 2×357 fb^{-1} with $S^{\pm}$ floated give results consistent with zero, as expected.

Bibliography

[1] A. D. Sakharov. "Violation of *CP* Invariance, C asymmetry, And Baryon Asymmetry Of The Universe", Pisma Zh. Eksp. Teor. Fiz. 5:32-35, 1967.

[2] T. D. Lee, Chen-Ning Yang, "Question of Parity Conservation In Weak Interactions", Phys. Rev.,104:254-258, 1956.

[3] C. S. Wu, E. Ambler, R. W. Hayward, D. D. Hoppes, and R. P. Hudson. Experimental Test Of Parity Conservation In Beta Decay. Phys. Rev., 105:1413-1414, 1957.

[4] M. Gell-Mann and A. Pais, Phys. Rev.**97**, 1387(1955).

[5] K. Lande *et al.*, Phys. Rev. **103**, 1901(1956).

[6] J. H. Christenson *et al.*, Phys. Rev. Lett. **13**, 138(1964).

[7] M. Gell-Mann. "A schematic model of Baryons and Mesons.", Phys. Lett.,8:214-215, 1964.

[8] G. Zweig. "An SU(3) model for strong interaction symmetry and it's breaking.2". CERN-TH-412.

[9] S. L. Glashow, J. Iliopoulos, and L. Maiani. "Weak Interactions with Lepton-Hadron asymmetry". Phys. Rev. D **2**, 1285 (1970).

[10] J. J. Aubert *et al.*, Phys. Rev. Lett., **33** 1404 (1974)

[11] J. E. Augustin *et al.*, Phys. Rev. Lett., **33** 1406 (1974)

[12] M. Kobayashi and T. Maskawa, "CP violation in the renormalizable theory of weak interaction". Prog. Theor. Phys. **49** 652 (1973).

[13] L. Wolfenstein, Phys. Rev. D **69** 016006 (2004).

[14] K. Abe *et al.* (Belle Collaboration), Phys. Rev. D **66** (2002) 071102(R).

[15] B. Aubert *et al.* (BaBar Collaboration), Phys. Rev. Lett. **89** (2002) 201802.

[16] I. Dunietz and R.G. Sachs, Phys. Rev. D **37** (1988) 3186, *Erratum*: Phys. Rev. D **39** (1989) 3515; I. Dunietz, Phys. Lett. B **427** (1998) 179.

[17] K.Abe, M.Satpathy and H.Yamamoto, Belle Note 419, hep-ex/0103002

[18] http://www.slac.stanford.edu/xorg/hfag/triangle/ichep2006/index.shtml

[19] B. Aubert, *et al.* (BaBar Collaboration), Phys. Rev. D **71** (2005) 112003

[20] B. Aubert, *et al.* (BaBar Collaboration), hep-ex/0310037

[21] B. Aubert,*et al* (BaBar Collaboration), BaBar CONF 04/018, hep-ex/0408038

[22] K. Abe *et al.* (Belle Collaboration), Belle CONF 0448, hep-ex/0408106

[23] K. Abe *et al.* (Belle Collaboration), Phys. Rev. D **73** (2006) 092003

[24] http://habapmac.kek.jp/svd2/SVD1−SVD2/z.jpg

[25] http://pdg.lbl.gov/

[26] T.R.Sarangi, Belle Note 589

[27] T.Gershon, Belle Note 546

[28] F.Ronga, Belle Note 857

[29] S. Kurokawa and E. Kikutani, Nucl. Instr. Meth. A **499** (2003) 1.

[30] S. Eidelman *et al.* (Particle Data Group), Phys. Lett. B **592**,1 (2004).

[31] A. Morita, OHO '04 (2004).

[32] G. Alimonti *et al.*, Nucl. Instr. Meth. A **453** (2000) 71.

[33] Y. Ushiroda, Nucl. Instr. and Meth. A **511**, 6 (2003).

[34] H. Hirano *et al.*, Nucl. Instr. Meth. A **455** (2000) 294;

[35] R. Früwirth, Nucl. Instr. Meth. A **262** (1987) 444;R. Harr, IEEE Trans. Nucl. Sci. **42** (1995) 134.

[36] T. Iijima *et al.*, Nucl. Instr. Meth. A **453** (2000) 321.

[37] T. Iijima *et al.*, Nucl. Instr. Meth. A **387** (1997) 64.

[38] H. Kichimi *et al.*, Nucl. Instr. Meth. A **453** (2000) 315.

[39] H. Ikeda *et al.*, Nucl. Instr. Meth. A **441** (2000) 401.

[40] K. Hanagaki *et al.*, Nucl. Instr. Meth. A **485** (2002) 490.

[41] A. Abashian *et al.*, Nucl. Instr. Meth. A **449** (2000) 112

[42] R. Santonico and R. Cardarelli, Nucl. Instr. Meth. **187** (1981) 377; Yu. N. Pestov, Nucl. Instr. Meth. **196** (1982) 45; R. Santonico, R. Cardarelli, A. Di Biagio, and A. Lucci, Nucl. Instr. Meth. Phys. Res. Sect. A **263** (1988) 20; E. Gorini, Nucl. Phys. B Proc. Suppl. **23** (1991) 249; L. Antoniazzi *et al.*, Nucl. Instr. Meth. Phys. Res. Sect. A **307** (1991) 312.

[43] A. Abashian *et al.*, Nucl. Instr. Meth. A **491** (2002) 69.

[44] R. Akhmetshin *et al.*, Nucl. Instr. Meth. Phys. Res. Sect. A **455** (2000) 324.